Universität Bremen
Institut für Umweltphysik

Dissertation
zur Erlangung des Grades Doktor der Naturwissenschaften

Investigating NO_2 distributions from satellite, airborne and ground-based measurements: spatiotemporal variability of NO_x emissions and validation of the TROPOMI NO_2 product

Kezia Verena Lange

2023

1. Gutachter: Prof. Dr. John P. Burrows
2. Gutachter: Prof. Dr. Thomas Wagner

Dissertation eingereicht: 16.05.2023
Datum des Kolloquiums: 14.08.2023

Abstract

Tropospheric columns of nitrogen dioxide, NO_2, a key air pollutant, can be retrieved by differential optical absorption spectroscopy (DOAS) measurements. These measurements can be performed from various observation platforms, including satellites, aircraft, cars, and stationary ground-based sites.

Satellite-based measurements provide a global data set of NO_2 pollution on a daily basis. With the high spatial resolution TROPOspheric Monitoring Instrument (TROPOMI) on Sentinel-5 Precursor, small-scale emission sources like individual cities and isolated power plants can be probed. This thesis uses TROPOMI tropospheric NO_2 columns to quantify the variability of NO_x emissions and lifetimes for 50 sources distributed around the world. The retrieved NO_x emissions reproduce the variability seen in power plant stack measurements reasonably well but are generally lower than emission inventory data. The NO_x emission estimates show a clear seasonality, depending on the dominating source type and location. NO_x lifetimes show only a weak seasonal variation but a systematic latitudinal dependence. Except for source regions dominated by industry or power plant emissions, NO_x emissions are found to be reduced on weekends compared to working days but with high variability for the analyzed source regions. Strong short-term reductions in NO_x emissions were attributable to the COVID-19 containment measures.

During the S5P-VAL-DE-Ruhr campaign, airborne imaging, ground-based stationary, and mobile car DOAS measurements were conducted in the Rhine-Ruhr region, one of the NO_2 pollution hotspots in Europe. This data set is used to validate TROPOMI's tropospheric NO_2 vertical column density (VCD) product and investigate the known underestimation. Ground-based stationary and car DOAS measurements are used to evaluate the airborne tropospheric NO_2 VCDs, showing a reasonably good agreement. The airborne data set is compared to the operational (V01.03.02), a modified reprocessed (V02.03.01), and scientific TROPOMI NO_2 products. It is demonstrated that the underestimation of the TROPOMI tropospheric NO_2 VCD has been significantly improved by modifications in the cloud product introduced in the V02.03.01 NO_2 retrieval. The comparison can be further improved with an additional cloud treatment. Minor improvements are achieved by spatially higher-resolved a priori NO_2 profiles and surface reflectivity data.

Mobile DOAS measurements are an excellent option to determine the spatial distribution of NO_2 or other trace gases but are mainly performed on a campaign basis. To perform daily mobile DOAS measurements, a robust small DOAS instrument was developed and installed on a tram in Bremen. The instrument is introduced, and comparisons to measurements from existing instruments are analyzed, which show good agreement. After installation on the tram, the instrument performed measurements all over the Bremen tram network. These measurements are investigated regarding their spatial distribution of NO_2 pollution and are compared to the TROPOMI tropospheric NO_2 VCDs, showing similar NO_2 distribution patterns.

List of publications

Peer reviewed articles:

- Lange, K., Richter, A., Schönhardt, A., Meier, A. C., Bösch, T., Seyler, A., Krause, K., Behrens, L. K., Wittrock, F., Merlaud, A., Tack, F., Fayt, C., Friedrich, M. M., Dimitropoulou, E., Van Roozendael, M., Kumar, V., Donner, S., Dörner, S., Lauster, B., Razi, M., Borger, C., Uhlmannsiek, K., Wagner, T., Ruhtz, T., Eskes, H., Bohn, B., Santana Diaz, D., Abuhassan, N., Schüttemeyer, D., and Burrows, J. P.: Validation of Sentinel-5P TROPOMI tropospheric NO_2 products by comparison with NO_2 measurements from airborne imaging DOAS, ground-based stationary DOAS, and mobile car DOAS measurements during the S5P-VAL-DE-Ruhr campaign, Atmospheric Measurement Techniques, 16, 1357–1389, `https://doi.org/10.5194/amt-16-1357-2023`, 2023.

- Lange, K., Richter, A., and Burrows, J.P.: Variability of nitrogen oxide emission fluxes and lifetimes estimated from Sentinel-5p TROPOMI observations. Atmospheric Chemistry and Physics, 22(4):2745-2767, `https://doi.org/10.5194/acp-22-2745-2022`, 2022

- Liu, S., Valks, P., Pinardi, G., Xu, J., Chan, K. L., Argyrouli, A., Lutz, R., Beirle, S., Khorsandi, E., Baier, F., Huijnen, V., Bais, A., Donner, S., Dörner, S., Gratsea, M., Hendrick, F., Karagkiozidis, D., Lange, K., Piters, A. J. M., Remmers, J., Richter, A., Van Roozendael, M., Wagner, T., Wenig, M., and Loyola, D. G.: An improved TROPOMI tropospheric NO_2 research product over Europe, Atmos. Meas. Tech., 14, 7297–7327, `https://doi.org/10.5194/amt-14-7297-2021`, 2021

- Schreier, S. F., Bösch, T., Richter, A., Lange, K., Revesz, M., Weihs, P., Vrekoussis, M., and Lotteraner, C.: Evaluation of UV–visible MAX-DOAS aerosol profiling products by comparison with ceilometer, sun photometer, and in situ observations in Vienna, Austria, Atmos. Meas. Tech., 14, 5299–5318, `https://doi.org/10.5194/amt-14-5299-2021`, 2021

Selected oral presentations:

- Lange, K., et al., First measurements of spatial NO_2 variability in Bremen with a newly developed tram DOAS instrument, EGU General Assembly 2023, Vienna, Austria, April 2023

- Lange, K., et al., Comparison of GEMS tropospheric NO_2 observations with stationary MAX-DOAS and car DOAS measurements, 13th International GEMS workshop, Seoul, Republic of Korea, November 11, 2022

- Lange, K. et al., Comparison of TROPOMI tropospheric NO_2 observations with airborne, stationary ground-based and car DOAS measurements during the S5P-VAL-DE-Ruhr campaign, Sentinel-5P Mission: 5 years anniversary 10 - 14 October 2022, Taormina, Italy, October 11, 2022
- Lange, K. et al., Representativeness and variability of the ground-based measurements from the S5P-VAL-DE-Ruhr campaign, MAX-DOAS Workshop, online, May 12, 2021
- Lange, K. et al., First results from the Sentinel-5P-VAL-DE-Ruhr campaign in 2020, Sentinel-5P Validation Team Meeting, online, October 20, 2020
- Lange, K. et al., Validation of TROPOMI S5P tropospheric NO_2 using ground-based MAX-DOAS and additional mobile DOAS campaign measurements, Copernicus Sentinel-5 Precursor Validation Team Workshop, Frascati, Italy, November 2019

Selected posters:

- Lange, K., Meier, A. C., Van Roozendael, M., Wagner, T., Ruhtz, T., and Schüttemeyer, D. and the S5p-VAL-DE-Ruhr campaign team: Validation of Sentinel-5P TROPOMI tropospheric NO_2 with airborne imaging, ground-based stationary, and mobile DOAS measurements from the S5P-VAL-DE-Ruhr campaign, EGU General Assembly 2021, online, 19–30 Apr 2021, EGU21-10637, `https://doi.org/10.5194/egusphere-egu21-10637`, 2021.
- Lange, K. Richter, A., Burrows, J.P.: Variability of nitrogen oxide lifetimes and emission fluxes estimated by Sentinel-5P observations, 9th DOAS workshop, online, July 2020
- Lange, K. Richter, A., Burrows, J.P.: Variability of nitrogen oxide emission fluxes and lifetimes estimated by Sentinel-5P TROPOMI observations, AGU fall meeting, online, December 2020
- Lange, K., Richter, A., Burrows, J.P., Lifetimes and emission fluxes of nitrogen oxides from cities and power plants estimated by Sentinel-5P observations, EGU General Assembly 2019, Vienna, Austria, April 2019

Contents

1 | Introduction

Nitrogen oxides NO_x, the sum of nitrogen monoxide NO, and nitrogen dioxide NO_2 are among the most important air pollutants. They are emitted into the atmosphere by natural and anthropogenic sources. Natural sources are lightning, soil microbial processes, and naturally occurring fires. The more significant part is emitted by anthropogenic activities such as biomass burning and using fertilizers but mainly by fossil fuel combustion for transportation, industrial energy production, and residential heating (Seinfeld and Pandis, 2006; John M. Wallace, 2006). NO_x are toxic, and at high concentrations in the troposphere a health hazard, which is especially relevant as most anthropogenic NO_x sources are concentrated in cities and urban areas (Faustini et al., 2014; Xue et al., 2023). Additionally, they substantially impact the tropospheric chemistry and are involved in the formation of tropospheric ozone O_3 and acid rain (Seinfeld and Pandis, 2006). Monitoring and understanding its behavior is of particular importance, especially in cities where high NO_x emissions from multiple sources are found in combination with high population density.

The majority of NO_x emissions are in the form of NO, which in the atmosphere is rapidly converted to NO_2 by the reaction with O_3. During daytime in the boundary layer, NO_x are short-lived, with a lifetime of several hours (Beirle et al., 2011; Valin et al., 2013). This, together with the heterogeneous distribution of sources and variations of meteorological conditions, explains the high spatial and temporal variability observed for atmospheric NO_2.

Due to its spectral characteristics, NO_2 can be observed by differential optical absorption spectroscopy (DOAS) and column densities of NO_2 can be retrieved (Ulrich Platt, 2008). There are various ways to remotely observe atmospheric NO_2 with DOAS instruments, including ground-based stations, moving platforms such as cars, ships, or aircraft, and environmental satellites.

Satellite observations are a very powerful tool as they can provide daily near-global coverage from low-earth orbits and with the upcoming geostationary platforms hourly observations for large areas. However, their spatial and temporal resolution is limited, even with the gradually improving spatial resolution, starting from the Global Ozone Monitoring Experiment (GOME) in 1995 with a ground footprint of $320\,\mathrm{km} \times 40\,\mathrm{km}$ (Burrows et al., 1999) to the recent TROPOspheric Monitoring Instrument (TROPOMI) with a footprint of 5.5 km × 3.5 km and daily global coverage (Veefkind et al., 2012; van Geffen et al., 2020) and the first geostationary instrument GEMS (Geostationary Environment Monitoring Spectrometer) over Asia, launched in 2020 with a footprint of 7 km × 4 km over Korea (Kim et al., 2020) and an hourly temporal resolution.

The first DOAS observations of NO_2 have been performed in the 1970s with stationary ground-based instruments (Noxon, 1975; Platt and Perner, 1980). Today, DOAS instruments are installed at various sites around the world. Measurements from stationary ground-based instruments are limited to their location but provide several measurements per hour and a continuous data set, which can be used for atmospheric science studies and is also very valuable for the validation of satellite data (e.g., Verhoelst et al., 2021).

Measurements from mobile ground-based platforms like cars facilitate investigating the spatial variability of NO_2 in addition to its temporal evolution (e.g., Wagner et al., 2010). Airborne DOAS measurements are an additional possibility for analyzing spatiotemporal variability of NO_2. They can cover large areas such as cities within a few hours and, due to the flight height of usually a few kilometers, with a higher spatial resolution than satellite measurements. Thus, airborne DOAS measurements are also well suited to validate satellite measurements, and to provide insights about their representativeness and the variability of NO_2.

OBJECTIVES OF THIS THESIS:

The high spatial resolution and good signal-to-noise ratio of the TROPOMI NO_2 observations provide the opportunity to disentangle NO_x sources, investigate NO_2 at city scales, and quantify short-term variability of NO_x emissions and lifetimes. This thesis uses two years of the TROPOMI NO_2 data to assess and compare the variability of NO_x emissions and lifetimes for various NO_x sources, consisting of cities, isolated power plants, oil fields, or a mix of sources around the world. Estimated NO_x emissions are compared to power plant stack measurements and emission inventories. The seasonal variability of NO_x emissions and lifetimes are analyzed, and dependencies on the source location and type are investigated. Due to human behavior, NO_x emissions change daily, especially between work and rest days, which is analyzed for the source regions disentangled from the 2 years TROPOMI data set. The TROPOMI data are also used to investigate the short-term variability of NO_x emissions caused by COVID-19 containment measures.

Each data product from satellite sensors needs to be validated, and its accuracy determined to ensure the quality of the product for use in policy-making, research, or other applications such as emission estimates. The first study of this thesis as well as other studies (e.g., Judd et al., 2020; Tack et al., 2021; Verhoelst et al., 2021) have shown a significant underestimation of the TROPOMI tropospheric NO_2 VCD product compared to emission inventories or validation data provided by stationary ground-based and airborne measurements. To better understand this underestimation, this thesis analyzes the data set of the S5P-VAL-DE-Ruhr campaign. The campaign is well suited to address this issue as it took place in the Rhine-Ruhr area, one of the NO_2 pollution hotspots in Europe, and measurements were conducted by several ground-based stationary and mobile car DOAS instruments as well as an airborne imaging DOAS instrument. For the campaign period, the operational and a modified reprocessed TROPOMI NO_2 product as well as several scientific products are available. The different products are used to evaluate the influence of their different retrieval methods and input data sets, such as the cloud treatment, a priori NO_2 vertical profiles, and the surface reflectivity database. The underestimation and possible ways to overcome it are investigated.

Mobile DOAS measurements, such as car and airborne measurements are a valuable source for satellite validation and investigation of spatial and temporal variability of NO_2. However, due to the large effort in performing these measurements, they are often only feasible on a campaign basis. This issue has been addressed by developing a new mobile DOAS instrument constructed for continuous operation on a tram in Bremen. The measurements of the newly developed tram DOAS instrument are used to validate the TROPOMI tropospheric NO_2 product. The spatial distribution of NO_2 pollution in Bremen observed by the tram DOAS and TROPOMI observations is analyzed.

OUTLINE:

The scientific background about the Earth's atmosphere, the problem of air pollution, with a focus on nitrogen oxides and their chemistry, the interaction of the Sun's radiation with the atmosphere, as well as the DOAS measurement technique and fundamental concepts of the instruments used in this thesis are introduced in Chapter 2.

Chapter 3 presents the analysis of NO_x emissions and lifetimes estimated from TROPOMI observations. The analysis includes 50 NO_x source regions distributed over the world. The variability of NO_x emissions and lifetime is investigated regarding seasons, rest and working days, and the COVID-19 period.

Chapter 4 presents the validation results from the S5P-VAL-DE-Ruhr campaign. The campaign site, instruments, and data sets are described. The TROPOMI tropospheric NO_2 VCD product is evaluated with the campaign data set and retrieval issues, and assumptions about input data are investigated.

Chapter 5 gives an overview of the newly developed mobile DOAS instrument for the operation on a tram and investigations of spatiotemporal variability of NO_2 observed by this instrument. Measurements are compared to well-established MAX-DOAS measurements and are used for the validation of the TROPOMI NO_2 product over Bremen.

Chapter 6 provides a summary and conclusions of the main findings of this thesis as well as an outlook with suggestions for possible future studies.

2 | Scientific background

2.1 The Earth's atmosphere

This section provides an overview of the vertical structure and composition of the Earth's atmosphere.

2.1.1 Vertical structure

The Earth's atmosphere can be described as a series of layers characterized by vertical changes in temperature, that are related to chemical and physical processes within the atmospheric layer. Atmospheric pressure and density decrease nearly exponentially with height. Figure 2.1a displays a typical vertical temperature profile of the atmosphere. The lowest layer, known as the troposphere, is characterized by temperatures decreasing with height at an average rate of about $6.5\,\mathrm{K\,km^{-1}}$, down to a minimum known as the tropopause. The temperature and altitude of the tropopause vary depending on latitude and season. While the tropopause in polar regions is at heights of about 8 km having a mean temperature of roughly 220 K, the tropopause can reach a height up to about 16 km and temperatures of about 190 K at the equator. Tropospheric air accounts for approximately 80 % of the atmospheric mass and is relatively well mixed. Above the tropopause, which is followed by the stratosphere, the temperature increases again with altitude, reaching a maximum of about 270 K at the stratopause height around 50 km. Due to the temperature inversion, only little vertical mixing occurs in the stratosphere. The major source of heat is provided by the absorption of ultraviolet (UV) radiation by ozone (O_3). The stratopause is followed by a layer referred to as mesosphere with again decreasing temperature up to the mesopause at 85 −100 km. In all these layers, the major atmospheric constituents have the same mixing ratios. Thus the mean molecular weight of air varies only little with altitude, which justifies grouping these layers into the so-called homosphere. The region above approximately 100 km is called the thermosphere. Here temperature increases very rapidly with height, and the atmospheric composition changes (Brasseur and Solomon, 2005; Wallace and Hobbs, 2006).

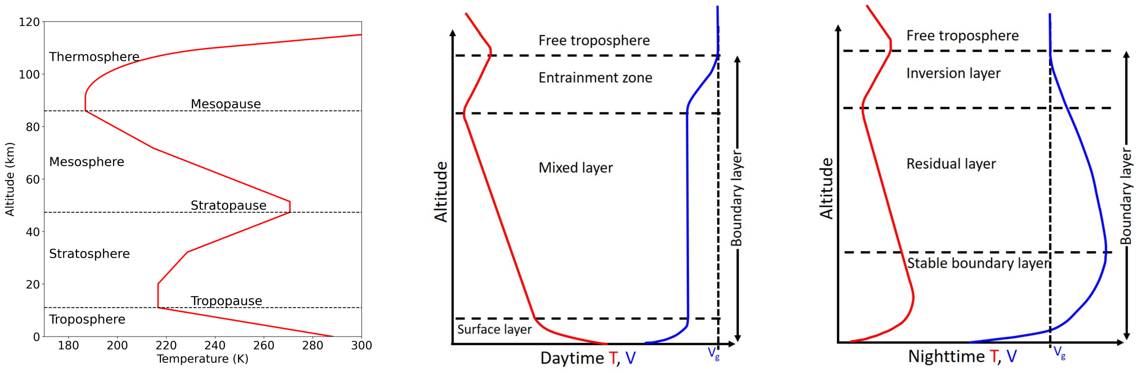

(a) (b) (c)

Figure 2.1: Illustration of the vertical structure of the atmosphere. (a) Temperature profile for the U.S. Standard Atmosphere, with atmospheric layers defined by temperature gradients. Sketch of the vertical structure of the planetary boundary layer at daytime (b) and nighttime (c) for temperature (red), and wind speed (blue) with V_g geostrophic wind. Panel (b) and (c) modified from Wallace and Hobbs (2006).

Of particular interest for this thesis is the troposphere; it contains most of the atmospheric mass, it is the layer where most weather occurs, where we live, and where most air pollutants are emitted. The troposphere can be further divided into the planetary boundary layer, extending from the Earth's surface up to around 1–3 km during the day, and the overlying part, the free troposphere. The boundary layer's extension is quite variable with location and time and is defined by the temperature profile. Figure 2.1 shows a sketch of a typical boundary layer temperature profile during the day (panel b) and during night (panel c). Boundary layer heights can range from 100 to 3000 m in altitude. It is the part of the atmosphere directly influenced by the Earth's surface. Heat transfer creates convection and turbulence. Depending on the vertical temperature structure, turbulent mixing is suppressed or enhanced within the boundary layer. Usually, the structure of the boundary layer shows a pronounced diurnal cycle. Around noon, there is typically a well-mixed convective layer above the surface layer into which emissions are injected. When the Sun sets, radiative cooling induces a stable nocturnal boundary layer, corresponding to radiation inversion. Above this is a residual layer, which contains the substances that were well mixed in the boundary layer during the day but do not mix rapidly with the underlying nocturnal boundary layer or the free troposphere at night. At sunrise, the warming of the Earth's surface causes the mixing of the nocturnal boundary layer and the overlying residual layer. These meteorological changes can thus significantly affect the spatial (horizontal and vertical) and diurnal distribution of pollutants emitted into the atmosphere and their chemistry. Superimposed on these diurnal variations are day-to-day, seasonal, and long-term variations associated with changing weather patterns. Strong and persistent inversions can cause pollutants to accumulate in the boundary layer over several days (Finlayson-Pitts and Pitts Jr, 2000; Wallace and Hobbs, 2006).

Winds in the planetary boundary layer are affected by a combination of surface heating-induced convection, generating turbulence, and by interaction with the surface, inducing wind shear, which is causing mechanical turbulence. The turbulence is largest in the surface layer and decreases towards the free troposphere, where the wind follows the geostrophic wind. Within the surface layer, vertical turbulent fluxes of momentum and heat are assumed to be constant with altitude. Above the surface layer, referred to as the Ekman layer, the wind direction is affected by the Earth's rotation, the Coriolis effect. Additionally, the wind speed generally increases rapidly with altitude, however with a decreasing rate in the upper boundary layer near the free troposphere. The exact vertical distribution of wind speed depends on several parameters, including surface characteristics and atmospheric stability (Wallace and Hobbs, 2006; Seinfeld and Pandis, 2006). Figure 2.1 shows a sketch of a typical wind profile during daytime (panel b) and at night (panel c) in the boundary layer.

2.1.2 Composition

The Earth's atmosphere is composed of a mixture of gases. Today's atmosphere primarily consists of nitrogen (N_2), oxygen (O_2), and argon (Ar), which account for 78.08 %, 20.95 %, and 0.93 %, respectively, thus in total 99.96 % of all molecules in dry air (Wallace and Hobbs, 2006). Table 2.1 provides an overview of the major atmospheric constituents. The abundance of N_2, O_2, and Ar is controlled by the biosphere, with uptake and release as well as degassing from the crust and interior of the Earth and change only over geological time scales. Since N_2 only reacts under the addition of high energy under high temperatures and the O_2 level is a balance of sources and sinks, they are stable within the largest part of the atmosphere. Noble gases are also insensitive to chemical processes (Brasseur and Solomon, 2005; Seinfeld and Pandis, 2006).

A highly variable constituent in the atmosphere is water vapor (H_2O). It is constantly added and removed by relatively fast processes such as evaporation and precipitation, depending strongly on local conditions. The amounts of H_2O can range from almost zero in cold, dry air to about 5 % in warm, humid air (Petty, 2008).

The remaining gaseous constituents represent together less than 1 % of the atmosphere and are referred to as trace gases. Despite their low concentrations, they play a crucial role in atmospheric chemistry and the Earth's radiative balance. The trace gases carbon dioxide (CO_2), methane (CH_4), nitrous oxide (N_2O), and ozone (O_3) are together with H_2O the most important greenhouse gases, which absorb infrared radiation from the Earth's surface and re-emit a portion of this radiation back to the surface, working as a thermal insulator. Despite their low abundances, some trace gases can have due to their high reactivity, a substantial impact on atmospheric chemistry; examples are the hydroxyl

Table 2.1: Major constituents of the atmosphere, in dry tropospheric air at a pressure of 1 atm. Data from Wallace and Hobbs (2006).

Gas	Chemical formula	VMR[a]	Residence time or lifetime	Major sources
Nitrogen	N_2	78.084 %	1.6×10^7 years	Biological
Oxygen	O_2	20.946 %	3000–4000 years	Biological
Argon	Ar	0.934 %	-	Radiogenic
Carbon dioxide	CO_2	419 ppm[b]	3–4 years[c]	Biological, oceanic, combustion
Neon	Ne	18.18 ppm	-	Volcanic
Helium	He	5.24 ppm	-	Radiogenic
Methane	CH_4	1.7 ppm	9 years	Biological, anthropogenic
Hydrogen	H_2	0.56 ppm	~2 years	Biological, anthropogenic
Nitrous oxide	N_2O	0.31 ppm	150 years	Biological, anthropogenic
Carbon monoxide	CO	40–200 ppb	~60 days	Photochemical, combustion, anthropogenic
Ozone (trop.)	O_3	10–100 ppb	Days–weeks	Photochemical
Formaldehyde	HCHO	0.1–1 ppb	~1.5 h	Photochemical
Nitrogen oxides	NO_x	10 ppt–1 ppm	Hours–days	Anthropogenic, solid, lightning
Ammonia	NH_3	10 ppt–1 ppb	2–10 days	Biological
Sulfur dioxide	SO_2	10 ppt–1 ppb	Days	Photochemical, volcanic, anthropogenic
Hydroxyl radical	OH	0–0.4 ppt	~1 s	Photochemical
Hydroperoxyl radical	HO_2	0–5 ppt	-	Photochemical

[a] Volume mixing ratio, fraction of volume of air occupied by gas. Units: Percentage, parts per million (ppm), parts per billion (ppb), parts per trillion (ppt).

[b] Annual mean 2022. Data source: Dr. Pieter Tans, NOAA/GML (gml.noaa.gov/ccgg/trends/) and Dr. Ralph Keeling, Scripps Institution of Oceanography (scrippsco2.ucsd.edu/).

[c] time until a CO_2 molecule is taken up by plants or dissolved in the ocean. 50–200 years for atmospheric CO_2 to adjust to a new equilibrium if sources or sinks are changed.

radical (OH), O_3, and also nitrogen oxides NO_x, which will be investigated in this thesis (Seinfeld and Pandis, 2006; Wallace and Hobbs, 2006).

In addition to gases, the atmosphere also contains aerosols, which are defined as fine solid or liquid particles suspended in a gas. Atmospheric aerosol particles range in size from a few nanometers to tens of micrometers in diameter (Seinfeld and Pandis, 2006). They originate from natural (e.g., sea salt and dust) and anthropogenic sources such as combustion and biomass burning (Wallace and Hobbs, 2006).

2.1.3 Spatial distribution and lifetime

The atmospheric constituents' horizontal and vertical spatial distribution is determined by several factors, mainly source distribution, transport, and lifetime determined by removal processes and transport. Sources can be chemical reactions within the atmosphere, biological and volcanic activities, radioactive decay, and anthropogenic activities. After the release, the constituent is transported until it is transformed respectively removed from the atmosphere. Gases are removed by chemical reactions, biological activity, physical processes, and deposition. The average lifetime of atmospheric constituents can range from seconds to millions of years, depending on the effectiveness of the removal mechanisms of an atmospheric constituent. The lifetime is defined as the ratio of the amount of the constituent and the removal rate (Seinfeld and Pandis, 2006)

$$\tau = \frac{\text{Mass}}{\text{Removal rate}}. \tag{2.1}$$

The removal rate can have different contributions, such as chemical reactions, photolysis, or physical processes. If multiple processes contribute to the removal, the overall lifetime τ in terms of for example the two individual lifetimes τ_A and τ_B is given by:

$$\frac{1}{\tau} = \frac{1}{\tau_\mathrm{A}} + \frac{1}{\tau_\mathrm{B}}. \tag{2.2}$$

Further details about atmospheric lifetimes and the determination of the $\mathrm{NO_x}$ lifetime are given in Sect. 2.2.2.1. Generally, the individual lifetime can deviate from the average lifetime, depending on the removal mechanism, especially if removal processes are locally concentrated. Depending on their lifetime, the atmospheric constituents show very different levels of spatial and temporal variability. $\mathrm{N_2}$ and $\mathrm{O_2}$ are so long-lived that they are well mixed and evenly spatially distributed. For gases with shorter lifetime such as $\mathrm{NO_2}$, spatial and temporal distributions are more variable (Seinfeld and Pandis, 2006; Wallace and Hobbs, 2006).

2.2 Air pollution

Air pollution is the contamination of air by any chemical, physical or biological substance that modifies the natural characteristics of the atmosphere and can be harmful to human health and the environment. Polluting substances of major public health concern include particulate matter, carbon monoxide, ozone, nitrogen dioxide, and sulfur dioxide (World Health Organization, 2023). The largest source of air pollutants are combustions in power plants, smelters, vehicles, and burning of vegetation. In addition to the immediate health risk, air pollution is also closely linked to environmental issues such as climate change, stratospheric ozone depletion, or acidification (Wallace and Hobbs, 2006). To address the issue of air pollution, detailed knowledge about the pollutants, their sources, their role in atmospheric chemistry, and their spatial and temporal variability is important.

Daytime chemistry of both polluted and clean air is driven by oxidation, especially by the hydroxyl radical (OH), which reacts rapidly with many atmospheric trace gases (Finlayson-Pitts and Pitts Jr, 2000). In the global troposphere, dominant sinks for OH are the oxidation of CO and CH_4. Because of its reactivity, the average lifetime of an OH molecule in the atmosphere is only about 1 s (see Table 2.1). Since a reaction with OH is the major sink for most atmospheric trace gases, it is also called the atmosphere's detergent (Wallace and Hobbs, 2006).

In the troposphere, OH is produced when O_3 is photolyzed at short wavelengths into molecular oxygen and energetically excited oxygen atoms $O(^1D)$

$$O_3 + h\nu \xrightarrow{\lambda < 320\,\mathrm{nm}} O_2 + O(^1D). \tag{2.3}$$

Most of the produced $O(^1D)$ atoms dissipate their excess energy as heat and eventually recombine with O_2 to form O_3, which has no chemical effect (called a null cycle). Even if only a small fraction of about 1 % of $O(^1D)$ reacts with water vapor

$$O(^1D) + H_2O \longrightarrow 2\,OH \tag{2.4}$$

it is the major source of OH in the atmosphere, which also implies that O_3 is critical for the self-cleaning ability of the atmosphere.

This thesis focuses on measurements of the air pollutant NO_2. Therefore, an overview of the role of NO_x in the atmosphere and its chemistry is given below.

2.2.1 Nitrogen oxides (NO_x)

Nitrogen oxides ($NO_x = NO + NO_2$) play a key role in atmospheric chemistry, air quality, and climate. Tropospheric NO_2 can lead to O_3 formation, which is known as harmful to human health, causing pollution-related deaths and contributes to global warming. NO_x are emitted into the atmosphere by natural processes such as lightning, microbial processes in soils, and naturally occurring wildfires, as well as anthropogenic activities including fossil-fuel combustion from traffic, residential heating, and the industry and energy sectors (Wallace and Hobbs, 2006; Seinfeld and Pandis, 2006). Figure 2.2 provides an overview of the global anthropogenic source composition of NO_x emissions given in the Emissions Database for Global Atmospheric Research (EDGAR) for the year 2015 (EDGAR Emissions Database for Global Atmospheric Research, last access: 2 April 2023). The majority of emissions originates from the transport sector which can be divided into road and non-road transport. The transport sector is followed by the power industry sector, causing 24.7 % of the anthropogenic NO_x emissions. The 'other industrial combustion' sector comprises NO_x emissions mainly from the manufacturing industry, transformation industry, and oil refineries. Smaller amounts of NO_x emissions can be attributed to the agricultural, residential and waste sector.

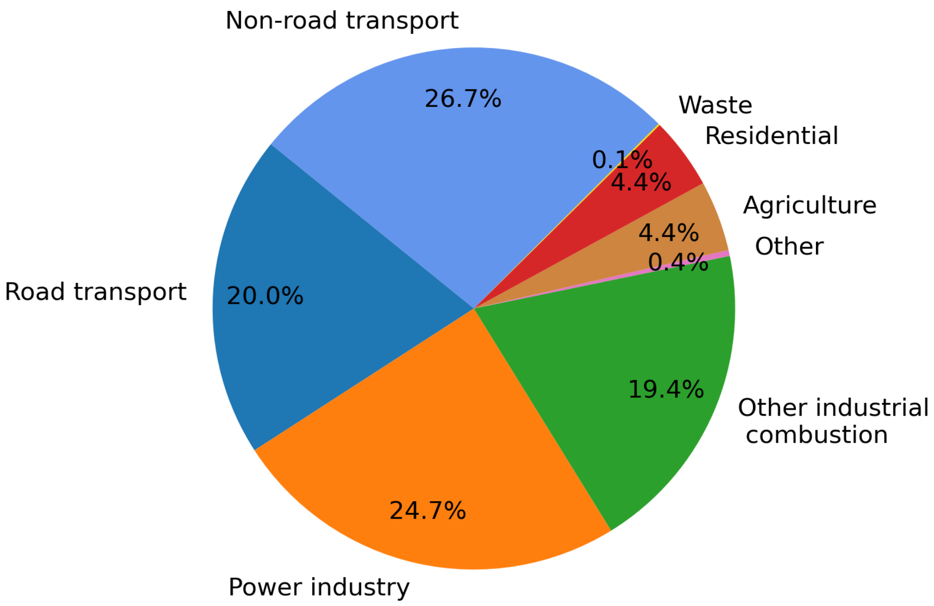

Figure 2.2: Global anthropogenic sources of NO_x emissions provided in the EDGAR emission inventory for 2015 (EDGAR Emissions Database for Global Atmospheric Research, last access: 2 April 2023).

In urban agglomerations where NO_x emissions are high, the bulk of atmospheric NO_x is located within the boundary layer, close to the surface. In rural, unpolluted regions, most atmospheric NO_2 is found in the stratosphere, between 25 and 35 km altitude (Seinfeld and Pandis, 2006). Figure 2.3 shows vertical NO_2 profiles from the global chemistry transport model TM5 (Williams et al., 2017). NO_2 partial columns are plotted from the surface up to 60 km for a polluted scenario in the Rhine-Ruhr metropolitan region in North Rhine-Westphalia, Germany and a background region over the Atlantic Ocean. Since most NO_x are emitted in the troposphere, tropospheric NO_x chemistry is of particular interest and is described in the following section.

2.2.2 NO_x chemistry in the troposphere

NO_x is emitted into the atmosphere primarily as NO. With the high temperatures during combustion processes, NO is formed resulting from the interaction of N_2 present in the

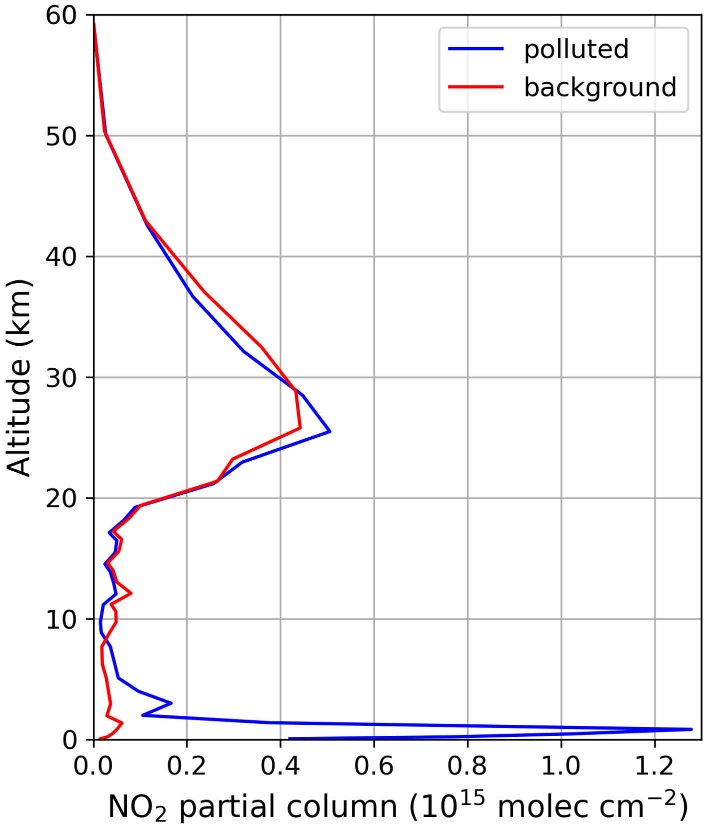

Figure 2.3: Vertical NO_2 profiles from the surface up to 60 km. Data are plotted from the TM5 model on 17 September 2020 for a polluted region in the Rhine-Ruhr metropolitan region (50.91° N, 6.41° E; blue) and a background region over the Atlantic Ocean (50.91° N, 40° W; red).

fuel with oxygen (fuel NO) and the oxidation from atmospheric N_2 (thermal NO).

$$\mathrm{O_2 + M \rightleftarrows 2\,O + M} \tag{R 1}$$

$$\mathrm{O + N_2 \rightleftarrows NO + N} \tag{R 2}$$

$$\mathrm{N + O_2 \rightleftarrows NO + O} \tag{R 3}$$

$$\mathrm{O_2 + N_2 + M \rightleftarrows 2\,NO + M} \tag{R 4}$$

NO_2 is emitted only in small amounts from combustion processes along with NO. However, it is produced rapidly in the atmosphere when NO reacts with O_3. During the day, NO rapidly establishes an equilibrium with NO_2 through the following null cycle.

$$\mathrm{NO + O_3 \longrightarrow NO_2 + O_2} \tag{R 5}$$

$$\mathrm{NO_2} + h\nu \xrightarrow{\lambda < 405\,\mathrm{nm}} \mathrm{NO + O} \tag{R 6}$$

$$\mathrm{O + O_2 + M \longrightarrow O_3 + M} \tag{R 7}$$

M represents an inert molecule that absorbs excess molecular energies. These reactions will reach a point where NO_2 is destroyed and reformed so fast that a steady-state cycle is maintained. Because of the rapid interconversion between NO and NO_2 on a time scale of a minute during daytime, they are often summarized as NO_x (Jacob, 1999). The equation linking the concentrations of NO, NO_2, and O_3 in steady-state is known as the Leighton relationship or photo stationary state relation. The steady-state $[NO]/[NO_2]$ ratio from the NO_x cycle is given by

$$\frac{[\mathrm{NO}]}{[\mathrm{NO_2}]} = \frac{J_{\mathrm{NO_2}}}{k_{\mathrm{NO+O_3}} \cdot [\mathrm{O_3}]} \tag{2.5}$$

depending on the photolysis frequency of NO_2 ($J_{\mathrm{NO_2}}$), which depends on the light intensity, the rate constant for the reaction of NO with O_3 ($k_{\mathrm{NO+O_3}}$), which depends on temperature, and the ozone concentration $[O_3]$. Under typical urban conditions and noontime sun at 298 K, typical $[NO]/[NO_2]$ ratios of approximately 0.32 are expected, thus most NO_x are present in the form of NO_2. Differences are expected close to sources. Since the photolysis frequency is highest at noon, it is the time when NO represents the largest possible proportion of NO_x. Due to the temperature dependence of $k_{\mathrm{NO+O_3}}$ and higher NO_2 photolysis rates with increasing altitudes, the $[NO]/[NO_2]$ shifts towards NO with height (Seinfeld and Pandis, 2006).

During nighttime, all NO reacts rapidly with O_3 forming NO_2 (see R 5). Since photolysis is not possible, NO_2 can react with O_3 producing the nitrate radical NO_3.

$$\mathrm{NO_2} + \mathrm{O_3} \longrightarrow \mathrm{NO_3} + \mathrm{O_2} \tag{R 8}$$

During nighttime, NO_3 replaces OH as the major reactive oxidant. Its lower reactivity compared to OH is compensated by a higher concentration. NO_3 reacts with NO_2 forming dinitrogen pentoxide N_2O_5.

$$\mathrm{NO_3} + \mathrm{NO_2} + \mathrm{M} \rightleftarrows \mathrm{N_2O_5} + \mathrm{M} \tag{R 9}$$

This can only happen at night because NO_3 is otherwise quickly photolyzed. N_2O_5 can thermally decompose back to NO_3 and NO_2, establishing an equilibrium on a timescale of only a few minutes. With decreasing temperature and increasing NO_2 levels, the equilibrium is shifted more to the right, causing a faster removal of NO_2 in the free troposphere. The N_2O_5 reacts with water on particles to produce HNO_3

$$\mathrm{N_2O_5} + \mathrm{H_2O\,(s)} \longrightarrow 2\,\mathrm{HNO_3} \tag{R 10}$$

which is finally removed from the atmosphere by wet deposition, contributing to acid rain formation (Seinfeld and Pandis, 2006; Wallace and Hobbs, 2006).

During the day NO_2 is oxidized by OH forming HNO_3

$$\mathrm{NO_2 + OH + M \longrightarrow HNO_3 + M} \tag{R 11}$$

which is removed by precipitation and is the principal daytime removal path of NO_2 (Seinfeld and Pandis, 2006).

2.2.2.1 NO_x lifetime

Under surface conditions (300 K, 1 atm), with $k_{\mathrm{OH+NO_2}} \approx 1 \times 10^{-11}\,\mathrm{cm^3\,molec^{-1}\,s^{-1}}$, and OH concentrations of about $10^6\,\mathrm{molec\,cm^{-3}}$, the resulting lifetime of NO_2

$$\tau_{\mathrm{NO_2}} = \frac{1}{k_{\mathrm{OH+NO_2}} \cdot [\mathrm{OH}]} \tag{2.6}$$

is approximately one day (Seinfeld and Pandis, 2006). Despite its crucial role as the primary NO_x sink, the rate constant $k_{\mathrm{OH+NO_2}}$ has remained difficult to determine under atmospheric conditions (Stavrakou et al., 2008). The $k_{\mathrm{OH+NO_2}}$ rate constant used in Seinfeld and Pandis (2006) has been recently revised to $2.8 \times 10^{-11}\,\mathrm{cm^3\,molec^{-1}\,s^{-1}}$ (Burkholder et al., 2020), which results in a shorter lifetime of NO_2 of around 10 h. The NO_x lifetime is given by applying Eq. 2.5 (Seinfeld and Pandis, 2006):

$$\begin{aligned} \tau_{\mathrm{NO}_x} &= \tau_{\mathrm{NO_2}} \left[1 + \frac{[\mathrm{NO}]}{[\mathrm{NO_2}]}\right] \\ &= \tau_{\mathrm{NO_2}} \left[1 + \frac{J_{\mathrm{NO_2}}}{k_{\mathrm{NO+O_3}} \cdot [\mathrm{O_3}]}\right] \end{aligned} \tag{2.7}$$

The tropospheric lifetime depends strongly on the involved species O_3 and OH, and the Leighton ratio, i.e. also temperature and photolysis frequency $J_{\mathrm{NO_2}}$, thus the actinic flux. Since there is a nonlinear relationship between the tropospheric concentrations of OH and NO_x which again depends in a complex fashion on the NO_x concentrations, the lifetime is non-linearly dependent on NO_x concentrations (Valin et al., 2013; Laughner and Cohen, 2019).

Consequently, the NO_x lifetime is highly variable within space and time. Diurnal, seasonal, and latitudinal differences, as well as location-specific variations are expected, depending on the chemical regime active within the given airmass (Stavrakou et al., 2008; Laughner and Cohen, 2019). Generally, NO_x has a relatively short tropospheric lifetime, ranging from a few hours close to the surface to weeks in the free troposphere (Valin et al., 2013; Seinfeld and Pandis, 2006). An estimation of the NO_x lifetime using satellite observations will be given in Chapter 3.

Other important reaction paths in the presence of NO_x are oxidation of carbon-containing compounds such as carbon monoxide CO, methane CH_4, and volatile organic compounds (VOCs), which result in O_3 production. The O_3 concentration increases with increasing NO_2 and/or increasing photolysis frequency (see Leighton relationship Eq. 2.5); this is further enhanced in a scenario with reduced carbon compounds. Details can be found, e.g., in Seinfeld and Pandis (2006).

2.2.3 NO_x chemistry in the stratosphere

Although this thesis mainly focuses on tropospheric NO_x, a brief overview of stratospheric NO_x chemistry is given here; further details can be found in, e.g., Brasseur and Solomon (2005). The main source of stratospheric NO_x is nitrous oxide N_2O. N_2O is mainly produced by microbiological activity in soils and the ocean. Since it is very stable in the troposphere, it can reach the stratosphere. In the stratosphere, most of the N_2O is photolyzed.

$$\mathrm{N_2O} + h\nu \longrightarrow \mathrm{N_2} + \mathrm{O(^1D)} \tag{R 12}$$

The remaining N_2O can react with $O(^1D)$ to produced NO

$$\mathrm{N_2O} + \mathrm{O(^1D)} \longrightarrow 2\,\mathrm{NO} \tag{R 13}$$

which is the main source of NO_x in the stratosphere. While tropospheric NO_x can increase the O_3 concentration, stratospheric NO_x causes O_3 depletion in the ozone layer (Seinfeld and Pandis, 2006). The main NO_x cycle (reaction R 5-R 7) also takes place, but in the middle and upper stratosphere, the concentration of O is high enough for reaction R 6 to be replaced by

$$\mathrm{NO_2} + \mathrm{O} \longrightarrow \mathrm{NO} + \mathrm{O_2}. \tag{R 14}$$

During the night, the reaction of NO_2 with O_3 forms NO_3, which reacts with NO_2 to N_2O_5, which slowly decreases the NO_2 concentration during nighttime.

$$\mathrm{NO_2} + \mathrm{O_3} \longrightarrow \mathrm{NO_3} + \mathrm{O_2} \tag{R 15}$$

$$\mathrm{NO_2} + \mathrm{NO_3} + \mathrm{M} \longrightarrow \mathrm{N_2O_5} + \mathrm{M} \tag{R 16}$$

Unlike the tropospheric situation, where N_2O_5 is in combination with water and precipitation a sink of tropospheric NO_x, N_2O_5 in the stratosphere represents a reservoir of NO_x with a relatively long lifetime. In the morning, NO_2 is photolyzed until an equilibrium between NO_2 and NO is reached, resulting in a minimum NO_2 concentration. During the day, the slow photochemical destruction of the N_2O_5 reservoir leads to an almost linear increase in NO_2 concentration (Seinfeld and Pandis, 2006; Brasseur and Solomon, 2005).

2.3 Atmospheric radiation

The retrieval of atmospheric trace gas concentrations such as NO_2 with remote sensing measurement techniques like the differential optical absorption spectroscopy (DOAS), as applied in this thesis, uses the interaction of solar radiation with matter on its light path (Burrows et al., 2011). Some characteristics of solar radiation and its interaction with Earth's atmosphere components are briefly described in the following, before the DOAS measurement technique is described in more detail.

2.3.1 Solar radiation

The Sun's high temperature causes it to permanently emit electromagnetic radiation in a broad energy spectrum. Following Planck's law for black body radiation

$$B_\lambda(T) = \frac{2hc^2}{\lambda(e^{hc/k_\mathrm{B}\lambda T} - 1)} \tag{2.8}$$

the Sun's average surface temperature of 5777 K determines the range of this spectrum and causes a peak of emission at a wavelength of approximately 500 nm, which can be calculated with Wien's law. Most of the radiation's energy is therefore located in the visible range from 400 to 700 nm, but significant portions of ultraviolet (UV) and infrared (IR) radiation are also emitted. Since several substances in the Sun's atmosphere interact with the radiation, the solar spectrum does not exactly follow a black body spectrum but shows, for example, the characteristic Fraunhofer lines. After entering the Earth's atmosphere, the spectrum is further modified (Seinfeld and Pandis, 2006). A measurement of the solar spectrum at the top of the atmosphere (TOA) and at sea level together with an equivalent black body spectrum are depicted in Fig. 2.4. Interaction between the emitted radiation and the components of Earth's atmosphere leads to several extinction mechanisms, which are explained in the following sections.

2.3.2 Absorption

This section describes absorption mechanisms in the atmosphere and is based on Burrows et al. (2011) and Petty (2006). In the atmosphere, absorption of radiation takes place

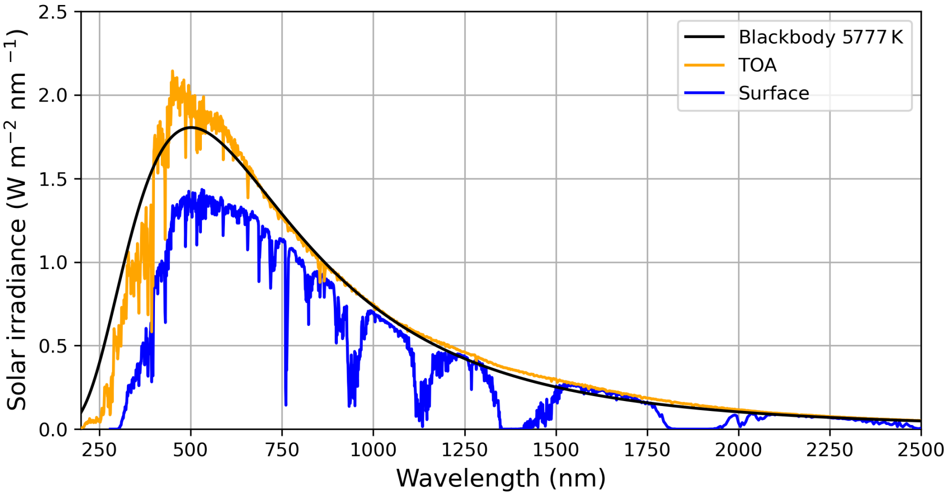

Figure 2.4: Solar irradiance at the top of atmosphere (TOA) before absorption in the Earth's atmosphere (orange), and at the surface after interaction with atmospheric absorbers (blue), compared to a Planck black body curve at a temperature of 5777 K (black). TOA and surface irradiance data are taken from ASTM (2022, 2020).

when a photon's energy

$$E = h\nu \tag{2.9}$$

equals the energy difference between two energy states of a molecule. The ability of a molecule to absorb radiation at a given wavelength is defined by the absorption cross section $\sigma(\lambda)$ in cm^2 molec^{-1}, which can be obtained from high-resolution laboratory measurements and is specific to each molecule. The absorption cross section for NO_2 at 298 K has been measured by Vandaele et al. (1998) and is shown in Fig. 2.5. The amount of ab-

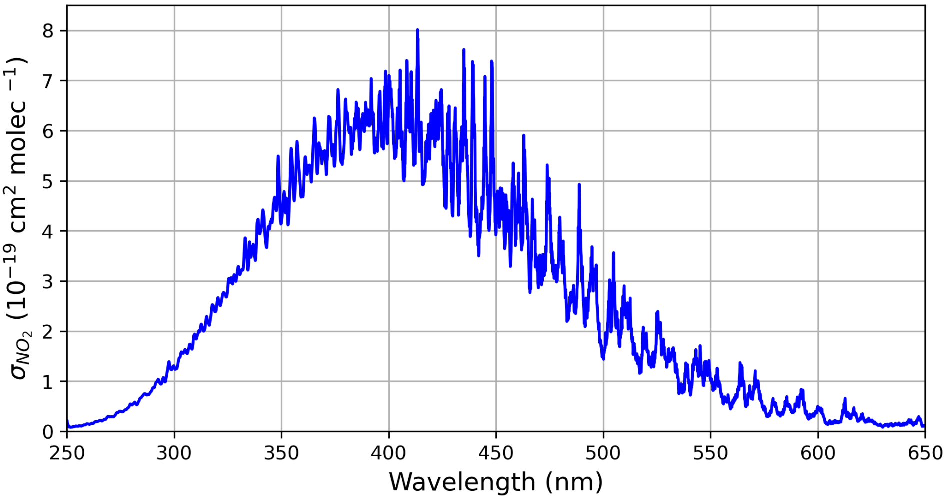

Figure 2.5: NO_2 absorption cross section at a temperature of 298 K, data from Vandaele et al. (1998).

sorbed radiation depends on the cross section σ and the molecule's number density ρ. The extinction of radiation due to absorption can be described by an absorption coefficient ϵ

$$\epsilon = \sigma(\lambda) \cdot \rho. \tag{2.10}$$

The absorption cross section is defined by the molecule's interaction with radiation; the transitions between the energy states of the molecule. It is differentiated between three molecular energy transitions: electronic, vibrational, and rotational transitions, which are described in the following.

A rotational transition changes the rotational state of the molecule. Since rotational energy states are rather closely spaced (see Fig. 2.6), this transition needs the lowest energy of the three molecular transitions, corresponding to wavelengths in the far IR or microwave range. Rotational transitions are not possible for monoatomic gases (e.g., Ar) or molecules without a dipole moment, i.e., an evenly distributed charge (e.g., N_2). Rotational transitions often occur simultaneously with the higher energy vibrational and/or electronic transition.

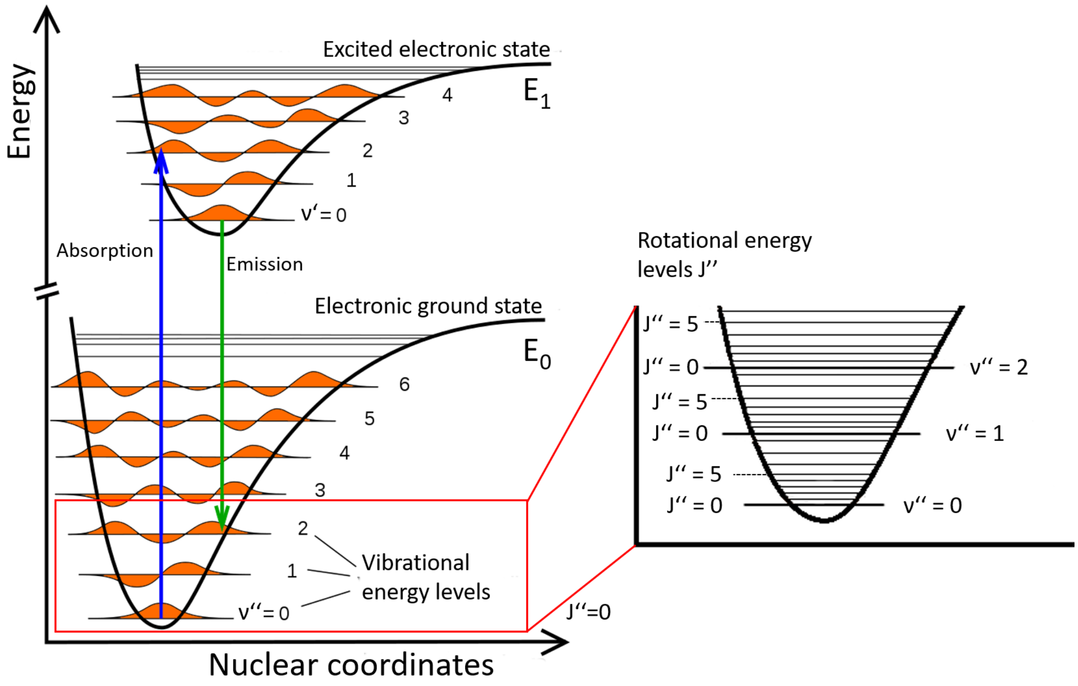

Figure 2.6: Sketch of rotational (J), vibrational (ν), and electronic (E) energy levels in a molecule's electronic potential curve. Wave functions of the vibrational modes are indicated in orange. The vibrational levels to and from which absorption (emission) occur are those with a minimal change in the nuclear coordinates, as indicated by the blue (green) arrow. Adapted from `https://commons.wikimedia.org/w/index.php?curid=2552083`, public domain, by Onno Gabriel.

A vibrational transition changes the vibrations of the atoms within the molecule, which in first approximation can be treated as harmonic oscillations. The energy levels are equivalent to wavelengths in the near and thermal IR spectral range. Depending on the number of atoms and if it is a linear or nonlinear molecule, various modes of vibrations, stretching and compression, bending, and symmetric and asymmetric stretching are possible. Therefore, vibrational absorption spectra can become rather complex. A vibrational excitation is often accompanied by a rotational energy transmission contributing to the observed spectra. Then, each vibrational state splits into a series of ro-vibrational states.
An electronic transition changes the configuration of the molecule's outer electron. Since the electronic energy states are the most widely separated states, this transition requires the highest energies (see Fig. 2.6), corresponding to photons with wavelengths in the visible or UV spectral range. Generally, a photon can be absorbed by a molecule if its energy corresponds to the excitation of an electron to a higher energy state, and discrete absorption lines can be observed. Electronic transitions are usually accompanied by the lower energy rotational and vibrational transition changes, so additional fine-scale structure from these changes is observed in measured absorption spectra. The probability of each transition is described by the Franck-Condon principle, which leads to strongly varying absorption cross sections, as can be seen in Fig. 2.5 for the NO_2 absorption cross section.

2.3.3 Scattering

In addition to absorption in the atmosphere, scattering by air molecules, aerosols, cloud droplets, and ice crystals must also be considered and are described in this section based on Ulrich Platt (2008) and Burrows et al. (2011). The scattering processes relevant in the atmosphere are Rayleigh, Mie, and Raman scattering. They can be differentiated into elastic scattering processes, including Rayleigh and Mie scattering, and the inelastic process, the Raman scattering. Which type of scattering dominates, depends on the so-called size parameter x, describing the relationship between the size of the scattering particle with radius r and the photon's wavelength λ

$$x = \frac{2\pi r}{\lambda}. \tag{2.11}$$

When a photon is scattered by an air molecule without changing the photon's energy but only its direction, it is an elastic scattering and either Rayleigh or Mie scattering. Rayleigh scattering occurs if the scattering particle size is much smaller than the photon's wavelength, so $r << \lambda$ and thus $x << 1$. The scattering efficiency is wavelength dependent, increasing towards shorter wavelengths, and can be expressed as scattering cross section. The Rayleigh scattering cross section describes that the scattering efficiency is

$\propto \lambda^{-4}$, thus shorter wavelengths have a higher probability for Rayleigh scattering. In the Rayleigh process, the scattering is evenly distributed in the forward and backward directions.

When elastic scattering (i.e., scattering without changing the photon's energy) occurs on particles that are more equal in size to the photon's wavelength ($x \approx 1$), for example aerosols or cloud droplets, it is called Mie scattering. For Mie scattering, the wavelength dependency is found to be weaker than for Rayleigh scattering with $\sigma_{\mathrm{Mie}} \propto \lambda^{-\alpha}$, with the Ångström exponent α typically in the range of 0.5–2.5, with an average value of 1.3. Another difference to Rayleigh scattering is that the larger particles involved in Mie scattering induce a strong dominance of the forward direction in the scattered light.

Raman scattering is an inelastic process that occurs if the scattering molecule changes its excitation state and therefore the involved photon changes its wavelength slightly. During this process, some energy is transferred between molecule and photon, changing the molecule's state of rotation or vibration. The energy can only be exchanged in discrete amounts corresponding to the induced molecular transition. Observations have shown that scattered light has less pronounced Fraunhofer lines than direct light. This filling-in of Fraunhofer lines is explained by rotational Raman scattering and is called the Ring effect, which must be considered in the DOAS retrieval. Generally, only a few percent of the scattering processes are inelastic Raman scattering.

2.3.4 Interaction at the surface

Additionally to absorption and scattering processes in the atmosphere, the interaction of radiation with the Earth's surface should be considered, especially for airborne or satellite observations. One parameter that must be considered is the ratio of reflected diffuse light to the incident irradiance at a specific wavelength, referred to as surface reflectance or albedo. It ranges from zero when all incident radiation is absorbed at the surface to one when everything is reflected. In the UV and visible spectral range, the Earth's albedo is relatively low, globally in the range of 2 to 30 %, and higher for snow or ice surfaces.

The direction characteristics of the reflected radiation are described by the bidirectional reflection distribution function (BRDF). It describes the dependency on both the angles of incident and reflected radiation. Often the reflectivity distribution is approximated with the simple model of a Lambertian reflector, which scatters equally into all directions independent of the incident radiation angle (isotropic), see Fig. 2.7a. Thus the Lambertian model assumes that the amount of reflected light is not dependent on the directions. This is a quite realistic description for rough surface types like sand, snow, or ice, but for other surfaces, more complex functions are more appropriate (Burrows et al., 2011). Since most surfaces, apart from water, when observed from larger distances, can be approximated as

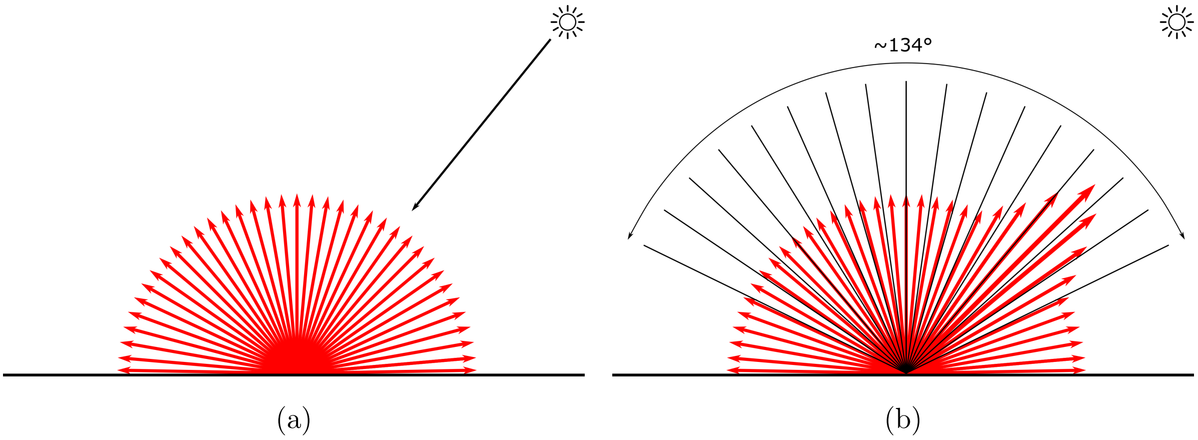

Figure 2.7: Illustration of the principle of Lambertian surface reflection (a) and a more realistic surface reflection distribution with a retroreflection lobe described by a surface BRDF (b), based on (Tilstra, 2022). The Lambertian model does not depend on the exact scattering geometry, while the BRDF depends on the direction of the incoming and reflected light. Over time, a certain location is observed for example by TROPOMI at many different viewing angles (which cover for TROPOMI approximately 134°), as illustrated in (b).

rough surfaces, the Lambertian reflection usually provides a sufficient approximation for the reflectance at the surface (Petty, 2006).

Assuming a Lambertian surface, the surface Lambertian equivalent reflectivity (LER) is determined analytically from the Earth's reflectance observed by a satellite. Additional required parameters are the total atmospheric transmission, the path reflectance, and spherical albedo. These are easily calculated by clear-sky radiative transfer model (RTM) calculations, using viewing and solar angles, ozone column, and surface height and type as input. With these determined parameters and the measured Earth reflectance, the surface albedo of the scene can be analytically determined, assuming a Lambertian surface. Since the atmosphere usually contains clouds and/or aerosols not accounted for in the RTM calculations, this does not yield the surface LER but a more general parameter, the so-called scene LER. Clouds and aerosols tend to increase the scene LER above the actual surface LER value. To retrieve the surface LER, cloud screening has to be applied. This can be done with a statistical method, which assumes that the lowest scene LER values are cloud-free cases. This method was for example applied in the GOME-2 and OMI LER database. Another possibility is a direct cloud filtering approach, which is applied for the TROPOMI database, using the Suomi NPP-VIIRS cloud product, which is in loose formation with S5P within a time difference of a few minutes and very similar orbits. When clear-sky conditions apply, the scene LER value provides the actual surface albedo. To account for outliers, scenes that still contain clouds or aerosols, only the 10 % lowest values of the clear-sky scene LER values are considered for the LER database, which is adapted from the statistical method. With several years of reflectance observations, a monthly global LER database is retrieved (Tilstra et al., 2021; Tilstra, 2022).

A more realistic method compared to the LER is the directionally dependent LER (DLER). The DLER database is retrieved as a function of the viewing geometry and therefore contains the anisotropy of the surface reflectivity, often called the BRDF effect, see Fig. 2.7. For TROPOMI, a DLER database was determined based on 3 years of TROPOMI observations. Over time, a certain location is observed many times by TROPOMI for several different viewing angles, spanning the entire viewing angle range of approximately 134°. The traditional LER algorithm is run separately for the different viewing angles. To gather enough clear-sky observations for all scenes and viewing geometries, multiple years of data are used to determine monthly DLER albedo values. Since only the lowest reflectance measurements are considered for determining the LER and DLER database, and the LER represents the absolute minimum over all viewing directions, while the DLER is determined for the different viewing angles, the LER database always provides lower values than the DLER database (Tilstra, 2022). Since the DLER database covers only the geometries from the actual measurements and only represents these, the DLER database e.g., retrieved from TROPOMI, cannot be used for the GEMS or Sentinel-4 data retrieval. The influence of the surface reflectance database on the TROPOMI NO_2 retrieval is further investigated in Chapter 4, Sect. 4.6.2.

2.4 Differential optical absorption spectroscopy

The atmospheric composition can be investigated by different measurement techniques. This thesis uses the differential optical absorption spectroscopy (DOAS). It is a remote sensing technique based on the absorption spectroscopy method. Absorption spectroscopy analyses the interaction of radiation and matter, more specifically, the attenuation of radiation through absorption (Burrows et al., 2011). The DOAS method was introduced in the 1970's (Noxon, 1975; Platt and Perner, 1980) and has been applied and improved for studies of atmospheric composition since then. First measurements were taken by ground-based instruments (e.g., Noxon, 1975; Platt and Perner, 1980; Solomon et al., 1987). Since the 1990's, DOAS measurements are also performed from satellite platforms (e.g., Bovensmann et al., 1999; Burrows et al., 1999). Today, several platforms have been used for DOAS measurements. The different measurement principles and possibilities are further explained in Sect. 2.5. In the following, the basic principle of absorption spectroscopy and the DOAS method is described, which is mainly based on Ulrich Platt (2008) and Burrows et al. (2011).

2.4.1 Absorption spectroscopy and Beer-Lambert law

The attenuation of radiation in a homogeneous absorbing medium is given by the Beer-Lambert law

$$I(\lambda) = I_0(\lambda) \cdot \exp(-\sigma(\lambda) \cdot \rho \cdot s) \tag{2.12}$$

with the incident intensity I_0, and I the radiations intensity after passing through the absorbing medium. It describes an exponential decrease of the initial intensity, depending on the particle density of the absorber ρ and its absorption cross section σ along the light path s through the absorbing medium.

In the atmosphere, several absorbing species and mechanisms reduce the incident intensity. Even if Rayleigh and Mie scattering and the Ring effect induced by Raman scattering are no absorption mechanisms, they still influence the light path intensity, and their extinction must be considered for atmospheric scenarios. Both the absorber densities and, through their temperature and pressure dependencies, the cross sections are generally a function of altitude over the absorbing path s. With these aspects, Eq. 2.12 can be extended to

$$\begin{aligned} I(\lambda) = I_0(\lambda) \cdot \exp\Bigg(-\int \quad & \sum_{j=1}^{J} \sigma_j(\lambda, s) \cdot \rho_j(s) \\ & + \sigma_{\text{Ray}}(\lambda, s) \cdot \rho_{\text{Ray}} + \sigma_{\text{Mie}}(\lambda, s) \cdot \rho_{\text{Mie}} \\ & + \sigma_{\text{Ring}}(\lambda, s) \cdot \rho_{\text{Ring}} \quad \mathrm{d}s\Bigg) . \end{aligned} \tag{2.13}$$

If the altitude respectively light path dependency of the cross sections is neglected, the Ring effect is treated as a normal absorber, and absorber densities along the atmospheric light path are integrated to the so-called slant column densities (SCDs)

$$\text{SCD}_j = \int \rho_j(s)\mathrm{d}s. \tag{2.14}$$

Eq. 2.13 can be simplified to:

$$\begin{aligned} I(\lambda) = I_0(\lambda) \cdot \exp\Bigg(\quad & -\sum_{j=1}^{J} \sigma_j(\lambda) \cdot \text{SCD}_j \\ & - \sigma_{\text{Ray}}(\lambda) \cdot \text{SCD}_{\text{Ray}} - \sigma_{\text{Mie}}(\lambda) \cdot \text{SCD}_{\text{Mie}} \Bigg) . \end{aligned} \tag{2.15}$$

Neglecting the altitude dependence of the cross sections is feasible for most gases and scenarios, especially as many are located in a well defined altitude thus temperature and pressure dependencies are not very pronounced. If dependencies are expected, as for ozone, this is usually compensated by including multiple cross sections of the relevant gas measured at different temperatures or by a subsequent temperature correction.

2.4.2 Principle of DOAS

The basic idea of the DOAS method is to separate the wavelength dependent extinction into a low and a high frequency component. The absorption cross sections are divided into the component slowly varying with wavelength σ^* and the part rapidly varying with wavelength σ', the differential cross section.

$$\begin{aligned} I(\lambda) = I_0(\lambda) \cdot \exp\Bigg(& -\sum_{j=1}^{J} \sigma_j^{'}(\lambda) \cdot \mathrm{SCD}_j \\ & -\sum_{j=1}^{J} \sigma_j^{*}(\lambda) \cdot \mathrm{SCD}_j \\ & - \sigma_{\mathrm{Ray}}(\lambda) \cdot \mathrm{SCD}_{\mathrm{Ray}} - \sigma_{\mathrm{Mie}}(\lambda) \cdot \mathrm{SCD}_{\mathrm{Mie}} \Bigg) \end{aligned} \tag{2.16}$$

This separation into the fast and slowly varying component is only possible for absorbers with structured absorption spectra in the observed wavelength range. Thus the number of species that can be observed with DOAS is limited but includes many key players in atmospheric chemistry, e.g., O_3 NO_2, SO_2, HCHO, and halogen oxides in the UV/visible spectral range, and O_2, H_2O, CO_2, CH_4, and CO towards the IR spectral range. The high frequency component of the absorption cross section is characteristic for each absorbing trace gas and is used for identifying the absorbing gases and their contribution to the total atmospheric absorption. The low frequency component accounts for all effects slowly varying with wavelength, such as instrumental effects and surface reflectance variations. They are combined with the Rayleigh and Mie scattering, which follow simple power laws (see Sect. 2.3.3), and are together approximated by a low-order polynomial.

$$I(\lambda) = I_0(\lambda) \cdot \exp\left(-\sum_{j=1}^{J} \sigma_j^{'}(\lambda) \cdot \mathrm{SCD}_j - \sum_p a_p \cdot \lambda^p \right) \tag{2.17}$$

Equation 2.17 expressed in terms of the optical depth τ is known as the DOAS equation:

$$\tau(\lambda) = \ln\left(\frac{I_0(\lambda)}{I(\lambda)}\right) = \sum_{j=1}^{J} \sigma_j^{'}(\lambda) \cdot \mathrm{SCD}_j - \sum_p a_p \cdot \lambda^p \tag{2.18}$$

The DOAS equation links the measurement signal, the optical depth $I_0(\lambda)/I(\lambda)$, in a linear equation with the desired quantities, the trace gas SCDs, and the polynomial coefficients. Based on absorption cross sections from laboratory measurements, this is solved in a simple linear least square fit within a spectral range called fitting window. The fitting window is chosen specifically for each gas according to its absorbing features. It must be chosen large enough not to underdetermine the fit but not too large to avoid interferences with other cross sections or strong Fraunhofer lines. Remaining smaller differences between the optical depth from laboratory measurements and the fit results, the so-called residual spectrum, contains spectral structures which have not been accounted for in the fit and are expected due to, e.g., measurement noise, but should be randomly distributed without any systematic structures. The residual is a simple criterion for the fit quality and is usually expressed as the root mean square (RMS) of the residual

$$\mathrm{RMS} = \sqrt{\frac{1}{N}\sum_{k=1}^{N} r_{\lambda_k}^2}. \tag{2.19}$$

providing the deviation of the fitted and the measured optical depth as a single number for each spectrum.

The initial intensity $I_0(\lambda)$, often also referred to as background or reference spectrum, and the actual spectrum $I(\lambda)$ are measured with the same instrument, which has the advantage that multiplicative effects appear in both measurements and are canceled out. This eliminates the need for radiometric calibration, which is one of the advantages of the DOAS method. For atmospheric measurements, a suitable reference spectrum $I_0(\lambda)$ with as little as possible absorbing atmospheric constituents has to be found. Different measurement procedures are possible depending on the measurement platform and geometry; further details are given in Sect. 2.5.

2.4.3 Air mass factor

The SCD retrieved with the DOAS method provides the column amount of the absorbing trace gas integrated along the light path. However, the light path and thus the SCD strongly depends on several parameters such as the measurement geometry with the instruments viewing geometry, the geometry relative to the Sun, surface reflection, and atmospheric conditions causing scattering and absorption. Therefore, the SCD is not very comparable between measurements and hard to interpret. Thus, the SCD is typically converted into the vertical column density (VCD), which is defined as the absorber concentration vertically integrated through the atmosphere. The conversion is performed with the so-called air mass factor (AMF) (Burrows et al., 2011)

$$\mathrm{AMF} = \frac{\mathrm{SCD}}{\mathrm{VCD}}. \tag{2.20}$$

A simple approximation of the AMF is the geometric AMF which only accounts for Sun and viewing geometry but not atmospheric conditions. For the satellite viewing geometry, the geometric AMF is described by:

$$\mathrm{AMF_{geo}} = \frac{\mathrm{d}s}{\mathrm{d}z} + \frac{\mathrm{d}s'}{\mathrm{d}z} = \frac{1}{\cos(\mathrm{VZA})} + \frac{1}{\cos(\mathrm{SZA})} \tag{2.21}$$

defined by the solar zenith angle (SZA) and the instruments viewing zenith angle (VZA) (Burrows et al., 2011), see Fig. 2.8a. For the ground-based observation geometry with a trace gas layer near the surface, the geometric AMF is given by:

$$\mathrm{AMF_{geo}} = \frac{\mathrm{d}s}{\mathrm{d}z} = \frac{1}{\sin(\alpha)} \tag{2.22}$$

strongly dependent on the instruments viewing elevation angle α (defined with respect to the surface) (Hönninger et al., 2004), see Fig. 2.8b.

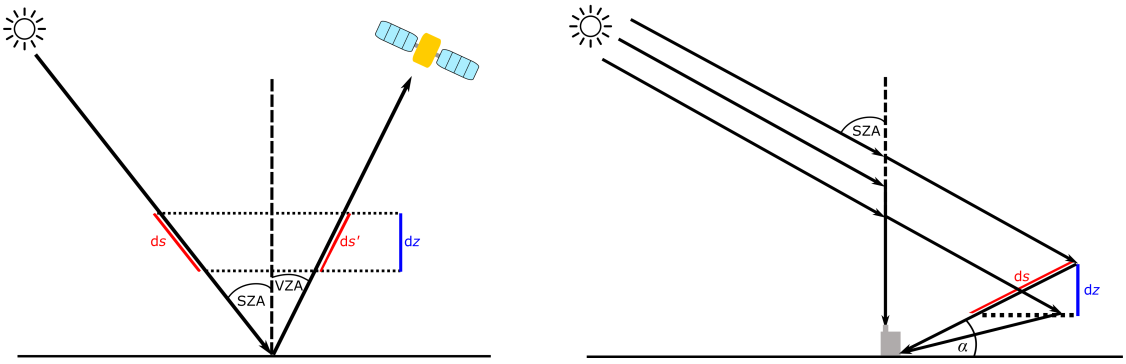

(a) (b)

Figure 2.8: Sketch showing satellite (a) and ground-based (b) viewing geometry, illustrating geometric AMF determination with solar zenith angle (SZA), viewing zenith angle (VZA), and viewing elevation angle (α).

A more precise way of estimating the relative light path through the absorbing layer is by numerical atmospheric radiative transfer simulations. One possibility is the radiative transfer model (RTM) SCIATRAN (Rozanov et al., 2014), used in this thesis. Besides the observation geometry, the RTM also considers the light path dependency on the wavelength, surface reflectance, and atmospheric conditions such as clouds, aerosol load, pressure, and trace gas profiles. Since radiative transfer model calculations are computationally expensive and the dependencies of the AMF and the influencing parameters are usually relatively straightforward, pre-calculated look-up tables (LUT) are often used. To best represent the light path during the observation, an AMF is interpolated from the LUT, matching best the observation conditions. However, this knowledge about the exact observation conditions, such as surface reflectance, vertical profiles of absorbers and scatterers during the observation, is often not available and has to be assumed a priori or taken from climatologies, which introduce large uncertainties in the AMF and also the VCD retrieval (Burrows et al., 2011; Boersma et al., 2004).

Another concept of the AMF is a height-resolved partial AMF, called box air mass factor (BAMF). The BAMF is defined for the specific atmospheric layer i by the ratio of the SCD and VCD within the individual layer i:

$$\mathrm{BAMF}_i = \frac{\mathrm{SCD}_i}{\mathrm{VCD}_i}. \tag{2.23}$$

With the BAMF, it is possible to quantify the vertical dependence of the measurement sensitivity. The total AMF is then calculated with the BAMF of the atmospheric layers i weighted by the relative absorber concentration profile $\mathrm{VCD}_i/\mathrm{VCD}$, also called shape factor:

$$\mathrm{AMF} = \frac{\mathrm{SCD}}{\mathrm{VCD}} = \sum \mathrm{BAMF}_i \cdot \frac{\mathrm{VCD}_i}{\mathrm{VCD}}. \tag{2.24}$$

The concept of the BAMF has the advantage that the total AMF can be determined from a pre-calculated LUT of BAMFs in combination with different a priori profile shapes without depending on the vertical absorber profile. The following section gives a more detailed description of the different steps for the tropospheric NO_2 VCD retrieval for the instruments used within this thesis.

2.5 Observation geometries of DOAS instruments

In general, the DOAS method has been applied to measurements by various instruments from different platforms and observation geometries. It can be differentiated between active DOAS, where measurements are carried out with an artificial light source, and passive DOAS, performed with a natural light source, usually the Sun. Passive DOAS measurements can be further differentiated into direct sun and scattered sunlight measurements. Within this thesis, scattered sunlight DOAS observations from satellite, airborne, and stationary and mobile ground-based platforms, more specifically the retrieved tropospheric NO_2 VCD, are analyzed. Therefore, an overview of the different platforms, instrument characteristics, and tropospheric NO_2 VCD retrieval details are given here.

2.5.1 Satellite observations - TROPOMI

Satellite-based atmospheric observations performed from satellites in Sun-synchronous orbits provide the unique possibility for global measurements under consistent measurement conditions. Satellite instruments using the DOAS method to retrieve atmospheric trace gas concentrations are available since the mid-1990s (Burrows et al., 2011).

The first satellite-based DOAS instrument, the Global Ozone Monitoring Experiment (GOME), was launched on the ERS-2 satellite in 1995 (Burrows et al., 1999). It provided for the first time observations at a large spectral range (237 −793 nm) with a spectral resolution of 0.2 −0.4 nm, and a standard ground pixel size of 320 km × 40 km, enabling global coverage each 3 days. By applying the DOAS method, global observations of atmospheric trace constituents, including NO_2, have been made possible. Since then, follow-up missions such as SCIAMACHY (2002–2012, Bovensmann et al. (1999)), GOME-2 (since 2007, Munro et al. (2006)), OMI (since 2004, Levelt et al. (2006)), and OMPS (since 2011, Dittman et al. (2002)) continued measurements in the UV and visible spectral range and thus the observation of atmospheric NO_2 and other trace gases. These instruments had increasing spatial coverage and resolution, OMI being the first instrument with daily global coverage and a spatial resolution of 13 km × 24 km at nadir, still one order of magnitude poorer than the follow-up instrument TROPOMI (since 2017, Veefkind et al. (2012)), whose observations are used in this thesis.

On 13 October 2017, the satellite Sentinel-5 Precursor (S5P) was launched into a Sun-synchronous polar orbit. On board, a hyperspectral push-broom nadir-viewing imaging spectrometer called TROPOMI measures radiation in the UV, visible, and IR spectral regions, monitoring several atmospheric contributions. TROPOMI's two-dimensional charge-coupled device (CCD) detector measures spectra across a swath width of ~2600 km in 450 viewing directions simultaneously in approximately 1 s. Figure 2.9 shows a sketch of the measurement principle. With the flight height of S5P at an altitude of 824 km, this

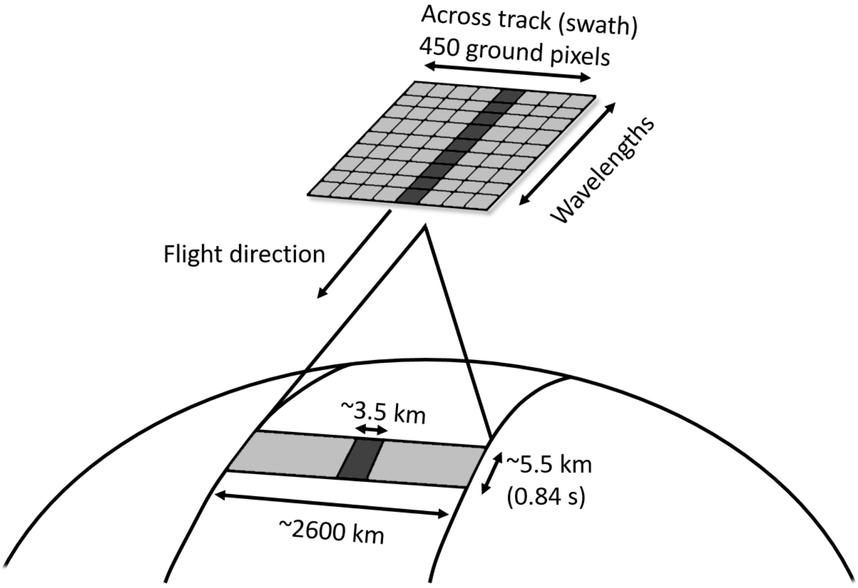

Figure 2.9: Sketch of the TROPOMI measurement principle, based on Veefkind et al. (2012). The dark gray ground pixel is imaged on the two-dimensional CCD detector as a spectrum. Ground pixel resolution of ~3.5 km × 5.5 km at nadir, before 5 August 2019 3.5 km × 7 km. All ground pixels in the 2600 km wide swath are measured simultaneously in 450 viewing directions.

results in TROPOMI ground pixel sizes of approximately 3.5 km × 7 km in the middle of the swath. Since 5 August 2019, the ground pixel size has been reduced to approximately 3.5 km × 5.5 km by shorter along-track averaging of only 0.84 s. With 4173 along-track scanlines, this leads to about 1.88 million ground pixels per orbit. With orbit times of 100 min and the wide swath, TROPOMI achieves nearly global coverage with equator crossing times at around 13:30 local time. TROPOMI is observing the distribution of atmospheric trace gas columns such as NO_2, HCHO, SO_2, O_3, CO, CH_4 and of aerosol and cloud properties (Veefkind et al., 2012; van Geffen et al., 2020).

The retrieval of tropospheric NO_2 VCDs is a three-step procedure; first the NO_2 SCD retrieval, followed by the separation in its stratospheric and tropospheric components, and then the conversion into NO_2 VCDs.

The NO_2 SCD retrieval using the DOAS technique is based on the measurements from the visible channel (400 −496 nm) with spectral resolution and sampling of 0.54 nm, and 0.20 nm. The level-1b radiance and irradiance spectra measured by TROPOMI are analyzed with the DOAS technique in the fitting window of 405 −465 nm. An extraterrestrial solar reference spectrum is measured once every 15 orbits (approx. every 25 h). The DOAS retrieval uses a fifth order polynomial, and the 220 K NO_2 cross section, with secondary fitted (pseudo-) absorbers: O_3, H_2O_{vap}, $O_2{-}O_2$, H_2O_{liq} and Ring spectrum. The retrieved NO_2 SCD represents the total amount of NO_2 along the effective light path, from the Sun through the atmosphere to the satellite (van Geffen et al., 2020).

NO_2 vertical profile information from the TM5 global chemistry transport model and a data assimilation system that assimilates the TROPOMI SCDs is used to separate the SCD into its stratospheric and tropospheric part (van Geffen et al., 2020).

The resulting tropospheric SCDs are converted into tropospheric VCDs by tropospheric AMFs derived from a pre-calculated LUT of altitude dependent AMFs (BAMFs) and actual daily NO_2 vertical profile shapes from the TM5 model. The TM5 vertical NO_2 profile shapes have a spatial resolution of 1° × 1° for 34 layers covering the troposphere and stratosphere. The BAMFs describing the vertically resolved sensitivity to NO_2 are provided in a 6-dimensional LUT as a function of SZA, VZA, relative azimuth angle, surface albedo, surface pressure, and (mid-level) atmospheric pressure. To account for the temperature difference between the fitted NO_2 cross section at 220 K and the effective temperature of the NO_2, a temperature correction factor is applied to the BAMFs. The surface albedo in the NO_2 spectral fitting window is provided by the OMI climatological LER database. The cloud pressure retrieval in the NIR spectral range is based on the GOME-2 LER database. Since processor V02.04 both LER products are replaced with the TROPOMI DLER database (see also Sect. 2.3.4). Pixel-specific AMFs are retrieved using the best estimates for forward model parameters and a 6-dimensional interpolation. Because of the still relatively coarse spatial resolution of satellite observations, only a small amount of the pixels are completely cloud-free. Most pixels are either partly or fully cloudy, and the influence of clouds and aerosols on the satellite observations and the NO_2 retrieval must be considered. There are many possible light paths between the sun and the instrument, which get even more complex under cloudy and aerosol-loaded conditions. Figures 2.10 and 2.11 illustrate some effects of clouds and aerosols on the light path and the resulting sensitivity for satellite observations.

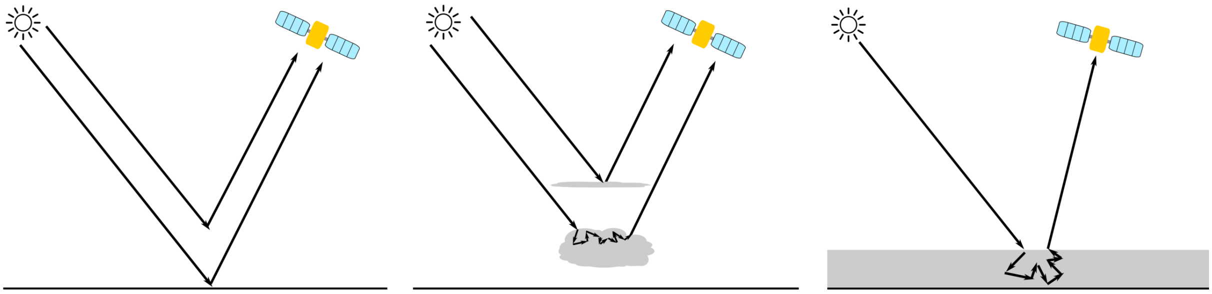

Figure 2.10: Sketch of possible light paths for satellite observations for clear-sky (left), cloudy (middle), and aerosol-loaded (right) conditions. For cloud-free scenes, light is scattered by air molecules or reflected at the surface (left). Scattering at high clouds can reduce the light path, while multiple scattering inside thick clouds can enhance the light path in the upper layers of the cloud (middle). The influence of aerosols depends on their specific characteristics. Non-absorbing aerosols can increase the light path and thus the sensitivity in the aerosol layer (right). Based on Burrows et al. (2011).

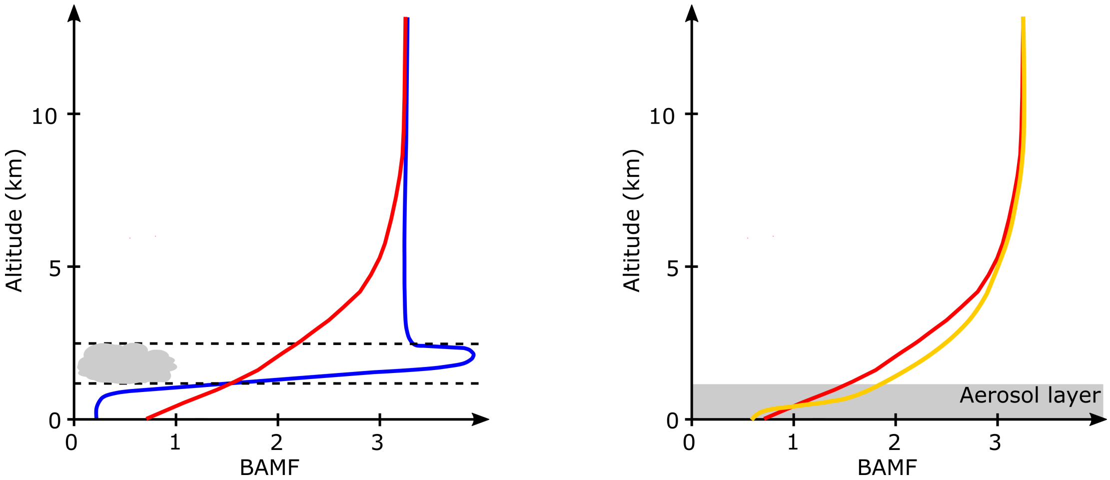

Figure 2.11: Sketch of the altitude-dependence of the satellite observations sensitivity for clear-sky (red), cloudy (blue, left), and aerosol-loaded (orange, right) conditions expressed as BAMFs. The effect depends on several parameters, such as wavelength, SZA, viewing geometry, surface reflectivity, and cloud and aerosol parameters. Based on Burrows et al. (2011) and Wang et al. (2005).

In cloud-free scenes, light is reflected at the surface or scattered by air molecules. Scattering at high clouds can reduce the light path and they shield the trace gases below. In the upper layers of thick clouds, multiple scattering can enhance the light path and thus the sensitivity significantly. Fewer photons reach the lower layers, and sensitivity decreases strongly towards the cloud bottom and further to the surface. Due to the high reflectance of the cloud top, the sensitivity above the cloud is enhanced compared to the clear-sky scenario. The effects of an aerosol layer can be; light path enhancements and therefore increased sensitivity within the aerosol layer due to multiple scattering, increased sensitivity above and within the aerosol layer due to larger scattering probability (enhancement/albedo effect), decreased sensitivity below the aerosol layer due to a shielding effect, and in case of strongly absorbing aerosols also decreasing sensitivity within the aerosol layer. The overall impact of clouds and aerosols depends on their specific characteristics, vertical distribution of clouds, aerosols, and the trace gas of interest, the SZA, viewing geometry, wavelength, and surface reflectivity. Sensitivity can be either increased or decreased compared to clear-sky conditions (Burrows et al., 2011; Leitão et al., 2010; Chimot et al., 2016).

To correct for cloud effects in satellite trace gas retrievals, the most relevant cloud parameters are the cloud fraction and the cloud pressure. In the AMF calculation, clouds are accounted for with the independent pixel approximation (IPA). With the IPA, the AMF for a partly cloudy pixel is calculated with a linear combination of a clear-sky AMF ($\mathrm{AMF}_{\mathrm{trop,\,clr}}$) and a cloudy AMF ($\mathrm{AMF}_{\mathrm{trop,\,cloudy}}$) weighted by the cloud radiance fraction w:

$$\mathrm{AMF}_{\mathrm{trop}} = w \cdot \mathrm{AMF}_{\mathrm{trop,\,cloudy}} + (1-w) \cdot \mathrm{AMF}_{\mathrm{trop,\,clr}}. \tag{2.25}$$

The clear-sky and cloudy AMF are calculated following Eq. 2.24, with the corresponding cloud pressure and albedo for the cloudy scenes. The cloud radiance fraction w is defined by the effective cloud fraction f_{eff}, the radiance from the cloudy part of the pixel I_{cloudy}, and the radiance from the clear part of the pixel I_{clr}, with R the total scene radiance (van Geffen et al., 2022a):

$$\begin{aligned} w &= \frac{f_{\mathrm{eff}} \cdot I_{\mathrm{cloudy}}}{R} && (2.26) \\ &= \frac{f_{\mathrm{eff}} \cdot I_{\mathrm{cloudy}}}{f_{\mathrm{eff}} \cdot I_{\mathrm{cloudy}} + (1-f_{\mathrm{eff}}) \cdot I_{\mathrm{clr}}}. && (2.27) \end{aligned}$$

The IPA assumes that the radiative properties of a single pixel are not dependent on neighboring pixels and allows an application of a 1-D pseudo-spherical RTM (Loyola et al., 2021). It should be noted that the TROPOMI cloud retrieval algorithm does not discriminate between cloud and aerosol signals. Therefore, cloud fraction and pressure are also retrieved over cloud-free scenes when including an aerosol load. With this, an implicit aerosol correction is done, assuming that the cloud correction scheme also accounts for a large part of the effects of aerosols (van Geffen et al., 2022a; Boersma et al., 2011). The TROPOMI NO_2 product uses the cloud (and implicit aerosol) correction via the IPA, motivated by the fact that most pixels have a degree of cloud cover, and the IPA consider the effects of clouds. Another approach is to consider only the clear-sky AMF for scenes with a sufficiently small cloud fraction, e.g., < 0.2 (Richter and Burrows, 2002). This is motivated by the fact that retrieved cloud fractions and pressures have relatively high uncertainties for these scenes, which inhibits reliable modeling. Sensitivity studies showed that the choice of cloud correction (clear-sky AMF for small cloud fractions or IPA) resulted in substantial AMF differences, especially in polluted conditions (Lorente et al., 2017). The effect of the cloud correction on the TROPOMI tropospheric NO_2 VCD retrieval is further analyzed and discussed in Chapter 4, Sect. 4.6.1.

The cloud parameters for the TROPOMI NO_2 product are retrieved from the FRESCO-S (Fast Retrieval Scheme for Clouds from Oxygen absorption bands – Sentinel) algorithm. The FRESCO-S algorithm uses the O_2 A-band around 760 nm and the brightness approach, where a cloud-free background from a surface reflectance database is assumed as dark compared to the bright clouds in the NIR region. As mentioned above, this was first based on the GOME-2 LER climatology, which was replaced by the TROPOMI DLER data set with the NO_2 processor V02.04. The FRESCO retrieval assumes clouds as reflecting surfaces using an optically thick Lambertian cloud model at the cloud pressure level with a fixed albedo of 0.8, which may be adapted over very bright scenes when the approach would lead to cloud fractions larger than 1. Since there is a large wavelength difference between the O_2 A-band and the NO_2 retrieval window, as well as a misalignment between the TROPOMI ground pixels of the O_2 A-bands and the NO_2 spectral window, the cloud parameters need to be adapted for the NO_2 retrieval. The cloud pressure from the FRESCO algorithm is corrected for the misalignment, and the cloud (radiance) fraction is retrieved from the NO_2 spectral region at 440 nm, very similar to the FRESCO approach. Early studies indicated that the retrieved cloud pressures for scenes with either low clouds or low aerosol layers show a positive bias, and in many cases, cloud pressures are retrieved at the surface height. This resulted in large AMF values and an underestimation of the tropospheric NO_2 VCDs. Therefore, the FRESCO algorithm was updated with NO_2 processor V01.04 using a wider window (named FRESCO-wide) which increases the sensitivity to low clouds (van Geffen et al., 2022a). This update is further analyzed and discussed in Chapter 4, Sect. 4.6.1.

During the 5 years of operation, there have been several modifications within the tropospheric NO_2 VCD retrieval. Changes before 2 December 2019, when V01.04 was activated, have been minor, and different versions during this period can be mixed. The analyses presented in Chapter 3 are based on the NO_2 products before V01.04. Since V01.04, significant changes have been introduced in the NO_2 retrieval. The main change was the update of the cloud retrieval, leading to a substantial increase in the tropospheric NO_2 VCD (van Geffen et al., 2022a). These modifications are further analyzed and discussed in Chapter 4.

2.5.2 Airborne instruments

Airborne and satellite platforms use similar measurement geometries. The airborne DOAS instrument used within this thesis is the Airborne imaging DOAS instrument for Measurements of Atmospheric Pollution (AirMAP). AirMAP has been developed at the University of Bremen for trace gas measurements from aircraft and is a nadir viewing push-broom imaging DOAS instrument. Due to the lower flight altitude compared to satellite instruments, airborne measurements have a much higher spatial resolution. Large areas like cities can be gaplessly mapped within a three hours flight. Thereby, the airborne imaging DOAS measurements provide the opportunity of mapping the variability of NO_2 within several satellite pixels, quantifying expected differences between satellite and ground-based stationary measurements.

The AirMAP instrument collects scattered sunlight from below the aircraft with a nadir viewing wide-angle entrance optic directing it via a sorted fiber bundle with 35 individual fibers into an imaging spectrometer. There, it is recorded by a two-dimensional Frame-Transfer CCD detector, so each fiber represents a different across-track viewing direction. The spectrometer is an Acton 300i imaging spectrograph with an f-number of $f/3.9$ and a focal length of 300 mm. The spectrometer is temperature stabilized at 35 °C. For the measurements presented in this thesis, it was equipped with a $400\,\mathrm{g\,mm^{-1}}$ grating blazed at 400 nm, providing measurements in the wavelength range of 429 to 492 nm with a spectral resolution between 0.9 nm and 1.6 nm full width at half maximum. The wide-angle objective used as entrance optic is allowing a large field of view of about 52°. The fiber bundle of 35 sorted single glass fibers is vertically aligned at the spectrometer entrance slit of approximately 100 µm width and is orthogonally oriented to the aircraft flight direction. With typical flight speeds of around $60\,\mathrm{m\,s^{-1}}$ and an exposure time of 0.5 s, the along track pixel size is around 30 m. At a typical flight altitude of around 3200 m, the swath width is about the same size, and the across-track pixel size is around 100 m. A more detailed instrument description can be found in Schönhardt et al. (2015) and Meier et al. (2017).

The reference spectrum used in the satellite DOAS retrieval, an extraterrestrial solar reference spectrum, contains no Earth atmospheric absorptions, only the Fraunhofer structures; thus absolute SCDs can be retrieved. From airborne and also ground-based platforms no such pure reference spectra can be measured. For airborne measurements, often one reference spectrum for each flight over an unpolluted region is used for the SCD retrieval. Since it still contains absorptions, the retrieved SCDs are not absolute but are referred to as differential SCDs (dSCDs) (Meier et al., 2017; Tack et al., 2019). For AirMAP; the NO_2 dSCDs were retrieved in a fitting window of 438 −490 nm. The retrieved dSCDs are corrected for the amount of NO_2 expected in the reference spectrum by typical values from the literature and additional car DOAS measurements. The SCDs are converted into tropospheric VCDs by AMFs simulated using the RTM SCIATRAN. Further details about the AirMAP tropospheric NO_2 VCD retrieval are given in Sect. 4.3.2.1.

2.5.3 Ground-based instruments

Ground-based DOAS measurements are usually performed stationary and first employed Zenith-DOAS instruments (Noxon, 1975; Solomon et al., 1987). Meanwhile, multi-axis DOAS (MAX-DOAS) instruments taking measurements at several elevation and azimuth angles (Hönninger et al., 2004; Wittrock et al., 2004) are very common. Zenith-DOAS and MAX-DOAS measurements have also been performed from moving ground-based platforms such as cars or ships, usually on a campaign basis (e.g., Shaiganfar et al., 2011; Peters et al., 2012; Behrens et al., 2019; Lange et al., 2023).

With MAX-DOAS viewing geometries, with measurements in elevation angles slightly above the horizon, long light paths through the boundary layer and thus high sensitivity to the absorbing gases can be achieved (visible also in Fig. 2.8b). Therefore, MAX-DOAS measurements are particularly suited for tropospheric observations (Hönninger et al., 2004). Typically, MAX-DOAS elevation scans start slightly above the horizon, going upwards in small steps (1°–2°) to 10° or 15°, followed by a 30° elevation and a zenith-sky (90°) measurement (Kreher et al., 2020). Elevation measurements different from the 90° direction are often called off-axis measurements. Similar to the airborne measurements, no extraterrestrial solar reference spectrum can be taken from ground-based instruments. Therefore, zenith measurements are used as a reference for the dSCD retrieval. Typically, the reference is a zenith measurement taken around noon, when the Sun is high and the light path is shortest, or a close-in-time zenith measurement (called sequential reference). As can be seen in Fig. 2.8b, measurements taken at similar SZA show a similar light path through the upper atmosphere independently of elevation angle. If zenith reference measurements are taken close in time, the retrieved dSCD has the effect that absorptions on the similar stratospheric light paths cancel out. Additionally, the sequential reference minimizes the effects of possible changing instrumental characteristics with time. For relatively stable instruments, another option is to take a fixed reference around noon on a day with low absorber concentrations and preferably high Sun position during summer and apply it for a longer time series (Hönninger et al., 2004; Ulrich Platt, 2008; Wagner et al., 2010).

Due to their high sensitivity to stratospheric absorption at low Sun observations, zenith-sky DOAS instruments are often used for stratospheric investigations (Solomon et al., 1987). With their simple measurements principle, they are also particularly suited for mobile ground-based measurements. Due to the lower sensitivity to tropospheric absorption, Zenith-DOAS measurements are less suitable for weak absorbers. However, zenith-sky only observations have the advantage for mobile ground-based measurements of a higher measurement frequency and a simpler measurement geometry by avoiding quick relative azimuth changes. For the dSCD retrieval from mobile Zenith-DOAS observations, usually a fixed reference spectrum taken in an unpolluted area is used for a longer period, depending on the instrument stability (Wagner et al., 2010; Schreier et al., 2019).

Usually, the conversion from dSCDs into tropospheric VCDs is either obtained using radiative transfer simulations or the simple geometrical approximation (Hönninger et al., 2004)

$$\mathrm{VCD_{trop}} = \frac{\mathrm{SCD}(\alpha) - \mathrm{SCD}(90°)}{\mathrm{AMF_{trop}}(\alpha) - \mathrm{AMF_{trop}}(90°)} \tag{2.28}$$

using the geometric AMF (see also Sect. 2.4.3)

$$\mathrm{AMF_{trop}} = \mathrm{AMF_{geo}} = \frac{1}{\sin(\alpha)}. \tag{2.29}$$

The geometric approximation is based on the assumption that first, the stratospheric absorption is similar in temporally close performed zenith-sky and off-axis measurements and therefore cancels out, and second that for higher off-axis viewing directions, such as 15° or 30°, the geometric light path enhancement is a good approximation for an absorber in the boundary layer. It assumes that the last scattering altitude is above the absorbing layer. Then the dependence of the AMF on the elevation angle α is close to geometric, i.e. proportional to $1/\sin(\alpha)$, see also Sect. 2.4.3 (Hönninger et al., 2004). It is known that the geometric approximation gets inaccurate for small elevation angles close to the horizon (Wittrock et al., 2004). Comparing the results of two relatively large elevation angles, e.g., 15° and 30°, and eliminating measurements that are not within a specific range, e.g., 10 %, eliminates measurements affected by horizontal inhomogeneities or clouds (Brinksma et al., 2008). However, also for observations at high elevation angles, especially in the presence of high aerosol loads, larger deviations between the geometric AMF and the true AMF can occur and cause larger errors in the tropospheric VCD determined by geometric approximation. Another important parameter, at least for the off-axis AMF, is the relative azimuth between viewing direction and solar position which gets additionally more important in high aerosol scenarios. The SZA dependence of the AMF is, however, relatively small for tropospheric absorbers (Wagner et al., 2010; Shaiganfar et al., 2011). Shaiganfar et al. (2011) quantified the deviations between the geometric and the true AMF, respectively the resulting tropospheric VCD, for various aerosol scenarios and NO_2 layer heights with RTM simulations. They found that for NO_2 layer heights $\leq 1\,\mathrm{km}$ and aerosol optical thickness (AOT) values < 1, deviations from the geometric approximation are in the order of $\pm\,20\,\%$. However, the geometric AMF seems to be systematically too low compared to the true AMF retrieved from the RTM simulation for most scenarios. Similar findings were found by Merlaud (2013), indicating that for the zenith-sky and the 30° elevation viewing direction, AMFs of 1.3 ± 0.2 and 2.5 ± 0.3 are closer to the true AMF then the geometric AMFs of 1 and 2.

Within this thesis, observations of several stationary and mobile car DOAS instruments, as well as the new tram DOAS instrument, are analyzed and discussed. More details on the specific tropospheric VCD retrieval for the individual instruments are given in the respective studies; see Chapter 4 and 5.

3 | Variability of nitrogen oxide emission fluxes and lifetimes – estimated from TROPOMI NO_2 observations[1]

3.1 Introduction

Satellite observations of NO_2 with high spatial and temporal resolution can be used to quantify the variability of NO_x emissions and lifetimes around the world on a daily and seasonal basis. The typically short daytime lifetime of NO_x in polluted environments allows disentangling of local sources of NO_x and quantifying their variations over time (e.g., Beirle et al., 2011; Lorente et al., 2019; Goldberg et al., 2021).

Several studies have investigated the variability of NO_x emissions using the tropospheric NO_2 column from TROPOMI and its predecessors. Analysis of the seasonal cycle of NO_2 time series from SCIAMACHY observations for specific regions enabled the disentanglement of NO_x sources like anthropogenic, biomass burning, soil emissions, and lightning and quantifying their individual contributions (van der A et al., 2008). The analysis of TROPOMI observations over Paris by Lorente et al. (2019) revealed that the main source of NO_x in winter is not from transport but residential heating. This contradicts current emission inventories, in which, following their analysis, residential heating is underestimated during winter and overestimated during summer.

As a consequence of human behavior, NO_x emissions also vary on a daily basis, especially between work and rest days. These patterns are readily identified and were first analyzed globally with GOME measurements by Beirle et al. (2003). Using the long-term observations of OMI combined with one year of TROPOMI data, Stavrakou et al. (2020) investigated the weekly NO_2 cycle and its trends over large cities. Over Europe and the US, a weakening trend is found. The opposite behavior is observed for regions with increasing anthropogenic emissions. Since natural emissions have no weekly cycle, this illustrates that the decline of anthropogenic emissions implies the dampening of the NO_2 weekly cycle. TROPOMI data enable the analysis of day-to-day variability using

---

[1] This section has been published in a similar form in Lange et al. (2022)

relatively short periods of observations. For Chicago, analysis of one season of TROPOMI observations found a significant weekend effect with reduced NO_x emissions of 30 % on weekends (Goldberg et al., 2019). Lorente et al. (2019) investigated day-to-day variations of NO_x emissions in Paris for individual days, with the lowest emissions on warm weekend days and the highest on cold working days.

With TROPOMI's higher spatial resolution compared to its predecessors, TROPOMI's measurements offer so far the best opportunity to deconvolve urban sources of NO_x and quantify their emissions. This facilitates the evaluation and improvement of emission inventories (Beirle et al., 2019, 2021). The catalog by Beirle et al. (2021) lists 451 sites that could be identified by a fully automated algorithm as NO_x point sources, such as power plants, metal smelters, cement plants, or industrial areas.

At the beginning of 2020, first China and subsequently most other countries took containment measures to limit the spread of the Coronavirus disease 2019 (COVID-19). These actions led to changes in human activities with reductions in transport and industrial activities, resulting in anthropogenic emissions. Temporally fine resolved emission estimates of these changes provide the opportunity to investigate source contributions and distinguish between natural and different anthropogenic sources of NO_x. Several studies have analyzed TROPOMI and OMI tropospheric NO_2 VCD observations during this period of containment measures in early 2020 and compared it with observations before COVID-19, reporting significant decreases of NO_2 over China (Liu et al., 2020a; Bauwens et al., 2020), northern Italy, the United States, and South Korea (Bauwens et al., 2020). As the tropospheric NO_2 VCD is also influenced by seasonality and meteorology in addition to behavioral patterns of anthropogenic activities, high variability cannot be directly attributed to changing NO_x emissions due to the COVID-19 containment regulations. Therefore, Goldberg et al. (2020) combined TROPOMI NO_2 observations with meteorological data and a chemical transport model and retrieved normalized changes of the tropospheric NO_2 VCDs which better represent the COVID-19 related NO_x emission changes.

In addition to determining NO_x emissions from satellite data, lifetimes of tropospheric NO_2 are also estimated from the observed tropospheric NO_2 VCDs (e.g., Leue et al., 2001; Beirle et al., 2003; Kunhikrishnan et al., 2004). Laughner and Cohen (2019) investigated the relation of NO_x lifetime to its own concentration by analyzing satellite data between 2005 and 2014 over North American cities, showing a significant change in NO_x lifetimes over this period, which is in the same order of magnitude as observed for NO_x emissions. Typical lifetimes range from 2 to 8 hours in polluted air masses and extend to about 1 day for more rural and cleaner background concentrations, for which nighttime chemistry must also be considered (Beirle et al., 2011; Valin et al., 2014; de Foy et al., 2014; Seinfeld and Pandis, 2006). The influence of the photolysis frequency on the NO_x lifetime was investigated by Beirle et al. (2011) using OMI data analyzing different seasons and locations showing lifetimes within a range of 2 to 6 h and a maximum of 8.5 h during wintertime for

Moscow. Studies analyzing winter data and especially winter months at higher latitudes are limited. Analyses with the chemical transport model GEOS-Chem show a tendency towards longer lifetimes of about 1 day (Martin et al., 2003; Shah et al., 2020).

Most studies using satellite data investigating NO_x emissions and lifetime are based on the method first developed by Beirle et al. (2011) and refined by later studies (Pommier et al., 2013; Valin et al., 2013). The analysis started on OMI data limited on a small number of particularly suited sources and using long periods of data (e.g., Beirle et al., 2011; Ialongo et al., 2014; de Foy et al., 2015; Lu et al., 2015; Liu et al., 2016). Follow-up studies applying this method to TROPOMI data show the ability to analyze NO_x emissions and lifetimes on much shorter periods of observations up to daily estimates (e.g., Lorente et al., 2019; Goldberg et al., 2019).

In the following, NO_x emissions and lifetimes are estimated from the high-resolution TROPOMI tropospheric NO_2 VCDs together with wind and ozone data based on the method by Beirle et al. (2011). For the first time, NO_x emissions and lifetimes are estimated for a large data set comprising 50 NO_x source regions well distributed around the world. The 50 sources include cities, isolated power plants, oil fields, industrial regions, and regions with a mix of sources. TROPOMI's good signal-to-noise ratio and spatial resolution make it possible to analyze a large number of sources using two years of data, and additionally divide and investigate the following periods: Seasons, working and rest days, and periods before and during COVID-19 restrictions. These analyses focus on evaluating the variability of NO_x emissions and lifetimes in space and time during the observation period.

3.2 Data set

The primary data set used to determine NO_x emission fluxes and lifetimes is the TROPOMI tropospheric NO_2 VCD. In addition, also wind speed, wind direction, and ozone volume mixing ratios are needed. Two different emission inventories are used to verify the determined NO_x emissions.

3.2.1 TROPOMI tropospheric NO_2 VCD

This study is based on the operational level-2 tropospheric NO_2 VCD product from March 2018 to November 2020. This includes the reprocessed (RPRO) and offline (OFFL) data of V01.00.01 to V01.03.02. Details about the TROPOMI NO_2 retrieval can be found in Sect. 2.5.1. Changes in the retrieval of the tropospheric NO_2 VCD data product between these different versions are minor, and the data can be mixed (van Geffen et al., 2020). On 2 December 2019, V01.04 was activated, including major updates in the NO_2 retrieval, which substantially increased the tropospheric NO_2 VCD. Further major modifications have been implemented in V02.02, released on 1 July 2021 (van Geffen et al., 2022b). To create a harmonized data set, a complete mission reprocessing based on V02.03.01 was performed and made available shortly after finishing this study. Therefore, the reprocessed data set could not be included in this study. However, the modifications in the TROPOMI NO_2 retrieval are further analyzed and discussed in the following Chapter 4.

The TROPOMI data with a spatial resolution of in the beginning $3.5\,\mathrm{km} \times 7\,\mathrm{km}$ and since 5 August 2019 $3.5\,\mathrm{km} \times 5.5\,\mathrm{km}$ are oversampled to a finer resolution grid of $0.01° \times 0.01°$. Each TROPOMI measurement is accompanied by a quality assurance value (qa_value) indicating the processing and retrieval result. Following the recommendation by Eskes and Eichmann (2022), only TROPOMI measurements with a qa_value greater than 0.75 are included in the analysis. In addition to removing problematic retrievals and partially snow/ice-covered scenes, this filter also excludes ground pixels with cloud radiance fractions of more than 50 %.

3.2.2 Wind data

To determine the NO_x emissions and lifetimes, wind speed and direction are needed for the same regions and period as the TROPOMI NO_2 data. Global wind data are provided by the European Centre for Medium-Range Weather Forecast (ECMWF) ERA5 reanalysis (Hersbach et al., 2018), which is given on an hourly basis with a horizontal resolution of $0.25° \times 0.25°$ on model levels. To merge the TROPOMI observations with the wind data in space and time, the wind data are oversampled to the same grid ($0.01° \times 0.01°$) as the TROPOMI data and interpolated to the S5P overpass time.

Since wind speed and direction change with height above the ground (see Sect. 2.1.1), the selected height of the wind data can be critical for the NO_x emissions and lifetime estimates. Beirle et al. (2011) compared NO_x emissions and lifetime estimates using wind data averaged from the ground up to 200 m, 500 m, and 1000 m, finding changes of less than 2 % respectively 5 % on average when using 200 m, respectively 1000 m instead of 500 m. For individual sources changes were found to be less than 15 %.

This study uses the boundary layer height data provided by ERA5 (Hersbach et al., 2018) to average the wind data over the boundary layer. Using boundary layer averaged wind data instead of a fixed height has the advantage that seasonal variations in the wind data caused by the seasonal variability of the boundary layer height are accounted for. Assuming that the boundary layer is well mixed for the early afternoon overpass of TROPOMI, wind information averaged over this layer is expected to be representative for the NO_x emissions and lifetimes investigated here (see Sect. 2.1.1).

3.2.3 Ozone volume mixing ratios

For converting the tropospheric NO_2 VCDs into NO_x columns to estimate emissions in terms of NO_x (see Sect. 3.3.3), ozone volume mixing ratios, taken from the ECMWF ERA5 reanalysis, are used. The ozone volume mixing ratios are hourly data with a horizontal resolution of $0.25^\circ \times 0.25^\circ$ on model levels, the same as the used wind data. The data are interpolated to the S5P overpass time, oversampled to the same 0.01° resolution as the TROPOMI data, and averaged over the boundary layer in the same way as the wind data.

3.2.4 Emission inventories

The TROPOMI-based NO_x emission estimates can be compared to estimates from bottom-up emission inventories. The Emissions Database for Global Atmospheric Research (EDGAR) is an independent, global database of anthropogenic emissions of greenhouse gases and air pollution. EDGAR provides monthly NO_x emission estimates on a $0.1^\circ \times 0.1^\circ$ spatial grid. It is based on activity data (i.e., population, energy, fossil fuel production, industrial processes, agricultural statistics), mainly from the International Energy Agency (IEA), corresponding emission factors, national and regional information on technology mix data, and end-of-pipe measurements. The input data sets comprising locations of energy and manufacturing facilities, road networks, shipping routes, human and animal population density, and agricultural land use, thus point, line, and area grids at various resolutions, have been resampled on a $0.1^\circ \times 0.1^\circ$ grid. The national sector totals are then distributed across the country's area using the specified percentages of the spatial proxies (Crippa et al., 2018, 2019).

Uncertainties in bottom-up inventories are inferred from the dependence of emission factors on the technology, fuel type, and combustion condition, as well as the low-resolution activity data and emission factors. The uncertainty in NO_x emissions from the EDGAR inventory v4.3.2 varies from 17 % to 69 % for different regions (Crippa et al., 2018). The limited temporal coverage of bottom-up emissions results in additional uncertainties. For this study, the most recent year available in EDGAR v5.0 was 2015, which does not reflect recent changes found from trend analysis of NO_2 column satellite data (Georgoulias et al., 2019). Considering that a large part of the regions analyzed in this study are located in highly populated and industrialized regions, where NO_2 has generally decreased according to Georgoulias et al. (2019), it can be assumed that the TROPOMI NO_x emission estimates for the majority of analyzed regions should be lower than the EDGAR estimates for 2015.

In the United States, emissions from large power plants are tracked hourly by the Continuous Emission Monitoring System (CEMS) of the Environmental Protection Agency (EPA) (`https://www.epa.gov/emc/emc-continuous-emission-monitoring-systems`, last access: 12 December 2022). Emission rates are measured continuously inside the power plant stacks and are made available as hourly mean values in the CEMS database. Since the CEMS data are limited to large power plants in the United States, comparison possibilities with TROPOMI-based emission estimates are much more limited than with EDGAR, but due to the high temporal resolution and up-to-date data, more detailed comparisons can be performed.

3.3 Method

The method for estimating NO_x emissions and lifetimes from satellite tropospheric VCDs independent of model data is based on the method introduced by Beirle et al. (2011) and further refined by later studies (Pommier et al., 2013; Valin et al., 2013). In this method, the in wind direction rotated NO_2 distributions are averaged for individual NO_x source areas and, assuming an exponential decay, emission strength and lifetime are determined. The method can be described in three major steps, exemplarily shown in Fig. 3.1 for the Medupi and Matimba power plants in South Africa. First, the source region is selected based on the mean tropospheric NO_2 VCD map, as shown in Fig. 3.1a. This selection of sources is described in more detail in Sect. 3.3.1. The tropospheric NO_2 VCD of each pixel is converted to tropospheric NO_x VCD. Each satellite measurement is rotated around the source location based on the ERA5 wind data, resulting in a common wind direction

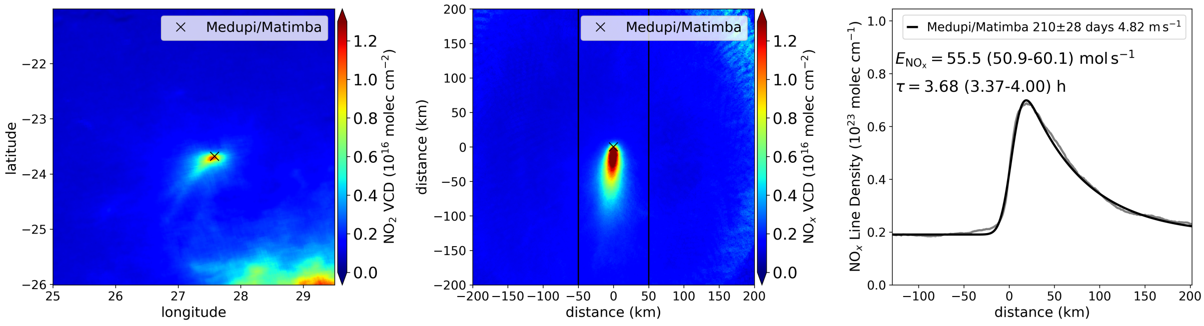

(a) (b) (c)

Figure 3.1: (a) Mean tropospheric NO_2 VCD from 1 March 2018 to 29 February 2020 for days with wind speed $> 2\,\mathrm{m\,s^{-1}}$ in the region of the power plants Medupi and Matimba, South Africa. (b) Each TROPOMI pixel is converted to NO_x and rotated with its wind direction around the source (cross), resulting in an upwind-downwind pattern. Black lines indicate a sector of ± 50 km around the source. (c) NO_x line density as a function of distance to the source calculated for the ± 50 km sector (gray), EMG fit results (black) with estimated emissions and lifetime and 1-sigma uncertainties derived by the fitting procedure.

and an upwind-downwind NO_x pattern, see Fig. 3.1b. More details are provided in Sect. 3.3.2. In the last step, an exponentially modified Gaussian (EMG) function is applied to the averaged tropospheric NO_x VCDs to estimate the NO_x emissions and lifetime (see section 3.3.4). The resulting function with estimated NO_x emissions and lifetime for the Medupi/Matimba NO_x distribution is plotted in Fig. 3.1c.

This study uses two years of TROPOMI tropospheric NO_2 VCD data from 1 March 2018 to 29 February 2020 for the general analysis (Sect. 3.4.1 to 3.4.5), which excludes data for which COVID-19 regulations might have influenced the NO_x emissions. Due to early COVID-19 regulations in China, the analyzed period for the two Chinese sites included in this study ends already on 22 January 2020. The analysis of the impact of COVID-19 containment measures on NO_x emissions (Sect. 3.4.6) uses TROPOMI data from January to November of 2019 and 2020.

3.3.1 Selection of sources

To obtain a representative analysis of the variability of NO_x emissions and lifetime, the emission sources must be well distributed around the world to provide information on latitudinal dependence, climatic conditions, and seasonal variation. By visually inspecting the global mean tropospheric NO_2 VCD distribution from March 2018 to February 2020 shown in Fig. 3.2, 50 target regions were selected, marked with red circles in the Figure. All analyzed source regions are listed with more details in the Appendix Table A.1.

The selected sources are a mix of cities with predominantly domestic and transport emissions, e.g., Madrid (Spain), cities with more industrial emitters, e.g., Chelyabinsk (Russia), power plants such as Medupi and Matimba (South Africa), or oil refinery areas such as Sarir Field (Libya). The best performance of the method is obtained for isolated point sources, which have a high contrast between source emissions and the background NO_2. In order to maximize the number of satellite observations, regions having little cloud cover are preferred. To obtain clear outflow patterns, target regions with additionally relatively homogeneous wind patterns are particularly suitable. Sources located in coastal or mountainous regions with inhomogeneous terrain often show inhomogeneous wind patterns that are more difficult to interpret and lead to greater uncertainties in NO_x emissions and lifetime. Thus, some originally promising sources, such as Santiago de Chile, were omitted. Further improvement of the outflow patterns is achieved by filtering out data with wind speeds of less than $2\,\mathrm{m\,s^{-1}}$. Even though many sources with high NO_2 signals are found in China, only two sources are selected for the analysis. Most sources are located in areas influenced by nearby emission sources, resulting in low contrast of tropospheric NO_2 VCDs between the target and the local background. For such conditions, other methods to determine NO_x emission rates and lifetimes are more appropriate (Liu et al., 2016).

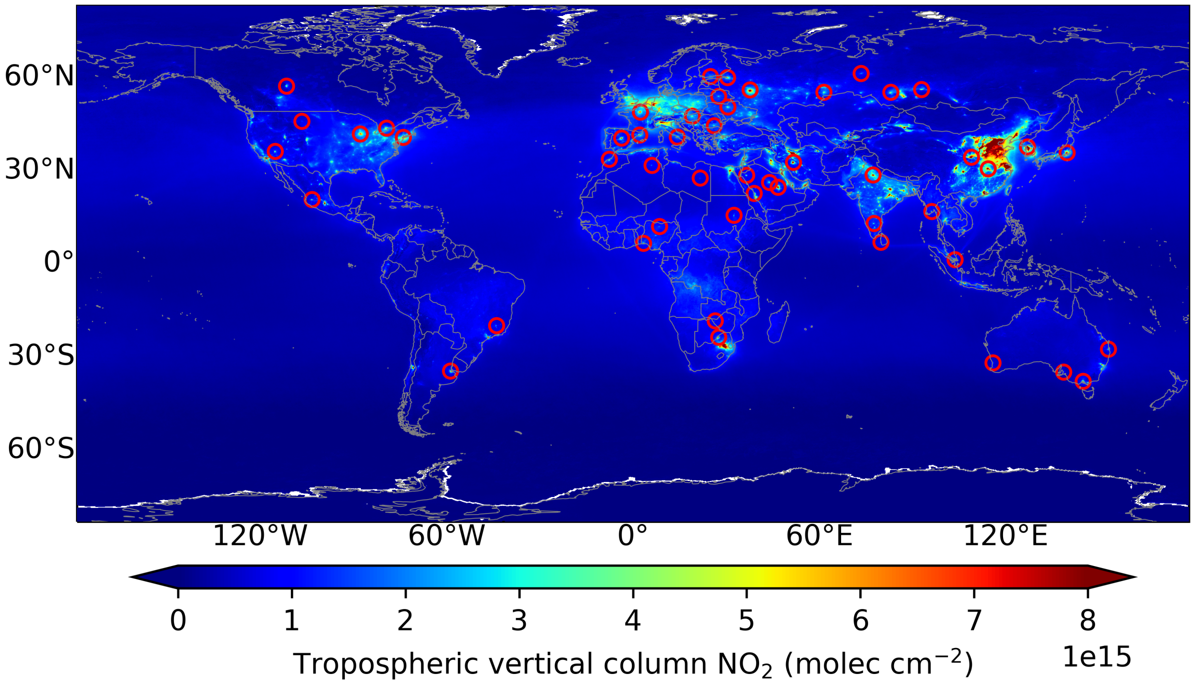

Figure 3.2: TROPOMI level-2 RPRO and OFFL V01.00.01 to V01.03.02 tropospheric NO_2 VCD product from March 2018 to February 2020. Red circles mark 50 NO_x emission sources analyzed in this study. All analyzed source regions are listed with more details in the Appendix Table A.1.

Although efforts were made to select a broad range of regions in many aspects, some selection bias may have been introduced, for example, by not analyzing regions with mostly cloudy conditions, low wind speeds, or regions with many emission sources and higher background levels.

3.3.2 Rotation technique

For investigating the spatial pattern of the NO_2 data, the directional classification to determine the distribution as a function of downwind distance by Beirle et al. (2011) is combined with a rotation technique. Therefore, each TROPOMI observation is rotated with its wind direction around the source to a common wind direction preventing a neutralization of outflow patterns of opposite wind directions (Pommier et al., 2013; Valin et al., 2013). Using the rotation to a common wind direction instead of directional filtering has the advantage of creating just one grouping instead of several for each wind direction. Thus, all data can be analyzed together, independently of their wind direction.
Figure 3.3 shows a scheme of the rotation procedure. Each TROPOMI observation is merged with the ERA5 wind data in time and space and rotated with its wind direction around the defined reference point, e.g., the city center or the power plant site. The

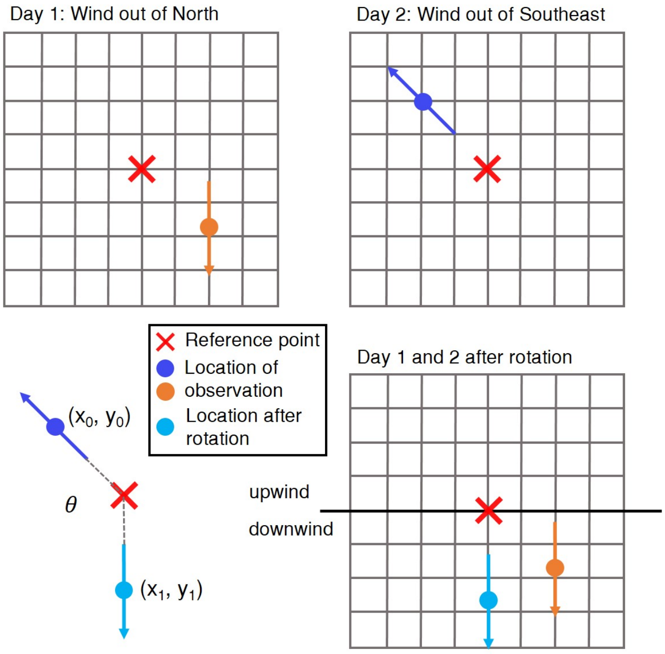

Figure 3.3: Scheme of the rotation procedure. Each observation is rotated with an angle θ, corresponding to the respective wind direction, around the defined reference point, e.g., the city center or the power plant site. After the rotation, all wind vectors are aligned and indicate a northerly wind direction.

rotation can be described with Eq. 3.1.

$$\begin{bmatrix} x_1 \\ y_1 \end{bmatrix} = \begin{bmatrix} \cos(-\theta) & \sin(-\theta) \\ -\sin(-\theta) & \cos(-\theta) \end{bmatrix} \cdot \begin{bmatrix} x_0 \\ y_0 \end{bmatrix} \tag{3.1}$$

If all observations are aligned to an effectively northerly wind, as done in this study, θ corresponds to the wind direction. After the rotation, all wind vectors are aligned in the same direction. Each observation preserves its upwind-downwind character. The NO_2, respectively NO_x enhancement is located downwind of the source reference point, and a clear outflow pattern becomes visible. This is shown in Fig. 3.1b for the Medupi/Matimba power plants in South Africa, where a clear plume and an upwind-downwind distribution is observed after rotation.

3.3.3 Conversion from NO_2 to NO_x

In previous studies, the emissions were usually calculated on the averaged NO_2 outflow distribution and then scaled to NO_x emissions by applying a fixed $[NO_x]/[NO_2]$ ratio of 1.32 (e.g., Beirle et al., 2011; Ialongo et al., 2014; Goldberg et al., 2019; Beirle et al., 2019), which is based on the recommendation by Seinfeld and Pandis (2006) for polluted conditions around noon (see also Sect. 2.2.2). A more differentiated determination of the conversion factor is required to calculate NO_x emissions for all seasons and sources distributed over the different areas of the globe. Assuming that the Leighton photostationary state applies to the polluted air masses of investigation, concentrations of NO_2 and NO are coupled by:

$$\frac{[\mathrm{NO_x}]}{[\mathrm{NO_2}]} = 1 + \frac{[\mathrm{NO}]}{[\mathrm{NO_2}]} = 1 + \frac{J_{\mathrm{NO_2}}}{k_{\mathrm{NO+O_3}} \cdot n_{\mathrm{O_3}}} \tag{3.2}$$

with $J_{\mathrm{NO_2}}$ the photolysis frequency of NO_2 and $k_{\mathrm{NO+O_3}}$ the rate constant for the reaction of NO with O_3 (Seinfeld and Pandis, 2006). Applying Eq. 3.2, a conversion factor is calculated for each TROPOMI observation.

Ozone data are taken from the ERA5 reanalysis, interpolated to the S5P overpass, and averaged within the respective sector around the source (see Fig. 3.1b) used for the emission calculation.

Under clear-sky conditions, the photolysis frequency in the boundary layer can be parameterized as a function of the SZA (Dickerson et al., 1982):

$$J_{\mathrm{NO_2}} = 0.0167 \exp\left(-\frac{0.575}{\cos(\mathrm{SZA})}\right) (\mathrm{s^{-1}}). \tag{3.3}$$

The rate constant $k_{\mathrm{NO+O_3}}$ for the reaction of NO with O_3 can, in general, be well represented by the Arrhenius expression, following the recommendation by Atkinson et al. (2004):

$$k_{\mathrm{NO+O_3}}(T) = 2.07 \cdot 10^{-12} \exp\left(-\frac{1400}{T}\right) (\mathrm{cm^3\,molec^{-1}\,s^{-1}}). \tag{3.4}$$

Temperature data are taken from the hourly ERA5 reanalysis data with a resolution of 0.25° × 0.25°, averaged about the boundary layer, oversampled to the same spatial resolution as the TROPOMI observations, and interpolated to the overpass time.

Figure 3.4 displays the course of the discussed parameters: the O_3 data, the photolysis frequency of NO_2 $J_{\mathrm{NO_2}}$, the reaction rate constant $k_{\mathrm{NO+O_3}}$ and the calculated $[\mathrm{NO_x}]/[\mathrm{NO_2}]$ ratio for Moscow and Riyadh from March 2018 to March 2020 for days on which TROPOMI observations are available within the source area. All parameters show a clear seasonality, but more pronounced for Moscow than for Riyadh. The resulting $[\mathrm{NO_x}]/[\mathrm{NO_2}]$ ratio shows a maximum in summer and a minimum in winter. For Moscow, the maximum values in summer are around 1.4, and the minimum in winter is close to 1. Due to Riyadh's not very pronounced seasonality, the resulting $[\mathrm{NO_x}]/[\mathrm{NO_2}]$ ratio shows much less variation, with maximum values in summer around 1.5 and minimum values in winter around 1.3.

$[\mathrm{NO_x}]/[\mathrm{NO_2}]$ ratios are calculated for each source area for the investigated period, and the tropospheric NO_2 VCD of each pixel is converted into tropospheric NO_x VCDs.

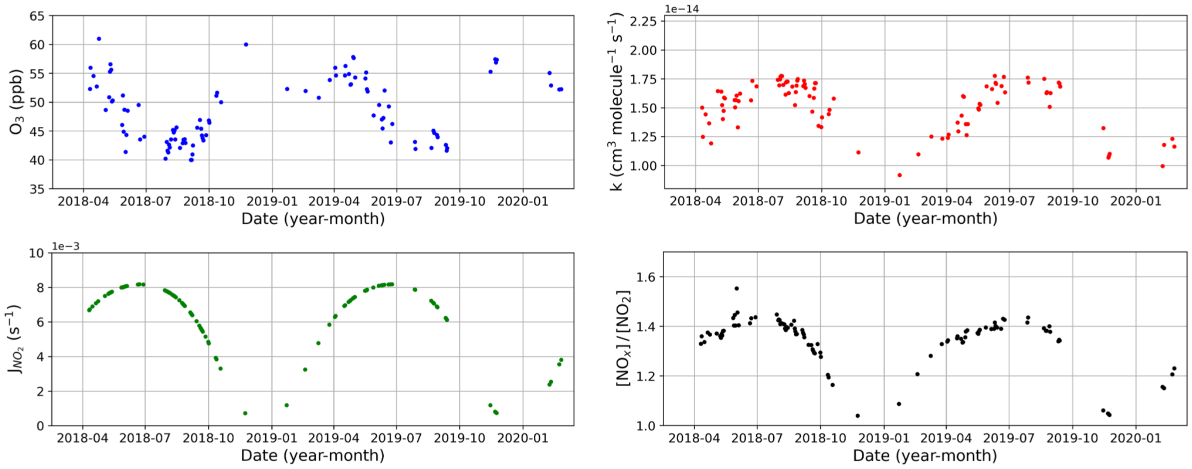

(a) Moscow, Russia

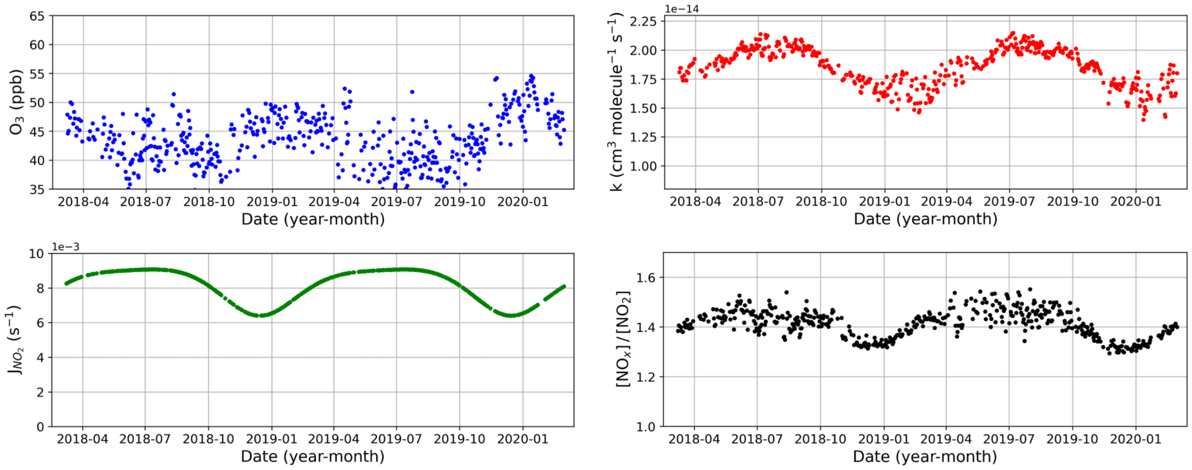

(b) Riyadh, Saudi Arabia

Figure 3.4: Plots of time series of the O_3 data, photolysis frequency of NO_2 J_{NO_2}, reaction rate constant k_{NO+O_3} and the resulting $[NO_x]/[NO_2]$ ratio for Moscow (a) and Riyadh (b) for days on which TROPOMI observations are available within the source area.

3.3.4 Line density calculation

The outflow pattern of the tropospheric NO_2 respectively NO_x VCD with a decay of the signal with distance from the source reflects the changes in NO_x over time. Beirle et al. (2011) suggested a method to estimate NO_x emissions and lifetime by integrating the VCDs perpendicularly to the wind direction and thus converting the two-dimensional maps into one-dimensional so-called line densities. After the rotation and conversion from NO_2 into NO_x on a single pixel basis, the NO_x VCDs are averaged for each source area. From the mean tropospheric NO_x VCDs, NO_x line densities are calculated by integrating perpendicularly to the wind direction. To reduce the influence of possible surrounding sources, the line density is calculated only in a defined sector around the source, which does not truncate the plume and thereby misses emissions (see Fig. 3.1b). Typical sector widths are between ± 15 and ± 70 km, depending on the plume's width. Depending on the plume length and the presence of other influencing sources, the sector length ranges from up to 200 km upwind and 400 km downwind of the source. As an additional quality filter, only days where at least 50% of the ground scenes in this sector contain measurements and are not filtered because of clouds or low wind speeds are included in the averaging and thus the analysis. Fig. 3.1c shows the calculated line density for the Medupi and Matimba power plants as a function of distance to the source. As a result of mixing and transport processes, the maximum is shifted in the wind direction, and the line density curve is steep in the upwind and less steep in the downwind sector with an exponential decay. The NO_x emissions and lifetime can be estimated by fitting this line density curve with the exponentially modified Gaussian (EMG) method as proposed by Beirle et al. (2011). The fitting model M as a function of distance x to the source is described by

$$M(x) = E' \cdot (e \otimes G)(x) + B, \tag{3.5}$$

with a convolution of the exponential function $e(x)$ and the Gaussian function $G(x)$ scaled by a multiplicative emission factor E' and shifted by a background concentration offset B. The exponential function $e(x)$ describes the transport and chemical decay with

$$e(x) = \exp\left(\frac{-(x-X)}{x_0}\right), \tag{3.6}$$

for $x \geq X$ (downwind) and else (upwind) zero, where X is the location of the apparent source relative to the source reference point and x_0 the distance over which the line density decreases by a factor of e (e-folding distance). The Gaussian function represents the broadening of the source by spatial smoothing with the Gaussian function width σ, which accounts for spatial smoothing caused by the extent of the spatial source, the TROPOMI pixel size and wind variations:

$$G(x) = \frac{1}{\sqrt{2\pi}\sigma} \exp\left(-\frac{x^2}{2\sigma^2}\right). \tag{3.7}$$

This results in:

$$\begin{aligned} M(x) &= E' \cdot \left(\exp\left(\frac{-(x-X)}{x_0}\right) \otimes \frac{1}{\sqrt{2\pi}\cdot\sigma} \cdot \exp\left(-\frac{x^2}{2\cdot\sigma^2}\right)\right) + B & (3.8)\\ &= \frac{E'}{2} \cdot \exp\left(\frac{\sigma^2}{2\cdot x_0^2} - \frac{x-X}{x_0}\right) \cdot \operatorname{erfc}\left(\frac{\sigma^2 - x_0(x-X)}{\sqrt{2}\cdot\sigma\cdot x_0}\right) + B. & (3.9) \end{aligned}$$

The fitted *e*-folding distance x_0 and the mean wind speed w within the line density sector, representing the plume transport speed, is then used to calculate the mean lifetime:

$$\tau = \frac{x_0}{w}. \tag{3.10}$$

Downwind changes, for example, due to changing $[NO_x]/[NO_2]$ ratios or effects of non-linearity in the NO_x chemistry on lifetime in the plume, can not be resolved by the described method. Since the calculated lifetime includes deposition effects, chemical conversion, and wind advection, it underestimates the chemical lifetime but can be considered as an effective mean dispersion lifetime (Beirle et al., 2011; de Foy et al., 2014).
From the multiplicative emission factor E', which describes the total amount of NO_x near the source, and the mean wind speed w within the line density sector, the NO_x emission flux in $\mathrm{mol\,s^{-1}}$ can be calculated by

$$E_{\mathrm{NO}_x} = \frac{E'}{N_\mathrm{A}} \cdot w \tag{3.11}$$

with the Avogadro constant N_A.
In the following, given uncertainties and error bars for the emission and lifetime estimates are based on one standard deviation derived by the EMG fit and are calculated with error propagation. Additional factors influencing the total uncertainty are, among other things, especially the TROPOMI tropospheric NO_2 VCD itself, which is low biased (see e.g., Verhoelst et al. (2021) and Chapter 4) and thus leading to a systematic underestimation of the derived NO_x emissions. More details on error sources are given in Sect. 3.4.7.

3.4 Results and discussion

The EMG method is applied to the averaged TROPOMI tropospheric NO_x VCDs of the 50 selected source regions, and NO_x emissions and lifetimes are calculated. The estimates are performed on the entire 2-year period from 1 March 2018 to 29 February 2020 and for separated periods like seasons, working days and weekends, and the COVID-19 pandemic period. Due to sometimes poor statistics, when separating the two years data set into shorter periods, not all source regions are included in all analyses.

3.4.1 Comparison to similar studies

First, the calculated emissions are compared to other recent studies by Beirle et al. (2019), Goldberg et al. (2019), and Lorente et al. (2019), which estimated NO_x emissions from TROPOMI data. These studies have investigated seven regions that can be compared with emission estimates from this study. Table 3.1 shows the NO_x emissions for the seven source regions estimated within this study for the 2-year period and the results of the three comparative studies. Since the studies refer to slightly different periods and the methods differ slightly, deviations are expected. Goldberg et al. (2019) analyzed TROPOMI data from May to September 2018, which is within the 2 years analyzed in this study. Thus, it is possible to estimate and compare the results for the same period and provide better comparability; these estimates are given in parentheses in Table 3.1.

Table 3.1: NO_x emission estimates for seven source regions are compared to emissions derived from studies by Beirle et al. (2019), Goldberg et al. (2019), and Lorente et al. (2019) also using TROPOMI data. Values in brackets are derived for the same data period as in Goldberg et al. (2019). Errors are 1 standard deviation derived by the EMG fitting procedure.

	NO_x emissions ($\mathrm{mol\,s^{-1}}$)			
Source region	This study	Beirle et al.	Goldberg et al.	Lorente et al.
Riyadh	186.1 ± 7	144.8–184.5	—	—
Medupi/Matimba	55.5 ± 4.5	37.2	—	—
Chicago	82.9 (62.3) ± 7 (8)	—	73	—
New York	101 (75.5) ± 8 (5)	—	57.4	—
Toronto	53.8 (50.8) ± 3.5 (4.5)	—	51.9	—
Colstrip	4.6 (4.9) ± 0.2 (0.4)	—	5.3	—
Paris	56.2 ± 4.5	—	—	53

Beirle et al. (2019) analyzed TROPOMI tropospheric NO_2 VCDs from December 2017 to October 2018 with a modified version of the operational data to reduce the negative bias. The NO_x emission estimates are based on the continuity equation. The emission range given for Riyadh in Table 3.1 is based on two estimates, one for the urban area and one for a greater area of 250 km × 250 km around Riyadh. Emissions retrieved in this study are slightly higher than those for Riyadh and significantly higher than those for Medupi/Matimba given in Beirle et al. (2019). Besides the difference in analyzed periods, additional reasons for deviations can be the use of different wind fields and NO_2 to NO_x conversion factors. Beirle et al. (2019) used a fixed $[NO_x]/[NO_2]$ ratio of 1.32 and wind data in the height of 450 m compared to the daily and region specific calculated NO_2 to NO_x conversion factors and the wind data averaged over the boundary layer applied in this study. For Riyadh, the estimated mean $[NO_x]/[NO_2]$ conversion factor is with 1.41 ± 0.05 slightly higher than the value of 1.32. For Medupi/Matimba, it is significantly higher with 1.54 ± 0.13, and can to a large extent explain the higher NO_x emissions estimated in this study compared to those in Beirle et al. (2019).

The NO_x emission estimates for Chicago, New York, Toronto, and the Colstrip power plant by Goldberg et al. (2019) are based on the operational TROPOMI NO_2 data from May to September 2018. The authors found that plumes are sometimes misaligned by up to 30° after the rotation based on ERA5 wind direction data. Therefore, the data were manually adjusted by visual inspecting every day. Due to their focus on summer months and generally lower NO_x emissions in summer than in winter (see also Sect. 3.4.3), lower NO_x emission estimates are expected compared to the 2-year average estimates. For a better comparison, Table 3.1 also includes emission estimates for the same period as used in Goldberg et al. (2019), and as expected, the agreement improves. Still, deviations remain and are particularly significant for New York; possibly, the wind information and rotation may have a greater influence here.

Lorente et al. (2019) estimated NO_x emissions for Paris from the operational TROPOMI tropospheric NO_2 VCDs on a single overpass using 36 orbits obtained on 34 days between February and June 2018. On average, they estimated NO_x emissions of $53\,\mathrm{mol\,s^{-1}}$, which agrees well with the $56.2\,\mathrm{mol\,s^{-1}}$ derived in this study.

Due to different periods, slightly different methods, and input parameters, deviations are expected, but generally, the estimated emissions are in reasonable agreement.

3.4.2 Comparison to emission inventories

The determined NO_x emissions are compared to those reported in the EDGAR emission database. Figure 3.5 shows the NO_x emissions derived by the EMG method from the 2 years of TROPOMI data for the 50 source regions vs. the reported emissions from the EDGAR database for the year 2015. The emission inventory data are integrated over the area where the top-down method based on TROPOMI data is sensitive. The comparison shows that most source regions have higher NO_x emissions received from the EDGAR database than the results from the EMG method. However, there are several possible reasons for the underestimation compared to the EDGAR emissions, and a perfect agreement is not expected.

One explanation for differences is the different periods the two emission estimates are based on. While the EDGAR emissions are based on data for 2015, the EMG method is performed on TROPOMI NO_2 data from March 2018 to February 2020. Thus the EDGAR emissions do not reflect the recent decreasing NO_x emissions in many places, which were found from trend analysis of NO_2 column satellite data (Georgoulias et al., 2019). In addition, the EDGAR database gives 24 h annual averages, whereas the EMG method is only sensitive to emissions up to a few hours before the TROPOMI measurement on nearly cloudless days.

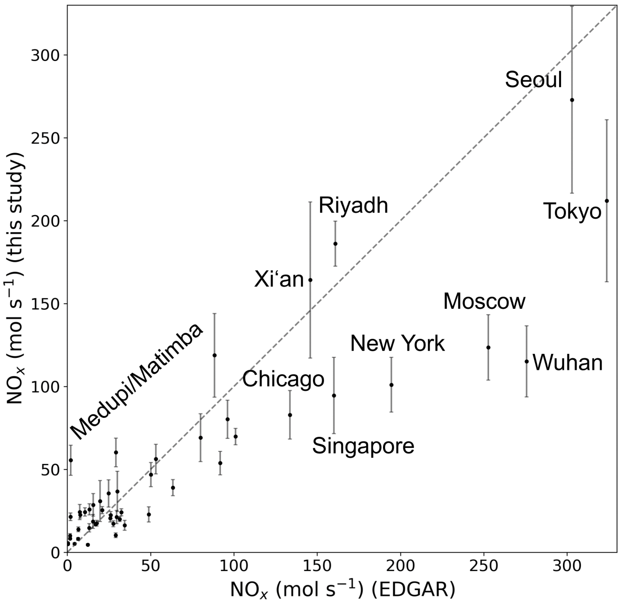

Figure 3.5: NO_x emissions derived from 2 years of TROPOMI data (1 March 2018 to 29 February 2020) for 50 sources calculated with the EMG method compared to the NO_x emissions derived from the EDGAR emission database (v.5.0, 2015). The dashed line shows the 1:1 ratio. Error bars are the standard deviation derived by the EMG fitting procedure for emission estimates.

Another reason for the underestimation compared to the EDGAR emissions is the known low bias of the TROPOMI tropospheric NO_2 VCD as compared to validation measurements (e.g., Dimitropoulou et al., 2020; Judd et al., 2020; Verhoelst et al., 2021; Lange et al., 2023). Verhoelst et al. (2021) showed that this negative bias is most pronounced for regions with larger tropospheric NO_2 VCDs, which is consistent with the result that the difference between EMG and EDGAR NO_x emission estimates is largest for source regions with high NO_x emissions such as Tokyo, Wuhan, Moscow, and New York. This underestimation of the TROPOMI tropospheric NO_2 VCD is reduced within later product versions, which is further analyzed in the following Chapter 4).

One prominent point in Fig. 3.5, which on the contrary, shows significantly higher emissions estimated by the EMG method ($55.5\,\mathrm{mol\,s^{-1}}$) than provided in the EDGAR database can be assigned to the Medupi and Matimba power plants. One likely explanation for this large deviation is that the Medupi power plant was put in operation only in 2015, the year to which the EDGAR database refers. Consequently, it can be assumed that Medupi was only partly or not at all included in the database. This shows the potential of satellite data and the EMG method to identify new NO_x emission sources before up-to-date emission inventory data are available or to identify sources missing in emission inventories.

The NO_x emissions determined for the Colstrip power plant (Montana, USA) can be compared to reported emissions within the EPA CEMS database. Due to the high temporal resolution and up-to-date data of the EPA CEMS database, the comparison can be performed in more detail. Figure 3.6 shows a time series of the NO_x emissions reported by the

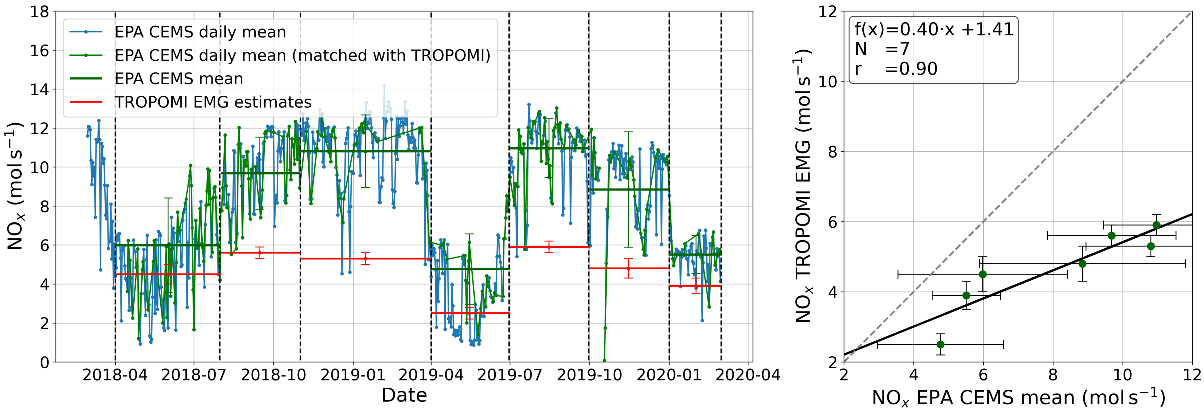

Figure 3.6: (left) Time series of CEMS reported NO_x emissions for the Colstrip (Montana, USA) power plant compared to the NO_x emissions estimated by the EMG method, using TROPOMI NO_2 data. CEMS data are averaged between 11–14 local time. Data in blue have a daily resolution. Data on TROPOMI measurement days are plotted in green. Means over seven selected periods, marked by the dashed black lines, are shown by horizontal green lines for the CEMS data and red lines for the TROPOMI EMG estimates.
(right) Scatter plot of TROPOMI EMG vs. CEMS NO_x emission estimates for the seven periods. The 1:1 line is indicated with the gray dashed line. The solid black line indicates the linear regression. Error bars are the standard deviation derived by the EMG fitting procedure for the EMG emission estimates and the monthly standard deviation for the CEMS mean values.

EPA CEMS for the Colstrip power plant from February 2018 to March 2020. Assuming that a typical NO_x lifetime for the Colstrip power plant is on average around 3 h, the reported NO_x emissions are averaged between 11 and 14 local time, which is about 3 h before the typical TROPOMI observation.

The EMG method is widely used to analyze emissions and lifetime using satellite data but is mostly used for data from spring to autumn. This study also extensively uses winter data, which brings larger uncertainties to the analysis, e.g., due to longer lifetimes in winter and often less data availability. The high temporal resolution EPA CEMS data are used to verify if the EMG method can reproduce the variability seen in the reported emissions independently of season. Therefore, seven periods of a range between 2 and 5 months are defined from February 2018 to March 2020. CEMS data reported on TROPOMI measurement days are averaged within the defined periods. In Fig. 3.6, they are shown as horizontal green lines. The horizontal red lines indicate the estimates from the EMG method. The averaged TROPOMI EMG and CEMS data show a similar pattern of the estimated emissions for the Colstrip power plant over the year, with an underestimation by the EMG method compared to the reported CEMS data for all periods. This low bias of the TROPOMI-based emissions can be explained by a loss of NO_x after its measurement in the stack or the early phase of NO_2 plume formation, and to a large extent also by the known low bias of the TROPOMI data discussed before. As found by Beirle et al. (2019), the underestimation is expected to be particularly pronounced for power plants, for which wrong vertical NO_2 profiles in the TM5 model cause too high AMFs.

Figure 3.6 shows a scatter plot of the two data sets for the seven defined periods. The linear regression reveals a slope of 0.4 ± 0.09 with a correlation of 0.9, reflecting the underestimation of the TROPOMI EMG estimates compared to the reported CEMS data but also the well-matching emission patterns.

Based on this comparison, it can be concluded that power plant emissions can fluctuate strongly over time and that TROPOMI-based NO_x emissions for power plants can be low by a factor of about 2, as already discussed in Beirle et al. (2019). It was also shown that the EMG method applied to TROPOMI NO_2 data reproduces the temporal variability seen in the CEMS data reasonably well and does not show a clear seasonal bias. Therefore, the method can be expected to produce good results even when analyzing winter data.

3.4.3 Seasonality of NO_x emissions

To investigate seasonal variations of NO_x emissions, the 2 years of TROPOMI data are separated into winter, spring, summer, and autumn, and emissions are calculated separately for each season. Winter months are defined as December, January, and February (DJF, Southern Hemisphere JJA), spring as March to May (MAM, Southern Hemisphere SON), summer as June to August (JJA, southern hemisphere DJF), and fall as September to November (SON, southern hemisphere MAM). Thus, the data set provides a maximum of 2 times 3 months for each season. Due to cloud cover, inhomogeneous wind patterns, and resulting partly poor statistics after separating the data set into seasons, only 34 of the 50 source regions are included in the seasonality analysis. For Wuhan, where COVID-19 regulations started early, and the resulting NO_x emission reductions may influence the investigation of a seasonality effect, the analysis is limited to data from March 2018 to 22 January 2020.

Fig. 3.7 shows the ratios of NO_x emissions in summer and winter for the 34 source regions. For most of the sources, NO_x emissions are found to be higher in the winter months than during summer. Naples (Italy), Wuhan (China), Novosibirsk, and Krasnoyarsk (Russia) are among the source regions which show much higher NO_x emissions in winter than during summer, with a summer-to-winter ratio of about 0.3. This is expected in regions where home heating contributes significantly to the NO_x emissions in winter. However, some source regions show unexpected emission ratios, e.g., the emission estimates for Casablanca (Morocco) result in a summer-to-winter ratio of 0.32 ± 0.17. Due to its location on the Atlantic coast, temperature fluctuations are mitigated, summers are warm but usually not very hot, and winters are mild, so lower seasonal variations in emissions are to be expected. An explanation for the contrary observation has not been found so far.

For Medupi/Matimba in South Africa and some other regions, NO_x emissions are actually higher during summer than during winter. Interestingly, the source regions with summer-

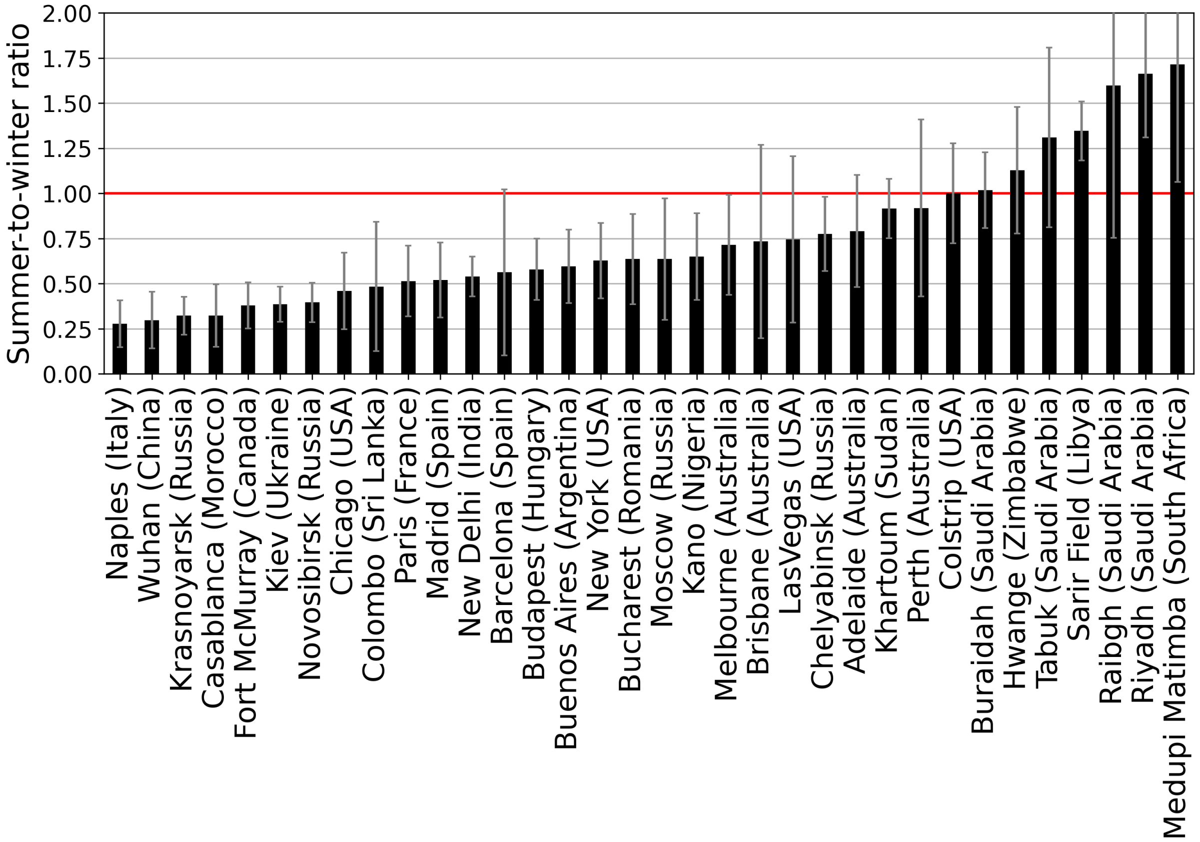

Figure 3.7: Summer-to-winter ratio of retrieved NO_x emission data (1 March 2018 to 29 February 2020). Data are separated into winter (Northern Hemisphere: DJF, Southern Hemisphere: JJA) and summer (Northern Hemisphere: JJA, Southern Hemisphere: DJF) for 34 source regions. From left to right in increasing ratio. The red line indicates the 1:1 line where summer and winter NO_x emissions are equal, below the line winter emissions are larger, and over the line summer emissions are predominant compared to the winter emissions. Error bars are the standard deviation derived by the EMG fitting procedure for emission estimates.

to-winter ratios above one or close to one in Saudi Arabia (Riyadh, Rabigh, Tabuk, Buraidah), Libya (Sarir field), and Sudan (Khartoum) are all located in hot desert climate regions that are warm and dry throughout the whole year, but where long periods of heat are common, especially in summer. Thus, a likely explanation for the higher NO_x emissions in summer is higher power consumption from the use of air conditioning in summer. Since most other emission studies focus on summer months for their analysis (Beirle et al., 2019; Goldberg et al., 2019; Ialongo et al., 2014), there are only a few studies investigating the seasonality of NO_x emissions. Beirle et al. (2011) found that NO_x emissions estimated from OMI NO_2 data are stable throughout the year for Madrid and Singapore and that variability found for other cities, which could reflect a change in emissions, was not significant. Analyzing TROPOMI NO_2 data from February to June 2018 for Paris, Lorente et al. (2019) showed that the highest NO_x emissions occur on cold weekdays in February and the lowest emissions on warm weekend days in spring. The authors concluded that this indicates the importance of the contributions from the residential heating sector to

NO_x emissions on cold winter days. The results of Lorente et al. (2019) are supported by the summer-to-winter ratio of 0.51 ± 0.2 estimated in this study for Paris using the 2 years of TROPOMI data.

In summary, the analysis of seasonality shows higher NO_x emissions during winter than during summer for most source regions. This is in agreement with expectations, considering that most of the selected source regions are in mid-latitudes and temperate climates. Not all source regions show significant differences between summer and winter NO_x emissions, and some results are unexpected. However, the trend from high latitude source regions with higher NO_x emissions in winter to desert climate regions with higher emissions in summer is plausible. In some parts, the strong seasonality found here contradicts the relatively weak seasonality found by Crippa et al. (2020) and Zheng et al. (2018) analyzing emission inventory data. This difference could be due to the use of average values for countries in these studies, which probably do not reflect the specific situation in individual cities. The composition of sources for a given city is expected to differ significantly from the average composition within a country. Nevertheless, further comparisons and detailed investigation would be helpful in understanding the deviations between the different studies. In general, it should be considered that the uncertainties of the NO_x emission estimates based on TROPOMI data are relatively large, especially for the winter analysis (see Sect. 3.4.2 and Sect. 3.4.7).

3.4.4 Latitudinal and seasonal dependence of lifetimes

Besides the NO_x emissions also the mean effective lifetime of NO_2 is retrieved from the TROPOMI data by the EMG method. Therefore, also the seasonality and latitudinal dependence of lifetimes has been investigated. When the TROPOMI data are averaged for the 2-years period, lifetimes can be estimated for all 50 source regions. After splitting the data into seasons, lifetimes can be calculated for 34 out of the 50 source regions, the same as for the NO_x emission estimates.

In Fig. 3.8a, the line density (light color) and EMG fit (intense color) are plotted separately for the four seasons as a function of distance to the source, in this case the city Madrid. For the two winters, from 1 March 2018 to 29 February 2020, 25 d are included in the analysis. With a mean wind speed of $5.5\,\mathrm{m\,s^{-1}}$ on these days, this results in NO_x emissions of $84.2 \pm 8.8\,\mathrm{mol\,s^{-1}}$ and a lifetime of $2.41 \pm 0.27\,\mathrm{h}$ during winter, which is the longest during the four seasons. During summer, the lifetime is estimated as $1.59 \pm 0.16\,\mathrm{h}$, the shortest of the four estimated lifetimes. The mean lifetime analyzing the complete 2-years period is $2.03 \pm 0.15\,\mathrm{h}$.

Figure 3.8b shows the calculated NO_x lifetimes for ten source regions as a function of season. The presented sources are only a selection of all the sources analyzed for seasonality. These sources are distributed over a large latitudinal range and differ regarding their

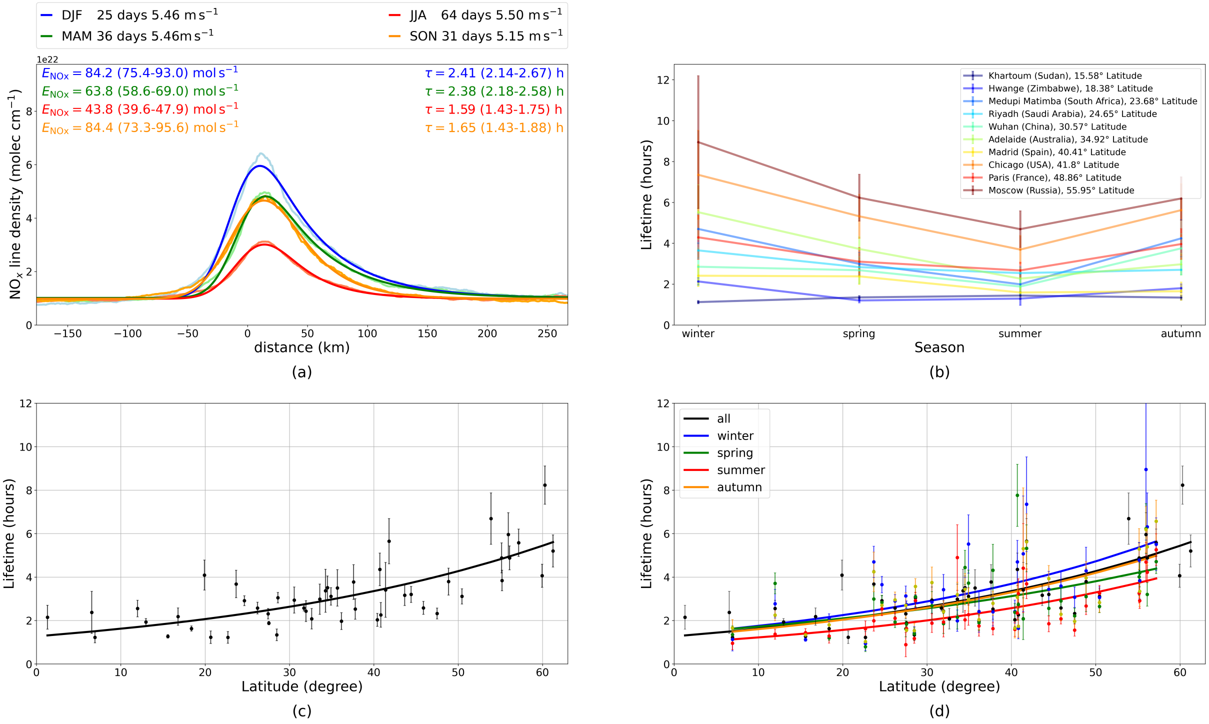

(a) (b) (c) (d)

Figure 3.8: (a) The seasonal NO$_x$ line densities for the city of Madrid. The line densities are in light colors, and the fit in intense colors. (b) Estimated lifetimes as a function of the season for ten source regions. (c) Estimated NO$_x$ lifetimes for the selected 50 sources as a function of latitude. (d) Estimated lifetimes in dependence on latitude (black) and separated into winter (blue), spring (green), summer (red), and autumn (yellow). All plots are based on TROPOMI NO$_2$ data from 1 March 2018 to 29 February 2020. Sources from the southern hemisphere are mirrored in latitude and season. Given uncertainties and error bars are the standard deviation derived by the EMG fitting procedure.

source type. The ten source regions generally show a similar behavior, with the longest lifetime in winter, the shortest in summer, and quite similar lifetimes in spring and fall between the summer and winter estimates. However, also deviations from this behavior are visible. In the case of Madrid, for example, the fall lifetime is much shorter than during the spring months (see also Fig. 3.7a). As expected, the seasonal differences are strongest for source regions at higher latitudes and lowest close to the equator.

Figure 3.7c shows the mean lifetime calculated based on the entire 2-years period for all 50 source regions as a function of latitude. Due to the lower Sun, resulting in lower photolysis, and the likely lower OH concentrations at higher latitudes, an increase in NO$_x$ lifetime with latitude is expected (Martin et al., 2003; Stavrakou et al., 2008). This is widely confirmed by the results, with the average lifetime increasing from about 2 h for low-latitude source regions close to the equator to about 6 h to 8 h for high-latitude source regions located at around 60°. Overall, the results agree with lifetimes estimated in Beirle et al. (2011). They analyzed eight source regions, with resulting lifetimes in a range of 2 to 6 h and a maximum of 8.5 h during the winter months for Moscow.

The determined lifetimes can also be used to estimate atmospheric OH concentrations. Assuming the NO_x decay is determined by the termolecular reaction of NO_2 and OH with the rate constant $k_{\mathrm{OH+NO_2+M}}$ for 298 K and 1 atm as reported by Burkholder et al. (2020), the OH concentration ranges from $0.3 \times 10^7 - 1 \times 10^7$ molec cm^{-3} for a range of NO_x lifetimes of two to eight hours. This estimate is in a reasonable range for OH concentrations at midday (Holland et al., 2003; Smith et al., 2006; Lu et al., 2013).

Figure 3.7d shows the lifetime dependency with latitude for the data separated into seasons. Due to the reduced number of data after separation, only 34 out of the 50 source regions are included. All seasons show a similar latitudinal dependence as described for the mean lifetime. Additionally, a seasonal dependence with the shortest lifetimes in summer and longer lifetimes in winter is visible.

To summarize, the analysis of the estimated NO_x lifetimes shows only a weak seasonality, which agrees with Beirle et al. (2011). However, the seasonality is significantly lower than expected from analyses with the chemical transport model GEOS-Chem by Martin et al. (2003) and Shah et al. (2020), which revealed much larger seasonality effects with lifetimes of around six hours in summer and about one day in winter. Possible explanations for the low seasonality may be partly insufficient statistics, a clear-sky bias, and the observation time of TROPOMI around noon, all leading to more balanced lifetimes between the seasons. In addition, it should be considered that the total uncertainty of the estimated lifetimes is significantly larger than just the EMG fit's standard deviation, especially in winter, and is further discussed in Sect. 3.4.7. Nevertheless, the large analyzed data set of 50 source regions distributed over a large range of latitudes shows a clear but partly complex latitudinal dependence of the NO_x lifetimes. These results can be included in analyses in which assumptions about lifetimes are necessary for the NO_x emission calculation, e.g., Beirle et al. (2019) and Beirle et al. (2021). Moreover, it can also provide relevant observational constraints for model simulations.

3.4.5 Weekend effect

The presence of weekday dependent patterns of NO_2 was first demonstrated by Beirle et al. (2003) using GOME measurements. Since anthropogenic activities are reduced during the weekend compared to regular working days, fewer NO_x emissions are expected in cities on weekends. The magnitude of the difference between weekends and weekdays depends on the types of NO_x emission sources and the patterns of anthropogenic activities in the source region. To investigate the weekend effect, the 2 years of TROPOMI observations are separated into weekday and weekend observations, and NO_x emissions and lifetimes are estimated for each data set separately. Depending on religious tradition, weekend days can differ and can be one or two days. For most of the analyzed source regions, in

Europe and the United States, weekend days are defined as Saturday and Sunday. For some source regions, e.g., in Saudi Arabia, weekend days are Friday and Saturday. Details can be found in Table A.1. Often, weekend days are not equivalent; for example, even if emissions on Saturdays are usually found to be lower than those from Monday to Friday, they are often not as low as those on Sundays (Crippa et al., 2020; Goldberg et al., 2021). Since a limitation of the weekend to only one day, would also result in a loss of statistics in the weekend data set, the analysis was conducted on two weekend days. However, it should be considered that limiting the weekend to one day would result in a strengthening of the weekend to week day ratio for some source regions.

Figure 3.9 shows the weekend-to-weekday ratios from the estimated NO_x emissions for 44 of the 50 source regions. For most of the source regions, NO_x emissions are higher during

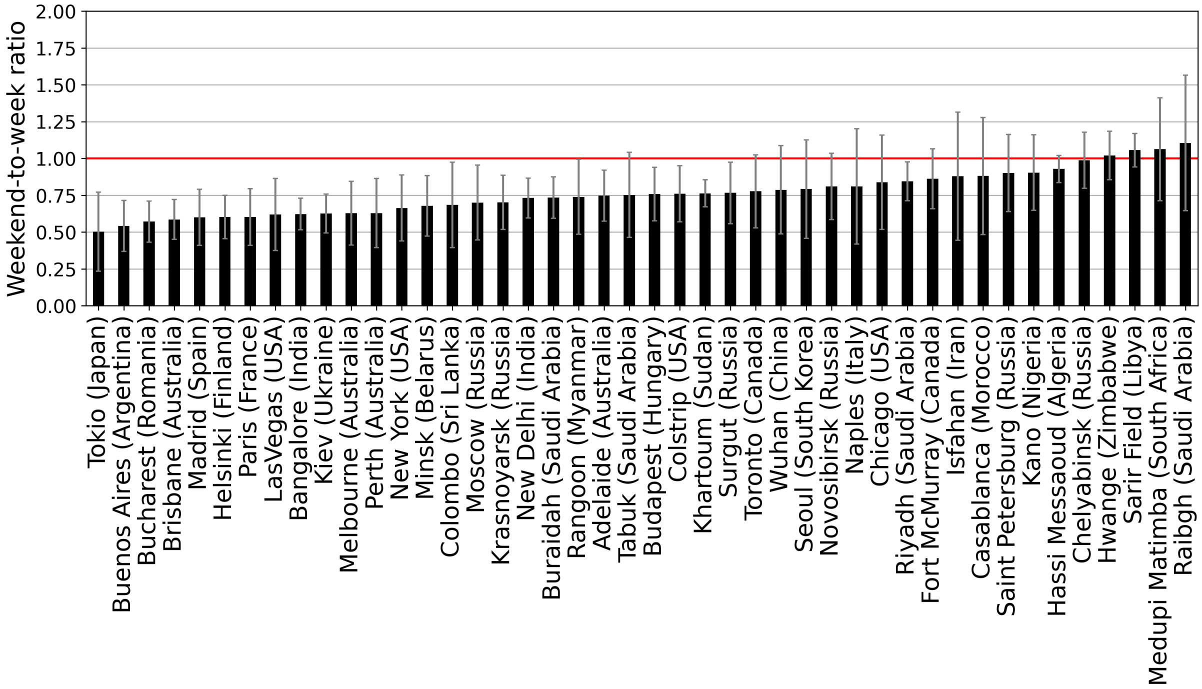

Figure 3.9: Weekend-to-weekday ratios from the NO_x emissions estimated from TROPOMI tropospheric NO_2 VCD data (1 March 2018 to 29 February 2020) for 44 source regions. The weekend can be one or two days, and those days can also differ according to religious tradition, which is considered. The red line indicates the 1:1 line where weekend and weekdays NO_x emissions are equal, below the line emissions during the week are predominant, above weekend emissions are higher. Error bars are the standard deviation derived by the EMG fitting procedure for emission estimates.

weekdays than on weekends, albeit with rather high variation. For Paris, the estimated NO_x emissions are reduced by 40 % on weekends, which is in good agreement with the 35 % found by Lorente et al. (2019). The estimates for Chicago show a reduction of 16 % on the weekend compared to weekdays, which is less than the reduction of 30 % found in Goldberg et al. (2019, 2021). These different reductions could be caused by the definition of weekend days, while the 16 % reductions were found for Saturday and Sunday, Goldberg et al. (2019, 2021) estimated weekend NO_x emissions only for Sundays, which is strengthening the weekend effect.

Some of the analyzed source regions are not showing any or only minimal reductions on the weekend. These source regions have in common that they are dominated by industry and power plant emissions. Rabigh (Saudi Arabia) is a small city with a large gas-fired power plant. Medupi and Matimba are two large coal-fired power plants near Lephalale in South Africa. Sarir Field is a large oil field in Libya. Hwange (Zimbabwe) is a small town with Zimbabwe's largest coal-fired power plant. Among these source regions without emission reductions on the weekend, Chelyabinsk has the largest population with nearly 1.2 million, but the city is also known as a center of heavy industry. Hassi Messaud (Algeria) is an oil refinery town. Source regions dominated by transport and domestic emissions and less industry, like Tokyo, Brisbane, or Madrid, show large emission reductions on the order of 50 % to 60 % over the weekend.

Although Chinese cities show very large tropospheric NO_2 VCDs, they have not shown a weekend effect in previous studies (Beirle et al., 2003; Stavrakou et al., 2020). Stavrakou et al. (2020) analyzed weekend-to-weekday tropospheric NO_2 VCDs ratios based on OMI (2005–2017) and TROPOMI (May 2018–April 2019) observations and found an average ratio over all large Chinese cities of 0.97 ± 0.02. It has to be considered that these ratios based on NO_2 columns are related but not identical to the NO_x emission ratios. The column rations are not considering effects like meteorology, lifetime and background values, which are accounted for in the NO_x emission ratios by the EMG method. Due to the small number of isolated point sources in China and the limited statistics from using only 2 years of data, it was only possible to analyze the weekend effect of NO_x emissions for Wuhan and not yet for other Chinese cities. Based on the TROPOMI tropospheric NO_2 VCDs from 1 March 2018 to 22 January 2020, the estimated NO_x emissions result in a weekend-to-week ratio of 0.79 ± 0.3 for Wuhan. The two data sets for weekdays and weekend include 67, respectively 27 days. While previous studies showed no weekend reduction effect, the estimated ratio for Wuhan is a possible indication that NO_x emissions on rest days have also decreased in China during recent years. Respectively, that the relative amount of NO_x emissions increased, with a weekly cycle due to more cars emitting NO_x, and probably less emissions from power plants because of new filter systems. This can be analyzed in more detail as more TROPOMI data become available.

A side-effect of the reduced NO_x emissions on rest days could be a slower production rate of OH from the $NO + HO_2$ reaction and therefore lower OH levels and longer NO_x lifetimes (Stavrakou et al., 2008). However, the lifetimes retrieved with the here analyzed data set for weekdays and weekend days do not show significantly longer lifetimes on weekends (see Fig. 3.10). This could be due to an insufficient number of data points needed to produce a statistically significant result, and the effect should be re-investigated once a larger TROPOMI data set becomes available.

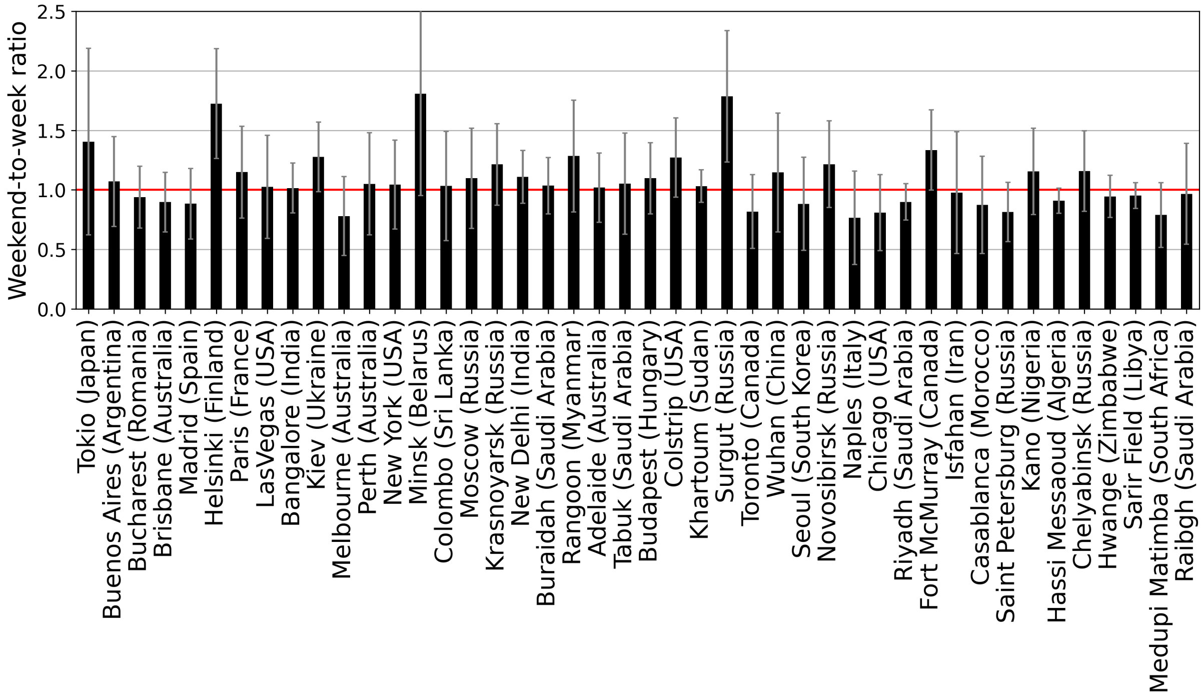

Figure 3.10: Weekend-to-weekday ratio of NO_x lifetimes (1 March 2018 to 29 February 2020). Data are separated into working and rest days for 44 source regions. Weekend can be one or two days and those days can also differ according to religious tradition, which is considered. The red line indicates the 1:1 line where weekend and weekday lifetimes are equal, below the line weekday lifetimes are longer and over the line weekend lifetimes are longer. Error bars are the standard deviation derived by the EMG fitting procedure for lifetime estimates.

3.4.6 COVID-19 effect

At the beginning of 2020, several countries implemented containment measures to reduce the spread of COVID-19, resulting in reduced traffic and industrial activity. Because of the strong direct link between human activities and NO_x emissions, the impact of the activity reductions can be investigated with TROPOMI tropospheric NO_2 VCD data. This was done by several studies (e.g., Bauwens et al., 2020; Liu et al., 2020a; Goldberg et al., 2020), and reductions in the TROPOMI tropospheric NO_2 VCD data were found for a wide variety of affected areas. However, some of the observed reductions may also be due to effects other than the COVID-19 containment measures, such as environmental policy regulations and also seasonal and meteorological variability, which are not considered in pure NO_2 column comparisons. Thus, it is challenging to determine a clear COVID-19 effect based on NO_2 VCD data alone. Besides using models to separate the COVID-19 effect from other factors as done by Goldberg et al. (2020), another possibility is to use the TROPOMI data combined with the EMG method. This approach accounts for wind conditions and NO_x lifetimes, which can result in deviating NO_2 VCDs for the same amount of NO_x emissions. The disadvantage of the EMG method is the limitation to well defined point sources. To minimize the effect of seasonality and meteorology, TROPOMI data are analyzed on the basis of monthly means. Therefore, the analysis of the COVID-19 effect is much more limited in terms of statistically significant data sets and thus potential analyzable source regions compared to the previous analyses in this study. The source regions included in the analysis are Buenos Aires, New Delhi, and Madrid. All three cities usually show large tropospheric NO_2 VCDs; thus, it is expected that even after activity reductions due to containment measures, NO_x emissions can still be analyzed. Due to cloud cover and/or low wind speeds, only a few days per month are available for some months. This can result in low quality fit results and missing statistics, which can cause biases if, for example, the variation of NO_x emissions on weekdays influences the estimated emissions. Thus not all months can be analyzed. Figure 3.11 shows the estimated NO_x emissions for the monthly averaged TROPOMI data from January to November 2019, before COVID-19, and 2020, when COVID-19 containment measures started. Thus the same months from the two years can be compared. If different months are compared with each other, the seasonality of NO_x emissions has a larger influence and must be considered.

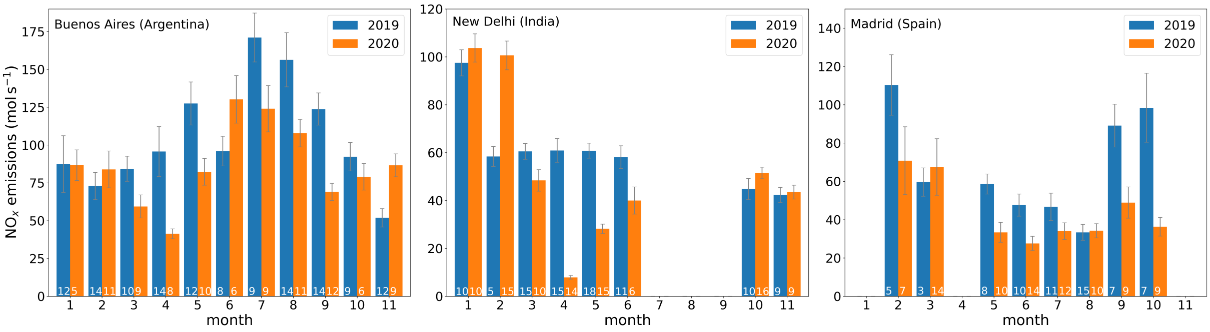

(a) (b) (c)

Figure 3.11: Monthly NO_x emissions calculated with the EMG method using TROPOMI NO_2 tropospheric column data for 2019 (blue) and 2020 (orange) from January to November for (a) Buenos Aires (Argentina), (b) New Delhi (India), and (c) Madrid (Spain). The numbers in the bars represent the number of available days for the monthly mean. Due to insufficient data availability of less than three days, comparisons are not possible for some months. Error bars are the standard deviation derived by the EMG fitting procedure for emission estimates.

To reduce the spread of COVID-19, Argentina began a strict nationwide lockdown on 20 March 2020, lasting for more than seven months in the capital Buenos Aires, ending on 8 November. Before the lockdown, from January to March, the estimated NO_x emissions from the two years are very comparable, with possibly first reductions visible in March when the lockdown started. The strongest reductions of 57 % are found for April 2020, the first complete month in lockdown, and also in May 2020, the emissions are estimated to be 36 % lower compared to May 2019. Even though the government did not make any major changes in the containment measures for June, the estimated NO_x emissions are higher in 2020 than in 2019. One possible explanation is that the June 2019 emissions are exceptionally low compared to May and July 2019 and do not follow the expected seasonal pattern, as visible from Fig. 3.11a. ERA5 temperature data, averaged over the boundary layer in the Buenos Aires target area for the TROPOMI observation days included in the emission estimates of May, June, and July 2019 and 2020, show that June 2020 temperatures were on average 3 °C lower than in June 2019. In contrast, May and July 2019 and 2020 data were very comparable. For July 2020, the emissions are again reduced by 26 %, similar to the reductions of 31 %, and 44 % found for August and September compared to 2019. In October, NO_x emissions are almost equal for both years and higher again in November 2020 than in 2019, which corresponds with the end of lockdown on 8 November.

Figure 3.11b shows the monthly averaged NO_x emissions for New Delhi. The estimated emissions are almost equal in January and significantly higher in February 2020 compared to 2019. This large difference is likely to result from the low number of clear-sky days and thus available TROPOMI observations in February 2019, revealing more NO_2 variability. After the lockdown was introduced on 24 March, the emissions reduced drastically compared to 2019 by 87 % in April, 54 % in May, and 31 % in June. Since due to cloud cover and/or wind situation in the respective months from July to September on average less than 3 days per month are available, and statistics and fit results are not good, these months are not included in the analysis. The emission estimates for October and November 2020 are almost equal to 2019 levels, suggesting that industrial and human activities and thus NO_x emissions are back to those before the COVID-19 containment measures.

Figure 3.11c shows the monthly averaged NO_x emissions for Madrid, one of the cities in Europe where strict containment measures were taken to prevent the spread of COVID-19. A strict lockdown was imposed in mid-March 2020, some measures were removed in mid-April, followed by a plan to slowly lose all lockdown measures starting in May. After again rising infections, new restrictions were imposed in early October 2020. Due to a lack of TROPOMI observations in January, April, and November, emission estimates are not possible for these months. The significantly higher NO_x emissions in February 2019 than 2020 have already been investigated in earlier studies (Bauwens et al., 2020; Levelt et al., 2021), and are probably mainly caused by a strong meteorological variability in Europe. Additionally, a persistent cloud cover results in a low number of TROPOMI observations, revealing more variability. Besides February, strong emission reductions of 43 % and 63 % are found for May and October. Bauwens et al. (2020) compared TROPOMI tropospheric NO_2 VCDs for Madrid from mid-March to early April and found a reduction of around 30 %, regarding the different methods and periods this is in reasonable agreement. One possible explanation for the larger reductions in October is stricter restrictions and thus less emissions. However, even when analyzing monthly averages, the high variability of NO_x emissions is not negligible and can have an influence.

Although the analysis is performed on relatively small data sets because of the often rapidly changing political decisions and to minimize the effects of seasonality and meteorology, it is possible to investigate the short-term variability of NO_x emissions due to COVID-19 containment measures using TROPOMI data and the EMG method. Strong NO_x emission reductions caused by the containment measures were found. Nevertheless, high variability of NO_x emissions must still be considered for particular months. For some months, the number of TROPOMI observations that can be included in the analysis is limited due to cloud cover, which is also an issue when comparing tropospheric NO_2 VCDs. Since the presented emission estimates account for wind conditions and NO_x lifetime, they provide a better estimate of the impact of COVID-19 containment measures on the NO_x emissions than comparing tropospheric NO_2 VCD levels.

3.4.7 Uncertainties

The uncertainties and error bars for the estimated emissions and lifetimes are calculated with error propagation based on the standard error (1 standard deviation) derived by the EMG fitting procedure. For the NO_x emissions, the given uncertainties are calculated by

$$\sigma_E = \frac{\overline{w} \cdot \sigma_{\mathrm{E'}}}{N_\mathrm{A}} + \frac{E' \cdot \sigma_{\overline{w}}}{N_\mathrm{A}} \tag{3.12}$$

and for lifetimes by

$$\sigma_\tau = \frac{\sigma_{x_0}}{\overline{w}} + \frac{x_0 \cdot \sigma_{\overline{w}}}{\overline{w}^2}. \tag{3.13}$$

With $\overline{w}$ the mean wind speed, the emission factor E', the e-folding distance x_0, Avogadro's constant N_A, the standard deviations $\sigma_{\mathrm{E'}}$ of E' and σ_{x_0} of x_0 derived from the EMG fitting procedure, and the standard deviation $\sigma_{\overline{w}}$ of $\overline{w}$ determined within in the line density sector. However, the estimated NO_x emissions and lifetimes are affected by additional error sources:

TROPOMI tropospheric NO_2 VCDs: The largest contributing error source is the accuracy of the TROPOMI tropospheric NO_2 VCD itself. This uncertainty is estimated to be 25 −40 % over the polluted regions, dominated by the uncertainty of the tropospheric AMF (van Geffen et al., 2022a). Studies comparing TROPOMI tropospheric NO_2 VCDs with co-located ground-based MAX-DOAS and airborne DOAS measurements reported low biased TROPOMI columns (Judd et al., 2020; Dimitropoulou et al., 2020; Tack et al., 2021; Verhoelst et al., 2021; Lange et al., 2023). The most discussed and investigated explanations are a priori information, such as the NO_2 vertical profile and the cloud-top-height information, used to calculate the tropospheric AMF (see also Chapter 4). Some studies scaled up the retrieved tropospheric NO_2 VCDs with a factor of 1.33 for Paris (Lorente et al., 2019) up to a factor of 1.98 for power plants in Germany (Beirle et al., 2019). The bias is more pronounced for regions with larger NO_2 columns and therefore varies by region (Verhoelst et al., 2021). Since this is not fully characterized for the various regions used in this study, the TROPOMI observations are not corrected. Therefore, the estimated NO_x emissions are systematically biased low. Modifications in the TROPOMI NO_2 retrieval led to a new product V02.02 released on 1 July 2021. On average, the tropospheric NO_2 VCD of the new data product is increased by 10 % to 40 % compared to the V1.x data, depending on pollution and season, with the largest increase found in the wintertime at mid and high latitudes (van Geffen et al., 2022b). In the meantime, a complete mission reprocessing, based on the V02.03.01 product activated on 14 November 2021, has been performed to get a harmonized data set (van Geffen et al., 2022a). In Chapter 4, a validation study, including the new reprocessed and the old V01.03.02 TROPOMI NO_2 product, gives further details about the influences of the modifications. Based on the found increase by 10 % to 40 % depending on pollution and season (van Geffen et al., 2022b), it is expected that the use of the reprocessed TROPOMI data for the emission calculations will increase the NO_x emissions and probably affect the seasonality analysis but not much the weekend-to-week day comparisons.

NO_2 to NO_x conversion: For calculating the NO_x emissions, each TROPOMI tropospheric NO_2 VCD was converted to NO_x, assuming that the Leighton photostationary state applies for the polluted air masses investigated. $[NO_x] / [NO_2]$ ratios were calculated for each source area and measurement day individually accounting for O_3 concentrations, photolysis frequency, and temperature. Especially for the analysis over a large latitudinal range and for different seasons, this is more accurate than using a fixed value of 1.32 with an assumed uncertainty of 10 % as done in many earlier studies (e.g., Beirle et al., 2011). However, the parameterization of the photolysis frequencies and the interpolation of the ERA5 temperature and ozone data to the S5P overpass time also add systematic errors in the NO_2 to NO_x conversion and thus in the emission estimates.

Clear-sky bias: The first two uncertainties affect the derived emissions but not the lifetime estimates. One factor affecting both estimates is the use of satellite data, which can only be included in the analysis on nearly cloud-free days. This probably favors specific emission patterns that may be different on cloudier days. Photolysis rates are systematically higher on nearly cloud-free days, thus, lifetimes are systematically lower than on cloudy days.

Observation time: This underestimation of lifetimes is further enhanced by the TROPOMI overpass time around noon. This observation time can also favor specific emission patterns. With geostationary observations such as GEMS, TEMPO, and Sentinel-4, this influence of the satellite measurement time can be further analyzed.

Wind: NO_x emission and lifetime estimates are strongly affected by the wind fields. First, TROPOMI observations are filtered on the corresponding wind speed, including only data with wind speed $> 2\,\mathrm{m\,s^{-1}}$ in the analysis. Due to the generally short lifetime of NO_2, it is assumed that the observed NO_2 distribution is dominated by the wind conditions around the TROPOMI observation. Nevertheless, rapidly changing wind directions around the satellite overpass time may affect the spatial patterns and thus the NO_x emission and lifetime estimates. On some days, curved plumes are observed for some of the selected source regions. In cases with a pronounced curvature, this can result in part of the plume being outside of the sector used for the estimates and thus an underestimation of emissions and lifetime. This effect can be especially large when analyzing single days or small data sets and is due to the longer lifetimes more pronounced in winter analyses. If not too many days are affected, the influence on the overall result is expected to be small. However, after the TROPOMI NO_2 column itself, the wind field is the largest uncertainty (systematic and random) influencing the NO_x emission and lifetime estimates. By modifying wind speeds by 20 %, Lorente et al. (2019) showed that emissions changed by 20 %, demonstrating the large influence of the wind speed on NO_x emissions. Beirle et al. (2011) estimated the uncertainty due to the choice of the wind field as 30 %. The uncertainties introduced by the wind field may vary for the different source regions. In general, an uncertainty of 30 % is assumed for this study.

EMG analysis area: The analysis can only be performed on isolated source regions. The EMG analysis is performed in defined sectors around the selected source to exclude possible contamination by surrounding sources. This sector size has to be chosen carefully. The sector size in the downwind direction is determined by the possible influence of surrounding sources, the spatial extent of the source region to be analyzed, and the wind speed. Typically, the sector starts 100 km upwind and spreads 200 km downwind of the source, in total 300 km. If necessary, it is adjusted visually by inspecting the averaged NO_x distribution and line density results. When considering possible influences by surrounding sources in the sector determination, the EMG fit results are robust with respect to variations in the sector size in wind direction, and uncertainties are negligible. The choice of sector width in the across-wind direction becomes critical when it is too small, and part of the plume is outside the sector due to curved plumes or strong wind dilution. In this case, an apparent additional loss of NO_x is induced, estimated NO_x emissions are underestimated, and the e-folding distance x_0 and thus the lifetimes are systematically biased low. Sector widths of the investigated source regions range between 30 and 140 km, are mainly influenced by the geographical extent of the source region and are adjusted visually by inspecting the averaged NO_x distribution after rotation. Beirle et al. (2011) estimated the uncertainty of NO_x emissions and lifetimes due to the sector width in across-wind direction as 10 %, which is also applied in this study.

Point source assumption: The EMG method is well suited for investigating point sourced. Power plants, like the Colstrip power plant in Montana, and also isolated smaller well defined sources such as the Sarir Oil Field in Libya, can easily be assumed to be point sources. In earlier studies, the Four Corners and San Juan power plants located 13 km apart in New Mexico, USA, were assumed to be one point source and analyzed using the EMG method (Beirle et al., 2011; Goldberg et al., 2019). With TROPOMI's higher spatial resolution compared to OMI, two separated plumes become clearly visible, showing that the situation is more complex; see Fig. 3.12. The resulting line density and EMG fit show strong irregularities, indicating that this region should not be considered as one point source and is therefore not included in this study. In this specific case, the analysis might be made possible by re-gridding the TROPOMI data to a coarser resolution. Many of the here analyzed sources are cities, also including rather large cities such as Seoul, Moscow, or Chicago; these are treated as extended point sources. Nevertheless, additional uncertainties must be considered. For example, since changes in the instantaneous NO_x lifetime downwind of the source cannot be considered by the EMG method, estimated lifetimes must be interpreted as an effective mean lifetime (see Sect. 3.3.4). The effect leads to low biased lifetimes and is expected to be especially pronounced in widespread source areas.

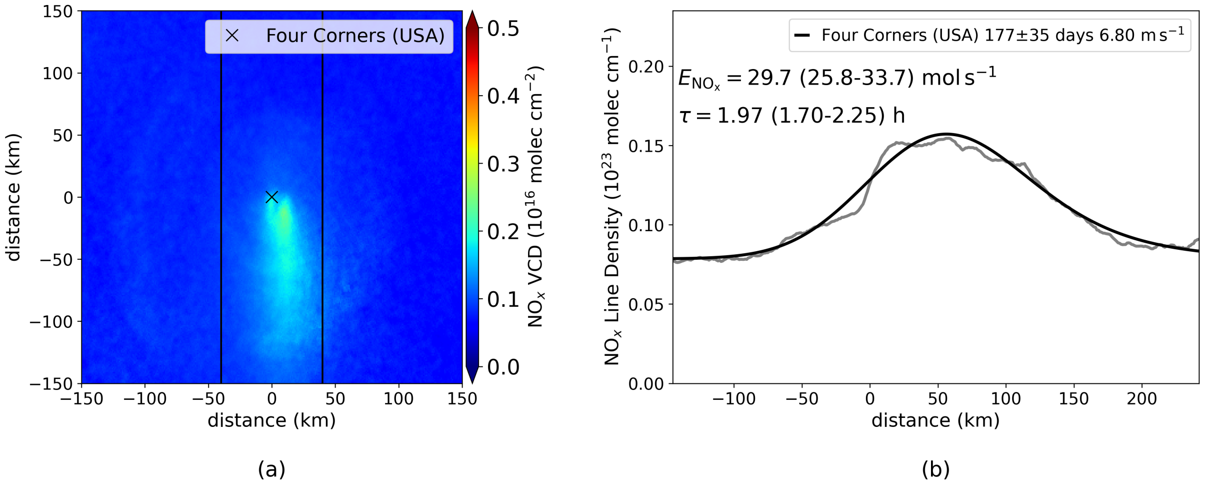

Figure 3.12: (a) Averaged tropospheric NO_x VCDs from 1 March 2018 to 29 February 2020 for days with wind speed $> 2\,\mathrm{m\,s^{-1}}$ in the region of the Four Corners and San Juan power plants in New Mexico, USA after rotation around the defined source point (black cross). (b) NO_x line density as a function of distance to the source calculated for the ±40 km sector (gray), EMG fit results (black) with estimated emissions and lifetime and 1-sigma uncertainties derived by the fitting procedure. Caused by the clearly visible separated two plumes, the line density shows several structures causing a poor fit.

In summary, additionally to the 1-sigma uncertainties derived by the EMG fitting procedure, the total uncertainty of the estimated NO_x emissions and lifetimes is influenced by various error sources. These are mainly systematic and result in low biased emission and lifetime estimates. The uncertainty on the derived NO_x emissions is dominated by the TROPOMI tropospheric NO_2 VCD itself ($30 - 50\,\%$) and the wind field ($30\,\%$). The sector width can lead to low biased emissions and lifetimes and is estimated to introduce an additional uncertainty of $10\,\%$. The TROPOMI observation time, the clear-sky bias, and the assumptions of analyzing point sources are further uncertainties that tend to cause low biased emission and lifetime estimates. Additional analyses are needed to resolve these issues. The error contributions summed in quadrature result in an overall uncertainty estimate for lifetimes and emissions in the range $43 - 62\,\%$.

3.5 Conclusion

This study investigated the variability of NO_x emissions and lifetimes estimated from S5P TROPOMI tropospheric NO_2 VCD observations of 50 NO_x source regions around the world. Source regions are predominantly cities, isolated power plants, industrial regions, oil fields, and regions with a mix of sources between the equator and 61° latitude. Emissions and lifetimes are estimated by combining TROPOMI tropospheric NO_2 VCD data with ERA5 wind and ozone information and analyzing downwind patterns of NO_2 columns by the EMG method. Due to TROPOMI's high spatial resolution and high signal-to-noise ratio, new investigations have been made possible: (1) investigating small NO_x emission sources not analyzed before; (2) seasonal analysis of NO_x emissions and lifetime, including winter data, based on only 2 years of data; (3) monitoring NO_x emission variability on a short-term temporal basis.

Comparing the estimated NO_x emissions with the EDGAR (v.5.0 2015) emission inventory shows that the emissions reported in the inventory are higher for most sources than those estimated using the EMG method. Part of the apparent overestimation by EDGAR could be related to low biased TROPOMI NO_2 data. Additionally, NO_x emission trends over the 5 years between the emission inventory reference year and the TROPOMI observations are likely also to have an impact.

EPA CEMS data provide up-to-date hourly emissions from power plants in the United States. Data for the Colstrip power plant, which is well suited for the EMG method, show that NO_x emissions vary strongly over time. The analysis of NO_x emissions for this power plant using the EMG method reproduces the temporal variability reasonably well without showing a significant seasonal bias. Thus, the comparison gives confidence in the analysis of seasonality using the EMG method, including the winter month, which are often excluded. However, the TROPOMI-based NO_x emissions are for the complete time series about a factor of 2 lower than the CEMS data, which is consistent with previous studies for other power plant sources.

The seasonal separation of the EMG emission estimates based on TROPOMI data indicates a clear seasonality for most analyzed source regions. Most of the analyzed source regions show the highest emissions during winter, particularly pronounced for source regions at higher latitudes. Whereas for source regions in hot desert climates, the highest emissions occur in summer. These differences are best explained by the different contributions of NO_x emissions for the corresponding sources, which are typically dominated by domestic heating in winter or air conditioning in hot summer months, depending on the climatic conditions. The degree of seasonality found in this study differs from previous studies. However, these studies analyzed seasonality based on emission inventories on a country scale and not for specific source regions. Given the particular situation in cities, where the composition of sources differs from a nationwide estimate, other seasonalities are expected. Nevertheless, further investigations would be helpful to understand the discrepancies between emission estimates based on the combination of satellite data and the EMG method and bottom-up emission inventories. In general, it should be considered that the uncertainties for emission estimates using satellite data and the EMG method can be large. Especially the analysis of winter data has not been performed often and is subject to even larger uncertainties.

The seasonal and latitudinal dependence of the NO_x lifetime shows increasing lifetimes from 2 to 6 h for increasing latitudes but a weak seasonal dependence with only slightly longer lifetimes in winter than in summer. Based on modeling studies, larger differences are expected. The comparatively weak seasonality of the NO_x lifetime found in this study could be explained by still insufficient statistics, the midday observation time of TROPOMI, and a clear-sky bias, all of which lead to more balanced lifetimes.

The separation of the data set into working and weekend days shows higher NO_x emission during weekdays than on the weekend for most source regions, albeit with rather high variability. Only for source regions dominated by industry or power plants, no or only small emission reductions are observed on weekends. The largest reductions are found for source regions dominated by city emissions and with little industry. In contrast to previous studies that show no weekend effect in China, the analyzed data set indicates NO_x emission reductions during weekends for Wuhan. When more high-resolution tropospheric NO_2 VCD data become available from TROPOMI and GEMS in the following years, this effect may be further investigated for other Chinese cities. In contrast to the NO_x emissions and expectations, the separately calculated lifetimes do not show longer lifetimes on weekends. This result also requires further investigation.

The analysis of NO_x emission on a short-term temporal basis indicates emission reductions attributable to COVID-19 containment measures. Since the EMG method accounts for the NO_x lifetime and wind conditions, it can provide a better estimate of the impact of the COVID-19 measures on NO_x emissions than methods based only on tropospheric NO_2 VCD observations. In particular, the first phase with strict containment measures shows strong NO_x emission reductions for the analyzed cities Buenos Aires, New Delhi, and Madrid.

It can be concluded that the combination of spatially high-resolved TROPOMI NO_2 data and the EMG method allows analyzing the high variability of NO_x emissions and lifetimes globally and also at short time scales. Depending on the purpose of the analysis, it is no longer necessary to average over many years, a few good days of satellite observations can be sufficient; for seasonal investigations, one to two seasons are sufficient, depending on local meteorological conditions. This ability to estimate NO_x emissions over relatively short periods will allow policymakers to better and more quickly evaluate NO_x emission regulations. The presented high variability of NO_x emissions and lifetime can be further investigated by geostationary satellites including GEMS and the upcoming TEMPO or Sentinel-4, which have the potential to additionally investigate diurnal variability.

4 | Validation of TROPOMI tropospheric NO_2 products: S5P-VAL-DE-Ruhr campaign [1]

4.1 Introduction

To ensure the accuracy of satellite data products for use in research like emission estimation as seen in Chapter 3, policy decisions on air quality development, or other applications, each data product must be validated, and its accuracy determined. Validation measurements are needed from independent instruments.

The most commonly used instruments are stationary ground-based MAX-DOAS instruments, developed to retrieve tropospheric columns of trace gases such as NO_2. Stationary ground-based measurements usually provide long time series of data providing continuous validation data and enabling the investigation of long-term trends, monitoring the satellite instrument stability and diurnal and seasonal variability. They are installed at various sites around the globe in polluted and clean regions. During the last 15 years, several studies have compared SCIAMACHY, GOME-2, and OMI tropospheric NO_2 VCD data products to MAX-DOAS measurements from various stations (e.g., Brinksma et al., 2008; Hains et al., 2010; Ma et al., 2013; Drosoglou et al., 2017; Pinardi et al., 2020). The recent TROPOMI tropospheric NO_2 VCD data products were validated with MAX-DOAS measurements by e.g., Dimitropoulou et al. (2020); Verhoelst et al. (2021); van Geffen et al. (2022b). All studies found a low bias of the TROPOMI tropospheric NO_2 VCDs compared to the ground-based MAX-DOAS data in urban, polluted conditions and a better agreement in rural, back-ground regions. One factor which can partly explain the discrepancies is local horizontal tropospheric NO_2 variability (Pinardi et al., 2020; Dimitropoulou et al., 2020). The horizontal spatial representativeness of MAX-DOAS measurements has been quantified and shown to range from a few kilometers to tens of kilometers depending on the aerosol load and the spectral region of the measurement (Irie et al., 2011; Seyler et al., 2017). While the MAX-DOAS can measure local NO_2 enhancements, the larger satellite pixel provides a smoothed view of the NO_2 field. Comparisons can be improved when making use of the multiple azimuthal viewing directions and improving the TROPOMI

---

[1] This section has been published in a similar form in Lange et al. (2023)

pixel selection criteria to pixels along the MAX-DOAS viewing direction and within the effective sensitivity length (Dimitropoulou et al., 2020).

DOAS measurements from mobile ground-based platforms like cars offer the advantage of covering larger areas at relatively low costs. They enable more detailed observations of spatial variability in addition to temporal evolution and can be used for the comparison with satellite observations (Wagner et al., 2010; Constantin et al., 2013; Wu et al., 2013). Some of the limitations of car DOAS measurements are that the need to follow the course of roads and possibly getting stuck in traffic jams. In addition, to directly validate satellite data, mobile car DOAS measurements are also often used for the validation of airborne remote sensing measurements (Meier et al., 2017; Tack et al., 2017; Merlaud et al., 2018).

Airborne imaging DOAS measurements are another valuable source of satellite validation data. They can map satellite pixel areas in a relatively short period around the satellite overpass. The measurement viewing geometry from an aircraft is similar to that of a satellite, but airborne measurements can measure at higher spatial resolution than satellite sensors. Airborne imaging measurements can link ground-based and satellite measurements by visualizing spatiotemporal variations of trace gas data products within a satellite pixel, thus providing insights into expected differences between the ground-based and satellite measurements. Airborne mapping activities for satellite validation have been performed in recent years over selected areas in Europe and the US using different airborne imaging DOAS instruments such as AMAXDOAS, AirMAP, GeoTASO, GCAS or APEX (Heue et al., 2005; Meier et al., 2017; Judd et al., 2020; Tack et al., 2021). Usually, airborne observations are performed during campaigns and are only available for short periods concentrated on the campaign region. The combination of airborne imaging and ground-based stationary and mobile measurements enables the validation of satellite data products over a long period and at a high spatial resolution.

Focusing on TROPOMI validation, Verhoelst et al. (2021) have compared TROPOMI tropospheric NO_2 VCD data from April 2018 to February 2020 (processor versions RPRO V01.02.02 and OFFL V01.02.00–V01.03.02) to 19 MAX-DOAS stations. Results depend strongly on the tropospheric NO_2 amount present at the station. Nevertheless, significant negative median differences are observed at all MAX-DOAS sites with significant tropospheric NO_2 pollution. Studies by Judd et al. (2020) and Tack et al. (2021), comparing TROPOMI tropospheric NO_2 VCD data of V01.02 and V01.03.01 to airborne tropospheric NO_2 VCD data, also show a significant negative bias of TROPOMI compared to the airborne observations.

Modifications in the TROPOMI NO_2 retrieval led to V02.02, operational since 1 July 2021. The main changes influencing the tropospheric NO_2 VCD is the new FRESCO-wide algorithm replacing the FRESCO-S algorithm (see Sect. 2.5.1), leading to lower cloud pressures and thus larger tropospheric NO_2 VCDs over polluted scenes with small cloud fractions, and a surface albedo correction over cloud-free scenes, which is also leading to larger tropospheric NO_2 VCDs. On average, comparisons to ground-based measurements show an improvement for the negative bias from −32 % to −23 % (van Geffen et al., 2022b).

Factors playing a role in the disagreement between TROPOMI tropospheric NO_2 VCDs and the validation data set are discussed in several studies (e.g., Dimitropoulou et al., 2020; Judd et al., 2020; Tack et al., 2021; Verhoelst et al., 2021; van Geffen et al., 2022b; Douros et al., 2023). Verhoelst et al. (2021) stated that the disagreement cannot be attributed to pure area-averaging differences, which is also supported by the disagreement seen in the airborne validation activities, which should nearly overcome this aspect by covering complete satellite pixel areas (Judd et al., 2020; Tack et al., 2021). Another possible reason for the underestimation of the TROPOMI tropospheric NO_2 VCD data, compared to the validation data, is limited knowledge of the NO_2 profiles and differences in the averaging kernels between instruments having different viewing geometries. Improvements in the comparisons were found when replacing the coarse a priori NO_2 profiles used in the TROPOMI data retrieval with high-resolution profiles from high-resolution regional air quality model (Judd et al., 2020; Tack et al., 2021; Douros et al., 2023) or profiles retrieved from MAX-DOAS-measurements (Dimitropoulou et al., 2020). Similarly, inaccuracies in the knowledge of the AOT and the aerosol vertical profile can cause underestimations in the NO_2 amounts from satellite retrieval as well as overestimations for MAX-DOAS (Compernolle et al., 2020; Liu et al., 2020b). Studies showed that the cloud pressure used in the TROPOMI NO_2 retrieval before V01.04 is too high, particularly for scenes with low cloud fractions and/or a significant aerosol load, which is treated as an effective cloud in the cloud algorithm, and is causing too low tropospheric NO_2 VCDs for these scenes (Compernolle et al., 2021; van Geffen et al., 2022b). In addition, the surface reflectivity and their treatment in the TROPOMI retrieval algorithm must be considered (Eskes and Eichmann, 2022).

In the following, results from a comprehensive field study conducted in North Rhine-Westphalia, Germany, in September 2020 are presented. The campaign used the imaging capabilities of AirMAP for mapping areas containing several TROPOMI pixels. Ground-based measurements for evaluating the AirMAP data set included six stationary DOAS instruments and three mobile car DOAS instruments. The measurements are used to validate the TROPOMI tropospheric NO_2 VCD products, comprising the operation OFFL V01.03.02, the reprocessed PAL V02.03.01, and several scientific products. Possible explanations for the found low bias of the TROPOMI tropospheric NO_2 VCD are investigated by systematically varying the relevant input parameters in the satellite retrieval, such as a priori NO_2 profiles, surface reflectivity, and the cloud treatment.

The campaign region and setup are described in Sect. 4.2. The instruments and data sets are explained in Sect. 4.3. After comparing the AirMAP data set to the stationary data (Sect. 4.4) and the car DOAS data (Sect. 4.5), the AirMAP data are used to evaluate the TROPOMI tropospheric NO_2 products (Sect. 4.6).

4.2 The S5P-VAL-DE-Ruhr campaign

The S5P-VAL-DE-Ruhr campaign took place in the Rhine-Ruhr metropolitan region in North Rhine-Westphalia, Germany, as part of the ESA QA4EO project. QA4EO includes four field studies with the objective of creating campaign data sets applicable to the assessment of the TROPOMI operational product uncertainties. The data set acquired during the S5P-VAL-DE-Ruhr campaign contributes to the validation of the TROPOMI tropospheric NO_2 VCD product. The campaign activities, including airborne, ground-based stationary, and mobile car DOAS measurements, were originally planned for late summer 2019. Due to bad weather conditions during the campaign time window, no research flights were conducted, and the main campaign activity time window was postponed to summer 2020. With the COVID-19 pandemic situation in Europe in 2020, the feasibility was uncertain for some time, but with some precautions, all measurements could be prepared. Due to good weather conditions, the main campaign activities took place on 7 consecutive days from 12 to 18 September 2020.

The Rhine-Ruhr metropolitan region is a densely populated urban agglomeration with more than 10 million inhabitants in the west of Germany. The region covers the Ruhr area with Dortmund, Essen, Duisburg, and Bochum in the north, the Düsseldorf metropolitan region, and in the south Leverkusen, Cologne, and Bonn. The region includes several highways, energy-intensive industrial areas, and large power plants. With the lignite-fired power plants Neurath, Niederaußem, and Weisweiler, three of the largest lignite-fired power plants in Germany and also Europe, are located in the campaign region (European Environment Agency, last access: 3 May 2023). The NO_x emissions originating from this region are clearly visible in the TROPOMI maps in Fig. 4.1 showing widespread amounts of NO_2 pollution and also the highest tropospheric NO_2 VCDs with $1.6 \times 10^{16}\,\mathrm{molec\,cm^{-2}}$ in the campaign region. The maps show the tropospheric NO_2 VCD of the TROPOMI PAL V02.03.01 product averaged for September 2020. Large tropospheric NO_2 VCDs are also visible over Paris, London, Milan, and Antwerp.

Within the designated campaign area, three regions of interest were determined. The three research areas are marked on the close-up map of the S5P-VAL-DE-Ruhr campaign region in Fig. 4.1. The research area around Jülich (blue) includes the mentioned lignite-fired power plants Neurath, Niederaußem, and Weisweiler but no larger cities. It is expected to be dominated by the power plant NO_x emissions. The research flight area around Cologne (red) is a mixture of urban and industrial emitters. The flight area around Duisburg (green) includes the Ruhr area, with around 5 million inhabitants and various industrial emitters.

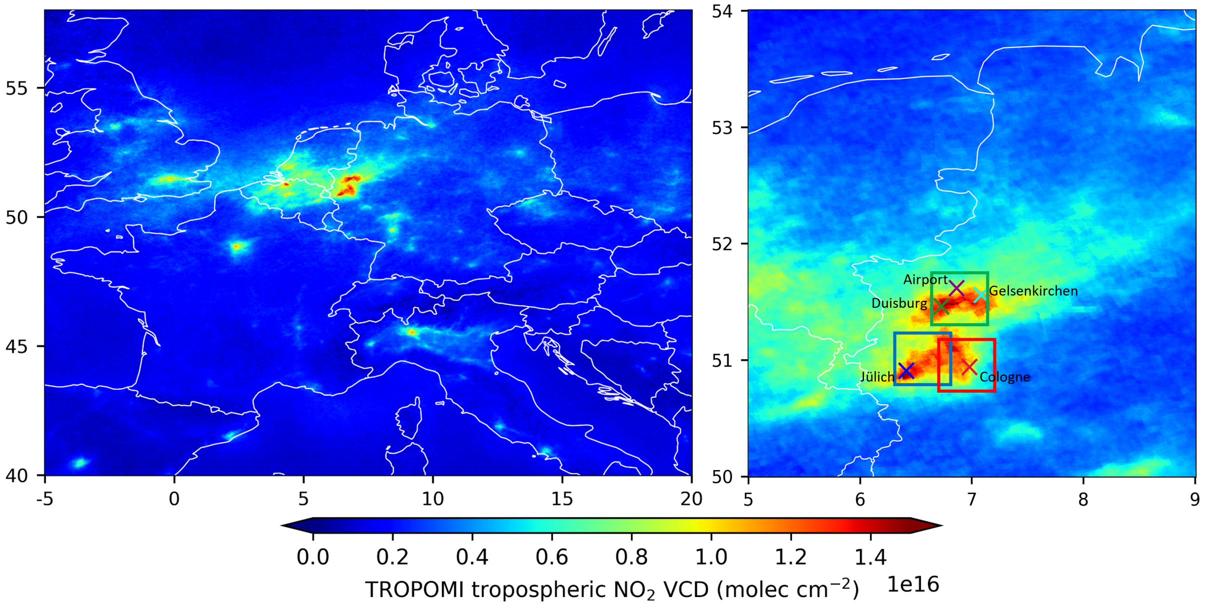

Figure 4.1: S5P TROPOMI tropospheric NO$_2$ VCD from the PAL V02.03.01 product for September 2020, in central Europe (left) and a close-up of the campaign target area, North Rhine-Westphalia (right). The research flight areas and the ground-based measurement sites are shown.

The main contribution to the campaign are airborne imaging DOAS measurements performed by the AirMAP instrument (see Sect. 4.3.2). AirMAP was flown on the FU-Berlin Cessna T207A aircraft, which was based at the airport Schwarze Heide close to Dinslaken in the northern part of the campaign area. Figure 4.2 shows a map of the campaign region with exemplary flight patterns in the three research flight areas around Jülich (blue), Cologne (red), and Duisburg (green). The flight areas with a size of approximately 30 km × 35 km are covered with 13 to 15 flight tracks with lengths of 35 km in a lawnmower style in North-South direction. Neighboring flight tracks are flown in opposite directions with an overlap of around 30 % at the edges of the 3 km wide instrument swath. Seven flights were conducted on the seven days from 12 to 18 September 2020. The individual research flight area on the measurement day was selected based on weather conditions, particularly cloud cover and wind direction. Each target area was measured during a nearly cloud-free situation, and measurements can be used for TROPOMI validation. Flight schedules were planned with the S5P overpass in the middle of the flight to optimize the amount of data for validation. On days with two overpasses, flights were optimized towards the overpass with the smaller TROPOMI viewing zenith angle (VZA). More information on the individual flights is given in Table 4.1.

Figure 4.2 also shows the locations of the six ground-based stationary instruments in Jülich, Cologne, at the airport Dinslaken, Gelsenkirchen, and Duisburg distributed over the three research areas. They give the possibility to compare AirMAP measurements from flights in all three areas with the ground-based stationary measurements. The trans-

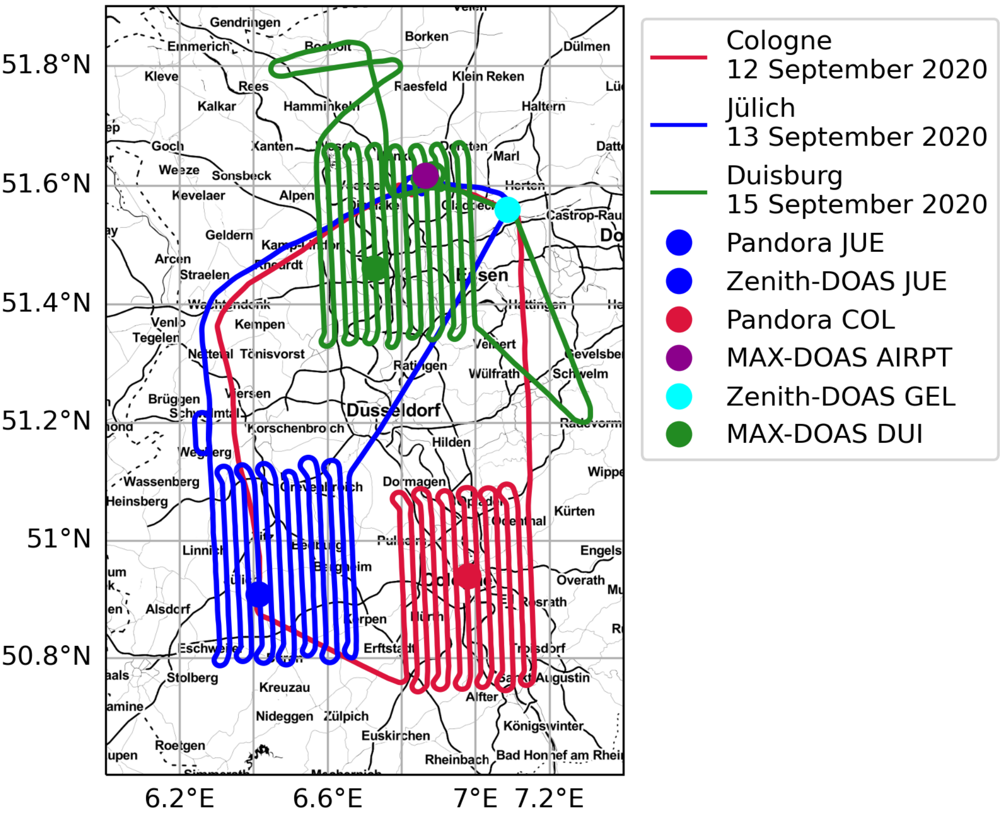

Figure 4.2: Map of the campaign flight area with exemplary flight patterns in the three target areas. Colorful dots indicate the locations of the stationary ground-based instruments in Jülich (blue), Cologne (red), Dinslaken airport (purple), Gelsenkirchen (cyan), and Duisburg (green).

fer flights between the airport and the research flight areas were used to overpass nearby stationary instruments to gather more collocated measurements. The different instruments consisting of two Zenith-DOAS, two MAX-DOAS, and two Pandora are explained in Sect. 4.3.4.

The ground-based mobile component consists of three car DOAS instruments introduced below in Sect. 4.3.3. The car DOAS measurements were planned in round trips covering a large part of the respective research flight area and passing by the stationary instrument. With this combination of airborne, ground-based stationary, and mobile car DOAS measurements, a comprehensive evaluation of the airborne measurements is possible before they are used to evaluate the TROPOMI tropospheric NO_2 VCD product. Thus the airborne measurements, well covering the satellite pixel areas, link the ground-based data with restricted spatial but good temporal coverage with the TROPOMI measurements.

Table 4.1: List of airborne activities and S5P overpass information. Flights were arranged to coincide with the S5P overpass at smaller TROPOMI VZA.

Date	Flight time (UTC)	Flight area	S5P overpass (UTC) with VZA	Comments
12 Sep 2020	10:17–13:37	Cologne	10:51 (67.4°), 12:31 (15.9°)	
13 Sep 2020	10:20–13:36	Jülich	12:12 (8.8°)	
14 Sep 2020	10:14–13:47	Duisburg	11:53 (30.7°), 13:35 (64.9°)	No TROPOMI data
15 Sep 2020	09:15–12:44	Duisburg	11:35 (46.7°), 13,15 (55.4°)	
16 Sep 2020	10:37–14:05	Duisburg	11:16 (57.7°), 12:56 (41.9°)	Only one car DOAS
17 Sep 2020	10:45–14:16	Jülich	10:57 (65.5°), 12:37 (22.6°)	
18 Sep 2020	10:48–14:08	Cologne	12:18 (1.6°)	

4.3 Instruments

All instruments that have been part of the S5P-VAL-DE-Ruhr campaign are passive remote sensing instruments using the DOAS technique, as described in Sect. 2.4, for retrieving tropospheric VCDs of NO_2. The instruments operate from satellite, airborne, car, and stationary ground-based platforms and are listed in Table 4.2. The data analysis was done independently by the operating institutes. The DOAS fitting window was chosen based on the spectrometer's spectral wavelength range and the group's experience with their instrument.

4.3.1 TROPOMI

TROPOMI, the single instrument on the satellite S5P, provides observations of the tropospheric NO_2 VCD over the campaign region between 10:50 and 13:45 UTC. On five of the seven campaign measurement days, data from two overpasses are available. With its good signal-to-noise ratio and spatial resolution of 3.5 km × 5.5 km, it is particularly well suited for measurements of small-scale NO_x emission sources as they are present in the campaign region.

This study analyzes different versions of the TROPOMI tropospheric NO_2 VCD product: the product of the official level-2 OFFL processor V01.03.02 operational during the campaign period, a reprocessed product using the V02.03.01 of the level-2 processor, provided by the Product Algorithm Laboratory (PAL), and several scientific data products based on these versions. The TROPOMI NO_2 products with their most important differences are summarized in Table 4.3, and further details can be found in the following sections.

Table 4.2: List of instruments that have been part of the S5P-VAL-DE-Ruhr campaign activities with location respectively platform and observation geometry. The car DOAS instruments are operated by: the Institute of Environmental Physics, University of Bremen (IUP); the Max Planck Institute for Chemistry in Mainz (MPIC); and the Royal Belgian Institute for Space Aeronomy (BIRA).

Instrument	Location/Platform	Observation geometry	Spectral range Fitting window (nm)	VCD retrieval AMF information (columns in molec cm^{-2})
TROPOMI	Sentinel-5P	Push-broom, nadir	310–500 405–465	van Geffen et al. (2022a)
AirMAP	Cessna T207A	Push-broom, nadir	429–492 438–490	$VCD_{trop, ref} = 1 \cdot 10^{15}$ RTM SCIATRAN
IUP car DOAS	Mobile car	Zenith-sky	290–550 425–490	$VCD_{trop, ref} = 1 \cdot 10^{15}$ AMF (90°) = 1.3
MPIC car DOAS	Mobile car	Zenith-sky and 22°	300–460 400–460	Using dSCD (22°), Wagner et al. (2010) AMF (90°) = 1.3, AMF (22°) = 3
BIRA car DOAS	Mobile car	Zenith-sky and 30°	200–750 450–515	dSCD (30°) sequential 90° reference AMF (90°) = 1.3, AMF (30°) = 2.5
Zenith-DOAS JUE	Jülich (50.91° N, 6.41° E)	Zenith-sky	290–550 425–490	$SCD_{ref} = 1 \cdot 10^{16}$ AMF (90°) = 1.3
Zenith-DOAS GEL	Gelsenkirchen (51.56° N, 7.09° E)	Zenith-sky	290–550 425–490	$SCD_{ref} = 1.7 \cdot 10^{16}$ AMF (90°) = 1.3
MAX-DOAS DUI	Duisburg (51.46° N, 6.73° E)	Multi-axis	282–414 338–370	dSCD (30°) sequential 90° reference AMF (90°) = 1.3, AMF (30°) = 2.5
MAX-DOAS AIRPT	Airport Dinslaken (51.62° N, 6.87° E)	Multi-axis	300–463 411–445	MMF inversion algorithm Friedrich et al. (2019)
Pandora COL	Cologne (50.94° N, 6.98° E)	Multi-axis	270–520 435–490	Cede et al. (2021)
Pandora JUE	Jülich (50.91° N, 6.41° E)	Multi-axis	281–523 43-5-490	Cede et al. (2021)

4.3.1.1 TROPOMI NO_2 operational OFFL V01.03.02 product

During the campaign period in September 2020, the TROPOMI level-2 NO_2 OFFL V01.03.02 product was generated operationally. This processor version operated from 26 June 2019 until 29 November 2020.

Validation with ground-based measurements have shown that the tropospheric NO_2 VCD of V01.02–V01.03. are biased low by typically -23 % to -37 % and reaching values of −51 % over highly polluted regions (e.g., Verhoelst et al., 2021). As discussed in several validation studies (see e.g., Judd et al., 2020; Verhoelst et al., 2021; van Geffen et al., 2022b), this underestimation could be caused by biases in the cloud pressure retrieval of the FRESCO-S retrieval, by too high cloud pressures, especially during periods of high aerosol loads (which is seen as an effective cloud by the FRESCO algorithm) and/or low cloud fractions.

Table 4.3: List of TROPOMI NO_2 product versions with the most important differences regarding the NO_2 vertical profile, reflectivity data, and cloud product.

TROPOMI NO_2 product versions	NO_2 vertical profile	Reflectivity	Clouds
OFFL V01.03.02 operational 26 Jun 2019–29 Nov 2020	TM5	OMI LER	FRESCO-S
OFFL V01.03.02 CAMS (scientific) based on OFFL V01.03.02	CAMS regional $< 3\,\text{km}$ CAMS global $> 3\,\text{km}$	OMI LER	FRESCO-S
PAL V02.03.01 respectively OFFL V02.03.01 operational 4 Nov 2021–17 Jul 2022 reprocessed 1 May 2018–14 Nov 2021	TM5	OMI LER	FRESCO-W
IUP V02.03.01 (scientific) campaign period, similar to PAL V02.03.01, a priori assumptions can be changed	TM5	OMI LER	FRESCO-W
IUP V02.03.01 REG (scientific) campaign period	CAMS regional $< 3\,\text{km}$ TM5 $> 3\,\text{km}$	OMI LER	FRESCO-W
IUP V02.03.01 REG TROPOMI LER (scientific) campaign period	CAMS regional $< 3\,\text{km}$ TM5 $> 3\,\text{km}$	TROPOMI LER	FRESCO-W
IUP V02.03.01 REG TROPOMI DLER (scientific) campaign period	CAMS regional $< 3\,\text{km}$ TM5 $> 3\,\text{km}$	TROPOMI DLER	FRESCO-W

Other stated factors that could contribute to the underestimation are (1) the low spatial resolution of the used a priori NO_2 profiles from the TM5 global chemistry transport model (e.g., Judd et al., 2020; Tack et al., 2021), (2) the use of the OMI LER climatology given on a grid of $0.5° \times 0.5°$ for the AMF and cloud fraction retrieval in the NO_2 fit window (van Geffen et al., 2022b), and (3) the GOME-2 LER climatology ($0.25° \times 0.25°$) measured at mid-morning used for the NIR-FRESCO cloud retrieval (van Geffen et al., 2022b). In addition to the lack in spatial resolution, these LER climatologies also do not consider the viewing angle dependency (Lorente et al., 2018; van Geffen et al., 2022b). In V02.04, operational since 17 July 2022, a directionally dependent LER (DLER) with a resolution of $0.125° \times 0.125°$ derived from TROPOMI observations is applied for AMF and cloud fraction retrieval in the NO_2 fit window and to the NIR-FRESCO cloud pressure retrieval (Eskes and Eichmann, 2022). Since V02.04 is not yet reprocessed and thus not available for the campaign period, it is not included and discussed here.

4.3.1.2 Scientific TROPOMI NO_2 V01.03.02 CAMS product

NO_2 plumes from various sources in highly polluted regions cannot be resolved in the coarse resolution of the originally used TM5 model with a resolution of $1° \times 1°$. A new scientific TROPOMI NO_2 level-2 data product for Europe, based on a replacement of the original TM5 a priori NO_2 profiles by the regional CAMS ensemble analyses was introduced by Douros et al. (2023). The product is based on the operational OFFL processor V01.03.02 for the campaign period but uses the CAMS European regional analyses with a resolution of $0.1° \times 0.1°$ up to 3000 m and above the CAMS global analyses. Using the averaging kernels and other AMF information from the original TROPOMI NO_2 level-2 files, AMFs and tropospheric NO_2 VCDs were recalculated. It was found that using the higher resolution CAMS regional NO_2 profiles in the retrieval increases the tropospheric NO_2 VCDs in highly polluted regions between 5 to 30 %, strongly depending on time and location (Douros et al., 2023).

4.3.1.3 TROPOMI NO_2 PAL V02.03.01 product

Modifications in the TROPOMI NO_2 retrieval led to V02.02, operational since 1 July 2021. The modifications leading to this version are described in detail in van Geffen et al. (2022b). After minor format changes and a few bug fixes, the version was replaced on 14 November 2021 by V02.03.01. To provide a harmonized data set with the updated retrieval, a complete mission reprocessing was performed based on the V02.03.01. The reprocessed NO_2 data, using the V02.03.01 of the official level-2 processor, is provided by the S5P Product Algorithm Laboratory (PAL) and is available from 1 May 2019 to 14 November 2021 (Eskes and Eichmann, 2022). Due to the mission reprocessing, the campaign data set can be compared to the OFFL V01.03.02 and the new PAL V02.03.01 NO_2 data product.

The main change influencing the tropospheric NO_2 VCD is the use of the FRESCO-wide instead of the FRESCO-S algorithm for retrieving the cloud pressures. The FRESCO-wide algorithm was first introduced with V01.04.00, operational from 29 November 2020 to 1 July 2021, but with the reprocessing now applied to the complete data set. A larger wavelength window in the FRESCO-wide algorithm includes weaker and narrower O_2 absorption lines, decreasing the cloud pressure in the order of 50 hPa and is mainly influencing clouds with cloud pressures close to the surface pressure. Therefore, the update provides more realistic lower cloud pressures and especially for scenes when cloud fractions are low. These lower cloud pressures (i.e., higher clouds) result in decreased tropospheric AMFs, leading to higher tropospheric NO_2 VCDs, bringing the TROPOMI data for many cases much closer to the validation data (van Geffen et al., 2022b). Figure 4.3 shows the BAMF of the OFFL V01.03.02 (blue) and the PAL V02.03.01 (red) product for the TROPOMI overpass on 17 September 2020 in the Rhine-Ruhr region (50.91° N, 6.41° E). For the OFFL V01.03.02 product, FRESCO-S retrieved a cloud height very close to the surface, resulting in a surface and cloud pressure difference of -3.43 hPa. The uncertainty of the cloud pressure retrieval is given as 50 hPa (van Geffen et al., 2022a). The

FRESCO-wide retrieval used in the PAL V02.03.01 product yields a 163 hPa lower cloud pressure, resulting in a surface and cloud pressure difference of 159.78 hPa. This results in decreased AMFs, with a tropospheric AMF of 0.69 compared to 1.19 before.

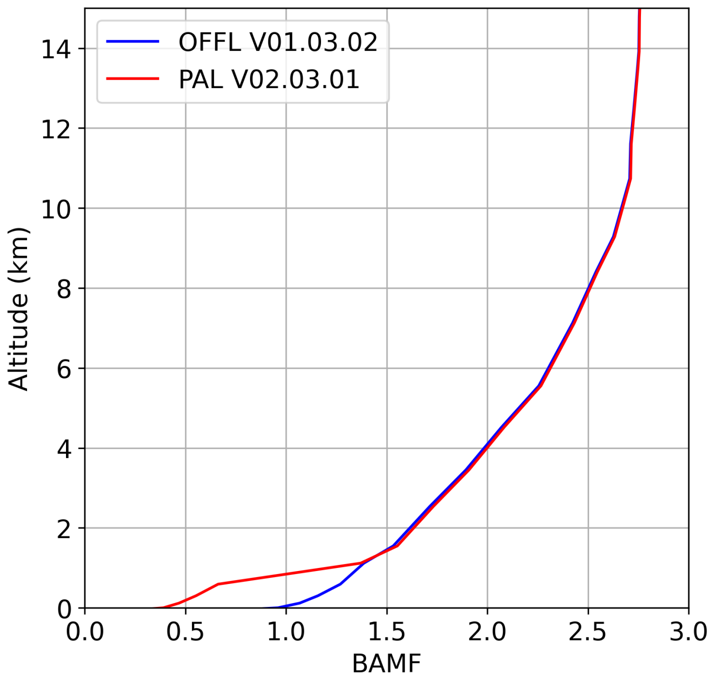

Figure 4.3: BAMF of the TROPOMI OFFL V01.03.02 (blue) and the PAL V02.03.01 (red) product on 17 September 2020 in the Rhine-Ruhr region (50.91° N, 6.41° E). The products provide a cloud radiance fraction of 0.22/0.23, a surface and cloud pressure difference of -3.43 hPa/159.78 hPa, and a tropospheric AMF of 1.19/0.69 for the OFFL V01.03.02 respectively the PAL V02.03.01 product.

Another update in the tropospheric NO_2 VCD retrieval is a correction of the surface albedo by the observed reflectance for cloud-free scenes. For these cases, the tropospheric NO_2 VCDs over polluted regions are increased by about 15 % (van Geffen et al., 2022b). Since only 1 out of the here analyzed 117 TROPOMI pixels is observed as cloud-free, the effect is negligible for this analysis. Furthermore, van Geffen et al. (2022b) also describes the following modifications, which have no or only a small impact on the tropospheric NO_2 VCD. Level-1b v2.0 (ir)radiance spectra are updated and are increasing the NO_2 SCD of about 3 %, which ends up mostly in a slightly increased stratospheric VCD. Additionally, the improved level-1b v2.0 also leads to a small increase of completely cloud-free pixels and slightly lower cloud pressures for pixels with a small cloud fraction, resulting in tropospheric NO_2 VCDs being about 5 % higher for these observations. An introduced outlier removal increases the number of good quality retrievals over the South Atlantic Anomaly and bright clouds where saturation can occur. The switch to a new spatially higher resolved snow and ice information increases the number of valid retrievals at high latitudes.

On average, the modifications in the new data V02.02/V02.03.01 increased the tropospheric NO_2 VCDs between 10 % and 40 % compared to the V01.x product. The increase depends on the season and the degree of pollution and is found to be largest at mid and high latitudes in winter. Comparisons to ground-based data show, on average, an improvement of the negative bias of the TROPOMI tropospheric NO_2 VCDs from -32 % to -23 % (van Geffen et al., 2022b).

4.3.1.4 Scientific TROPOMI NO_2 IUP V02.03.01 product

For further analysis of the influence of a priori assumptions on the TROPOMI tropospheric NO_2 VCD retrieval, a scientific product based on the operational V02.03.01 data product was developed at IUP Bremen. This product, labeled as IUP V02.03.01, enables the possibility to change auxiliary data and investigate their influence, such as the NO_2 profiles but also the surface reflectance, which is not possible using the averaging kernel approach as done for the V01.03.02 CAMS product.

To demonstrate the impact of higher resolved a priori NO_2 vertical profiles, AMFs and the tropospheric NO_2 VCDs were recalculated with the radiative transfer model SCIATRAN (Rozanov et al., 2014) using a priori tropospheric profiles from the 0.1° × 0.1° CAMS regional analyses for altitudes between the surface and 3 km. Above 3 km to the tropopause, where horizontal variability is generally small, the TM5 analyses are used. This data version using the CAMS regional analyses is called IUP V02.03.01 REG in the following. Fig. 4.4 shows maps depicting the NO_2 distribution of the CAMS regional and the TM5 analyses for the campaign region. The CAMS regional analyses clearly show individual plumes of NO_2 originating from the source regions, whereas the NO_2 distribution from TM5 analyses is much smoother and shows in general lower values.

For the operational TROPOMI AMF calculations, surface reflectivity information is taken from the 5-year OMI LER climatology, which has a resolution of 0.5° × 0.5°. Since, in the meantime, a large data set of TROPOMI observations became available, a TROPOMI surface reflectivity database, based on 36 months of TROPOMI v1.0 level-1b data, has been provided by Tilstra (2022). It includes LER data as a function of the month, wavelength, latitude, and longitude, and due to the smaller pixel size of TROPOMI it has a resolution of 0.125° × 0.125°. In addition, also a DLER, which includes the TROPOMI viewing direction dependence, has been generated. The DLER database provides generally higher reflectivities than the LER (see Sect. 2.3.4 and Tilstra (2022)). Recalculating AMFs using the regional CAMS NO_2 profiles and the TROPOMI LER, respectively DLER, results in the product named IUP V02.03.01 REG TROPOMI LER/DLER. The use of the TROPOMI reflectivity database is limited to the NO_2 AMFs. Cloud parameters are not recalculated.

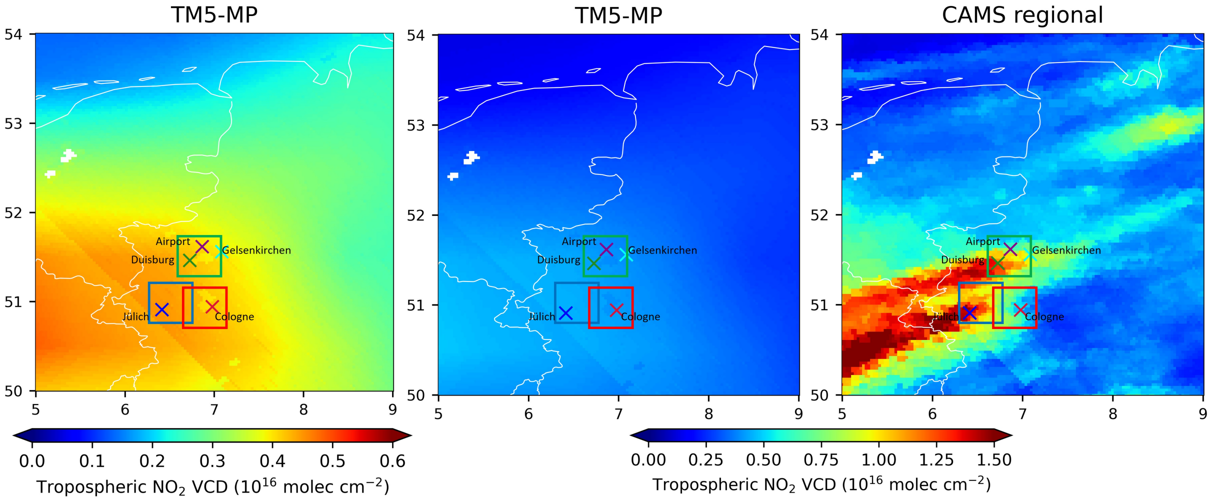

Figure 4.4: Tropospheric NO_2 VCD of the TM5 (1° × 1°) and the CAMS regional (0.1° × 0.1°) analyses for the campaign region on 17 September 2020, interpolated to TROPOMI pixels and oversampled to a 0.03° × 0.03° resolution.

4.3.1.5 TROPOMI data set

The described TROPOMI tropospheric NO_2 VCD product versions are evaluated on the airborne campaign measurement days from 12 September to 18 September 2020 over the campaign region. Due to ground-segment anomalies, TROPOMI data are not available over the campaign region on 14 September. The quality of the processing and retrieval result is indicated by a quality assurance value (qa_value). Following the recommendation by Eskes and Eichmann (2022), only TROPOMI observations with a qa_value greater than 0.75 are used. In addition to removing problematic retrievals, also observations with cloud radiance fractions of more than 50 % are excluded. Since the campaign measurement days were mostly cloud-free, the cloud radiance fraction retrieved in the TROPOMI NO_2 spectral window was on average for the 117 pixels coinciding with the airborne measurements 0.21 ± 0.10 with a maximum of 0.48. Thus all coinciding TROPOMI data are included in the analysis. Daily maps of TROPOMI PAL V02.03.01 tropospheric NO_2 VCDs are depicted in Fig. 4.13.

4.3.2 AirMAP

The airborne DOAS measurements during the campaign were conducted by the AirMAP instrument, described in further detail in Sect. 2.5.2. The flights were performed in the Cessna 207-Turbo, operated by the FU-Berlin. AirMAP is a push-broom imaging DOAS instrument with the ability to create spatially continuous and nearly gap-free measurements. The typical flight altitude of around 3200 m, flight speeds of around $60\,\mathrm{m\,s^{-1}}$, and an exposure time of 0.5 s result in a ground pixel size of about 30 m × 100 m. The AirMAP measurements link the TROPOMI and the ground-based measurements and are used to validation the TROPOMI tropospheric NO_2 VCDs.

4.3.2.1 AirMAP NO_2 retrieval

For the NO_2 retrieval, the measured spectra are analyzed using the DOAS method (see Sect. 2.4) in a fitting window of 438 to 490 nm. The NO_2 dSCDs are retrieved relative to reference background spectra, measured during the same flight over a region with low NO_2 amounts. The retrieved dSCDs are converted to tropospheric SCDs by correcting for the amount of NO_2 in the reference background spectra ($\mathrm{SCD_{ref}}$):

$$\begin{aligned}\mathrm{SCD^{trop}} &= \mathrm{dSCD} + \mathrm{SCD_{ref}} \\ &= \mathrm{dSCD} + \mathrm{VCD^{trop}_{ref}} \cdot \mathrm{AMF^{trop}_{ref}}\end{aligned} \tag{4.1}$$

For the correction of NO_2 in the reference background measurement, we assume a value of $1 \times 10^{15}\,\mathrm{molec\,cm^{-2}}$ for the tropospheric VCD over the region, which is a typical value in Europe during summer (Popp et al., 2012; Huijnen et al., 2010). This assumption can be supported by the car DOAS measurements, see Sect. 4.3.3.1.

The tropospheric VCDs are calculated by dividing the tropospheric SCDs by the tropospheric AMF:

$$\begin{aligned}\mathrm{VCD^{trop}} &= \frac{\mathrm{SCD^{trop}}}{\mathrm{AMF^{trop}}} \\ &= \frac{\mathrm{dSCD} + \mathrm{VCD^{trop}_{ref}} \cdot \mathrm{AMF^{trop}_{ref}}}{\mathrm{AMF^{trop}}}\end{aligned} \tag{4.2}$$

All airborne campaign measurements were performed close to the S5P overpass around noon, are relatively short, lasting about 3 h, and the time difference between the actual measurement and the reference measurement is rather small. Therefore, it is assumed that the effect of the diurnal variation of the stratospheric NO_2 amount and the changing SZA is small, and a stratospheric correction of the measurements is not necessary.

The tropospheric AMFs are simulated using SCIATRAN. Since information about the NO_2 profile in the campaign area are limited and the profile shapes are expected to vary from day to day, and within each flight region, a typical urban NO_2 profile is assumed, which is based on an old WRF-Chem (Weather Research and Forecasting model coupled with Chemistry) run and scaled to a height of 1 km (see Appendix Fig. B.1). This assumption is supported by ERA5 boundary layer height data with typical heights of approximately 1 km during the flight times and in the respective flight regions (see Appendix Fig. B.2). Aerosol input parameters (AOT, asymmetry factor, and single-scattering albedo) were taken from the AERONET station FZJ-JOYCE at the Jülich research center, the only known source of local ground-based aerosol information in the campaign region. The aerosol profile is approximated with a 1.5 km height box profile. The daily averages of the AOT measured at the station on the campaign measurement days ranged from 0.235 up to 0.398, with a mean value of 0.285. A sensitivity study evaluating the effect of using AMFs in the AirMAP VCDs retrieval based on AOTs in the range of 0.003 to 0.6 showed that the impact on the AirMAP tropospheric NO_2 VCD data is small. Figure 4.5 shows a scatter plot of AirMAP tropospheric NO_2 VCDs for AMFs based on an AOT of 0.003 vs. a data set calculated assuming an AOT of 0.6, with a correlation coefficient of 1 and a slope of 1 ± 0.01. The comparison of TROPOMI and AirMAP tropospheric NO_2 VCDs for AOTs of 0.003, 0.3, and 0.6 also showed small influence of the AOT on the AirMAP NO_2 retrieval (see Appendix Fig. B.3). Considering the result of the sensitivity study and the mean measured AOT of 0.285, the AirMAP data set was determined with a fixed AOT of 0.3 for all measurements. The following discussions will make additional use of the pre-operational TROPOMI AOT product (de Graaf, 2022), which can provide a larger picture of the aerosol situation (see Appendix Fig. B.8). Generally, it shows AOT values in the same range as investigated within the sensitivity study.

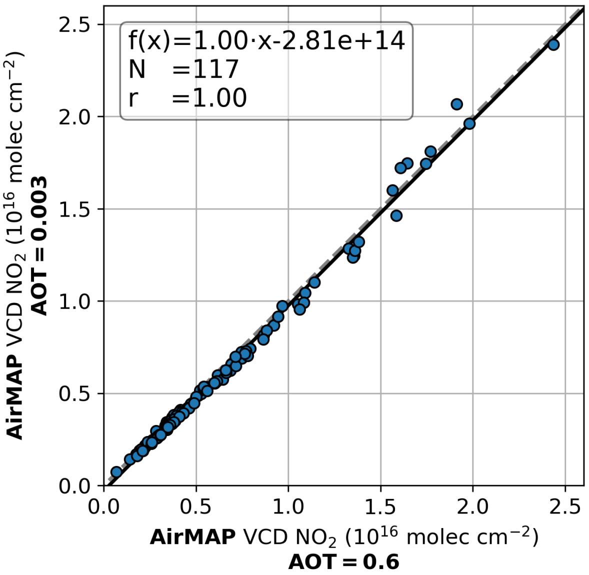

Figure 4.5: Scatter plot of AirMAP tropospheric NO_2 VCDs for an AOT of 0.003 vs. a data set based on an AOT of 0.6.

Bright surfaces enhance the relative contribution of light reflected from the surface to the signal received by AirMAP and thus increase the sensitivity to NO_2 near the ground. Therefore, areas of high surface reflectance in the fitting window generally show larger dSCDs for the same amount of NO_2. Thus, AMF calculations must account for surface reflectivity differences. Surface reflectance data with a sufficient spatial resolution for airborne measurements are not available for the campaign region. Therefore, the individual intensities measured by AirMAP are used together with a technique based on a reference area with known surface reflectance from the ADAM database (a surface reflectance database for ESA's earth observation missions, (Prunet et al., 2013)) and a LUT of AirMAP radiances. Maps of the determined surface reflectance can be found in the Appendix Fig. B.4. More detailed information on the surface reflectance derivation can be found in Meier et al. (2017).

4.3.2.2 AirMAP NO$_2$ retrieval uncertainties

The total uncertainty on the tropospheric NO$_2$ VCD originates from error sources in the retrieved dSCDs, the estimation of the reference background column, and the AMF calculation. Assuming uncorrelated uncertainties, the total uncertainty of the AirMAP tropospheric NO$_2$ VCD follows the error propagation of the three error sources given by:

$$\sigma_{\mathrm{VCD}^{\mathrm{trop}}} = \sqrt{\left(\frac{\sigma_{\mathrm{dSCD}}}{\mathrm{AMF}^{\mathrm{trop}}}\right)^2 + \left(\frac{\sigma_{\mathrm{SCD}_{\mathrm{ref}}^{\mathrm{trop}}}}{\mathrm{AMF}^{\mathrm{trop}}}\right)^2 + \left(\frac{\mathrm{SCD}^{\mathrm{trop}}}{\mathrm{AMF}_{\mathrm{trop}}^2} \cdot \sigma_{\mathrm{AMF}^{\mathrm{trop}}}\right)^2} \tag{4.3}$$

with:

$$\sigma_{\mathrm{SCD}_{\mathrm{ref}}^{\mathrm{trop}}} = \sqrt{\left(\mathrm{AMF}_{\mathrm{ref}}^{\mathrm{trop}} \cdot \sigma_{\mathrm{VCD}_{\mathrm{ref}}^{\mathrm{trop}}}\right)^2 + \left(\mathrm{VCD}_{\mathrm{ref}}^{\mathrm{trop}} \cdot \sigma_{\mathrm{AMF}_{\mathrm{ref}}^{\mathrm{trop}}}\right)^2} \tag{4.4}$$

The error from the retrieved dSCDs σ_{dSCD} is estimated from the fit residuals in the DOAS analysis. Since no direct measurement of the NO$_2$ amount in the reference background scene exists, a systematic error with an uncertainty of 100 % is assumed for the estimated $\mathrm{VCD}_{\mathrm{ref}}^{\mathrm{trop}}$ of 1×10^{15} molec cm^{-2}. The dominating uncertainty originates from the AMF calculation, which comprises error sources from the surface reflectance determination, the NO$_2$ vertical profile assumptions, and the aerosol information. Following Meier et al. (2017), the total error on the AMF is assumed to be 25 %, which is dominated by the uncertainties on the aerosol information, followed by the surface reflectance and the NO$_2$ profile assumptions. Taking the mean dSCD value (1.2×10^{16} molec cm^{-2}) and the mean dSCD error (2×10^{15} molec cm^{-2}) as typical values, the total error of the tropospheric NO$_2$ VCD is ~35 %.

4.3.2.3 AirMAP data set

Measurements from AirMAP are available for 7 flight days from 12 September to 18 September 2020. Figure 4.6 shows time series of tropospheric NO$_2$ VCD for each day. The mean over the 35 viewing directions is shown in dark colors and their standard deviation in

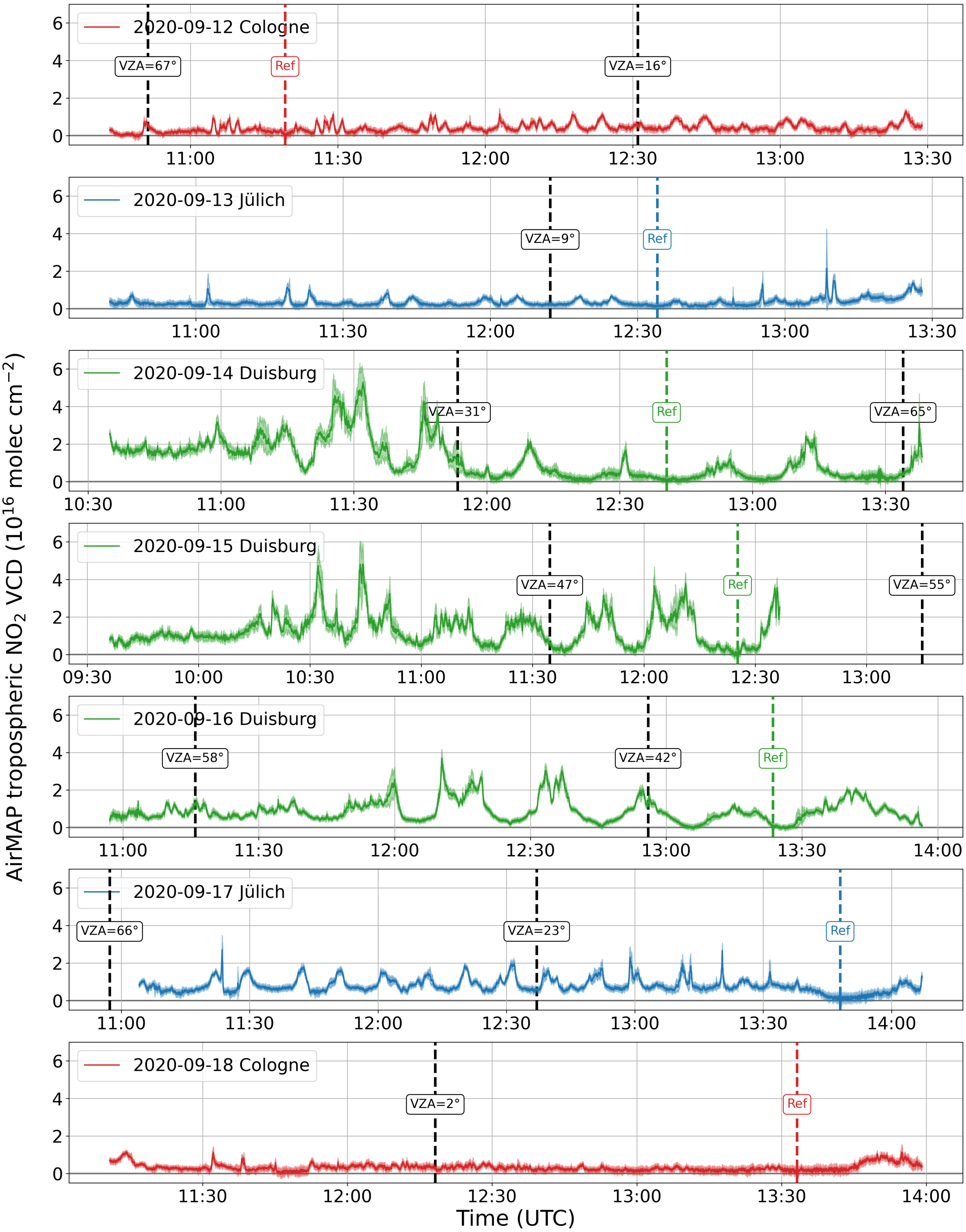

Figure 4.6: Plots of the AirMAP time series of tropospheric NO$_2$ VCD (mean over the 35 viewing directions with standard deviation as dark line and bright area, respectively) for the 7 flight days from Saturday 12 September 2020 to Friday 18 September 2020. The dashed colored vertical lines indicate the times of the AirMAP reference measurement. The dashed black vertical lines indicate S5P overpass times with their viewing zenith angle.

light colors. The colors red, blue, and green represent the respective flight areas Cologne, Jülich, and Duisburg. The times of the AirMAP reference measurement are marked by the colored vertical dashed lines. The black dashed vertical lines indicate the S5P overpass times with their respective VZA. Two flights were performed over the research flight area Cologne (red), two flights over the Jülich area (blue), and three flights over the Duisburg area (green). The first two flights, shown in Fig. 4.6, were performed on weekend days, a Saturday and a Sunday. The tropospheric NO_2 VCDs show strong variability from day to day and between the three target areas. The highest NO_2 amounts of ~ 5×10^{16} molec cm^{-2} were measured over the Duisburg area on Monday 14 and Tuesday 15 September.
The corresponding daily maps of tropospheric NO_2 VCDs are displayed in Fig. 4.7. For the Cologne research flight area, the two AirMAP measurement flights show only slightly enhanced NO_2 amounts compared to the background tropospheric NO_2 VCD.

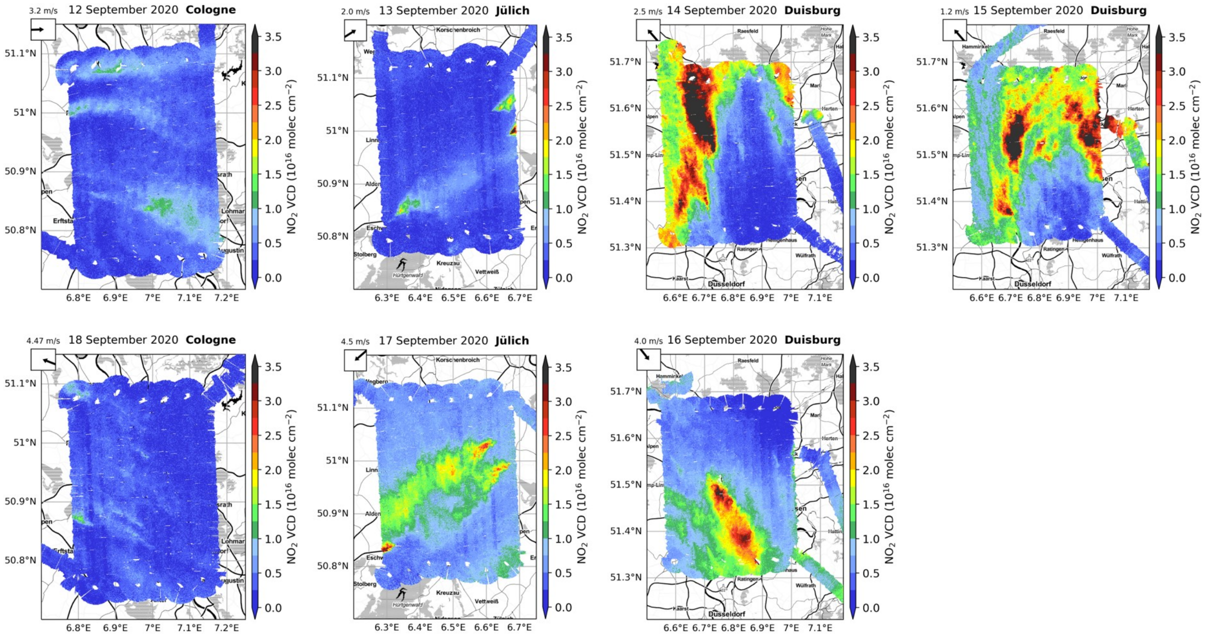

Figure 4.7: Maps of tropospheric NO_2 VCD from AirMAP flights from 12 to 18 September 2020. Two flights in the research flight area around Cologne (left column), two flights in the flight area around Jülich (second column), and three flights in the flight area around Duisburg (third and fourth column). The mean wind direction and speed in the flight area, determined from ERA5 10 m wind data for the middle of the flight, are given in the top left corner.

Over the Jülich flight area, the tropospheric NO_2 VCD is smaller during the flight on Sunday 13 September than on Thursday 17 September, where several peaks in the NO_2 VCD up to 2.5×10^{16} molec cm^{-2} are visible. These peaks are caused by NO_2 plumes which are clearly visible in the AirMAP NO_2 VCD maps and originate from three large power plants in this area. One power plant is located in the southwest, and two in the northeast of the Jülich research flight area. The plumes, which clearly show enhanced NO_2 amounts compared to the lower background outside the plume, are blown in the mean wind direction. Mean wind speed and direction in the flight area for the middle of the flight determined from ERA5 10 m wind data (Hersbach et al., 2018) are given in the top left corner of the maps in Fig. 4.7. The differences between the two measurements over the Jülich area can be related to wind conditions and are potentially enhanced by a weekday effect. On Sunday 13 September, a weak wind from the southwest blew the plumes mostly outside of the flight area, and cleaner air from a more rural area dominated. On Thursday 17 September, a stronger wind from the opposite direction blew the plumes to the southwest.

The maps from the three flights over the Duisburg area show strong NO_x emissions from several sources in the industrial area in Duisburg, with plumes oriented according to the wind direction.

4.3.3 Mobile car DOAS instruments

Mobile car DOAS measurements were performed with three instruments by the three institutions, IUP Bremen, the Royal Belgian Institute for Space Aeronomy (BIRA), and the Max Planck Institute for Chemistry in Mainz (MPIC). For the majority of measurements, the instruments measured in zenith-sky mode. Focusing on zenith-sky measurements has the advantage that buildings cannot block measurements, the viewing direction is stable when the driving direction changes, and variations from relative azimuth changes are avoided. In addition, measuring only in zenith-sky mode achieves the highest horizontal resolution. The BIRA and MPIC instruments can perform off-axis measurements, which were primarily done during breaks and are used to estimate the NO_2 SCD in the reference spectrum and the stratospheric NO_2 contribution of the two data sets. The car DOAS instruments and their data retrieval are described in more detail in Schreier et al. (2019); Donner (2016); Merlaud (2013).

4.3.3.1 IUP car DOAS instrument and data retrieval

The IUP Bremen car DOAS instrument is based on an Avantes spectrometer (282 −412 nm) placed inside the car with the measurement computer and a GPS receiver. A light fiber is threaded through a light fiber holder in the car window to the outside of the car with a fixed viewing elevation angle to the zenith. A cylindrical tube connected to the light fiber prevents direct sunlight from entering the light fiber. Measured spectra are averaged over 10 s, depending on the car's driving speed. This results in a spatial resolution of 80 m to 300 m. The instrument can be powered using the integrated battery of the measurement computer or through a connection to the car cigarette lighter.

The tropospheric NO_2 VCD is determined similarly as done for the AirMAP measurements by the following equation:

$$\mathrm{VCD_{trop}} = \frac{\mathrm{dSCD} + \mathrm{SCD_{ref}} - \mathrm{VCD_{strat}} \cdot \mathrm{AMF_{strat}}}{\mathrm{AMF_{trop}}} \tag{4.5}$$

with

$$\mathrm{SCD_{ref}} = \mathrm{VCD_{trop,\,ref}} \cdot \mathrm{AMF_{trop,\,ref}} + \mathrm{VCD_{strat,\,ref}} \cdot \mathrm{AMF_{strat,\,ref}}. \tag{4.6}$$

The dSCDs are retrieved relative to reference background spectra, measured in a region with small NO_2 concentrations on 13 September around noon. With the described zenith-sky only setup, the $\mathrm{SCD_{ref}}$ cannot be measured directly. As for the AirMAP measurements, a tropospheric NO_2 VCD of 1×10^{15} molec cm^{-2} is assumed over the reference background region. Since the MPIC and BIRA car DOAS instruments take additional measurements at lower elevation angles, they do not rely on this value but determine the tropospheric column in the reference measurement with their additional off-axis measurements. Figure 4.8 depicts a comparison of collocated measurements of the three car DOAS instruments, showing a very good agreement and is thus supporting the assumption of a $\mathrm{VCD_{trop,\,ref}}$ of 1×10^{15} molec cm^{-2}. Using a significantly larger or lower $\mathrm{VCD_{trop,\,ref}}$ in the IUP car DOAS VCD retrieval would introduce a larger offset compared to the MPIC and BIRA car DOAS tropospheric NO_2 VCD data, which is with -1.28 $\times$ 10^{14} molec cm^{-2} in the shown comparison reasonably small.

Since all dSCDs are retrieved with one fixed reference background measurement, a stratospheric correction is applied to the car DOAS data. The stratospheric correction is based on the Bremen 3D chemistry transport model (B3dCTM, Hilboll et al. (2013b)), which provides diurnal cycles of the stratospheric NO_2 VCDs. Since the absolute values are off, the model values are scaled to the TROPOMI stratospheric VCDs retrieved within the measurement area during the overpass on the specific day. Stratospheric AMFs are calculated with the radiative transfer model SCIATRAN as a function of the SZA.

The tropospheric SCDs are converted into tropospheric NO_2 VCDs with a constant tropospheric AMF of 1.3. The AMF of 1.3 is closer to the true AMF derived from RTM simulations than the simple geometric approximation for the tropospheric AMF at an elevation angle of 90°, defined as 1 (see Sect. 2.5.3 and Shaiganfar et al. (2011); Merlaud (2013); Schreier et al. (2019). Merlaud (2013) analyzed the AMF distribution for measurements in 90° viewing zenith angle for a large number of RTM simulations, including several scenarios, resulting in a mean AMF of 1.33 ± 0.2. Since this analysis only uses data close to the AirMAP overpass, which was performing measurements around noon, the SZA and thus the AMF does not vary much. Following the mentioned studies, an uncertainty of 20 % is assumed for the AMF. The total uncertainty on the tropospheric NO_2 VCD

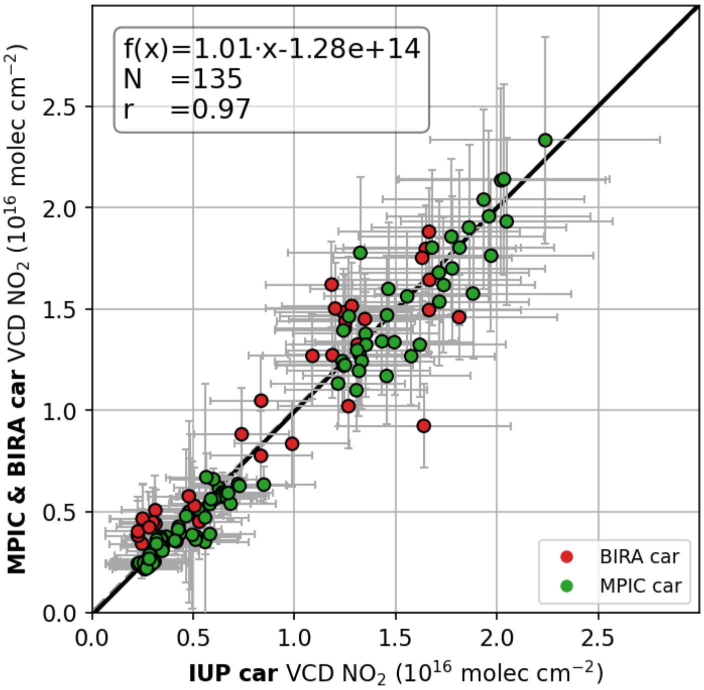

Figure 4.8: Scatter plot between collocated car DOAS measurements (± 5 min time window) of MPIC and BIRA car DOAS data vs. IUP car DOAS tropospheric NO_2 VCDs averaged within 200 m × 200 m grid boxes and 5 min time intervals. The data points from the BIRA and MPIC car DOAS instruments are color coded in red and green. The thick solid black line represents the orthogonal distance regression. Error bars represent the tropospheric NO_2 VCD retrieval error, averaged within the 200 m × 200 m grid boxes and 5 min time intervals.

is determined following Eq. 4.3. Since only measurements around noon are considered in the analysis, the uncertainty of the stratospheric correction can be neglected.

4.3.3.2 MPIC car DOAS instrument and data retrieval

The MPIC car DOAS setup is based on an actively temperature stabilized Avantes spectrometer (300 – 460 nm) with a light fiber connected to a telescope which is mounted on a stepper motor placed on the roof of the car. The stepper motor allows easy adjustment of the elevation angle of the telescope (see also Donner (2016)). Before and after the validation measurements, the instrument performed measurements in an elevation angle of 22°. Measured spectra are integrated over a time of 30 s.

The DOAS analysis is performed in a 400 – 460 nm wavelength range using a daily fixed reference background measurement at 90° elevation, close to noon in a region with low NO_2 concentrations. The retrieved dSCDs are converted to tropospheric NO_2 VCDs by Eq. 4.5. The combination of the 22° and zenith-sky measurements allows the determination of the absorption in the stratosphere, as well as in the reference spectrum SCD_{ref} (see e.g. Wagner et al., 2010; Ibrahim et al., 2010). Tropospheric AMFs for the 22° and

90° elevation angle measurements of 3 and 1.3 with an uncertainty of 20 % are based on RTM calculations for NO_2 box profiles of 500 m or 1000 m with a moderate aerosol load (Shaiganfar et al., 2011).

4.3.3.3 BIRA car DOAS instrument and data retrieval

The BIRA car DOAS setup is similar to the IUP Bremen instrument but uses two Avantes spectrometers and light fibers with fixed viewing elevation, enabling simultaneous measurements in 90° and 30° elevation (see Merlaud (2013)). Individual spectra are co-added, and the DOAS analysis in a wavelength interval of 450 −515 nm is performed on spectra averaged over 30 s using a single pair of time-coincident zenith reference spectra around noon at small SZA for all measurement days. The tropospheric NO_2 VCDs are determined using the differences in dSCDs and AMFs for the 30° and 90° elevation angle simultaneous measurements following the geometrical approximation (see Sect. 2.5.3):

$$\mathrm{VCD_{trop}} = \frac{\mathrm{dSCD}(30)}{\mathrm{AMF_{trop}}(30) - \mathrm{AMF_{trop}}(90)} \tag{4.7}$$

The AMFs are based on average AMFs calculated with a large number of RTM simulations, including several scenarios, resulting in AMFs of 2.5 and 1.3 for the 30° and 90° measurements (Merlaud, 2013).

4.3.3.4 Car DOAS data set

The car DOAS measurements were organized in a way that each car took measurements during a round trip over a large part of the area covered by the airborne measurements. The routes were planned to pass by the stationary ground-based measurement sites. Regular collocations of the three cars at meeting points and overlapping measurement routes were used to verify the car measurements by each other. Figure 4.8 shows a scatter plot of the collocated car DOAS measurements and demonstrates the good agreement between the three instruments. The duration of the car DOAS measurements was usually about 4 h per day, taking measurements throughout the complete AirMAP flight and during the S5P overpass to gather many closely collocated measurements. Depending on traffic conditions, about three to four round trips were performed during this time and are showing temporal changes in addition to the spatial variation of NO_2.

Figure 4.9 shows daily maps of tropospheric NO_2 VCDs from car DOAS measurements from 12 to 18 September taken in the research flight areas around Cologne, Jülich, and Duisburg within ± 1 h of the S5P overpass time. On five out of the seven measurement

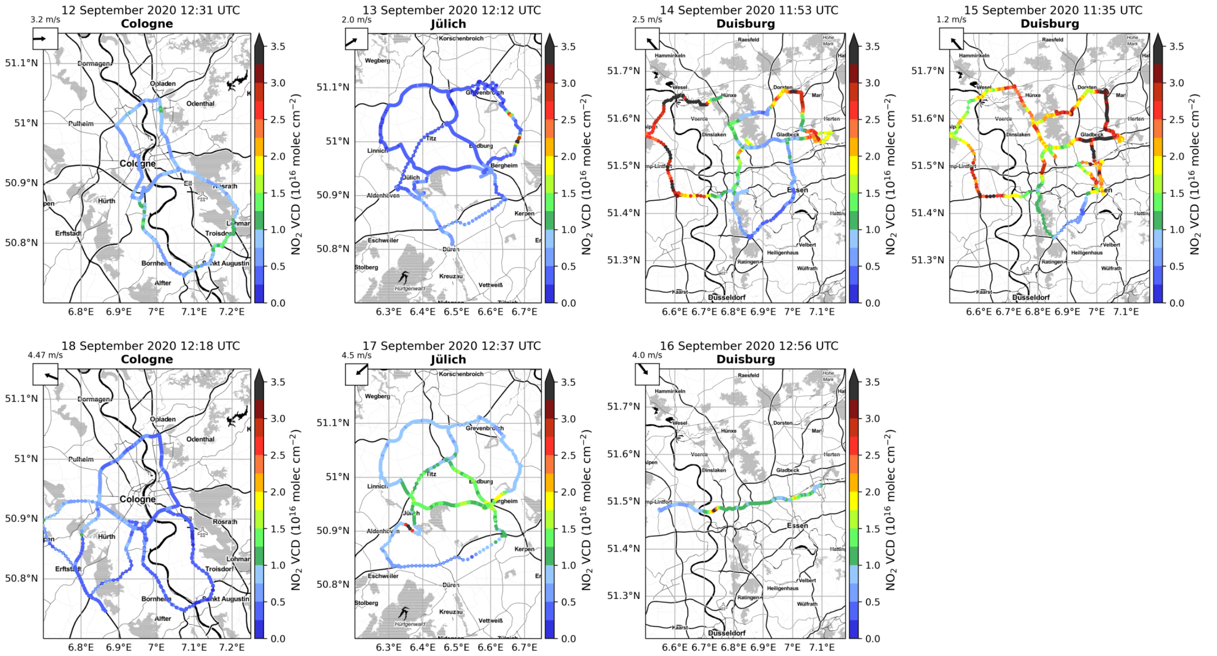
12 September 2020 12:31 UTC
Cologne

13 September 2020 12:12 UTC
Jülich

14 September 2020 11:53 UTC
Duisburg

15 September 2020 11:35 UTC
Duisburg

18 September 2020 12:18 UTC
Cologne

17 September 2020 12:37 UTC
Jülich

16 September 2020 12:56 UTC
Duisburg

Figure 4.9: Maps of tropospheric NO_2 VCDs from car DOAS measurements from 12 September to 18 September 2020 in the research flight area around Cologne, Jülich, and Duisburg. Measurements are within ± 1 h of the S5P overpass time given in the title.

days, three car DOAS instruments were operating. On 12 September only two instruments and on 16 September only one instrument was operating. Similar to the AirMAP measurements, also the car DOAS measurements observed strong variability between the different flight areas. The highest amounts of NO_2 were measured in the Duisburg area, but additionally, there is high spatial variability with lower NO_2 in the southern part. The lowest amounts of NO_2 are visible in the Cologne area, which confirms the results from the AirMAP measurements. The car DOAS measurements in the Jülich area show the same differences between the two measurement days as seen in the AirMAP data, and enhanced NO_2 is visible where the plumes of the power plants were seen in the maps of the AirMAP measurements.

4.3.4 Stationary ground-based instruments

The stationary ground-based measurements were conducted by two Zenith-DOAS, two MAX-DOAS, and two Pandora instruments deployed at five sites in the research flight areas. The ground-based measurement sites are marked on the flight overview map in Fig. 4.2 and the TROPOMI tropospheric NO_2 VCD map in Fig. 4.1.

4.3.4.1 Zenith-DOAS

The two Zenith-DOAS instruments operated for several months in the campaign area. The setup comprises an Avantes spectrometer for a wavelength range of 290 to 550 nm and an optical light fiber aligned to the zenith. Due to their simple setup, they can be installed easily also in non-scientific environments. One instrument was deployed at a local residence in Gelsenkirchen (Zenith-DOAS GEL) in the Duisburg flight area. The second instrument was set up at the Jülich research center (Zenith-DOAS JUE) in the Jülich flight area.

The dSCDs are retrieved relative to a fixed reference background spectra taken during summer around noon with low SZA on a clean day. The tropospheric NO_2 VCDs are calculated using Eq. 4.5. The amount of NO_2 in the reference background spectrum, SCD_{ref}, is estimated from the long time series using the lowest measured NO_2. For the Zenith-DOAS JUE this results in a SCD_{ref} of 1×10^{16} molec cm^{-2}. For the Zenith-DOAS GEL this is a SCD_{ref} of 1.7×10^{16} molec cm^{-2}. Compared to the assumed $VCD_{trop,\,ref}$ these estimates appear to be quite high, but the given $SCDs_{ref}$ include the stratospheric and tropospheric NO_2 and are taken during summer; thus a large part can be attributed to stratospheric NO_2. The uncertainty for the SCD_{ref} is assumed to be 30 %. The stratospheric VCDs is estimated from twilight Langley fits (e.g., Richter, 1997) with an uncertainty of 2×10^{14} molec cm^{-2}. The stratospheric AMFs are obtained from SCIATRAN calculations. For the tropospheric AMF, the same value of 1.3 as for the car DOAS data is used. Since only measurements close to the AirMAP overpass, i.e., around noon, are analyzed, the SZA does not vary much, and the influence on the AMF is negligible.

4.3.4.2 MAX-DOAS measurement truck

The IUP Bremen measurement truck includes a MAX-DOAS instrument and was deployed in the harbor area of Duisburg (MAX-DOAS DUI) from 7 September to 19 September 2020. The MAX-DOAS instrument comprises a UV spectrometer for measurements from 282 to 414 nm and an optical light fiber connected to a telescope on a pan-tilt head, allowing measurements in multiple elevation and azimuthal angles.

The tropospheric NO_2 VCDs are determined from the dSCD measurements in 30° elevation angle with a sequential zenith-sky reference spectrum, following the geometric approximation, see Eq. 4.7. AMFs for the 30° and 90° elevation measurements in the UV fitting window are determined as 2.5 and 1.4 based on SCIATRAN AMF calculations with an assumed uncertainty of 20 %.

4.3.4.3 BIRA SkySpec MAX-DOAS

A second MAX-DOAS instrument was operated from 3 August to 29 September 2020 at the airport Schwarze Heide in Dinslaken (MAX-DOAS AIRPT) in the Duisburg flight area. The instrument of type Airyx Compact SkySpec is based on an Avantes spectrometer measuring in a wavelength range of 300 to 463 nm. A scanning prism in elevation direction rotating by 180° enables measurements in multiple elevations and two azimuthal angles (Airyx GmbH, last access: 14 July 2022; Kreher et al., 2020). During the campaign, the instrument measured in multiple elevation angles in an azimuthal direction of 132° and 312°. This analysis uses only measurements in northwesterly direction (312°).

The dSCDs are retrieved with the spectral fitting software QDOAS (Danckaert et al., 2017) using the FRM4DOAS settings and setup, in a wavelength range of $411 - 445$ nm (Hendrick et al., 2016). The tropospheric NO_2 VCDs are determined with the Mexican MAX-DOAS Fit (MMF, Friedrich et al. (2019)) inversion algorithm. The tropospheric NO_2 VCD error is calculated from the covariance measurement noise error matrix, the covariance smoothing error matrix, and a systematic error as a fixed fraction of the VCD, based on the systematic uncertainty of the cross section, for NO_2 as 3 % based on Vandaele et al. (1998).

4.3.4.4 Pandora

The Pandora instrument is based on a UV-Vis spectrometer providing additionally to sky scan MAX-DOAS tropospheric column observations also direct sun total columns. Two Pandora instruments were deployed in the campaign area in August 2019 and are still in operation in 2022 to provide long-term measurements and complement the measurements during the campaign period. One Pandora is located in the Jülich flight area at the Jülich research centre (Pandora JUE), and the second one is in the Cologne flight area on the roof of an office building in Cologne, district Deutz.

Measurements are processed within the Pandonia Global Network (PGN, `https://www.pandonia-global-network.org/`, last access: 18 March 2022). Tropospheric NO_2 VCDs are retrieved using coincident direct sun and sky-scan MAX-DOAS observations and are calculated based on the Spinei et al. (2014) approach (Cede et al., 2021). Only data with a quality flag accounting for high and medium quality are included in the analysis.

4.3.4.5 Stationary ground-based data set

The six ground-based instruments measured during the flight period from 12 to 18 September 2020 in the campaign area, and most of them also for a more extended period before and after the flight period. Data for many months are available. During the flight period, only for the Pandora JUE, one day of data is missing on 12 September. The NO_2 time series in Fig 4.10 shows that the period from 12 to 18 September 2020 was not exceptional regarding amounts or temporal evolution of NO_2. Similar values were also observed at other times during the displayed month of September.

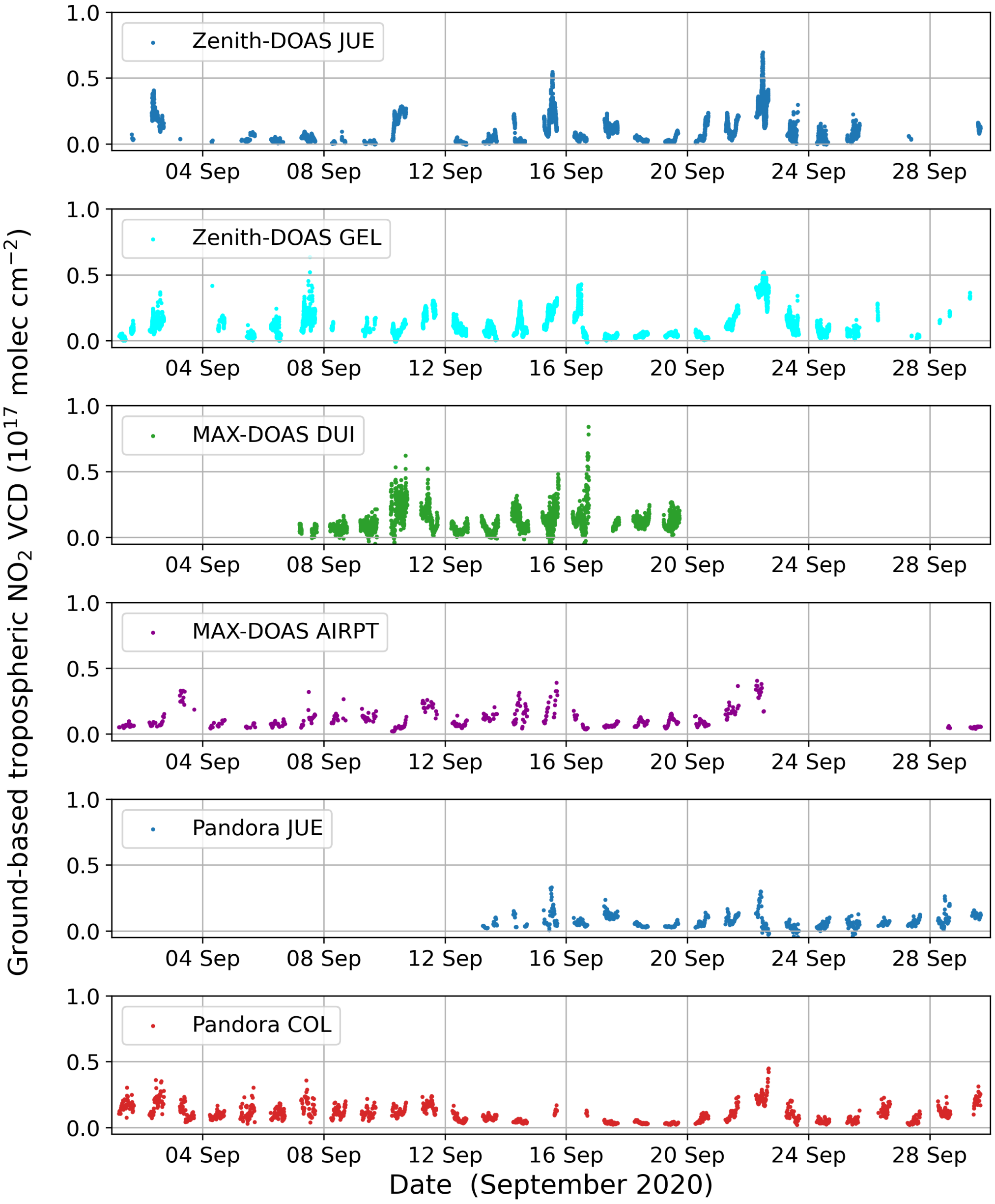

Figure 4.10: Plots of time series of tropospheric NO_2 VCD from the six stationary ground-based instruments for September 2020.

4.4 Evaluating airborne tropospheric VCD with stationary ground-based data

The data set of the stationary ground-based instruments is used to evaluate the AirMAP tropospheric NO_2 VCD. Together with the car DOAS measurements, they are the basis for using the AirMAP data to evaluate the TROPOMI tropospheric NO_2 VCD. AirMAP overflights were performed for all ground-based sites during the campaign. On the one hand, transfer flights between the airport and the target areas were used for overflights, and on the other hand, AirMAP overflew the stations during flights covering the respective flight area. A scatter plot of all coincident measurements is shown in Fig 4.11. Points are colored according to their ground-based instrument type and location. The ground-based stationary measurements are averaged in time intervals of 20 min around the AirMAP overpass time. The AirMAP tropospheric NO_2 VCDs are averaged measurements over a 500 m × 500 m area around the ground-based station and are then assigned to the selected ground-based stationary measurements. With this procedure, 25 coincident measurements were obtained during the 7 flight days. The error bars in Fig. 4.11 represent the error in the tropospheric NO_2 VCD estimation, averaged over the 500 m × 500 m grid boxes and

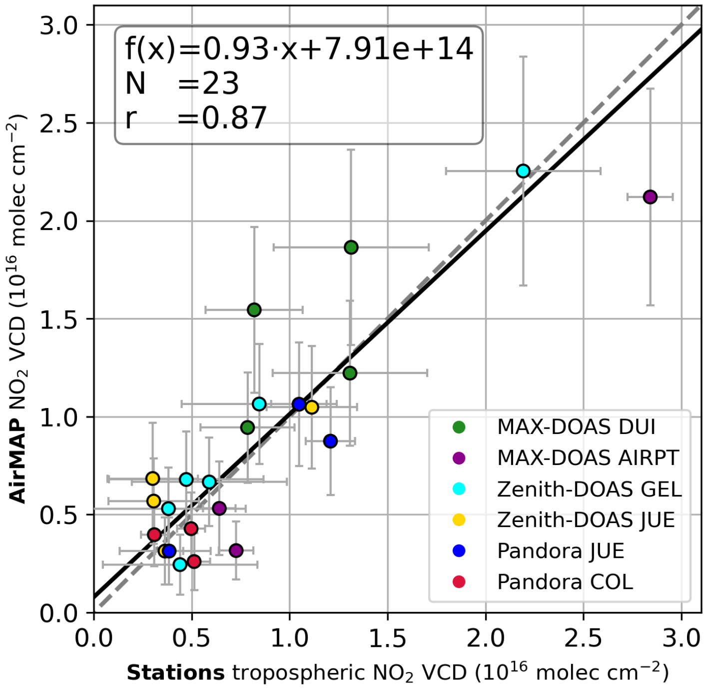

Figure 4.11: Scatter plot of AirMAP data and the stationary ground-based NO_2 VCDs averaged over a time interval of 20 min closest to the AirMAP overpass data, averaged over a 500 m × 500 m area around the ground-based station. Each point is colored according to its instrument type and location. Error bars represent the error in the tropospheric NO_2 VCD retrieval, averaged within the 500 m × 500 m grid boxes and 20 min time intervals. The dashed gray line indicates the 1:1 line. The solid black line represents the orthogonal distance regression.

the 20 min time intervals. The data were fitted with orthogonal distance regression, as for all the following data. The AirMAP and ground-based tropospheric NO_2 VCDs are highly correlated (Pearson correlation coefficient of r = 0.88) with a slope and standard deviation of 0.90 ± 0.09 and an offset of $1.16 \pm 0.15 \times 10^{15}$ molec cm^{-2}. Part of the deviation and scatter may be due to the instrument specific retrieval algorithms with different assumptions on radiative transfer, aerosols, and reference background spectra. Additionally, the spatiotemporal variability of NO_2 influences the agreement of the comparison. To illustrate the spatiotemporal variability, Fig. B.5 shows the same as Fig. 4.11, but bars extending from coincident measurement represent the spatial and temporal variability at the time of measurement with the 10th and 90th percentile of measured tropospheric NO_2 VCD within the 500 m × 500 m grid boxes and 20 min time intervals. Vertical bars illustrate the spatial variability in the 500 m × 500 m grid boxes seen by AirMAP. Horizontal error bars illustrate the temporal variability at the station site within the 20 min time interval of the AirMAP overpass.

4.5 Evaluating airborne tropospheric VCD with car DOAS data

During the AirMAP flights, car DOAS measurements were performed by the three instruments from BIRA, MPIC, and IUP. The car DOAS measurements were conducted during the entire flight time distributed over the flight area to gather many closely collocated measurements. Compared to the stationary measurements, the mobile measurements have the advantage of covering larger and more diverse areas with a broader range of NO_2 values. Since the car DOAS measurements are planned to overlap at several points with the aircraft tracks, there are more opportunities for nearly simultaneous measurements, and more collocated measurements can be gathered. For the comparison, the AirMAP and car DOAS measurements are gridded in 500 m × 500 m areas and are averaged in intervals of 15 min. Figure 4.12 shows scatter plots between measurements fulfilling a time criterion of ± 15 min and were taken in the same grid box. Using these criteria, 572 pairs of coincident measurements are considered for the comparison. In the left scatter plot, points are colored by the corresponding car DOAS instrument. In the right plot, the color coding indicates the absolute time difference between the AirMAP and DOAS measurements. Error bars extending from each coincident measurement illustrate the error from the tropospheric NO_2 VCD retrieval, averaged within the 500 m × 500 m grid box and 15 min interval. The comparison of the airborne and car DOAS tropospheric NO_2 VCDs reveals an offset of $-1.29 \pm 0.15 \times 10^{15}$ molec cm^{-2}. This offset could be adjusted to be closer to zero by increasing the estimated $VCD_{trop,ref}$ in the AirMAP retrieval by more than a factor of 2. However, the offset in the comparison of AirMAP and ground-based stationary data is with $1.16 \pm 0.15 \times 10^{15}$ molec cm^{-2} positive instead of negative. A larger

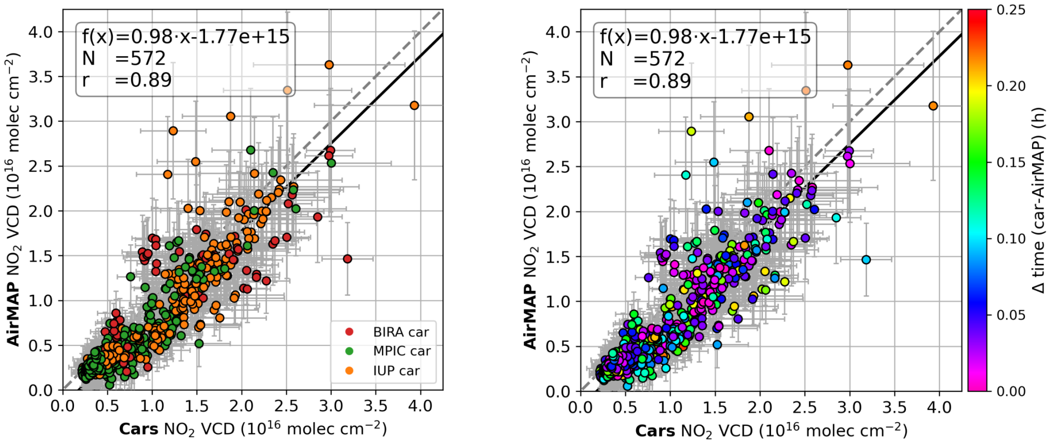

Figure 4.12: Scatter plots between collocated car DOAS (± 15 min window from the aircraft overpass) and AirMAP NO_2 VCDs using grid boxes of 500 m × 500 m and 15 min time intervals. The data points from BIRA, MPIC, and IUP car DOAS instruments are color coded in red, green, and orange (left). The color coding in the right plot shows the time difference between the AirMAP and car DOAS measurements. The dashed gray line indicates the 1:1 line. The thick solid black line represents the orthogonal distance regression. Error bars represent the error in the tropospheric NO_2 VCD retrieval, averaged within the 500 m × 500 m area and 15 min time intervals.

$VCD_{trop, ref}$ in the AirMAP retrieval would further increase this offset. Because of this, and a lack of justification for a large difference between the $VCD_{trop, ref}$ for the AirMAP and car data set, the $VCD_{trop, ref}$ is not adjusted. Nevertheless, it is clear that the validation of the offset in the satellite data has a large relative uncertainty as there may be offsets in the reference measurements. Besides that, the coincident airborne and car DOAS data show a good correlation ($r = 0.89$) with a slope of 0.89 ± 0.02 and an offset of -1.77×10^{15} molec cm^{-2}. Considering errors of the tropospheric NO_2 VCD retrieval and that the data from the different instruments were retrieved independently by the different groups, with only partly harmonized retrieval methods, using different assumptions about the radiative transfer, aerosols and reference background spectra, the data show good agreement. As visible from the right plot in Fig. 4.12, most of the measurements that are farther away from the 1:1 line are coincident measurements with time differences towards the outer edge of the ± 15 min filter criterion and thus may be caused by the fast natural NO_2 variability. To illustrate the spatiotemporal variability, Fig. B.6 shows the same as Fig. 4.12, but bars extending from coincident measurement are the 10th and 90th percentile of measured tropospheric NO_2 VCD within the 500 m × 500 m grid boxes and 15 min time intervals. Vertical bars illustrate the spatial variability in the 500 m × 500 m grid boxes seen by AirMAP. For car DOAS measurements spectra are averaged over 10 s respectively 30 s, depending on the driving speed (usually 30 km h^{-1} to 100 km h^{-1}), resulting in typical spatial resolutions of 80 m to 850 m. Thus, they can only partly give insights into the spatiotemporal variability.

4.6 Evaluating TROPOMI tropospheric VCD with AirMAP data

The evaluation of the AirMAP tropospheric NO_2 VCD with the ground-based stationary and car DOAS data provides a consistent basis for using the AirMAP data to assess TROPOMI tropospheric NO_2 VCDs. The airborne observations can map several TROPOMI pixels in a relatively short time. During the S5P-Val-DE-Ruhr campaign, aircraft flight times are 3 h, with AirMAP measurements over the designated research flight area planned to be taken at least ± 1 h around the S5P overpass with the smallest VZA. For the comparison of TROPOMI and AirMAP tropospheric NO_2 VCDs, TROPOMI pixels are only considered if they are at least 75 % mapped by AirMAP measurements. AirMAP data are considered when they were taken ± 30 min around the S5P overpass time. These spatial and temporal coincident criteria follow the suggestion by Judd et al. (2020). With these criteria, AirMAP data coincide with 117 TROPOMI pixels during the 7 flight days, for which, due to ground-segment anomalies, TROPOMI data are only available on six days. To evaluate the TROPOMI data, the AirMAP measurements are averaged within the coincident TROPOMI pixel. Figure 4.13 depicts the six daily TROPOMI PAL V02.03.01 and AirMAP tropospheric NO_2 VCDs maps over the designated flight area and the AirMAP measurements scaled to the coincident TROPOMI pixel.

The averaged AirMAP tropospheric NO_2 VCDs are compared to the coincident satellite data for the available TROPOMI NO_2 data versions. Scatter plots and the orthogonal distance regression analysis of the TROPOMI operational OFFL V01.03.02 tropospheric NO_2 VCDs, the adapted scientific TROPOMI V01.03.02 CAMS data using CAMS-based NO_2 profiles, and the reprocessed data product PAL V02.03.01 vs. the AirMAP tropospheric NO_2 VCDs are presented in Figure 4.14.

Vertical error bars represent the error estimate (precision) of the TROPOMI tropospheric NO_2 VCD resulting from the spectral fit and other retrieval aspects. The horizontal bars illustrate the spatial variability within the respective TROPOMI pixel by showing the 10th and 90th percentiles of the averaged AirMAP measurements. Error bars are shown to illustrate their magnitude and are not shown for any further plots for better visibility of the data.

Analyzing the different behavior (statistics, scatter, bias) in comparing the various available TROPOMI NO_2 data versions with the AirMAP data, provides further understanding of the different a priori assumptions made in each retrieval. Figure 4.14a shows the comparison of the TROPOMI operational OFFL V01.03.02 and AirMAP tropospheric NO_2 VCDs, with a high correlation (r = 0.86), a slope of 0.38 ± 0.02, an offset of $2.54 \pm 0.15 \times 10^{15}$ molec cm^{-2} and a median percent difference of -9 % with an interquartile range of -28 % to +16 %. Figure B.7 shows box-and-whisker plots summarizing the bias and spread of the difference between the TROPOMI versions and AirMAP tropospheric NO_2 VCDs. The statistics from the comparisons between the different TROPOMI tropo-

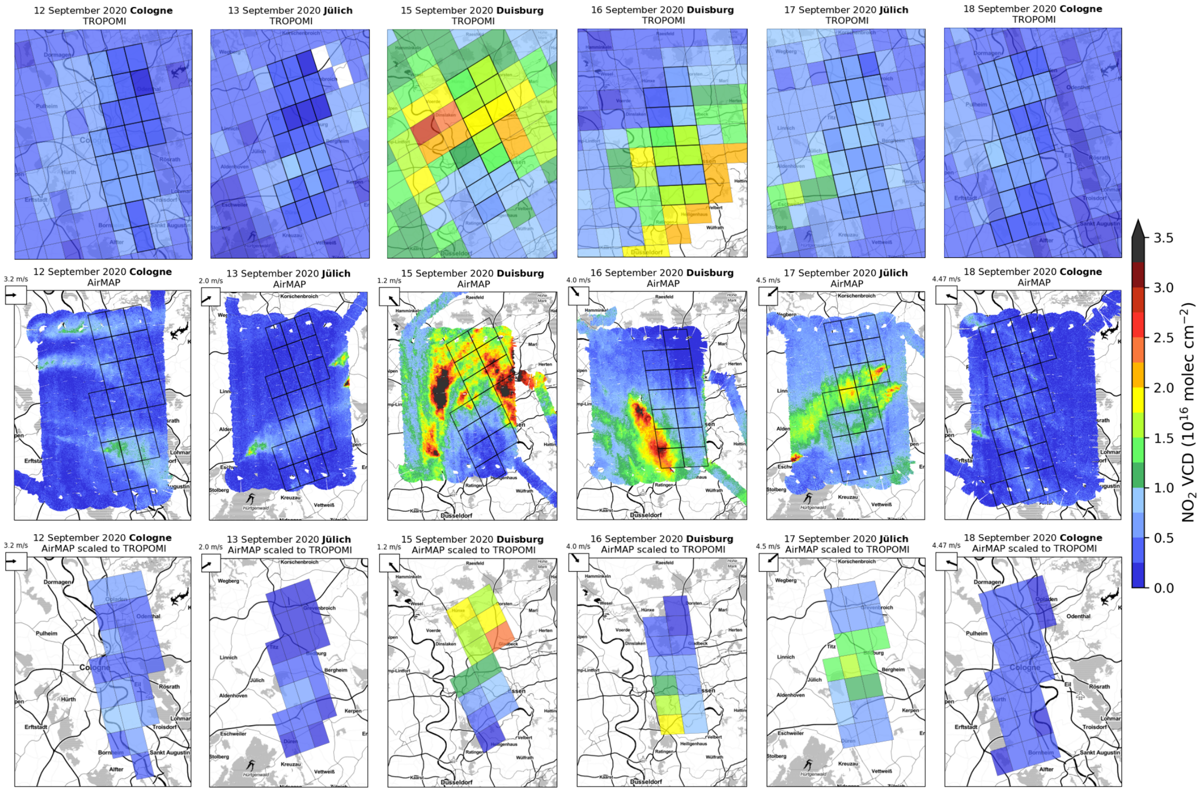

Figure 4.13: Daily maps of tropospheric NO_2 VCDs demonstrating how AirMAP data are matched to TROPOMI measurements. (top) TROPOMI PAL V02.03.01 tropospheric NO_2 VCDs where qa_value > 0.75. (middle) AirMAP tropospheric NO_2 VCDs with overlaid TROPOMI pixel outlines which fulfill the collocation criteria of a coverage of at least 75 % and AirMAP measurements ±30 min around the S5P overpass. (bottom) AirMAP tropospheric NO_2 VCDs scaled to the TROPOMI pixel.

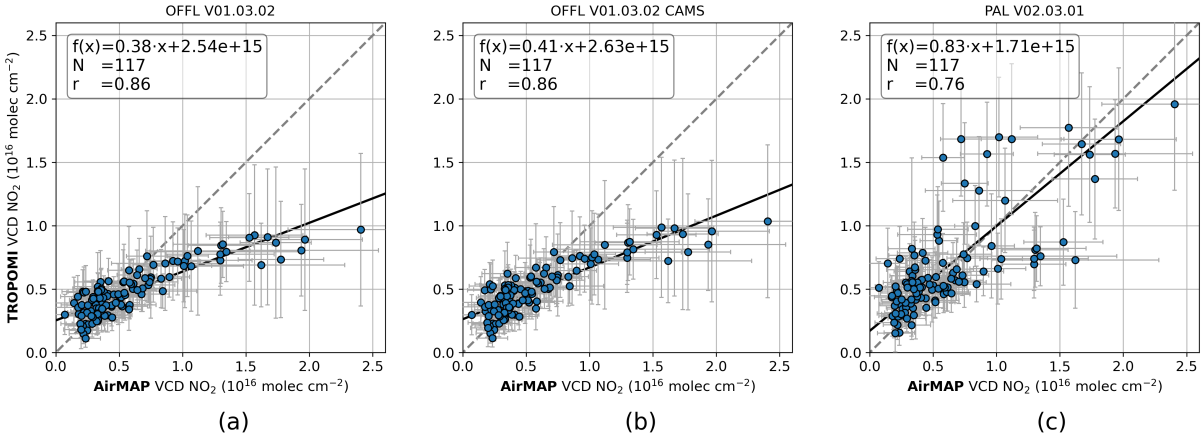

(a) (b) (c)

Figure 4.14: Scatter plots of TROPOMI NO_2 VCDs vs. coincident AirMAP NO_2 VCDs for different versions of TROPOMI data: (a) operational OFFL V01.03.02, (b) V01.03.02 based on the CAMS NO_2 profiles, (c) PAL V02.03.01. Coincident criteria for AirMAP: ±30 min around S5P overpass, gridded to TROPOMI pixels covered by at least 75 %. Vertical error bars show the reported precision of the TROPOMI tropospheric NO_2 VCD. The horizontal bars represent the 10th and 90th percentiles of the AirMAP measurements within the TROPOMI pixel.

spheric NO_2 VCDs data versions and the AirMAP data set are summarized in Table B.1 in the Appendix. All orthogonal distance regression statistics and their standard errors are calculated for the plotted data points. Accounting for the uncertainties of the data points and considering the parameters of the orthogonal distance regression over the full range of these uncertainties results in a standard deviation for the slope of $\pm\,0.14$ and $\pm\,0.39 \times 10^{15}\,\mathrm{molec\,cm^{-2}}$ for the offset. The regression slope of 0.38 determined here is significantly lower than the 0.68 reported from TROPOMI V01.03.02 and aircraft comparisons conducted during the 2018 campaign in the New York City/Long Island Sound region by Judd et al. (2020), and the 0.82 from comparisons of TROPOMI V01.03.02 and airborne APEX measurements over Belgium reported by Tack et al. (2021).

The scientific TROPOMI data version based on the OFFL data V01.03.02 but with the spatially higher resolved $0.1° \times 0.1°$ CAMS profiles replacing the $1° \times 1°$ TM5 NO_2 profiles has the purpose of investigating the influence of the NO_2 profile resolution on the TROPOMI NO_2 retrieval. Figure 4.14b shows the comparison of this TROPOMI data version with the AirMAP data. The two data sets have a correlation coefficient of 0.86, unchanged from the original data version, and a slope of 0.41 ± 0.02. The median relative difference increases from -9 % to -5 %. The slope increased only slightly compared to the original data version, illustrating that replacing the coarse NO_2 profile with the higher resolved profile has only a small impact on this data set.

Douros et al. (2023) showed that replacing the a priori profile in the NO_2 retrieval increases the dynamical range of the tropospheric NO_2 VCDs with the largest impact in emission hotspots by $5-30\,\%$ strongly dependent on location and time. For the TROPOMI and airborne comparisons over Belgium by Tack et al. (2021), the slope increased from 0.82 to 0.93 using the TROPOMI V01.03.02 CAMS product instead of the original V01.03.02. Thus, the relative difference in slope between the original V01.03.02 and the V01.03.02 CAMS data product to airborne data is similar, with 13 % reported in Tack et al. (2021) and 8 % found in this comparison.

After several validation activities for the TROPOMI tropospheric NO_2 VCDs data V01.02–01.03 indicated a negative bias for these products, updates in the TROPOMI NO_2 retrieval led to the development of V02.03.01 (see Sect. 4.3.1.3). Due to a complete mission reprocessing, the new data product is also available for the campaign period and is compared to the AirMAP data set in Fig. 4.14c. The comparison shows much more scatter than for the OFFL V01.03.02 product, resulting in a significantly poorer correlation coefficient, decreasing from 0.86 to 0.76. The modifications in the NO_2 retrieval also have a large impact with respect to the slope, which increases by more than a factor of 2 from 0.38 ± 0.02 to 0.83 ± 0.06. Because of the large scatter and the large number of measurements with tropospheric NO_2 VCDs of less than $7 \times 10^{15}\,\mathrm{molec\,cm^{-2}}$, the PAL V02.03.01 product has a positive median relative difference of +20 % with an interquartile range of -14 % to +66 % (see Fig. B.7).

As described in Sect. 4.3.1.3, the main change from V01.03 to V02.03.01 is the switch to the FRESCO-wide product, yielding more realistic higher cloud heights for measurements with cloud fractions greater than zero. Higher cloud heights result in lower tropospheric AMFs and thus higher tropospheric NO_2 VCDs. Since only 1 of the 117 analyzed TROPOMI pixels has a cloud fraction of zero, this update could largely affect the data set. As shown in Fig. 4.14c, many of the 117 data points have increased TROPOMI NO_2 VCDs compared to the old V01.03.02 product, are closer or even over the 1:1 line and thus increasing the slope and the median relative difference. However, a branch of data points with low TROPOMI NO_2 but large AirMAP NO_2 VCDs is not significantly affected by the modified retrieval and still matches the pattern of the old V01.03.02 comparison, shown in Fig. 4.14a. This lower branch is dominated by observations from 17 September, for which the retrieved cloud pressures remain close to the surface even with the used FRESCO-wide product. Figure 4.15 shows daily scatter plots of the 6 measurement days of the TROPOMI OFFL V01.03.02 and PAL V02.03.01 vs. the collocated AirMAP tropospheric NO_2 VCDs measurements. The data points are color coded regarding the surface and cloud pressure difference.

In general, the comparison on the basis of single days shows different magnitudes of the described impact from the TROPOMI NO_2 retrieval change. In the OFFL V01.03.02 product, 110 out of 117 pixels show cloud heights within 50 hPa to the surface. In the new PAL V02.03.01 product, only 28 of the 117 pixels still show cloud heights close to the surface. Except for the 17 September, this results in higher slopes of the individual days' regression line, which is also visible in the overall comparison. Since the observations are affected by the modifications to a varying degree, it results in more scatter.

Previous studies have shown that for scenes with clouds close to the surface, the FRESCO implementation determined an altitude even closer to the surface. Since the cloud algorithm does not distinguish between clouds and aerosols, this is also true for low aerosol layers. In many cases, FRESCO then determines the surface height as cloud height, which is incorrect (Compernolle et al., 2021; van Geffen et al., 2022b). Images from the Visible Infrared Imaging Radiometer Suite (VIIRS) on board Suomi NPP having a time difference of about 3.5 min to the TROPOMI observations and observations during the AirMAP measurement flights, revealed nearly perfect cloud-free conditions over the target area on all measurement days. Therefore, the retrieved high cloud pressures are presumed to be caused by a larger aerosol load, identified as a cloud in the retrieval. This assumption is supported by the pre-operational TROPOMI AOT product (de Graaf, 2022). Figure B.8 depicts daily maps of the AOT product, showing a quite variable AOT over the region and between the days, without any apparent correlation with the TROPOMI NO_2 product. However, the largest AOT is detected on 17 September over the Jülich area covering the pixels for which the TROPOMI NO_2 retrieval shows much lower NO_2 amounts than retrieved by AirMAP, causing the lower branch in the scatter plot.

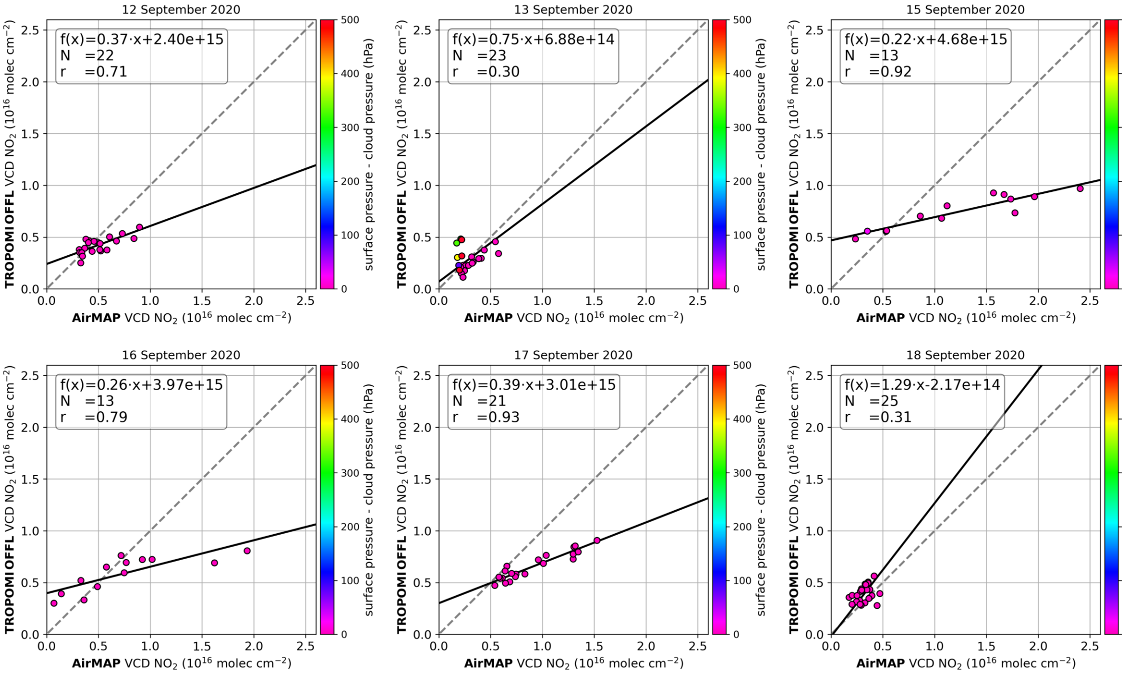

(a) TROPOMI OFFL V01.03.02 vs. AirMAP NO_2 VCD

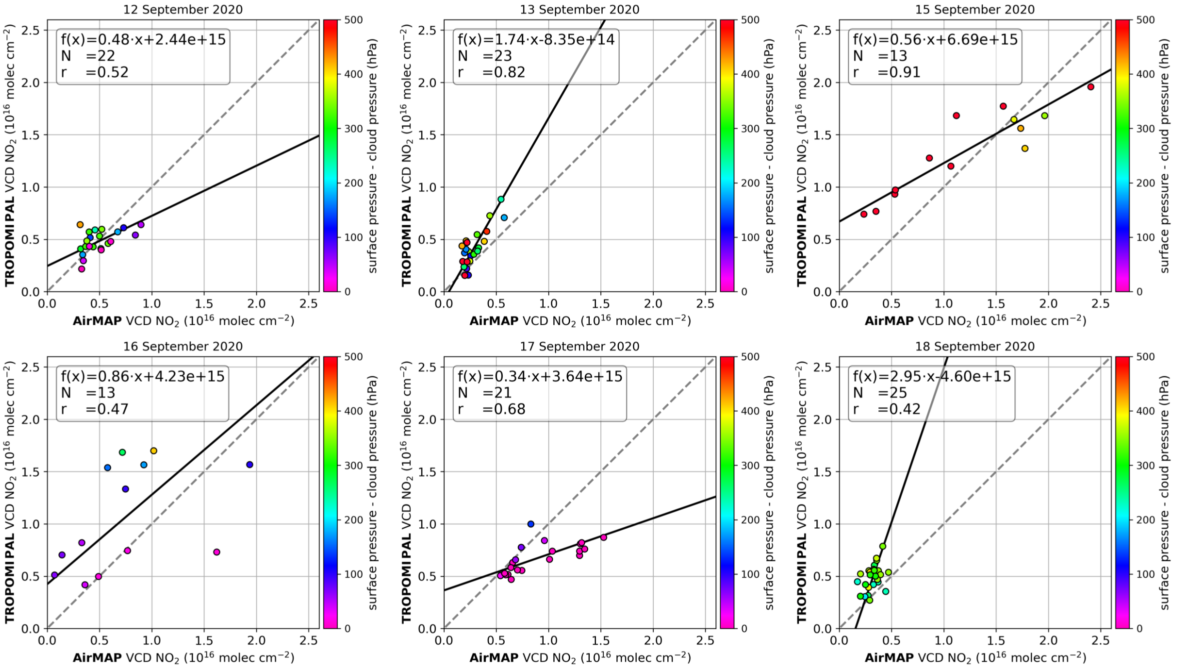

(b) TROPOMI PAL V02.03.01 vs. AirMAP NO_2 VCD

Figure 4.15: Daily scatter plots of TROPOMI OFFL V01.03.02 (a) and PAL V02.03.01 (b) tropospheric NO_2 VCDs vs. collocated AirMAP tropospheric NO_2 VCDs for the 6 measurement days. Points are color coded in the surface and cloud pressure difference. AirMAP measurements are considered co-located and gridded to the TROPOMI pixel if they are taken ± 30 min around the S5P overpass and cover at least 75 % of the TROPOMI pixel.

4.6.1 Cloud effects

The cloud radiance fraction retrieved from the TROPOMI NO_2 window is on average 0.21 ± 0.10 with a maximum of 0.48. As mentioned earlier, based on observations during the measurement flights, the VIIRS images, and the TROPOMI AOT product, these clouds detected by the cloud retrieval must be mainly aerosols. For nearly cloud-free observations, the cloud correction is more of an aerosol correction (Boersma et al., 2011). In the TROPOMI retrieval, tropospheric NO_2 VCDs are corrected for cloud and aerosol effects by the AMF accounting for cloud respectively aerosol contaminated observations with a combination of a clear-sky tropospheric AMF ($\mathrm{AMF}_{\mathrm{trop,\,clr}}$) and a cloudy tropospheric AMF (IPA, as described in Sect. 2.5.1). To evaluate the effect of the cloud correction on the TROPOMI tropospheric NO_2 VCDs, the VCDs are recalculated without the cloud correction by the following equation:

$$\mathrm{VCD}_{\mathrm{trop,\,no\;cc}} = \frac{\mathrm{VCD}_{\mathrm{trop}} \cdot \mathrm{AMF}_{\mathrm{trop}}}{\mathrm{AMF}_{\mathrm{trop,\,clr}}}. \tag{4.8}$$

A comparison of these VCDs without cloud correction with the AirMAP tropospheric NO_2 VCDs (see Fig. 4.16b) shows a high correlation of 0.85, a slope of 0.73 ± 0.04, and a median relative difference of +16 %. Compared to the original PAL V02.03.01 product (see Fig. 4.16a) the slope decreased from 0.83 ± 0.06 to 0.73 ± 0.04 but the correlation increased significantly from 0.76 to 0.85. The scatter plot with the PAL V02.03.01 product without cloud correction is not showing the discussed lower branch anymore, and the upper branch is also reduced. Consequently, the product has a much better correlation than the original product and shows that the cloud correction causes the two branches.

Compared to the original PAL V02.03.01 product (see Fig. 4.16a), the slope decreased from 0.83 ± 0.06 to 0.73 ± 0.04 but the correlation increased significantly from 0.76 to 0.85. The scatter plot with the PAL V02.03.01 product without cloud correction is not showing the discussed lower branch anymore, and the upper branch is also reduced. Consequently, the product has a much better correlation than the original product and shows that the cloud correction causes the two branches.

To further examine the impact of TROPOMI observations with cloud pressures close to the surface, the TROPOMI data are separated into observations where clouds, respectively aerosols, are retrieved near the surface and cases where they are not. Based on the reported uncertainty of the cloud pressure retrieval of 50 hPa (van Geffen et al., 2022a) and the study by Judd et al. (2020), observations with a surface and cloud pressure difference (ΔCS) of 50 hPa are separated. However, in contrast with Judd et al. (2020), observations with $\Delta\mathrm{CS} > 50$ hPa are kept, and pixels for which low clouds are retrieved are filtered out or replaced. For the 117 analyzed pixels of the 6 measurement days, the cloud retrieval of the PAL V02.03.01 product yields a cloud height within 50 hPa to the surface for

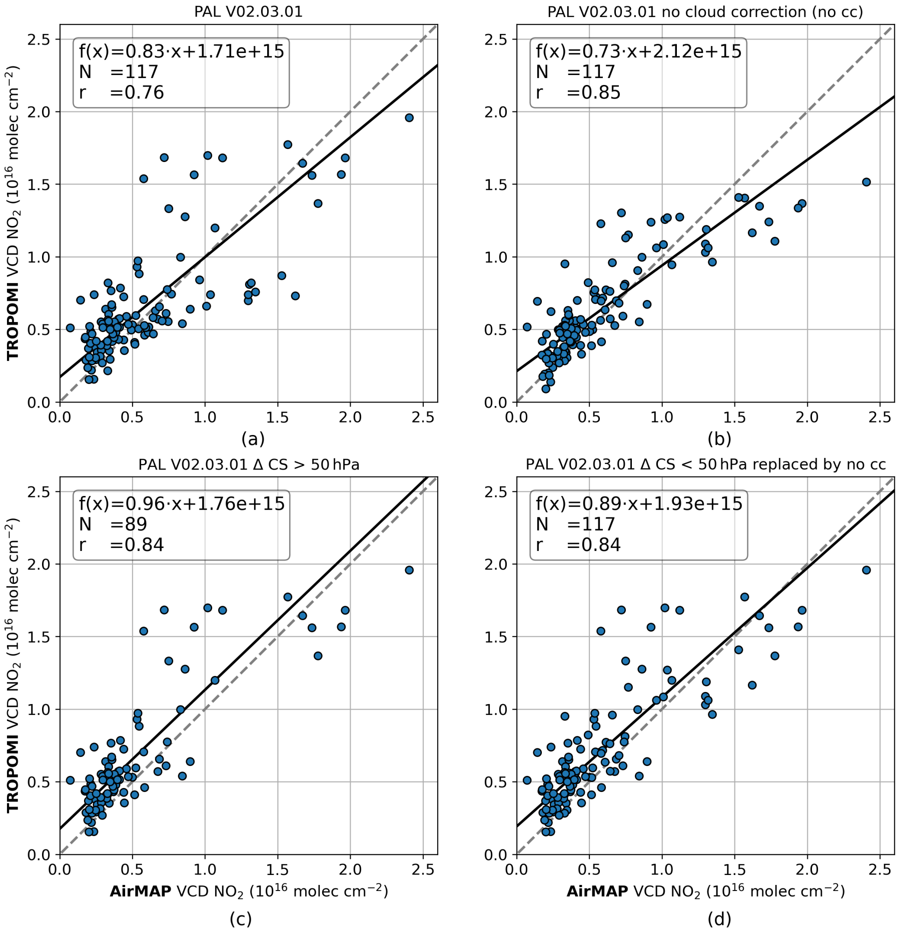

Figure 4.16: Scatter plots of TROPOMI NO_2 VCDs vs. co-located AirMAP NO_2 VCDs for different versions of TROPOMI data: (a) PAL V02.03.01, (b) PAL V02.03.01 without cloud correction, (c) PAL V02.03.01 only pixels with a surface and cloud pressure difference of $\Delta CS >$ 50 hPa, (d) PAL V02.03.01 pixels with $\Delta CS <$ 50 hPa are replaced by NO_2 VCDs without cloud correction.

28 pixels, 23 % of the observations. Thus, this filter reduces the coincidences between the TROPOMI PAL V02.03.01 and the AirMAP data set from 117 to 89. Before the modifications, 97 % of the 117 TROPOMI V01.03.02 product pixels show a cloud height within 50 hPa to the surface. For comparison, the study by Judd et al. (2020) analyzed TROPOMI NO_2 data of V01.02, based on the same cloud product as in V01.03.02, and found 53 % of the observations with cloud heights within 50 hPa to the surface, showing a strong dependence on on-site conditions. Figure 4.16c shows the coincidences of the TROPOMI PAL V02.03.01 and the AirMAP NO_2 VCDs for the 89 observations with surface and cloud pressure differences of $\Delta CS >$ 50 hPa. Compared to the unfiltered comparison, the slope and correlation increased from 0.83 ± 0.06 to 0.96 ± 0.06 and 0.76 to 0.84, respectively. The median relative difference increased from +20 % to +29 %. To maintain the number of coincidences, the filtered 28 observations are replaced with the VCDs without cloud correction. Figure 4.16d depicts the scatter plot showing a slope of

0.89 ± 0.05, a correlation of 0.84, and a median relative difference of +26 %.

Compared to earlier data versions, the new TROPOMI V02.03.01 product provides a more realistic estimate of the cloud pressure for a large part of the analyzed observations. Nevertheless, for certain scenes with a larger aerosol load, which are treated as clouds in the retrieval, the retrieved cloud pressure remains close to the surface pressure, which leads to large AMFs and thus low biased TROPOMI tropospheric NO_2 VCDs. In some cases, the results can be better if no cloud correction is applied. Whether the cloud correction improves the NO_2 retrieval in the presence of aerosols depends on the details of the vertical distributions of aerosols and NO_2. To investigate this further, additional information is needed on the vertical distributions of aerosols and NO_2 in the campaign area.

4.6.2 NO_2 profile shape and surface reflectivity effects

The influence of auxiliary data, such as the a priori NO_2 vertical profiles and the surface reflectivity, on the TROPOMI NO_2 retrieval, are investigated with a custom TROPOMI NO_2 product developed at IUP. The product is based on the PAL V02.03.01 NO_2 retrieval but has the advantage that auxiliary data can be modified, and thus their influence evaluated.

First, the custom IUP V02.03.01 tropospheric NO_2 VCD product is compared with the original PAL V02.03.01 product. Figure 4.17a shows a scatter plot of both products compared to the AirMAP data set. The correlation is 0.76 for both products. The slope of the IUP V02.03.01 is with 0.88 ± 0.06 slightly higher than for the original product with 0.83 ± 0.06, but is within the uncertainties. Since the agreement between the IUP V02.03.01 and the PAL V02.03.01 product is reasonably good, it can be assumed that the effects of changing the auxiliary data are similar for both products.

To evaluate the impact of higher resolved a priori NO_2 vertical profiles on the TROPOMI NO_2 retrieval, the $1° \times 1°$ TM5 model profiles are replaced by the $0.1° \times 0.1°$ regional CAMS-Europe analyses in the AMF calculation, as described in Sect. 4.3.1.4. The recalculated tropospheric NO_2 VCDs are compared to the AirMAP data in Fig. 4.17b. The use of the spatially more highly resolved CAMS-Europe NO_2 profiles increases the slope from 0.88 ± 0.06 (IUP V02.03.01) to 1.00 ± 0.07 (IUP V02.03.01 REG). The correlation remains nearly the same, with 0.75 compared to 0.76. With a relative slope difference of 14 %, the higher resolved a priori NO_2 vertical profiles show a slightly larger influence on the IUP V02.03.01 data set than for the OFFL V01.03.02 product, where a replacement of the TM5 with the CAMS-Europe profiles resulted in a relative slope difference of 8 %. The spatially more highly resolved profile information improves the profile shape, especially over source regions in the sense that more NO_2 is located close to the surface. This reduces the AMF and thus increases the tropospheric NO_2 VCD and compensates more for the

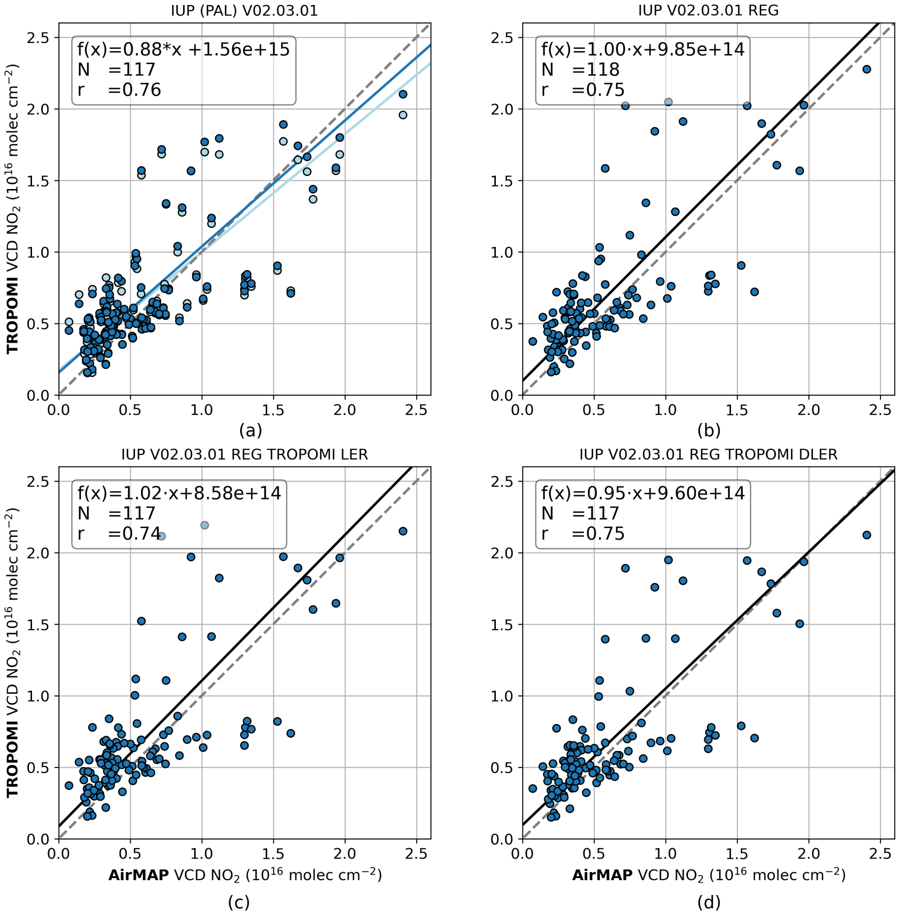

Figure 4.17: Scatter plots of TROPOMI NO_2 VCDs vs. co-located AirMAP NO_2 VCDs for different versions of TROPOMI data: (a) the IUP V02.03.01 in dark blue and the PAL V02.03.01 in light blue, regression information are given for IUP V02.03.01, (b) the IUP V02.03.01 with regional CAMS profiles replacing the TM5 profile information, (c) the IUP V02.03.01 with regional CAMS profiles and TROPOMI LER replacing the OMI LER, and (d) the IUP V02.03.01 with regional CAMS profiles and TROPOMI DLER.

reduced sensitivity of TROPOMI to NO_2 near the ground. This effect is expected to be larger for the more realistic higher cloud altitudes. In the case of the IUP V02.03.01 REG product, observations for which cloud heights are still close to the surface, represented by the lower branch of coincident data points, are less affected by replacing the NO_2 profile information. However, combined with the improved cloud pressures, the spatially higher resolved NO_2 profiles reveal their positive impact for most observations.

To investigate the influence of the surface reflectivity on the TROPOMI NO_2 retrieval, the originally used OMI LER database is replaced by the TROPOMI LER database. AMFs and tropospheric NO_2 VCDs are recalculated with the regional CAMS NO_2 profiles and the TROPOMI LER results, resulting in the IUP V02.03.01 REG LER product. Cloud parameters, based on the GOME-2 LER climatology, are not recalculated. Figure 4.17c shows a scatter plot of this IUP V02.03.01 REG LER product and the AirMAP tropospheric NO_2 VCDs. The change from the OMI LER to the TROPOMI LER database shows only a small effect on the analyzed data set. The slope increased only slightly from 1.00 ± 0.07 to 1.02 ± 0.07, and the correlation barely changed from 0.75 to 0.74. The median relative difference changed from +31 % to +24 %. Differences between the OMI LER and TROPOMI LER are found to be relatively small in the campaign region and season in the NO_2 fit window but can be larger in other regions or seasons, and a change can have a greater impact there.

In addition to the traditional LER database, a TROPOMI DLER database has been generated. Recalculating AMFs and the tropospheric NO_2 VCDs with the regional CAMS NO_2 profiles and the TROPOMI DLER result in the IUP V02.03.01 REG DLER product. The comparison of this product with the AirMAP data set (Fig. 4.17d) reveals a slope of 0.95 ± 0.07 and a median relative difference of +21 % and shows that the DLER climatology leads to lower TROPOMI NO_2 VCDs as compared to the products using the TROPOMI LER (Fig. 4.17c) or the OMI LER (Fig. 4.17b). The correlation of 0.75 hardly changed between the different versions. It can be concluded that the directional aspect of the surface reflectivity only plays a minor role in the NO_2 retrieval for the analyzed data set with nearly could-free conditions and from this specific campaign region and season. Results could differ for different areas, months, and cloud conditions. Larger differences are, for example, expected for snow-covered surfaces with high reflectivity. Figure B.9 shows three scatter plots comparing the TROPOMI NO_2 VCD retrieved with TROPOMI LER (IUP V02.03.01 REG LER) vs. the TROPOMI NO_2 DLER product for (a) the 117 TROPOMI pixels used throughout the study, (b) a larger orbit segment over western Europe, and (c) one complete orbit. All three data sets show only a minor influence from the directional component. However, since only observations from September are compared, no significant snow-covered areas are expected. A more detailed analysis covering different periods and areas would be needed to examine possible larger differences.

For a compact summarizing overview, all statistics of the comparisons between the various TROPOMI NO_2 data versions and the AirMAP measurements are summarized in Table B.1 and the box-whisker plots in Fig. B.7.

4.7 Conclusion

This study presented a validation of the TROPOMI tropospheric NO_2 VCD retrieval based on airborne imaging DOAS measurements obtained by the AirMAP instrument supported by ground-based stationary and car DOAS measurements. During the S5P-VAL-DE-Ruhr campaign in North Rhine-Westphalia from 12 to 18 September 2020, AirMAP covered 117 TROPOMI ground pixels on six measurement days.

The ground-based stationary DOAS measurements were performed by two Zenith-DOAS, two MAX-DOAS, and two Pandora instruments distributed over the flight area. They provide well-established, high-precision, and independent data for evaluating the AirMAP data set. The 25 coincident stationary ground-based and AirMAP measurements show highly correlated tropospheric NO_2 VCDs (r = 0.88) with a slope of 0.90 ± 0.09.

The car DOAS measurements were performed by three cars. These measurements have the advantage of being mobile, allowing them to cover larger and more diverse areas. They have a high temporal resolution and can be well coordinated with the AirMAP measurements in the respective flight area to gather many co-located measurements. The evaluation of the AirMAP data set considers 572 coincident measurements which are highly correlated (r = 0.89) with a slope of 0.89 ± 0.02.

Despite the pretty good spatial resolution of 3.5 km × 5.5 km of the TROPOMI measurements, the spatial NO_2 variability within a TROPOMI pixel can be large and cannot be fully captured by ground-based instruments. Since the AirMAP measurements, with their resolution of about 100 m × 30 m can map several TROPOMI pixels in a relatively short time, they are more representative of the TROPOMI measurements than point measurements, can quantify expected differences (representative errors), and can link the ground-based and TROPOMI measurements. The ground-based stationary and car DOAS data sets are used to assess the AirMAP data and give confidence for using the AirMAP data set to evaluate the TROPOMI tropospheric NO_2 VCDs.

TROPOMI observations are evaluated with AirMAP measurements if these are taken ± 30 min around the S5P overpass and cover at least 75 % of the TROPOMI pixel. Over the six measurement flights, this results in 117 TROPOMI pixels coinciding with AirMAP measurements. For these pixels, the cloud radiance fraction retrieved in the TROPOMI NO_2 spectral window was on average 0.21 ± 0.10 with a maximum of 0.48 and thus below the recommended filter criterion of 0.5. Due to these nearly cloud-free conditions, all 117 coinciding pixels are included in the analysis.

The TROPOMI tropospheric NO_2 VCD data are evaluated for the operational OFFL V01.03.02 product, the reprocessed PAL V02.03.01 product, and several scientific data products to investigate the influence of different cloud retrievals, a priori NO_2 profile, and surface reflectivity information. The various TROPOMI and AirMAP data sets are correlated with correlation coefficients between 0.74 and 0.86, with slopes of 0.38 ± 0.02 to 1.02 ± 0.07, and relative mean differences between -9 % and 31 %. The operational OFFL V01.03.02 and the scientific V01.03.02 CAMS product show a significant underestimation of the TROPOMI data compared to the AirMAP tropospheric NO_2 VCDs, with slopes of 0.38 ± 0.02 and 0.41 ± 0.02, and median relative differences of -9 % and -5 %, respectively. However, both products show with 0.86 the highest correlation among all analyzed TROPOMI product versions.

Modifications in the cloud pressure retrieval implemented in the TROPOMI PAL V02.03.01 product lead to more realistic higher cloud altitudes and thus lower tropospheric AMFs and higher tropospheric NO_2 VCDs for most of the analyzed observations compared to the

OFFL V01.03.02 product. While this improves the slope from 0.38 ± 0.02 to 0.83 ± 0.06, it significantly increases the scatter (r = 0.76). Due to the large scatter and the large number of observations with tropospheric NO_2 VCDs of less than about 7×10^{15} molec cm^{-2}, the product has a mean relative difference of +20 % with an interquartile range of -14 % to +66 %. Most of the 117 analyzed TROPOMI pixels are affected by the modifications and are thus closer or even over the 1 : 1 line, increasing the slope and the median relative difference. However, even after the modifications, 28 pixels remain with cloud pressures close to the surface and thus low TROPOMI NO_2 VCDs and large AirMAP NO_2 VCDs. This different level of impact separates the data set into two branches, one branch of low-biased TROPOMI observations close to the distribution seen in OFFL V01.03.02 and one around the 1 : 1 line, and causes the significantly decreased correlation. This lower branch of data points for which cloud pressures are still close to the surface are dominated by observations from a single day. Based on observations during the measurement flights and VIIRS images, it is suspected that the retrieved cloud fractions and high cloud pressures are caused by a larger aerosol load identified as a cloud in the retrieval. This is supported by the TROPOMI AOT product, which shows a high AOT for the pixels causing the lower branch.

If NO_2 VCDs are determined without cloud correction, the slope decreases from 0.86 ± 0.06 (PAL V02.03.01 with cloud correction) to 0.73 ± 0.04, while the correlation significantly improves from 0.76 to 0.84. This illustrates that the separation into two branches is caused by the cloud correction. Filtering observations with cloud pressures within 50 hPa to the surface or replacing these observations with NO_2 VCDs without cloud correction can increase the slope and the correlation significantly compared to the original PAL V02.03.01 product. It can be concluded that the PAL V02.03.01 product provides a more realistic estimate of the cloud pressure for a large part of the observations compared to earlier versions. However, for some cases with a larger aerosol load, cloud pressures remain high, leading to low biased tropospheric NO_2 VCDs and a larger scatter, which can be improved if no cloud correction is applied.

The modification of the scientific TROPOMI NO_2 product based on the PAL V02.03.01 retrieval with the CAMS-Europe a priori NO_2 profiles replacing the TM5 analyses increased the slope from 0.88 ± 0.06 to 1.00 ± 0.07 with consistent correlation. This improvement in slope is slightly bigger than observed for replacing the TM5 NO_2 profile information in the OFFL V01.03.02 product. The replacement of the OMI LER data used in the NO_2 fit window with the TROPOMI LER or DLER data shows only a small influence on the analyzed TROPOMI data set. However, impacts can differ for other regions, cloud conditions, and seasons, especially over snow-covered scenes. A larger impact is expected when the TROPOMI DLER is also applied in the NIR-FRESCO cloud retrieval, as done in V02.04, operational since 17 July 2022 but not yet reprocessed for the campaign period in September 2020.

Future validation activities in other regions with different pollution levels, surface reflectances, and aerosol and cloud conditions would help to further evaluate the performance of the TROPOMI NO_2 retrieval and confirm the results found in this study. When a reprocessed data set of the new V02.04 NO_2 retrieval becomes available, comparisons with the campaign data set can be used to investigate the impact of the consistent implementation of the TROPOMI DLER climatology. The presented validation strategy can be applied to upcoming validation activities for satellite missions such as GEMS, TEMPO, Sentinel-4, and Sentinel-5.

5 | Investigation of spatiotemporal variability of NO_2 with tram DOAS observations

5.1 Introduction

A good possibility to determine spatial distributions of NO_2 or other trace gases are mobile DOAS measurements. Most commonly, mobile DOAS measurements are performed from aircraft or cars on a campaign basis. These measurements can fill the gap between ground-based and satellite measurements.

Ground-based DOAS measurements are typically performed continuously and at fixed locations. MAX-DOAS systems performing measurements in several azimuthal directions can provide some information about the spatiotemporal variability of NO_2 (e.g., Schreier et al., 2020; Dimitropoulou et al., 2022). Due to measurement sensitivity, usually, several systems are needed to investigate the spatial distribution within a city. Schreier et al. (2020) analyzed measurements of two MAX-DOAS instruments in Vienna and found the highest amounts of NO_2 when the MAX-DOAS instruments were pointing toward the city center and/or busy roads and industrial areas.

Satellite measurements have the advantage of daily global coverage. However, despite the increased spatial resolution of satellite sensors, it is difficult to resolve NO_2 distributions within a city. Even with TROPOMI's high spatial resolution of 3.5 km × 5.5 km at nadir, cities with highly variable NO_x emissions are covered by only a few TROPOMI ground pixels. Bremen, for example, is covered by around nine TROPOMI ground pixels.

Airborne measurements perform higher resolved measurements and can deliver more detailed images of the spatial NO_2 distribution under the flight track. Airborne imaging DOAS measurements as performed by AirMAP with a resolution of around 30 m × 90 m can map several satellite pixels and thus also an entire city in a relatively short time of around 3 h (see Chapter 4). Flights with the AirMAP instrument over Bucharest revealed distinct horizontal distribution patterns and strong spatial NO_2 gradients across the city with background values in the outskirts located upwind and a polluted city center (Meier et al., 2017). The disadvantage of airborne measurements is the usually limited availability of only short-term measurement campaigns for specific campaign regions. Due to the lack of regularity in the measurements, it is difficult to investigate, for example, meteorological and seasonal influences on the NO_2 distribution.

In recent years, especially since high-quality and low-cost compact spectrometers have become available, several ground-based mobile DOAS measurements have been performed from cars. Car DOAS measurements have been used in various applications. By encircling cities or other sources, car DOAS measurements are used to estimate emissions (Ibrahim et al., 2010; Shaiganfar et al., 2011). They are an additional opportunity for validating satellite data (Wagner et al., 2010; Constantin et al., 2013; Wu et al., 2013). Variability within satellite pixels can be mapped, and representative errors for satellite and stationary ground-based comparisons can be quantified. Compared to airborne observations that can perform these measurements more efficiently, car DOAS measurements are relatively low-cost and more flexible in the organization. As presented in Chapter 4, car DOAS measurements are also used to validate airborne measurements. In general, the car as a measurement platform offers a good way to determine the spatial distribution of tropospheric trace gases such as NO_2 in a larger area in a relatively short period (e.g., Schreier et al., 2019). However, one large disadvantage is the time required to drive the car, so these measurements cannot be performed regularly.

Therefore, a new DOAS instrument was developed and installed on a tram in Bremen in November 2021. Bremen has the distinction of a continuous above-ground tram network and is, therefore, particularly well suited for this kind of measurements. The advantage of the tram DOAS instrument is that it performs measurements during the regular operation of the tram. As a result, measurements along the route network are performed without additional time spent driving and can be used to estimate the spatial distribution of NO_2 in Bremen and for comparison with satellite measurements.

In the following, the construction (Sect. 5.2) and characterization (Sect. 5.2.1) of the new tram DOAS instrument are presented. One year of data is investigated with respect to spatiotemporal variability of NO_2 in Bremen and compared with corresponding TROPOMI data (Sect. 5.3).

5.2 Construction of a DOAS instrument for the tram

First, the tram DOAS instrument had to be developed and built to be integrated on a tram. The Bremer Straßenbahn AG (BSAG, `https://www.bsag.de/`) made the instrument installation on one of their trams possible. For an operation on a tram, the instrument has to fulfill several requirements that have to be considered in the construction process: Compact in size, resistant to weather conditions, suitable for unattended long-term measurements, data transfer and maintenance via LTE, GPS for location determination, fulfillment of the safety requirements of the BSAG, resistance against vibrations and shocks during the tram operation, powered by the 24 V DC voltage of the tram and insensitivity to power failures. The MAX-DOAS and car DOAS instruments already successfully used at IUP for several years served as a starting point for developing the tram DOAS instrument.

All parts are encased in a stainless steel control housing, which is waterproof and fulfills the safety requirements of the BSAG. Figure 5.1 shows the CAD drawings made for planning and acceptance by BSAG. An overview of the internal structure of the finalized instrument is shown in Fig. 5.2a; the installation on the tram is shown in Fig. 5.2b.

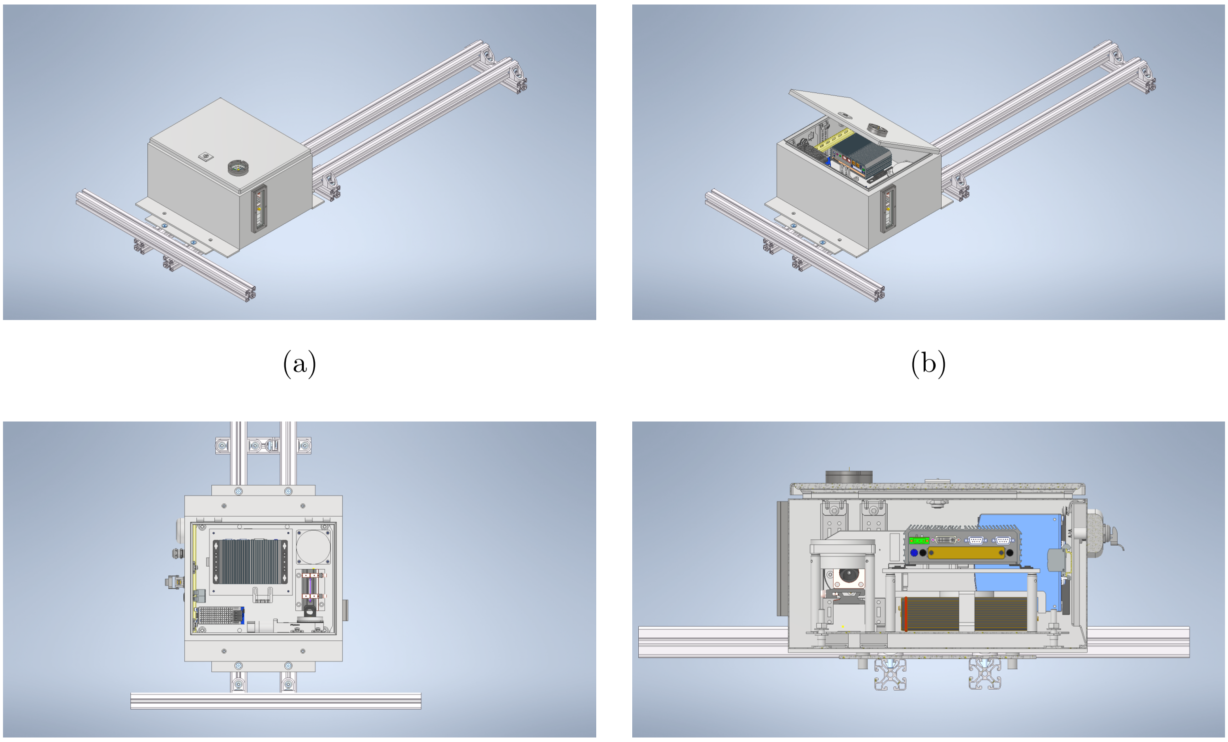

(a) (b)

(c) (d)

Figure 5.1: CAD drawing of the tram DOAS setup seen from (a) the top right, (b) the top right with an open lid, (c) the top, and (d) a cut seen from the side.

The instrument's total weight is 17.8 kg and its dimensions are 28 cm in height, 38 cm in length, and 40 cm in width. It's only connections to the outside are the power supply connected to the tram and its GPS and LTE antennas mounted on the housing. To compensate for possible voltage fluctuations in the tram power supply, the instrument's power supply is realized via a DC/DC converter. The instrument has an exterior switch that allows the entire system to be easily restarted without opening it. To reduce vibrations and shocks during tram operation, the instrument housing is mounted on rubber feet. The installation of the instrument on the tram is realized with profile bars that can be attached to already existing profile bars so that no major constructional changes to the tram are necessary. To keep the window for horizon measurements as clean as possible,

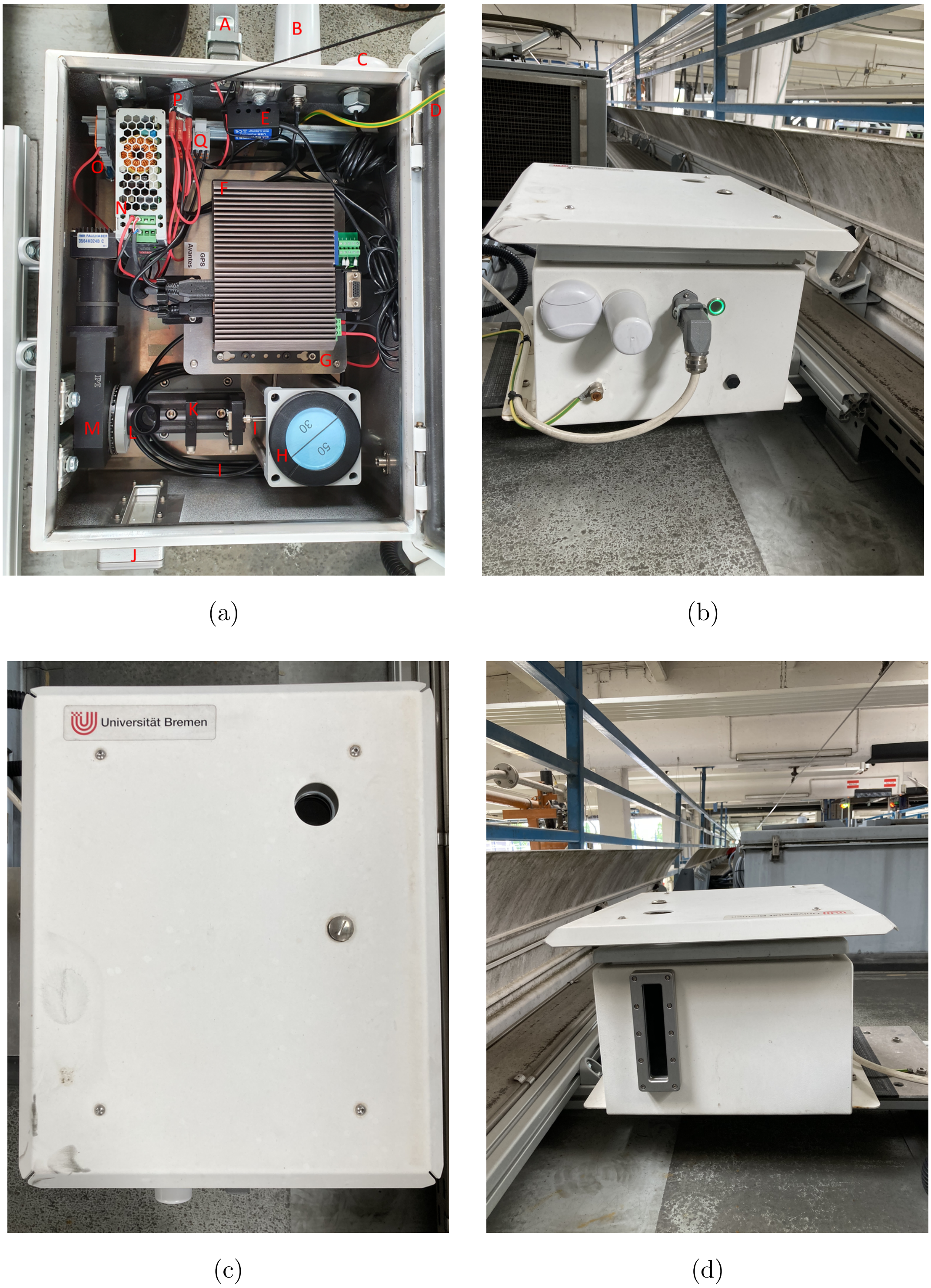

(a)
(b)

(c)
(d)

Figure 5.2: (a) Interior view of the tram DOAS with (A) power connection, (B) LTE antenna, (C) GPS antenna, (D) grounding, (E) temperature and humidity sensor, (F) computer, (G) spectrometer under the table, (H) desiccant, (I) light fiber bundle, (J) side window, (K) lens, (L) 45° mirror, (M) rotating table, (N) DC/DC-Converter, (O) fuse, (P) switch, (Q) distribution blocks. Tram DOAS installed on the tram 3117 of BSAG; (b) side view with GPS antenna, LTE antenna, power connection, switch, and pressure equalization valve, (c) top view with zenith window, (d) side view with off-axis window.

the instrument is mounted with the window opposite the direction of travel and several meters in front of the current collectors. To prevent excessive heating of the instrument, the instrument housing is painted white and equipped with a separate roof working as a sun shield, which also serves as additional rain protection (not included in Fig. 5.1 but visible in Fig. 5.2b). Active cooling was omitted to keep the device as compact and simple as possible, even if this means a loss of data quality in summer. A pressure equalization valve was installed to compensate for pressure fluctuations due to temperature differences that can cause moisture to be drawn through the sealing into the housing. For removing still incoming air moisture, desiccant is added in the instrument housing. Temperature and humidity are monitored by a sensor inside the housing.

The instrument housing has two fused silica windows through which measurements can be made in horizon and zenith directions. The choice of measurement directions is enabled by a 45° mirror mounted on a rotating table at a reflection angle of 90°. This setup allows measuring under the same mirror geometry and thus the same mirror characteristics for all viewing directions so that possible optical effects of the mirror are canceled out in the DOAS analysis by taking the ratio of I and I_0 (see Sect. 2.4.2). The light is focused through a converging lens, limiting the field of view (FOV) (see Sect. 5.2.1), into a quartz light fiber bundle, which effectively depolarizes the light and enables a high light throughput into the spectrometer. The spectrometer is a commercial compact Avantes spectrometer, AvaSpec-ULS2048x64. The AvaSpec-ULS2048x64 spectrometer is small in size ($175 \times 110 \times 44\,\mathrm{mm}$), robust, and lightweight ($855\,\mathrm{g}$). It performs measurements between $290\,\mathrm{nm}$ and $550\,\mathrm{nm}$ at a spectral resolution of approximately $0.66\,\mathrm{nm}$. The measurements are operated by the IUP Bremen measurement program AMAX_OMA on a passively cooled industrial computer (Cincooze DA-1100-N22-R10). In addition, the computer is connected with the sensor for monitoring the temperature and humidity in the instrument housing, the rotating table, and the antennas for GPS and LTE. The LTE connection enables daily data transfer and remote maintenance of the measurement computer.

After delays due to COVID-19 pandemic measures, the tram DOAS instrument was completed in November 2020. First, the instrument was characterized (Sect. 5.2.1). Due to COVID-19 access regulations at BSAG, the installation on the tram was delayed to November 2021. In the meantime, several months of measurements were performed on the roof of the IUP Bremen close to the operationally operated MAX-DOAS instruments, which were useful for some comparisons.

5.2.1 Characterization

An important parameter of the instrument is its FOV. The FOV is mainly determined by the size of the optical fiber bundle entrance and the focal length of the lens. The used lens is a plano-convex lens with a diameter of 17 mm and a focal length f of 40 mm. The fiber bundle consists of 14 fibers arranged in a slit configuration with a height of 1.26 mm on the spectrometer side and in a bundle with a diameter d_f of 0.4 mm on the other side. Figure 5.3 illustrates the optical path of the lens-fiber setup in the tram DOAS instrument. It follows that the half FOV θ is determined by:

$$\theta = \arctan\left(\frac{d_\mathrm{f}}{2f}\right) \tag{5.1}$$

which results for the tram DOAS instrument with $d_\mathrm{f} = 0.4\,\mathrm{mm}$ and $f = 40\,\mathrm{mm}$ in a theoretically possible FOV of 0.57°. Since the 14 fibers of the fiber bundle form a slit with a height of 1.26 mm but the spectrometer slit height is only 1 mm, only light of 11 fibers can enter the spectrometer, this may reduce the relevant fiber bundle diameter and thus also the actual FOV.

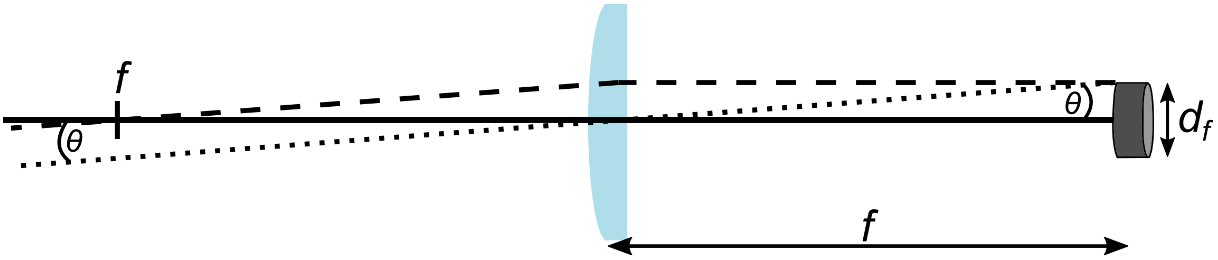

Figure 5.3: Sketch of parameters determining the FOV (2θ) of the instrument. The diameter d_f of the optical fiber bundle and the focal length f of the lens.

The FOV can also be experimentally determined using horizon scan measurements of the instrument. These scans were made during the test measurement period on the roof of the IUP. The instrument mirror scanned stepwise in 0.1° steps from -2° to +2° over the assumed horizon. Figure 5.4a shows the measured intensity as a function of the elevation angle. With the fitted derivative of the intensity shown in Fig. 5.4b the full width at half maximum (FWHM) is determined as 0.38°. This is in reasonable agreement with the theoretical value of 0.57° and indicates an accurate adjustment since the FOV increases when the optical fiber is not in the lens's focal length.

Figure 5.5 shows the temperature and humidity development from mid of March 2022 after a maintenance visit at BSAG, where the instrument was opened and the desiccant exchanged, to the end of July 2022. After the opening of the instrument housing, the humidity increases slightly but remains then relatively constant. The temperature inside the instrument housing fluctuates mainly between 20 °C and 40 °C but can reach up to 50 °C.

Figure 5.6 shows a time series of the root mean square of the residual spectrum, which is a measure of the fit quality (see Sect. 2.4.2). It shows a quite stable behavior with a

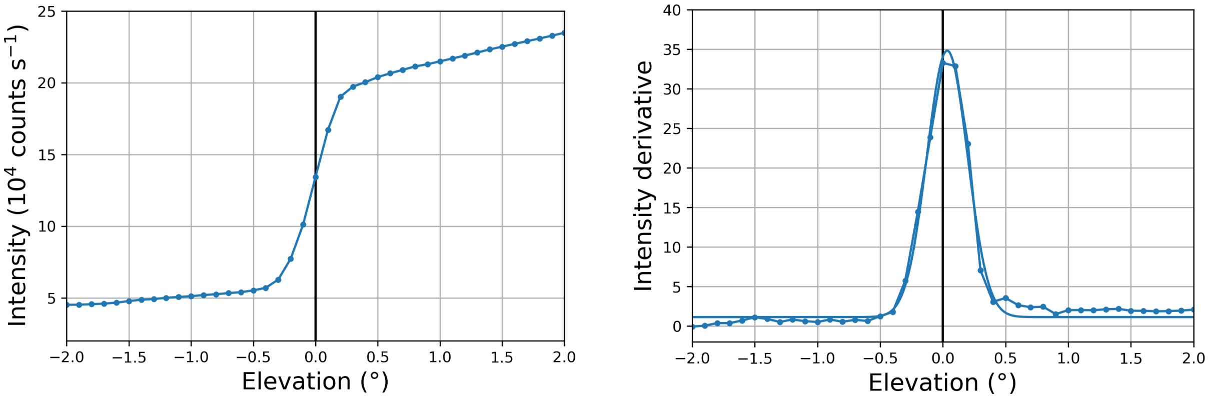

(a) (b)

Figure 5.4: (a) the intensity and its derivative (b) as a function of the pointing elevation resulting from a horizon scan measurement from the roof at IUP Bremen on 14 October 2021 used for the FOV determination.

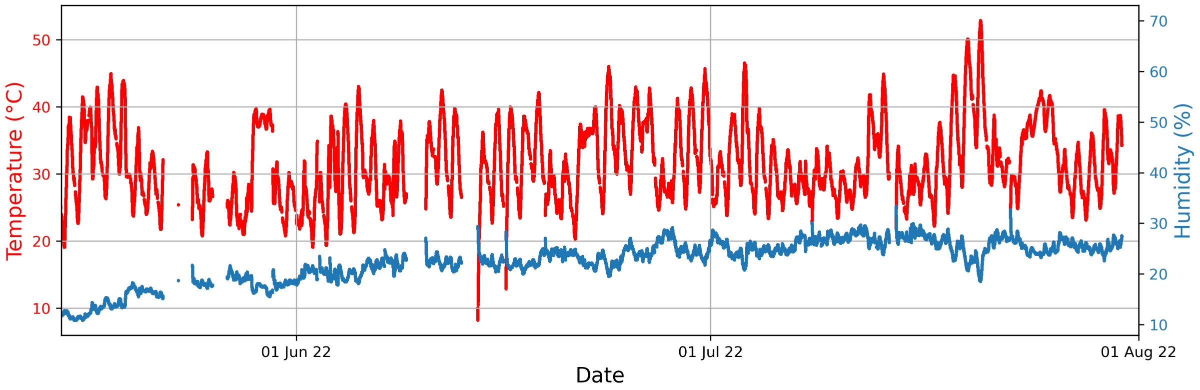

Figure 5.5: Temperature (red) and humidity (blue) from mid-March 2022 to end of July 2022 in the tram DOAS housing.

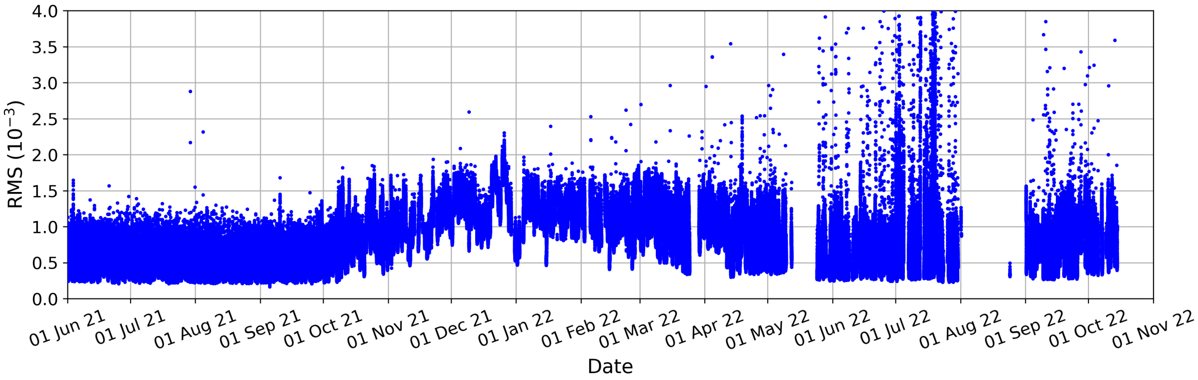

Figure 5.6: Root mean square of the residual spectrum from 1 June 2021 to 1 November 2022 including tram DOAS measurements on the roof at IUP (1 June 2021–10 November 2021) and the complete measurement period on the tram (11 November 2021–15 October 2022). Data are unfiltered, gaps in the time series are caused by actual gaps in the measurements.

minimum around 0.25×10^{-3} which is only increasing during the winter months and return back to the minimum around 0.25×10^{-3}. Most RMS values are below 1.5×10^{-3}. Large RMS values can be assigned to cloudy measurement conditions, measurements where the zenith viewing direction is obstructed by tunnels, bridges or other objects, and especially high temperatures during summer.

The instrument's spectral resolution, as determined by the FWHM of the slit function based on an HgCd line lamp measurement, is approximately 0.66 nm at 346.62 nm and 0.87 nm at 546.07 nm.

5.3 Tram DOAS measurements

With the two windows, the instrument can perform measurements in zenith and horizon directions. This allows using the instrument also as a stationary MAX-DOAS instrument. The tram's movement creates the problem that the relative azimuth of the measurements can change quickly and unpredictably. In addition, especially in urban areas, buildings and trees often block the view to the horizon. Furthermore, other installations on the tram's roof partly block the lower viewing angles. Therefore, it was decided to operate the instrument on the tram mainly in zenith-sky mode and to take measurements at 20° elevation only every 7 min. This allows a high measurement frequency in the zenith-sky mode and the possibility of using the 20° elevation measurements as verification for separating the troposphere and stratosphere. Additionally, dark measurements to the inside of the instrument housing are performed every 7 min, which can be used for regular corrections of the dark signal of the spectrometer, especially on days with strong temperature gradients.

5.3.1 Tram DOAS data retrieval

The NO_2 dSCDs are retrieved using a fitting window of $425 - 490$ nm and a polynomial degree of 5. The spectral calibration is done done based on an HgCd line lamp measurement. The fit included absorption cross sections of O_3, NO_2, O_4, H_2O, and a pseudo-cross section accounting for rotational Raman scattering. Details on the DOAS fit are summarized in Table 5.1. These fit settings or very similar ones have been commonly used in recent studies for the NO_2 retrieval from ground-based DOAS-type measurements (e.g., Kreher et al., 2020). The dSCDs are retrieved relative to reference background spectra, measured on 5 September 2021, a day with small tropospheric NO_2 concentrations averaged between 11:12 and 11:14 UTC. Using a fixed reference has the risk that instrumental characteristics changing with time do not cancel out. However, as seen in Fig. 5.6, no

Table 5.1: NO_2 DOAS fit settings for the retrieval of NO_2 dSCDs in the visible spectral range.

Fitting window	425 –490 nm
Polynomial degree	5 (6 coefficients)
Reference spectrum	5 September 2021 averaged between 11:12 and 11:14 UTC
Cross section O_3	223 K, Serdyuchenko et al. (2014)
Cross section NO_2	298 K, Vandaele et al. (1998)
	220 K, pre-orthogonalized Vandaele et al. (1998)
Cross section O_4	293 K, Thalman and Volkamer (2013)
Cross section H_2O	293 K, Lampel et al. (2015)
Ring	computed with QDOAS (Danckaert et al., 2017)

long-term drifts in the fit quality are visible, indicating that the used Avantes spectrometer is very stable.

The tropospheric NO_2 VCD is determined similarly as done for the IUP car DOAS instrument (see Sect. 4.3.3.1) by the following equation:

$$\mathrm{VCD_{trop}} = \frac{\mathrm{dSCD} + \mathrm{SCD_{ref}} - \mathrm{VCD_{strat}} \cdot \mathrm{AMF_{strat}}}{\mathrm{AMF_{trop}}} \tag{5.2}$$

with

$$\mathrm{SCD_{ref}} = \mathrm{VCD_{trop,\,ref}} \cdot \mathrm{AMF_{trop,\,ref}} + \mathrm{VCD_{strat,\,ref}} \cdot \mathrm{AMF_{strat,\,ref}} \tag{5.3}$$

For the correction of NO_2 in the reference background measurement, a tropospheric VCD of $1 \times 10^{15}\,\mathrm{molec\,cm^{-2}}$ is assumed. The stratospheric VCDs are determined from the B3dCTM, which provides a daily diurnal cycle of the stratospheric NO_2 VCDs. Due to an deviation between the modeled and the measured stratospheric NO_2 VCDs during the TROPOMI overpass (t_{overpass}), the B3dCTM data are scaled to the TROPOMI observations over the tram DOAS measurement region with

$$s = \frac{\mathrm{VCD_{strat,\,TROPOMI}}(t_{\mathrm{overpass}})}{\mathrm{VCD_{strat,\,B3dCTM}}(t_{\mathrm{overpass}})}. \tag{5.4}$$

The daily scaling factors for the tram DOAS measurement period are shown in Fig. C.1. Stratospheric NO_2 VCDs over Bremen obtained from the B3dCTM are shown exemplary for 5 September 2022 in Fig. 5.7a. As the dSCD retrieval only uses a NO_2 absorption cross section at one temperature (298 K), a temperature correction is applied to the determined stratospheric SCDs using a factor of 1.3 (see also Bucsela et al. (2013), and van Geffen et al. (2022a)). Stratospheric AMFs are calculated with SCIATRAN as a function of SZA

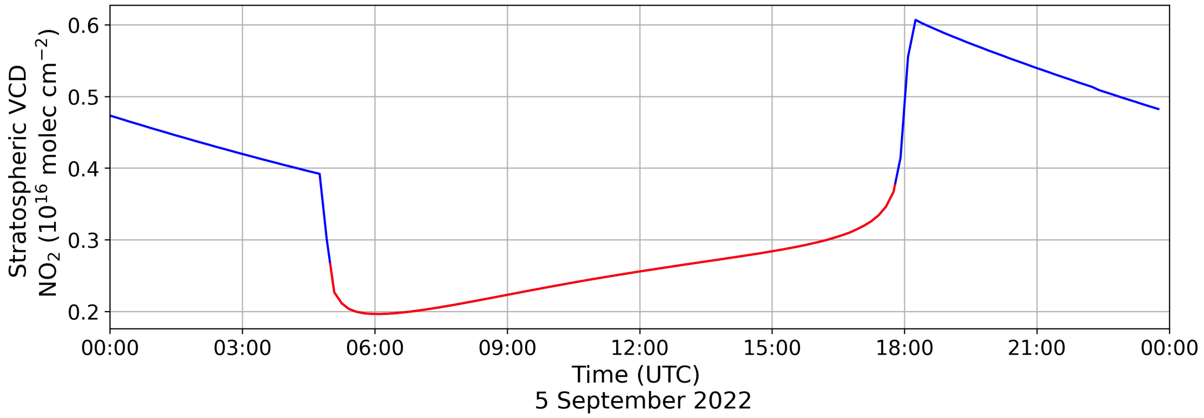

(a)

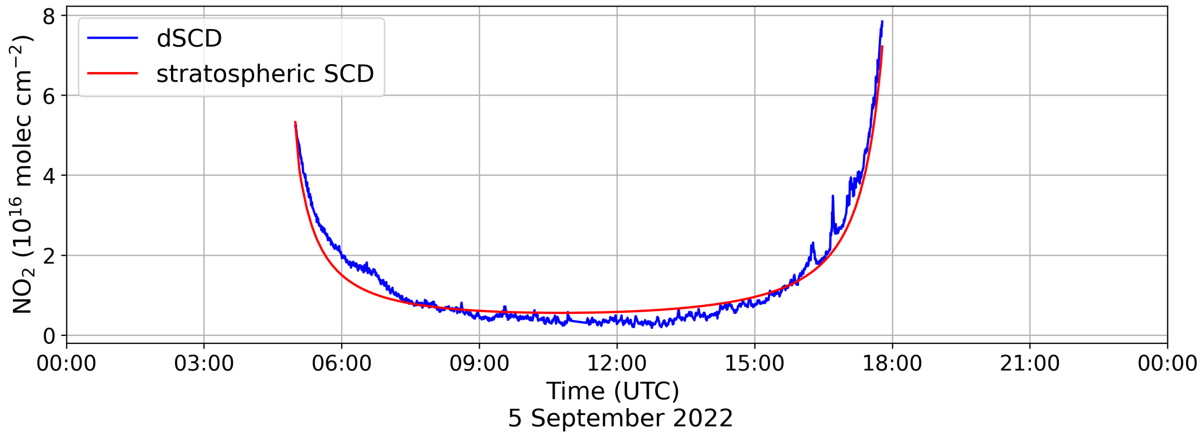

(b)

Figure 5.7: (a) Stratospheric NO_2 VCD above Bremen on 5 September 2022 obtained from the B3dCTM diurnal cycle scaled to the TROPOMI stratospheric NO_2 VCD observation on this day. The red part is used for the tram DOAS VCD calculation. (b) Retrieved dSCDs from tram DOAS measurements on 5 September 2022 in blue and stratospheric SCD retrieved from B3dCTM and TROPOMI stratospheric NO_2 VCDs after scaling with the temperature correction factor 1.3 and multiplying with the stratospheric AMF in red.

(see Fig. C.2). Figure 5.7b shows the retrieved NO_2 dSCD and the stratospheric SCD retrieved from B3dCTM, and TROPOMI stratospheric NO_2 VCDs scaled with the temperature correction factor 1.3 and multiplied with the stratospheric AMF. The determined stratospheric SCD fits well to the morning and evening part of the dSCD curve, usually dominated by stratospheric NO_2, indicating a good assumption of the stratospheric SCD. For the conversion of tropospheric SCDs to tropospheric NO_2 VCDs, a tropospheric AMF of 1.3 was used. Following Eq. 5.3, the residual amount of NO_2 in the reference SCD taken on 5 September 2021 is determined as $5.51 \times 10^{15}\,\text{molec}\,\text{cm}^{-2}$.

The total uncertainty on the tropospheric NO_2 VCD originates from error sources in the retrieved dSCDs, the estimation of the reference background column, the stratospheric correction, and the AMF calculation. Assuming uncorrelated uncertainties, the total uncertainty of the tropospheric NO_2 VCD $\sigma_{\mathrm{VCD}_{\mathrm{trop}}}$ follows the error propagation of the error sources given by:

$$\sigma_{\mathrm{VCD}_{\mathrm{trop}}} = \Bigg(\left(\frac{\sigma_{\mathrm{dSCD}}}{\mathrm{AMF}_{\mathrm{trop}}}\right)^2 + \left(\frac{\sigma_{\mathrm{SCD}_{\mathrm{trop,\,ref}}}}{\mathrm{AMF}_{\mathrm{trop}}}\right)^2 + \left(\frac{\sigma_{\mathrm{SCD}_{\mathrm{strat,\,ref}}}}{\mathrm{AMF}_{\mathrm{trop}}}\right)^2 + \left(\frac{\sigma_{\mathrm{SCD}_{\mathrm{strat}}}}{\mathrm{AMF}_{\mathrm{trop}}}\right)^2 + \left(\frac{\mathrm{SCD}_{\mathrm{trop}}}{\mathrm{AMF}_{\mathrm{trop}}^2} \cdot \sigma_{\mathrm{AMF}_{\mathrm{trop}}}\right)^2 \Bigg)^{\frac{1}{2}} \tag{5.5}$$

with:

$$\sigma_{\mathrm{SCD}_{\mathrm{trop,\,ref}}} = \sqrt{\left(\mathrm{AMF}_{\mathrm{trop,\,ref}} \cdot \sigma_{\mathrm{VCD}_{\mathrm{trop,\,ref}}}\right)^2 + \left(\mathrm{VCD}_{\mathrm{trop,\,ref}} \cdot \sigma_{\mathrm{AMF}_{\mathrm{trop,\,ref}}}\right)^2}, \tag{5.6}$$

$$\sigma_{\mathrm{SCD}_{\mathrm{strat,\,ref}}} = \sqrt{\left(\mathrm{AMF}_{\mathrm{strat,\,ref}} \cdot \sigma_{\mathrm{VCD}_{\mathrm{trop,\,ref}}}\right)^2} \tag{5.7}$$

and

$$\sigma_{\mathrm{SCD}_{\mathrm{strat}}} = \sqrt{\left(\mathrm{AMF}_{\mathrm{strat}} \cdot \sigma_{\mathrm{VCD}_{\mathrm{trop,\,ref}}}\right)^2}. \tag{5.8}$$

The error from the retrieved dSCDs σ_{dSCD} is estimated from the fit residuals in the DOAS analysis. Since no direct measurement of the NO_2 amount in the reference background scene exists, a systematic error with an uncertainty of 100 % is assumed for the estimated $\mathrm{VCD}_{\mathrm{ref}}^{\mathrm{trop}}$ of 1×10^{15} molec cm^{-2}. For the tropospheric AMF, an uncertainty of 25 % is assumed. The error originating from the stratospheric correction is dominated by the determination of the stratospheric column and is assumed to be 20 %. On average, the total error of the tropospheric NO_2 VCD is around 40 %.

5.3.2 Comparison to Bremen MAX-DOAS measurements

Due to the delay caused by the COVID-19 containment measures, several months of measurements were taken on the roof of IUP before the instrument was installed on the tram. During this time, the instrument was used together with the Bremen MAX-DOAS and a simple Zenith-DOAS instrument for investigations on the temporal variability of NO_2 columns. The fast temporal variability of NO_2 can influence the accuracy and significance of measurements. This effect was analyzed by parallel measurements with the three DOAS instruments operating in different measurement frequencies. The MAX-DOAS instrument performs zenith-sky measurements every approximately 10 min. At certain times, rapid and strong variations in the NO_2 column from one zenith-sky measurement to the other are visible. Figure 5.8 shows an exemplary measurement of NO_2 dSCDs on 4 March 2021 from 7 to 8 UTC. The time resolution of the tram DOAS and the Zenith-DOAS instrument is 10 s and can be used to verify the variability seen in the MAX-DOAS zenith measurements. The FOV of the instruments is similar for the Bremen MAX-DOAS and the tram DOAS with 1° respectively 0.38°. The simple Zenith-DOAS instrument is operated without a lens and has a larger FOV of approximately 25°. The measurements of the tram DOAS and Zenith-DOAS measuring in the fast 10 s frequency are in excellent agreement. Also, the measurements of the Bremen MAX-DOAS instrument agree very well with those of the higher frequency measurements are only much rarer. The strong variability in the NO_2 column between the measurements of the MAX-DOAS instrument is resolved with the high frequency measurements of the tram DOAS and Zenith-DOAS instrument. Thus, the comparison shows that the variability seen in the measurements is a natural variation of NO_2 in the atmosphere and not an inaccuracy of the instrument. It shows that the natural variability of NO_2 in urban areas can be rather large and that in case of large variability, measurements are not very representative of the atmospheric condition if the measurement rate is not high enough. This can partly explain deviations in instrument comparisons or satellite validation. Simple Zenith-DOAS instruments operating in a high-frequency measurement mode close to MAX-DOAS instruments with a measurement schedule focusing on spatial variability provide an opportunity to investigate temporal and spatial variability.

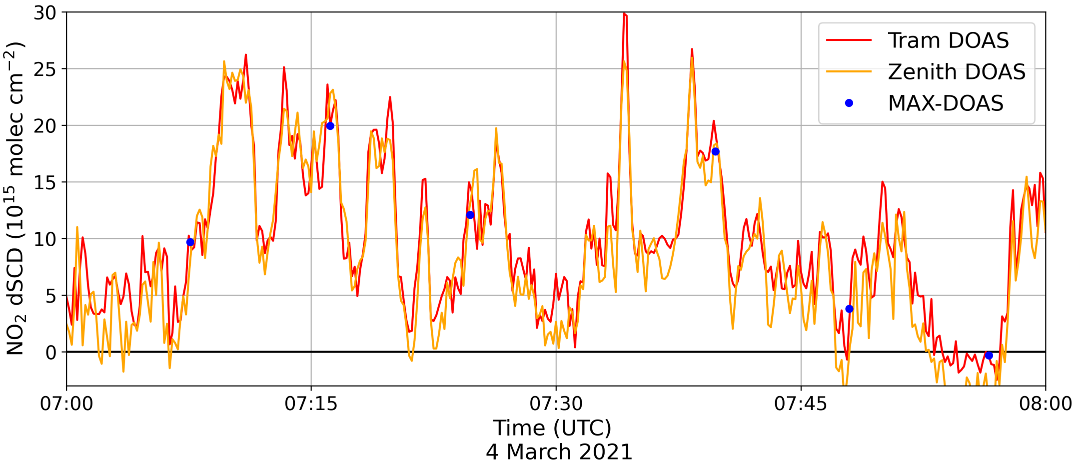

Figure 5.8: Comparison of NO_2 dSCD time series on 4 March 2021 from 7 to 8 UTC of the Bremen MAX-DOAS zenith measurements (blue), the tram DOAS zenith measurements (red), and a Zenith-DOAS instrument (orange). The time resolution of the two fast instruments (red and orange) is 10 s. The MAX-DOAS performs zenith measurements approximately every 10 min.

Additionally, the long measurement period on the roof of IUP close to the MAX-DOAS provides the opportunity for a longtime comparison of the new tram DOAS instrument to the Bremen MAX-DOAS instrument used for several years. Figure 5.9 shows scatter plots of tram DOAS vs. MAX-DOAS tropospheric NO_2 VCDs from individual measurements and daily means taken on the roof at IUP from 1 June 2021 to 10 November 2021. For the Bremen MAX-DOAS instrument, VCDs are calculated from the 30° elevation measurements from all azimuthal viewing directions (see Eq. 4.7) with a differential AMF of 1.1. For the tram DOAS instrument, VCDs are calculated from the zenith-sky measurements as described in Sect. 5.3.1. Measurements are included in the comparison if they are taken within a time difference of 1 min and for SZA $< 85°$. The comparison of the 2564 individual measurements shows quite a large scatter with a correlation coefficient of 0.67. The slope is with 0.99 ± 0.02 close to unity. The comparison of the daily averages shows less scatter with a correlation coefficient of 0.74 and a slope of 1.00 ± 0.07. Considering the different viewing geometries, the different VCD determination, and the discussed NO_2 variability, the agreement between the two instruments is quite good and gives confidence in the tropospheric NO_2 VCD data retrieved from the tram DOAS instrument.

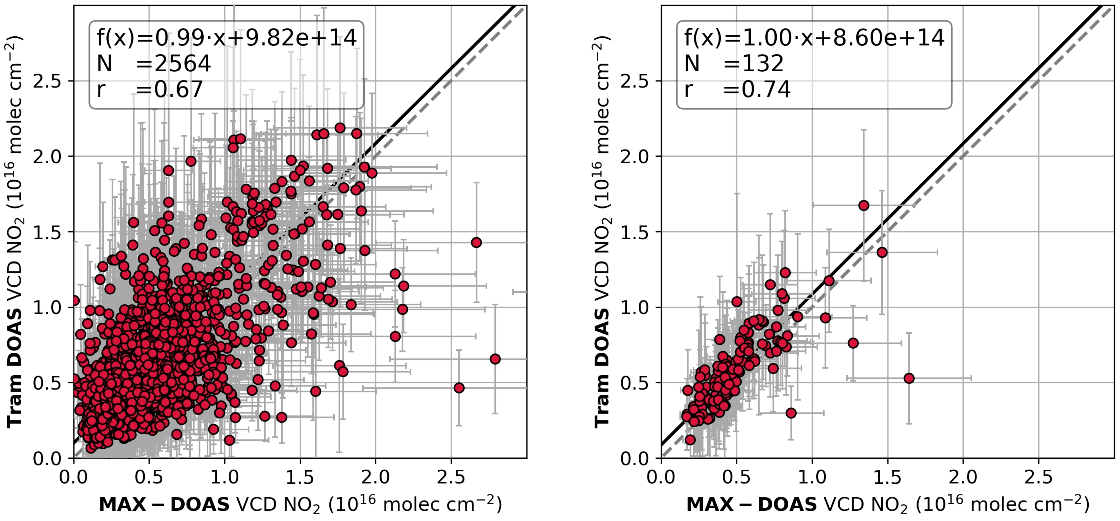

(a) (b)

Figure 5.9: Scatter plots of tram DOAS vs. MAX-DOAS tropospheric NO_2 VCDs. For all measurements taken within ± 1 min (a) and daily means of these measurements (b) on the roof at IUP from 1 June 2021 to 10 November 2021.

5.3.3 Measurements from the tram

On 10 November 2021, the tram DOAS instrument was installed on the tram 3117 of BSAG. It has performed measurements pretty much continuously since 11 November 2021. Mostly, there have been only short interruptions due to workshop visits that are regularly necessary for the tram. Due to a longer workshop stay and additional problems with Windows updates on the measurement computer, there is a larger data gap in August

2022. Additionally, there are days, mostly on the weekend, when the tram is often not operated, and the instrument performs stationary measurements at the BSAG depot. Due to another longer workshop stay and measurement computer problems after 15 October 2022, data analyzed here are from 11 November 2021 to October 2022, spanning nearly one year of measurements.

Figure 5.10 shows tropospheric NO_2 VCDs retrieved from the tram DOAS instrument during six rounds on 12 October 2022 on line 1. It can be seen that the areas of elevated NO_2 pollution can change throughout the day. However, particular areas show reproducible NO_2 levels. Reoccurring high NO_2 values are found approximately in the middle of the track. One explanation can be the Bremen-Hastedt coal-fired power plant which lies 2 km southeast close to the Weser river, marked on the map by the blue dot and the number 1. With the southeasterly wind direction prevailing on that day, the plume is blown across the middle of the track. Table 5.2 provides a list of NO_x emitters in Bremen given in the European Pollutant Release and Transfer Register (E-PRTR, European Environment Agency (last access: 3 May 2023)) for the year 2017. The largest emitters are the steel factory and the power plant Bremen-Hafen, both located in the northwest of Bremen.

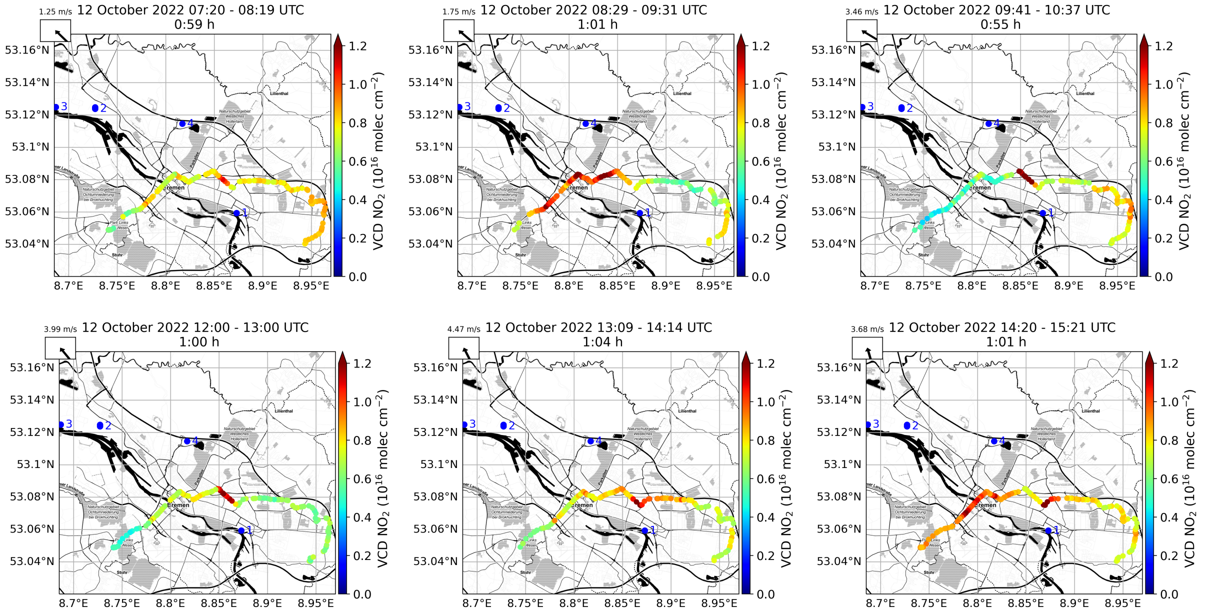

1.25 m/s 12 October 2022 07:20 - 08:19 UTC
0:59 h

1.75 m/s 12 October 2022 08:29 - 09:31 UTC
1:01 h

3.46 m/s 12 October 2022 09:41 - 10:37 UTC
0:55 h

3.99 m/s 12 October 2022 12:00 - 13:00 UTC
1:00 h

4.47 m/s 12 October 2022 13:09 - 14:14 UTC
1:04 h

3.68 m/s 12 October 2022 14:20 - 15:21 UTC
1:01 h

Figure 5.10: Maps of tropospheric NO_2 VCDs from tram DOAS observations on 12 October 2022 performed on line 1. Start and end times as well as the duration of the six individual rounds are given in the title. Blue dots mark the locations of the largest NO_x emitters in Bremen given in the European Pollutant Release and Transfer Register (E-PRTR) listed in Table 5.2.

Since the tram operates on different lines depending on the BSAG's operational planning, the measurements are performed in large parts of Bremen over time. Figure 5.11 shows the averaged tropospheric NO_2 VCDs from tram DOAS measurements performed over the period of nearly one year between 11 November 2021 and 15 October 2022. The map in the upper left shows the mean value over all measurements regardless of the line on

Table 5.2: List of NO_x emitters in Bremen given in the European Pollutant Release and Transfer Register (E-PRTR, European Environment Agency (last access: 3 May 2023)).

Name	Label in maps	NO_x/NO_2 (t/a)	Reporting year
Heat and power plant Hastedt	1	486	2021
Heat and power plant Hafen	2	838	2019
Waste incineration plant Hafen	2	240	2021
Steel factory ArcelorMittal	3	1770	2021
Steel factory ArcelorMittal-Walzwerk	3	402	2021
Heat and power plant ArcelorMittal	3	168	2020
Waste incineration plant Mid	4	393	2021

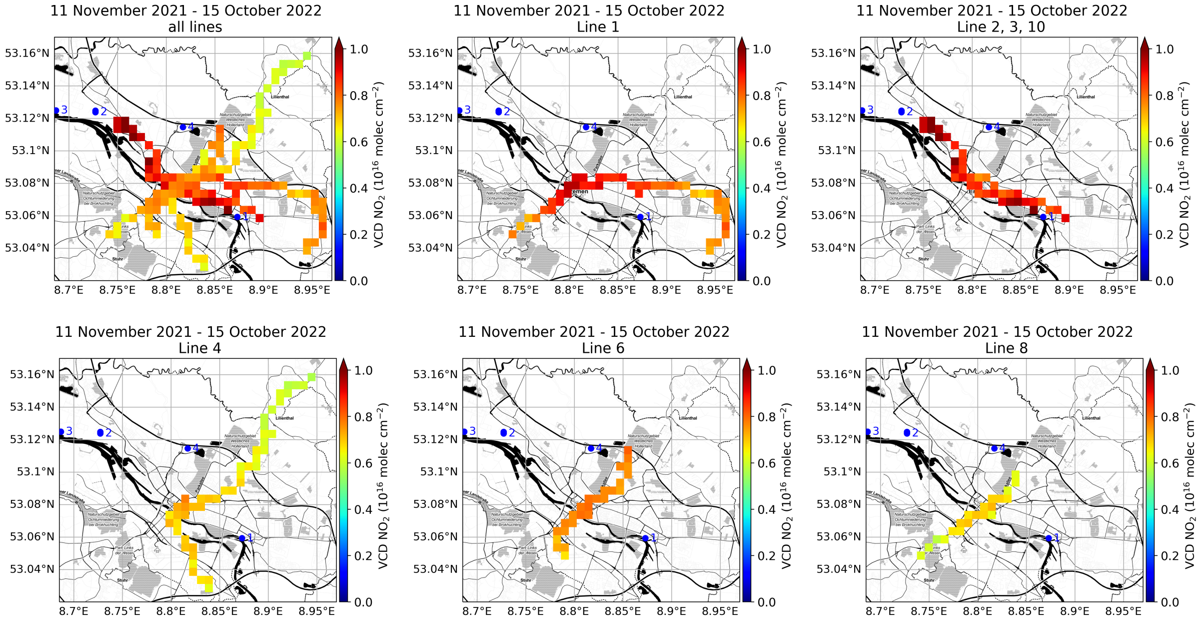
11 November 2021 - 15 October 2022 all lines

11 November 2021 - 15 October 2022 Line 1

11 November 2021 - 15 October 2022 Line 2, 3, 10

11 November 2021 - 15 October 2022 Line 4

11 November 2021 - 15 October 2022 Line 6

11 November 2021 - 15 October 2022 Line 8

Figure 5.11: Maps of averaged tropospheric NO_2 VCDs from tram DOAS measurements performed from 11 November 2021 to 15 October 2022. Data are averaged for all lines together and separately for line 1, 4, 6, and line 8. Since line 2, 3, and 10 overlap to a large extent, they are considered together. Blue dots mark the locations of the largest NO_x emitters in Bremen given in the E-PRTR, listed in Table 5.2.

which they were recorded. Data are averaged and plotted in 500 m × 500 m boxes. It shows elevated NO_2 values in the industrialized northwest, where the largest emitters (marked with the blue dots 2, 3) are located and close to the power plant Bremen-Hastedt (blue dot 1). The lowest NO_2 VCDs are found in the northeast, where the line 4 of the BSAG network reaches up to Lilienthal, a more rural area. Also, the line sections south of the city center have lower NO_2 values than the industrialized regions and the city center. The other maps in the figure show the measurements averaged for the individual lines of the

BSAG tram network. The network consists of 9 lines, including lines 1, 2, 3, 4, 5, 6, 8, and 10. Since lines 2, 3, and 10 overlap to a large part, they are considered as one line in the analysis. Line 5 is a relatively short line between the Bürgerpark and Gröpelingen and is challenging to be separated from the other lines; therefore, it is not analyzed separately, and their measurements are only included in the overall analysis. The longest lines are line 4, which has a north-south course, and line 1, which has an east-west course. They both cover the city center as well as more rural areas. As visible in Fig. 5.10, they are well suited to indicate gradients in the NO_2 distribution over Bremen. Line 6 is special as it passes by the IUP, and measurements can be compared with the MAX-DOAS measurements on the roof. Even if data are already averaged over nearly one year, sampling issues are visible, for example, for lines 1 and 8, which share the southwesterly section. The measurements on line 1 clearly show higher NO_2 VCDs than the averaged measurements on line 8.

5.3.4 Comparison to TROPOMI tropospheric NO_2 VCD

The tram DOAS measurements provide insight into the NO_2 distribution within Bremen and can be used to verify the NO_2 distribution as seen by TROPOMI. Figure 5.12 shows the map of the averaged tropospheric NO_2 VCDs from tram DOAS measurements performed from 11 November 2021 to 15 October 2022 on all lines and the TROPOMI measurements for the same period over the area. The TROPOMI tropospheric NO_2 VCDs are produced from the operational OFFL NO_2 retrieval of V02.03.01 (14 November 2021–17 July 2022) and V02.04.00 (17 July 2022–15 October 2022). The comparison of both maps indicates similar distributions with clearly elevated NO_2 VCDs in the industrialized

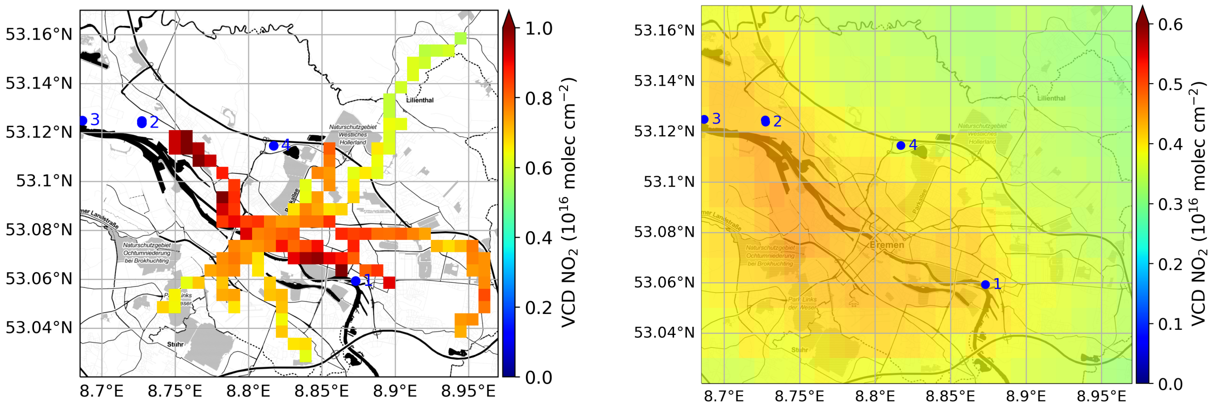

(a)

(b)

Figure 5.12: Maps of tropospheric NO_2 VCDs from (a) tram DOAS and (b) TROPOMI observations from 11 November 2021 to 15 October 2022. Due to the difference in the absolute values, the figures each have an individual color bar with different maximum values. Blue dots mark the locations of the largest NO_x emitters in Bremen given in the E-PRTR, listed in Table 5.2.

northwest and the city center and a decline to lower values in the northeast. However, absolute values differ, with significantly higher tropospheric NO_2 VCDs observed by the tram DOAS than seen by TROPOMI. One explanation is that the observations are not taken at the exact same time. To avoid sampling issues in the tram DOAS NO_2 distribution map, they are averaged over all measurements available after quality filtering, while the TROPOMI overpass over Bremen is between 10:30 UTC and 13:40 UTC. Additionally, not exactly the same days are considered for the two averages. Since the TROPOMI data set only includes nearly cloud-free conditions, filtered with a cloud radiance fraction of 0.5, the tram DOAS data set is only filtered by a simple and not very strict color index filter (Bösch, 2019) chosen by analyzing the longtime data set of the instrument. Nevertheless, the comparison shows that the overall distribution is well captured.

Figure 5.13a shows a scatter plot of coinciding TROPOMI and tram DOAS observations from 11 November 2021 to 15 October 2022. To directly compare the two data sets, the tram DOAS measurements taken ± 30 min around the TROPOMI overpass are averaged within the coinciding TROPOMI pixel. All pixels are considered regardless of the area covered by tram DOAS measurements. This results in 60 coinciding TROPOMI pixels

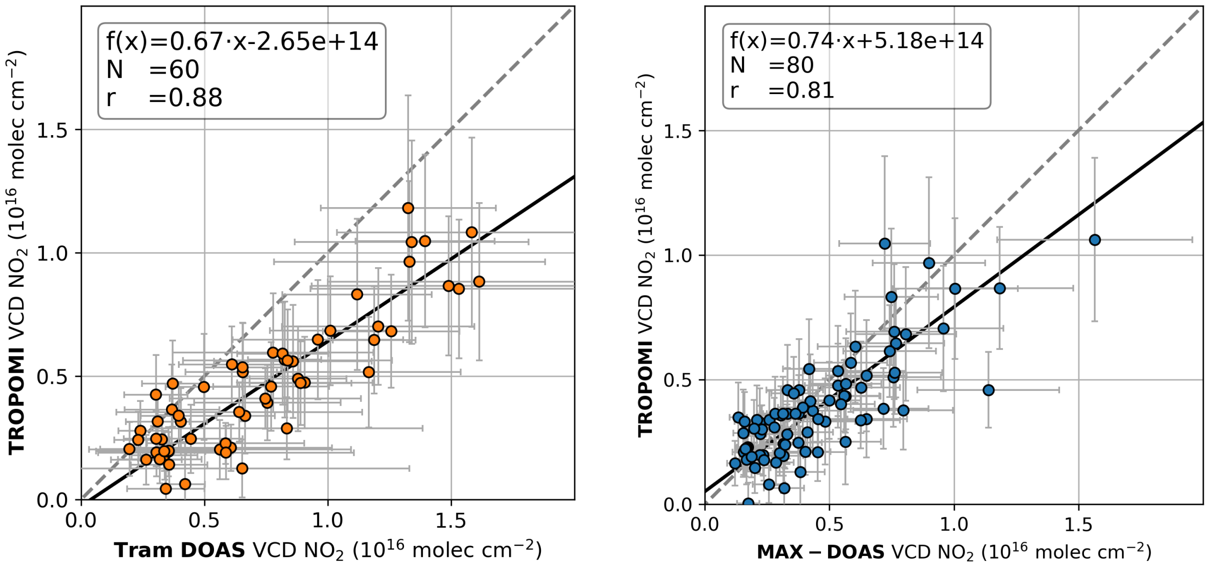

(a) (b)

Figure 5.13: Scatter plots of TROPOMI tropospheric NO_2 VCDs vs. collocated tram DOAS (a) and MAX-DOAS (b) observations from 11 November 2021 to 15 October 2022. Measurements are regarded as collocated if they are taken ± 30 min around the TROPOMI overpass within the TROPOMI pixel. The gray dashed line indicates the 1:1 line. The thick solid black line represents the orthogonal distance regression. Vertical error bars show the reported precision of the TROPOMI tropospheric NO_2 VCD. The horizontal error bars in the tram DOAS comparison represent the standard deviation of tram DOAS measurements within the TROPOMI pixel ± 30 min around the TROPOMI overpass. The horizontal error bars in the tram DOAS comparison represent the standard deviation of MAX-DOAS measurements ± 30 min around the TROPOMI overpass.

which show a high correlation of r = 0.88 with the tram DOAS data and a slope of 0.67 ± 0.04. This negative bias of the TROPOMI tropospheric NO_2 VCDs confirms the low bias seen in the distribution map comparison and other TROPOMI validation activities (see Chapter 4). With a value of 0.88, the comparison shows a much better correlation than the 0.76 found in the TROPOMI PAL V02.03.01 vs. AirMAP comparison during the S5P-VAL-DE-Ruhr campaign. However, for the S5P-VAL-DE-Ruhr campaign data set, it was found that the large scatter was caused by a large aerosol load not accounted for correctly in the cloud correction. Thus a better correlation was expected for Bremen, which is much less industrialized and thus expected to have lower aerosol loads. The slope of 0.67 ± 0.04 is significantly lower than the slope of 0.83 ± 0.06 found in the AirMAP comparison. However, it is reported that modifications in the TROPOMI NO_2 have a different influence depending on the site, the range of tropospheric NO_2 VCD values, and season (van Geffen et al., 2022b). Both correlation and slope generally agree quite well with the values found in other validation analyses from Dimitropoulou et al. (2022), and van Geffen et al. (2022b). The horizontal error bars represent the standard deviation of tram DOAS measurements within the TROPOMI pixel ± 30 min around the TROPOMI overpass, illustrating the spatiotemporal variability within the comparison criteria.

Figure 5.13b shows a scatter plot of coinciding TROPOMI tropospheric NO_2 VCDs and Bremen MAX-DOAS observations from 11 November 2021 to 15 October 2022. The comparison considers the TROPOMI pixel located over the MAX-DOAS site and MAX-DOAS measurements performed ± 30 min around the TROPOMI overpass. This results in 80 coincidences showing a good correlation of r = 0.81 and a slope of 0.74 ± 0.06, which is in reasonably good agreement with the tram DOAS comparison. It confirms the tram DOAS measurements and shows that the simple zenith method provides comparable results to the 30° elevation method. Since the tram DOAS instrument has the advantage of covering a larger area with a broader range of tropospheric NO_2 VCD values, the coinciding measurements cover the range of NO_2 values more evenly than for the MAX-DOAS comparison and provide a more representative evaluation of the TROPOMI data set.

5.4 Conclusion

A new DOAS instrument was developed and installed on a tram in Bremen. The tram DOAS instrument provides mobile measurements without the high costs of airborne DOAS measurements and the effort of driving needed for car DOAS measurements. It regularly performs measurements during the tram operation and can fill the gap between stationary ground-based and satellite measurements.

It is a compact and straightforward instrument setup fulfilling the requirements for a longtime remote operation on a tram. Measurements can be performed in the horizon and zenith directions. During the operation on the tram, the instrument mainly operates in zenith-sky mode to avoid viewing directions against buildings and trees and to have a high measurement frequency.

The instrument's FOV was characterized as 0.38°, which is in reasonable agreement with the theoretically possible values of 0.57° and well suited for accurate off-axis measurements. Due to the omission of a cooling system, peak temperatures inside the instrument housing can reach 50 °C in summer, and the temperature often fluctuates by ± 10 °C. However, the humidity stays rather constant.

Due to COVID-19 pandemic measures, the installation on the tram was postponed, which offered the opportunity to operate the tram DOAS instrument close to the Bremen MAX-DOAS instrument on the roof at IUP for several months. During this time, a detailed comparison of both instruments was possible. Parallel measurements of the MAX-DOAS, tram DOAS, and an additional Zenith-DOAS performing zenith measurements at different frequencies (every 10 min for the MAX-DOAS and every 10 s for the two other instruments) were used to investigate the temporal variability of NO_2 columns. The comparison of the measurements shows that all three instruments are in excellent agreement and that the strong variability seen from one MAX-DOAS zenith measurement to the next is in agreement with the temporally higher resolved tram DOAS and Zenith-DOAS measurements. Thus, the measurements revealed that the observed variability is true NO_2 variability and not an inaccuracy of the instrument. It shows that the natural variability of NO_2 can be large in urban areas close to NO_x sources, which can cause representativity issues and deviations in instrument comparisons. Additionally, several months of tropospheric NO_2 VCDs retrieved from coinciding tram DOAS zenith and 30° MAX-DOAS measurements are compared. Considering the different measurement geometries, the agreement is quite good and gives additional confidence in using the tram DOAS tropospheric NO_2 VCD data for further analyses.

Tram DOAS measurements performed from the tram are analyzed for nearly one year of operation. The instrument is installed on the tram 3117 and operates on the different lines covering Bremen depending on the BSAG's operational planning. It can be seen that the areas of increased tropospheric NO_2 VCDs change throughout the day, but certain regions show reproducibly higher NO_2 pollution. Depending on the wind direction, the plume of the coal-fired power plant Bremen-Hastedt can be detected on tram DOAS courses downwind of the source throughout the day. The mean over all tram DOAS measurements performed over the BSAG network during this year results in a tropospheric NO_2 VCD distribution map of Bremen, which shows elevated NO_2 levels in the industrially dominated northwest and lower levels in the more rural northeast of Bremen. The comparison of the tram DOAS and the TROPOMI NO_2 map of Bremen indicates a good agreement regarding distribution. Still, it shows a significant underestimation of TROPOMI compared to the tram DOAS data, which can partly be explained by deviations in observation

times. However, a similar underestimation is also visible when comparing closely coinciding TROPOMI and tram DOAS, respectively MAX-DOAS measurements. Scatter plots of TROPOMI vs. tram DOAS and MAX-DOAS tropospheric NO_2 VCDs show slopes of 0.67 ± 0.04 and 0.74 ± 0.06 with correlation coefficients of 0.88 and 0.81, respectively.
A larger data set of tram DOAS measurements would help to further investigate the spatial distribution of NO_2 within Bremen, especially regarding the time of the day and meteorological conditions. The measurements can be helpful for the validation of the upcoming Sentinel-4 mission. They can be used to analyze intra-pixel variability as well as for the evaluation of diurnal spatial variability.

6 | Conclusion and outlook

Due to the variety of NO_x emission sources and its short lifetime, especially in urban areas, tropospheric NO_2 is spatially and temporally very variable. As NO_2 poses a health risk to humans and because of its importance in tropospheric chemistry, accurate knowledge about the distribution of NO_2 and its spatial and temporal variability is of great relevance. In this thesis, NO_2 tropospheric columns retrieved from measurements of TROPOMI on Sentinel-5P are investigated regarding the spatial and temporal variability of NO_x emissions and lifetime on a global basis. The analysis of a campaign data set comprising ground-based stationary, car, airborne and TROPOMI observations in the Rhine-Ruhr region, shows that tropospheric NO_2 columns vary significantly depending on meteorological conditions, weekday, and emission sources. The study highlights the importance of satellite validation and the benefits of validation activities in various conditions. A newly developed tram DOAS instrument demonstrates a new opportunity for continuous mobile DOAS measurements and its potential for investigating spatial and temporal NO_2 variability and satellite validation.

VARIABILITY OF NO_X EMISSIONS AND LIFETIMES

In the first part of this thesis, tropospheric NO_2 VCDs retrieved by TROPOMI on S5P have been investigated together with meteorological and ozone data regarding the spatial and temporal variability of NO_x source strength and lifetime for 50 NO_x emission sources. The analyzed source regions are distributed around the world between the equator and 61° latitude, comprising cities, industrial areas, isolated power plants, oil fields, and regions with a mix of sources. The high spatial resolution and good signal-to-noise ratios of the TROPOMI observations enable the analysis of weak emission sources from only 2 years of data, which can be separated even further for the investigation of short-term variability caused by seasonality, the weekday or COVID-19 containment measures.

The retrieved NO_x emissions reproduce the variability seen in power plant stack measurements reasonably well, demonstrating the method's robustness, but are generally low by a factor of two. A similar underestimation is also found for most of the 50 source regions compared to the EDGAR emission inventory, in particular for the regions with the highest emissions. A large part of this underestimation is assumed to be caused by the negative bias of the TROPOMI tropospheric NO_2 VCDs and is further investigated in the second part of the thesis.

The seasonal analysis of the estimated NO_x emissions shows higher NO_x emissions during winter for most of the analyzed source regions, especially at higher latitudes. Isolated power plants and sources in hot desert climates show only a weak seasonality or even higher emissions in summer than in winter. The corresponding NO_x lifetimes show only a weak seasonal dependence but a systematical latitudinal dependence, increasing from around 2 h for low-latitude sources close to the equator to around 6 h for high-latitude sources.

The separate analysis of NO_x emissions on working and rest days shows that emissions are generally significantly reduced on rest days compared to working days but with high variability for the analyzed source regions. The largest deviations with weekend-to-weekday ratios of up to 0.5 are found for source regions expected to be dominated by traffic emissions. Source regions strongly dominated by power plant or industry emissions do not show any significant emission reductions during rest days. The corresponding lifetimes, estimated for rest days and working days, do not show any significant weekday dependencies.

Strong short-term reductions in NO_x emissions were found for New Delhi, Buenos Aires, and Madrid attributable to the COVID-19 containment measures.

VALIDATION OF TROPOMI TROPOSPHERIC NO_2 - S5P-VAL-DE-RUHR CAMPAIGN

The S5P-VAL-DE-Ruhr campaign provides a data set of airborne imaging, ground-based stationary, and mobile car DOAS measurements conducted in the Rhine-Ruhr region in September 2020. In this region, three smaller areas of $30\,\mathrm{km} \times 35\,\mathrm{km}$ are defined as target research areas. Due to the different characteristics of the measurement areas, meteorological conditions and the weekday, large variability of the measured NO_2 amount and distributions is observed. A comparison of this campaign data set with the TROPOMI tropospheric NO_2 VCDs retrieved during these days enables investigating the influence of the observed variability on the validation and to further analyze the known underestimation of TROPOMI NO_2.

Stationary ground-based and mobile car DOAS measurements are used to evaluate the airborne tropospheric NO_2 VCDs. They show a reasonably good agreement with correlation coefficients of 0.88 and 0.89 and slopes of 0.90 ± 0.09 and 0.89 ± 0.02, respectively.

The airborne imaging DOAS measurements performed by AirMAP instrument cover several TROPOMI pixels within one flight of around 3 h and link the ground-based and TROPOMI measurements. The airborne data set is compared to the operational (OFFL V01.03.02), a modified reprocessed (PAL V02.03.01) TROPOMI NO_2 product, and several scientific products. The airborne and TROPOMI OFFL V01.03.02 data show a high correlation but low biased TROPOMI tropospheric NO_2 VCDs. Comparing the airborne data set to the modified TROPOMI PAL V02.03.01 product reveals that updates implemented in the NO_2 retrieval increased the slope but significantly decreased the correlation. It is demonstrated that the main modification, a switch from the FRESCO-S to the FRESCO-wide cloud product, results in more realistic higher cloud altitudes, therefore decreased tropospheric AMFs and higher tropospheric NO_2 VCDs. This modification affects most of the analyzed TROPOMI observations, but not all. Some pixels remain with too high cloud pressures and thus too low tropospheric NO_2 VCDs. These pixels are dominated by observations from one day, and are found to coincide with a higher aerosol load, as indicated by the TROPOMI AOT product. These scenes are identified as clouds in the cloud retrieval and are not accounted for adequately in the cloud correction, resulting in too high cloud pressures. It is demonstrated that the agreement with AirMAP can be improved when no cloud correction is made for the TROPOMI NO_2 product. The comparison of the scientific TROPOMI NO_2 products and the airborne data set shows a minor influence of the surface reflectivity database and a more significant effect of spatially higher-resolved a priori NO_2 vertical profiles on the modified TROPOMI NO_2 retrieval compared to the original product. The evaluations have shown that the underestimation of the TROPOMI tropospheric NO_2 VCD product has been improved by the implemented modifications but can be further reduced by additional modifications.

TRAM DOAS OBSERVATIONS OF NO_2 SPATIOTEMPORAL VARIABILITY

Mobile DOAS measurements are a valuable source for investigating spatial and temporal variability of NO_2 and validating satellite data. Due to the large effort in performing these measurements, they are often only feasible on campaign basis. This issue is addressed by a newly developed mobile tram DOAS instrument, which has been developed as part of this thesis for continuous operation on a tram in Bremen.

The installation on the tram had to be postponed due to COVID-19 containment measures. During this delay, the instrument was operated close to the Bremen MAX-DOAS instrument for comparison measurements. Parallel measurements of the two instruments and an additional Zenith-DOAS were used to investigate the temporal variability of NO_2 columns. The variability seen in the 10 min resolved zenith-sky measurements of the MAX-DOAS system can be resolved in the 10 s resolved tram DOAS and Zenith-DOAS measurements. All three instruments are in excellent agreement, and the parallel measurements demonstrate that the observed variability is natural variability and not instrument inaccuracy. This analysis shows that variability of NO_2 in urban areas close to NO_x emission sources can be large even within a few minutes and can cause representativity issues, for example, in satellite validation activities.

Tram DOAS measurements were performed on the Bremen tram network for nearly a year. The data show that areas of increased NO_2 pollution can change throughout the day, but that certain regions show reproducible higher NO_2 values. The mean tropospheric NO_2 VCD distribution of all tram DOAS measurements performed on the Bremen tram network shows elevated NO_2 levels in the industrially dominated district and lower NO_2 levels in more rural parts. The observed pattern agrees well with the NO_2 distribution observed by TROPOMI, albeit with generally lower NO_2 amounts in the TROPOMI observation. The validation of closely coinciding TROPOMI and tram DOAS observations shows a similar underestimation with a slope of 0.67 ± 0.04, but a good correlation of 0.88. These comparisons have shown the potential of the new tram DOAS instrument for investigating spatial and temporal variability of NO_2 on a regular basis in cities and the use for satellite validation.

The studies presented in this thesis provide a detailed analysis of spatial and temporal variations of NO_x emissions and lifetime, important validation results for the TROPOMI tropospheric NO_2 VCD product, insights into spatial and temporal variability of tropospheric NO_2 and its influence on validation activities, as well as a new instrument for these investigations.

OUTLOOK

The presented NO_x emission estimates are based on two years of TROPOMI measurements and can be repeated on a longer data set as a reprocessed data set becomes available. However, emission changes caused by the COVID-19 pandemic must be considered when analyzing other variability parameters. A longer data set can help to confirm NO_x emission reductions for Chinese cities on rest days compared to working days, as indicated for Wuhan in this study. The insufficient statistic and midday observation time as possible reasons for the weak seasonal dependence of the NO_x lifetime can be further investigated by a longer data set and the follow-up sensors on geostationary satellites, for example, GEMS, Tempo, or Sentinel-4, providing hourly measurements during the day. In general, the presented methods can be used with geostationary sensors to additionally investigate diurnal variability of NO_x emissions and lifetimes.

The validation results of the S5P-VAL-DE-Ruhr campaign show an improvement of the modified TROPOMI NO_2 product compared to the operational product in place during the time of the campaign. However, larger scatter than in previous versions was found and analyzed in detail in this study. Further validation activities using more extensive data sets in more regions and seasons with different pollution levels, surface reflectance, aerosol, and cloud conditions would help to evaluate the performance of the TROPOMI NO_2 product under other conditions and confirm the results found with the Ruhr campaign data set.

The presented validation approach can be applied to future validation activities of other satellite instruments such as GEMS, TEMPO, Sentinel-4, and Sentinel-5. The GEMS instrument was already launched in 2020, and first validation activities were carried out in 2021 and 2022. During this time, a Bremen MAX-DOAS instrument was located in Incheon, Korea, for validation measurements. Figure 6.1 shows a first comparison of the diurnal variation of tropospheric NO_2 VCD from these MAX-DOAS measurements and the IUP NO_2 retrieval on GEMS data. The GEMS observations generally show lower NO_2 values by around 25 %, but both instruments show a similar diurnal cycle with a maximum in the mid to late morning and decreasing NO_2 towards the afternoon. The comparison demonstrates the potential of MAX-DOAS measurements for validating GEMS and, in the future Sentinel-4, data and the investigation of diurnal variability first time observed by satellite measurements.

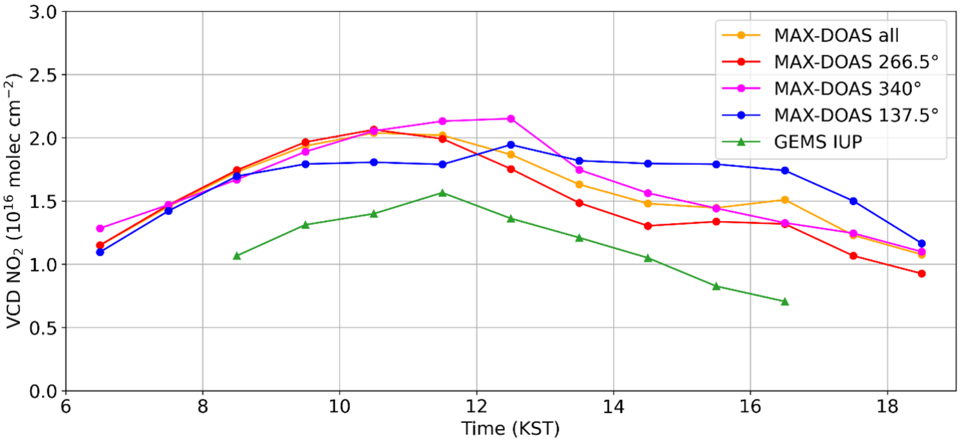

Figure 6.1: Diurnal cycle of tropospheric NO_2 VCDs from MAX-DOAS observations at Incheon, Korea, and GEMS observations above this location averaged between October 2021 and May 2022.

The high temporal variability of NO_2 columns observed with the tram DOAS and MAX-DOAS instrument in Bremen suggests that it would be helpful to increase the measurement frequency of MAX-DOAS instruments or to operate a second, fast-measuring instrument in the zenith direction to detect atmospheric variability. Continuing the tram DOAS measurements, providing a larger data set would help further investigate the spatial distribution of NO_2 within Bremen. The results can be interpreted regarding seasonality, diurnal variability, and meteorological conditions. The measurements can be helpful for the validation of the diurnal spatial variability observed by the upcoming Sentinel-4 mission.

A | Appendix: Variability of NO_x emission fluxes and lifetimes

Table A.1: NO$_x$ source regions sorted by increasing latitude with mean NO$_x$ lifetime and emissions, wind speed, available days, season flag, and weekly cycle flag (possible: x or assumed rest days, not possible: –). Errors are 1-sigma uncertainties derived by the EMG fitting procedure.

Source region	Latitude (degree)	Longitude (degree)	Lifetime (h)	Emissions $(\mathrm{mol\,s^{-1}})$	Wind $(\mathrm{m\,s^{-1}})$	Days	Season flag	Weekday flag
Singapore (Singapore)	1.30	103.69	2.15 ± 0.28	94.5 ± 11.5	5.44	24	–	–
Lagos (Nigeria)	6.55	3.40	2.37 ± 0.49	30.9 ± 6.1	4.31	29	–	–
Colombo (Sri Lanka)	6.93	79.85	1.22 ± 0.12	22.8 ± 2.3	6.17	61	x	Sat, Sun
Kano (Nigeria)	11.98	8.51	2.55 ± 0.19	5.1 ± 0.3	4.65	317	x	Sat, Sun
Bangalore (India)	12.98	77.59	1.93 ± 0.08	20.0 ± 0.8	4.66	155	–	Sun
Khartoum (Sudan)	15.58	32.52	1.27 ± 0.04	16.9 ± 0.4	5.85	494	x	Fri, Sat
Rangoon (Myanmar)	16.78	96.15	2.18 ± 0.20	14.7 ± 1.2	3.64	127	–	Sat, Sun
Hwange (Zimbabwe)	-18.38	26.47	1.63 ± 0.06	5.0 ± 0.1	4.72	254	x	Sat, Sun
Belo Horizonte (Brazil)	-19.91	-43.98	4.09 ± 0.34	10.3 ± 0.7	3.76	64	–	–
Guadalajara (Mexico)	20.66	-103.34	1.23 ± 0.14	35.5 ± 4.1	5.00	175	–	–
Raibgh (Saudi Arabia)	22.69	39.03	1.22 ± 0.13	69.1 ± 7.2	6.32	311	x	Fri, Sat
Medupi/Matimba (S. Africa)	-23.68	27.58	3.68 ± 0.32	55.5 ± 4.5	4.81	211	x	Sat, Sun
Riyadh (Saudi Arabia)	24.65	46.71	2.91 ± 0.11	186.1 ± 6.8	6.32	360	x	Fri, Sat
Buraidah (Saudi Arabia)	26.20	43.99	2.57 ± 0.14	25.4 ± 1.1	5.74	418	x	Fri, Sat
Brisbane (Australia)	-27.47	153.03	2.31 ± 0.12	24.1 ± 1.0	5.66	166	x	Sat, Sun
Sarir Field (Libya)	27.55	21.63	1.88 ± 0.04	5.5 ± 0.1	5.84	442	x	Fri, Sat
Tabuk (Saudi Arabia)	28.48	36.52	1.34 ± 0.14	24.3 ± 2.3	5.47	342	x	Fri, Sat
New Delhi (India)	28.62	77.22	3.05 ± 0.12	69.8 ± 2.5	5.09	204	x	Sun
Wuhan (China)	30.57	114.28	2.94 ± 0.30	115.1 ± 10.7	5.10	94	x	Sat, Sun
Hassi Messaoud (Algeria)	31.70	6.05	2.57 ± 0.06	8.2 ± 0.2	6.17	394	–	Fri, Sat
Perth (Australia)	-31.95	115.85	2.43 ± 0.24	16.2 ± 1.5	6.35	232	x	Sat, Sun
Isfahan (Iran)	32.64	51.67	2.08 ± 0.24	118.8 ± 12.6	5.38	178	–	Fri
Casablanca (Morocco)	33.59	-7.61	2.98 ± 0.35	18.6 ± 2.1	4.93	265	x	Sat, Sun
Xi‘an (China)	34.27	108.94	3.37 ± 0.49	164.2 ± 23.5	4.90	33	–	–
Buenos Aires (Argentina)	-34.50	-58.80	3.51 ± 0.27	80.2 ± 5.8	6.45	207	x	Sat, Sun
Adelaide (Australia)	-34.92	138.60	3.11 ± 0.20	20.5 ± 1.1	6.97	175	x	Sat, Sun
Tokio (Japan)	35.68	139.77	3.50 ± 0.42	212.0 ± 24.5	7.36	39	–	Sat, Sun
LasVegas (USA)	36.16	-115.19	1.97 ± 0.20	21.2 ± 2.0	6.23	235	x	Sat, Sun
Seoul (South Korea)	37.60	127.00	3.77 ± 0.40	272.9 ± 28.2	6.28	124	–	Sat, Sun
Melbourne (Australia)	-37.80	144.95	2.53 ± 0.24	46.8 ± 3.7	7.19	137	x	Sat, Sun
Madrid (Spain)	40.41	-3.70	2.03 ± 0.15	60.2 ± 4.3	5.43	155	x	Sat, Sun
New York (USA)	40.71	-74.01	4.35 ± 0.37	101.0 ± 8.3	7.21	133	x	Sat, Sun
Naples (Italy)	40.83	14.25	2.26 ± 0.28	28.6 ± 3.4	6.17	109	x	Sat, Sun
Barcelona (Spain)	41.40	2.17	3.41 ± 0.63	36.7 ± 6.1	6.94	52	x	–
Chicago (USA)	41.80	-87.80	5.65 ± 0.52	82.9 ± 7.4	7.26	83	x	Sat, Sun
Toronto (Canada)	43.66	-79.38	3.16 ± 0.24	53.8 ± 3.5	6.93	69	–	Sat, Sun
Bucharest (Romania)	44.43	26.10	3.20 ± 0.18	8.1 ± 0.4	5.20	142	x	Sat, Sun
Colstrip (USA)	45.88	-106.61	2.58 ± 0.15	4.6 ± 0.3	6.55	165	x	Sat, Sun
Budapest (Hungary)	47.50	19.05	2.32 ± 0.13	17.5 ± 0.9	5.60	143	x	Sat, Sun
Paris (France)	48.86	2.35	3.79 ± 0.31	56.2 ± 4.4	5.99	116	x	Sat, Sun
Kiev (Ukraine)	50.45	30.50	3.11 ± 0.18	24.3 ± 1.2	6.03	143	x	Sat, Sun
Minsk (Belarus)	53.90	27.55	6.69 ± 0.59	13.8 ± 0.7	6.92	128	–	Sat, Sun
Novosibirsk (Russia)	55.15	82.98	4.88 ± 0.34	25.9 ± 1.7	6.52	105	x	Sat, Sun
Chelyabinsk (Russia)	55.21	61.44	3.84 ± 0.23	22.6 ± 0.9	6.70	104	x	Sat, Sun
Moscow (Russia)	55.95	37.62	5.96 ± 0.50	123.6 ± 9.9	6.66	70	x	Sat, Sun
Krasnoyarsk (Russia)	56.10	92.93	4.88 ± 0.27	17.2 ± 0.9	5.78	96	x	Sat, Sun
Fort McMurray (Canada)	57.17	-111.59	5.58 ± 0.31	21.4 ± 1.1	6.25	93	x	Sat, Sun
Saint Petersburg (Russia)	59.95	30.40	4.06 ± 0.27	39.0 ± 2.5	6.69	75	–	Sat, Sun
Helsinki (Finland)	60.29	24.96	8.23 ± 0.44	22.4 ± 1.1	7.27	87	–	Sat, Sun
Surgut (Russia)	61.25	73.43	5.20 ± 0.37	10.0 ± 0.6	6.83	70	–	Sat, Sun

B | Appendix: Validation of TROPOMI tropospheric NO_2 products

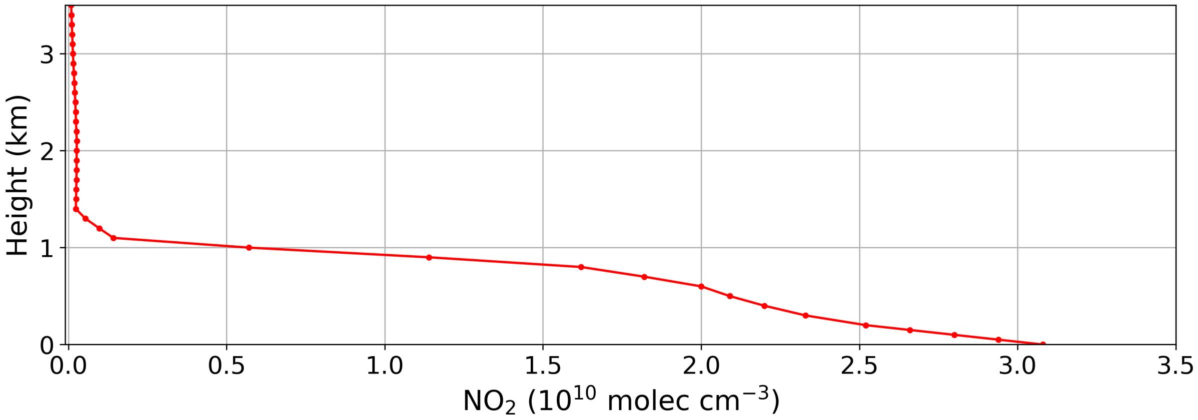

Figure B.1: NO_2 profile used in the SCIATRAN tropospheric AMF calculations. The profile is based on WRF-Chem model runs and scaled to the typical boundary layer height during the measurement days around noon.

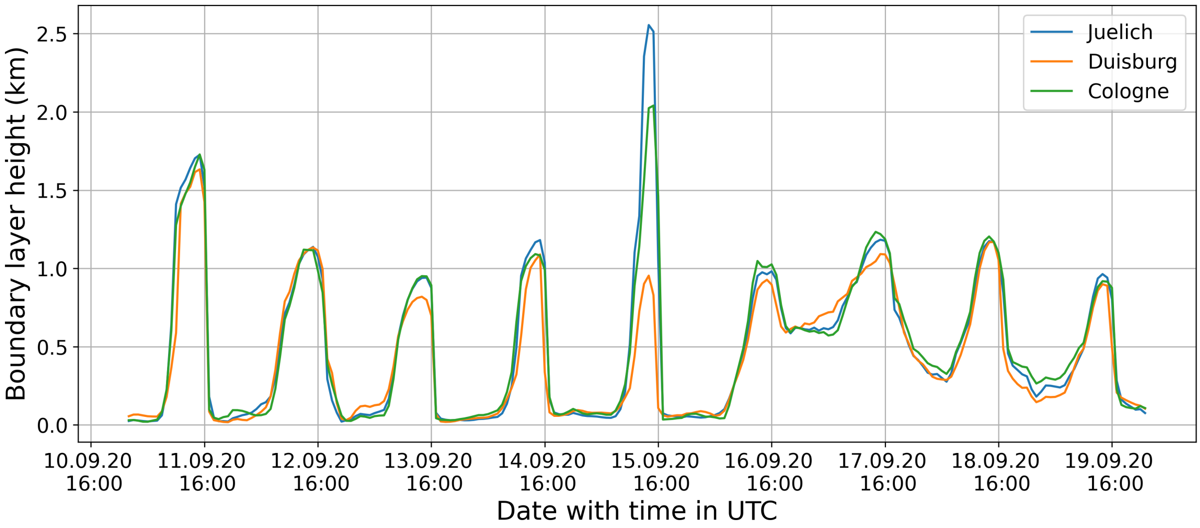

Figure B.2: Time series of ERA5 boundary layer height extracted for the three research flight areas from 11 to 19 September 2020.

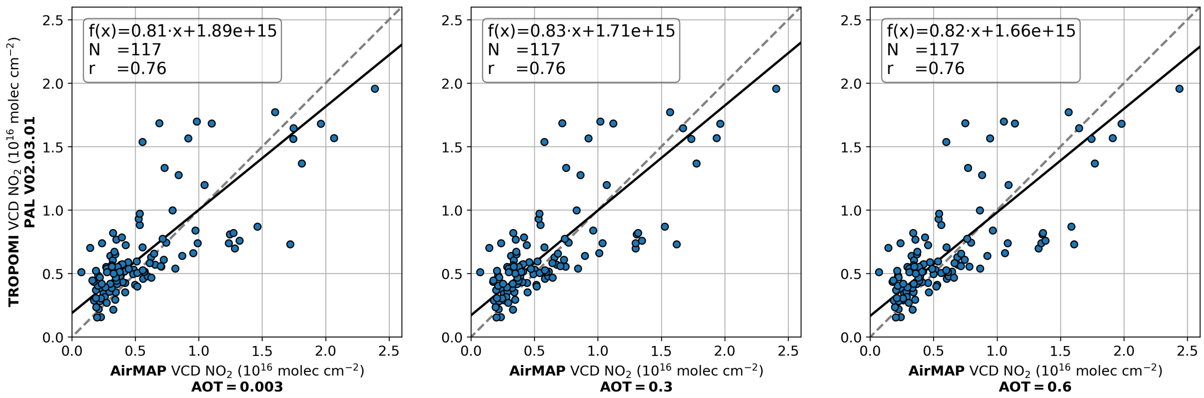

(a) (b) (c)

Figure B.3: Scatter plots of TROPOMI PAL V02.03.01 tropospheric NO_2 VCDs vs. collocated AirMAP tropospheric NO_2 VCDs with (a) AOT of 0.003, (b) AOT of 0.3 and (c) AOT of 0.6. Collocation criteria for AirMAP: ± 30 min around S5P overpass, gridded to the TROPOMI pixels and covering them at least to 75 %.

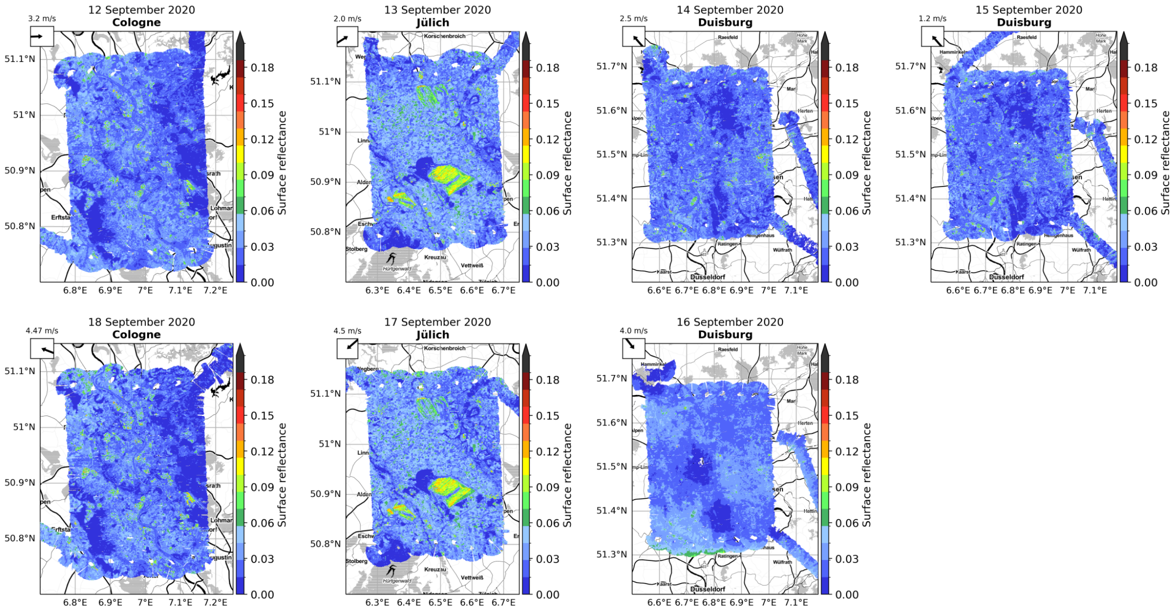

Figure B.4: Surface reflectance maps determined from the ADAM database and AirMAP radiances for flights from 12 September to 18 September 2020. Two flights in the research flight area around Cologne (left column), two flights in the flight area around Jülich (second column) and three flights in the flight area around Duisburg (third and fourth column).

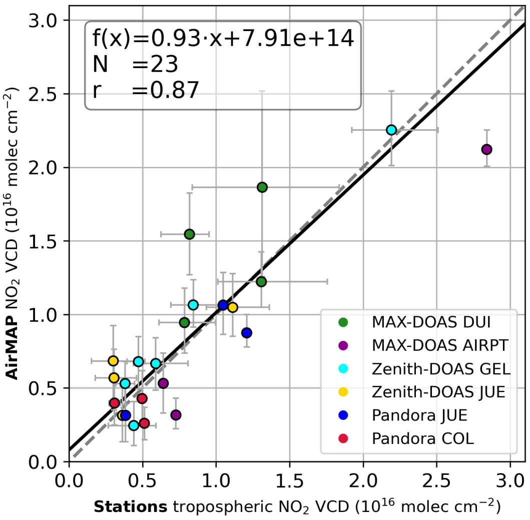

Figure B.5: Same as Fig. 4.11 with different error bars. Scatter plot showing the stationary ground-based NO_2 VCDs averaged in a time interval of 20 min closest to the AirMAP data which are averaged over a 500 m × 500 m area around the station site. Error bars represent the ± 10th − 90th percentiles within the 500 m × 500 m grid boxes and 20 min intervals.

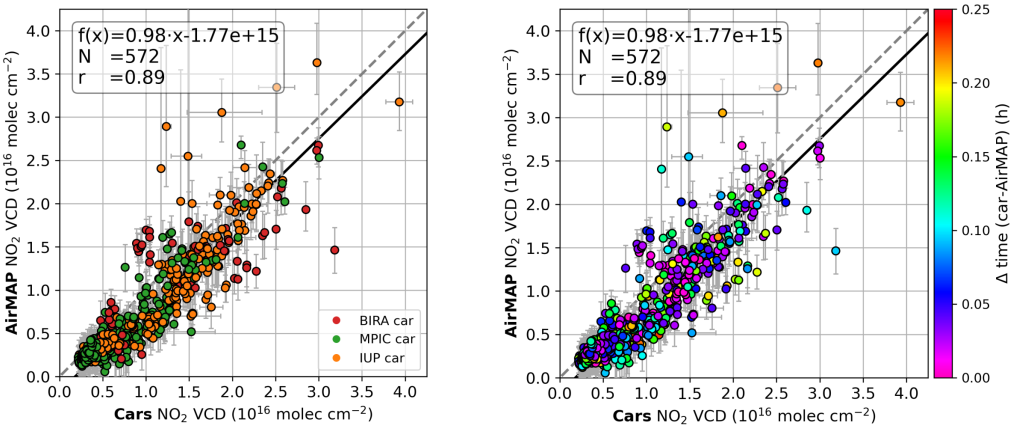

Figure B.6: Same as Fig. 4.12 with different error bars. Scatter plots showing collocated car DOAS (± 15 min window from the aircraft overpass) and AirMAP NO_2 VCDs using grid boxes of 500 m × 500 m and 15 min time intervals. Error bars represent the ± 10th − 90th percentiles within the 500 m × 500 m grid boxes and 15 min intervals.

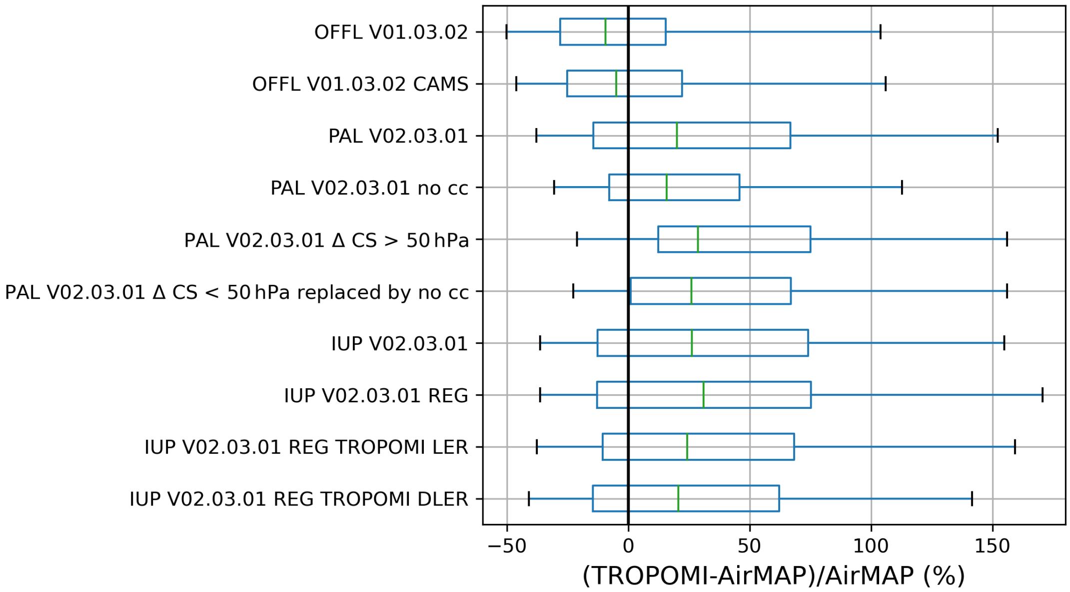

Figure B.7: Box-and-whisker plots summarizing the bias and spread of the difference between the different TROPOMI versions and AirMAP tropospheric NO_2 VCDs. The green line inside the box represents the median relative difference. Box bounds mark the 25 and 75 percentiles while whiskers represent the 5 and 95 percentiles.

Table B.1: Statistics of the comparisons between the different TROPOMI tropospheric NO_2 VCDs data versions and the AirMAP data set. Slope and offset ± standard deviation (SD) of the orthogonal distance regression, median relative difference and Pearson correlation coefficient.

TROPOMI NO_2 data version	Slope ± SD	Median difference (%)	Offset ± SD 10^{15} molec cm^{-2}	Correlation
OFFL V01.03.02	0.38 ± 0.02	-9	2.54 ± 0.15	0.86
OFFL V01.03.02 CAMS	0.41 ± 0.02	-5	2.63 ± 0.16	0.86
PAL V02.03.01	0.83 ± 0.06	20	1.71 ± 0.42	0.76
PAL V02.03.01, AirMAP AOT=0.003	0.81 ± 0.06	24	1.89 ± 0.41	0.76
PAL V02.03.01, AirMAP AOT=0.6	0.82 ± 0.06	17	1.66 ± 0.43	0.76
PAL V02.03.01 no cloud correction (no cc)	0.73 ± 0.04	16	2.12 ± 0.29	0.85
PAL V02.03.01 ΔCS > 50 hPa	0.96 ± 0.06	29	1.76 ± 0.41	0.84
PAL V02.03.01 ΔCS > 50 hPa replaced with no cc	0.89 ± 0.05	26	1.93 ± 0.37	0.84
IUP V02.03.01	0.88 ± 0.06	26	1.56 ± 0.45	0.76
IUP V02.03.01 REG	1.00 ± 0.07	31	0.99 ± 0.51	0.75
IUP V02.03.01 REG TROPOMI LER	1.02 ± 0.07	24	0.86 ± 0.54	0.74
IUP V02.03.01 REG TROPOMI DLER	0.95 ± 0.07	21	0.96 ± 0.50	0.75

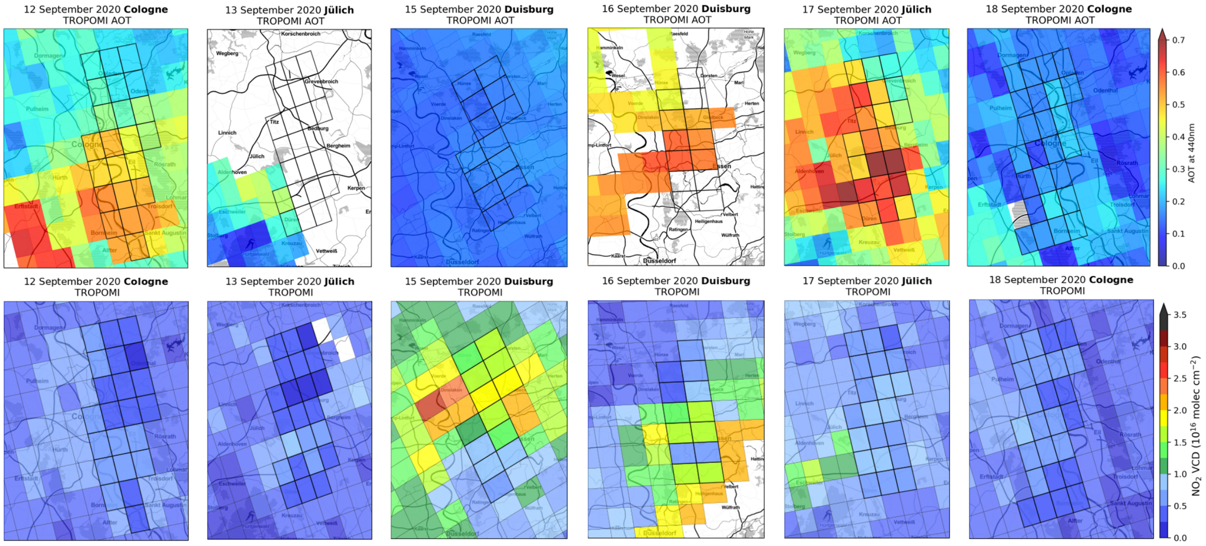

Figure B.8: Daily maps of (top) TROPOMI AOT at 440 nm filtered with the recommend qa_value of 0.5 and (bottom) TROPOMI PAL V02.03.01 tropospheric NO_2 VCDs. Black boxes represent TROPOMI pixel outlines that fulfill the collocation criteria of having an AirMAP coverage of at least 75 % and AirMAP measurements performed ± 30 min around the S5P overpass (see also Fig. 4.13).

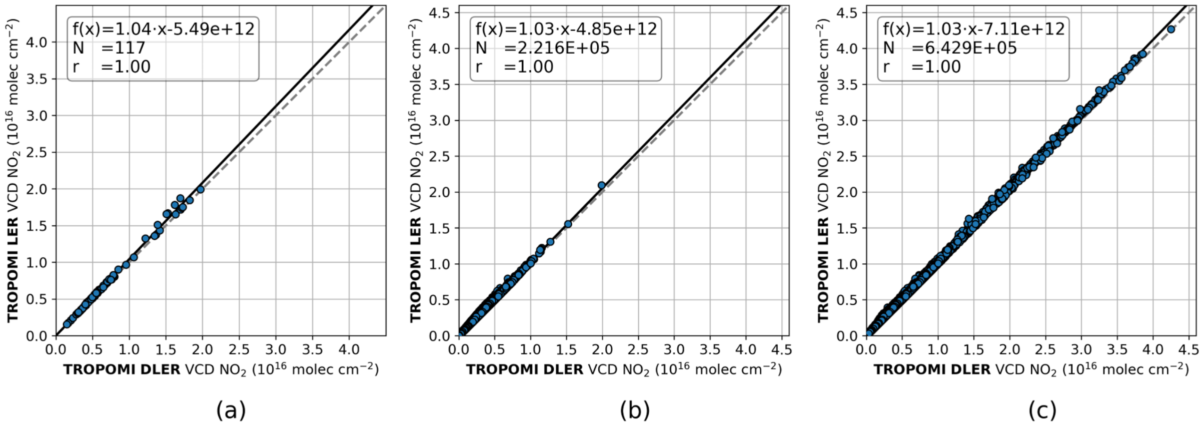

Figure B.9: Scatter plots of TROPOMI IUP V02.03.01 tropospheric NO_2 VCDs with TROPOMI LER respectively TROPOMI DLER for: (a) the 117 TROPOMI pixels coinciding with the AirMAP measurements used throughout the study, (b) a larger orbit segment over western Europe on 13 September 2020, and (c) one full orbit including the campaign area on 13 September 2020. All data are quality and cloud filtered using the qa_value of 0.75.

C | Appendix: Tram DOAS

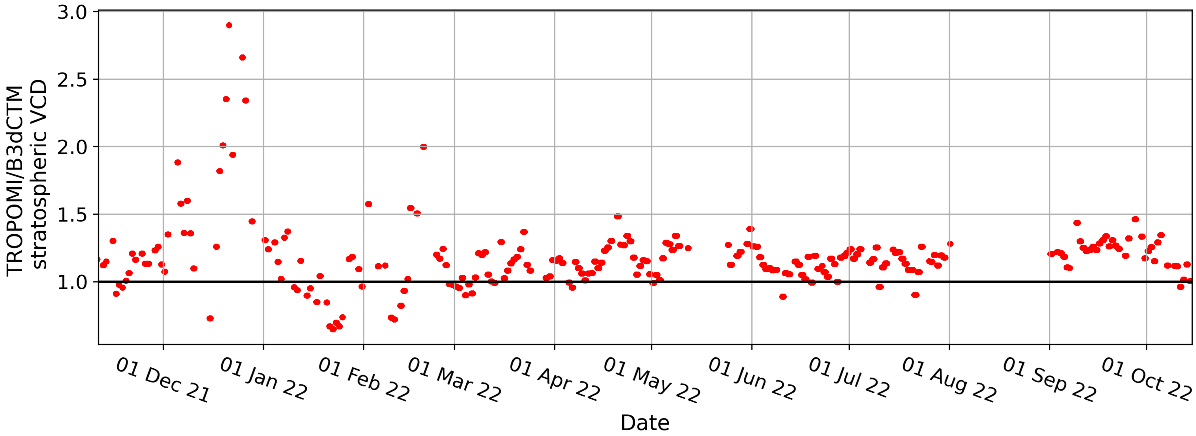

Figure C.1: Scale factor for B3dCTM stratospheric NO_2 VCDs determined from the difference of TROPOMI and B3dCTM stratospheric NO_2 VCD at the TROPOMI overpass for the tram DOAS measurement period from 11 November 2021 to 15 October 2022.

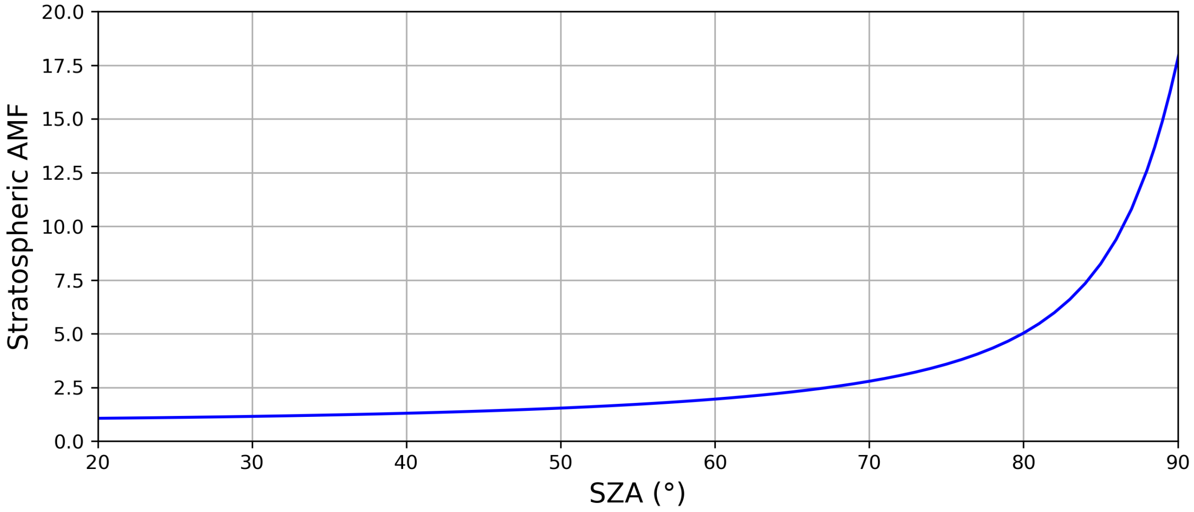

Figure C.2: Stratospheric AMF as a function of SZA simulated with SCIATRAN.

Bibliography

Airyx GmbH: SkySpec Compact Instrument v.200, URL `https://airyx.de/wp-content/uploads/2022/05/SkySpec-Compact_v200.pdf`, last access: 14 July 2022.

ASTM: G173-03: Standard Tables for Reference Solar Spectral Irradiances: Direct Normal and Hemispherical on 37° Tilted Surface, 2020.

ASTM: E-490-00: Standard Solar Constant and Zero Air Mass Solar Spectral Irradiance Tables, 2022.

Atkinson, R., Baulch, D. L., Cox, R. A., Crowley, J. N., Hampson, R. F., Hynes, R. G., Jenkin, M. E., Rossi, M. J., and Troe, J.: Evaluated kinetic and photochemical data for atmospheric chemistry: Volume I - gas phase reactions of O_x, HO_x, NO_x and SO_x species, Atmospheric Chemistry and Physics, 4, 1461–1738, https://doi.org/10.5194/acp-4-1461-2004, 2004.

Bauwens, M., Compernolle, S., Stavrakou, T., Müller, J.-F., Van Gent, J., Eskes, H., Levelt, P., van der A, R., Veefkind, J., Vlietinck, J., and Zehner, C.: Impact of coronavirus outbreak on NO2 pollution assessed using TROPOMI and OMI observations, Geophysical Research Letters, 47, e2020GL087 978, https://doi.org/10.1029/2020GL087978, 2020.

Behrens, L. K., Hilboll, A., Richter, A., Peters, E., Alvarado, L. M. A., Kalisz Hedegaard, A. B., Wittrock, F., Burrows, J. P., and Vrekoussis, M.: Detection of outflow of formaldehyde and glyoxal from the African continent to the Atlantic Ocean with a MAX-DOAS instrument, Atmospheric Chemistry and Physics, 19, 10 257–10 278, https://doi.org/10.5194/acp-19-10257-2019, 2019.

Beirle, S., Platt, U., Wenig, M., and Wagner, T.: Weekly cycle of NO_2 by GOME measurements: a signature of anthropogenic sources, Atmospheric Chemistry and Physics, 3, 2225–2232, https://doi.org/10.5194/acp-3-2225-2003, 2003.

Beirle, S., Boersma, K. F., Platt, U., Lawrence, M. G., and Wagner, T.: Megacity emissions and lifetimes of nitrogen oxides probed from space, Science, 333, 1737–1739, https://doi.org/10.1126/science.1207824, 2011.

Beirle, S., Borger, C., Dörner, S., Li, A., Hu, Z., Liu, F., Wang, Y., and Wagner, T.: Pinpointing nitrogen oxide emissions from space, Science advances, 5, eaax9800, https://doi.org/10.1126/sciadv.aax9800, 2019.

Beirle, S., Borger, C., Dörner, S., Eskes, H., Kumar, V., de Laat, A., and Wagner, T.: Catalog of NO_x emissions from point sources as derived from the divergence of the NO_2 flux for TROPOMI, Earth System Science Data, 13, 2995–3012, https://doi.org/10.5194/essd-13-2995-2021, 2021.

Boersma, K. F., Eskes, H. J., and Brinksma, E. J.: Error analysis for tropospheric NO2 retrieval from space, Journal of Geophysical Research: Atmospheres, 109, https://doi.org/10.1029/2003JD003962, 2004.

Boersma, K. F., Eskes, H. J., Dirksen, R. J., van der A, R. J., Veefkind, J. P., Stammes, P., Huijnen, V., Kleipool, Q. L., Sneep, M., Claas, J., Leitão, J., Richter, A., Zhou, Y., and Brunner, D.: An improved tropospheric NO_2 column retrieval algorithm for the Ozone Monitoring Instrument, Atmospheric Measurement Techniques, 4, 1905–1928, https://doi.org/10.5194/amt-4-1905-2011, 2011.

Bösch, T.: Detailed analysis of MAX-DOAS measurements in Bremen: spatial and temporal distribution of aerosols, formaldehyde and nitrogen dioxide, Ph.D. thesis, Universität Bremen, URL `https://media.suub.uni-bremen.de/handle/elib/1572`, 2019.

Bovensmann, H., Burrows, J., Buchwitz, M., Frerick, J., Noël, S., Rozanov, V., Chance, K., and Goede, A.: SCIAMACHY: Mission objectives and measurement modes, Journal of the atmospheric sciences, 56, 127–150, 1999.

Brasseur, G. P. and Solomon, S.: Aeronomy of the Middle Atmosphere, Springer Netherlands, URL `https://www.ebook.de/de/product/5271761/guy_p_brasseur_susan_solomon_aeronomy_of_the_middle_atmosphere.html`, 2005.

Brinksma, E. J., Pinardi, G., Volten, H., Braak, R., Richter, A., Schönhardt, A., van Roozendael, M., Fayt, C., Hermans, C., Dirksen, R. J., Vlemmix, T., Berkhout, A. J. C., Swart, D. P. J., Oetjen, H., Wittrock, F., Wagner, T., Ibrahim, O. W., de Leeuw, G., Moerman, M., Curier, R. L., Celarier, E. A., Cede, A., Knap, W. H., Veefkind, J. P., Eskes, H. J., Allaart, M., Rothe, R., Piters, A. J. M., and Levelt, P. F.: The 2005 and 2006 DANDELIONS NO2 and aerosol intercomparison campaigns, Journal of Geophysical Research: Atmospheres, 113, https://doi.org/10.1029/2007JD008808, 2008.

Bucsela, E. J., Krotkov, N. A., Celarier, E. A., Lamsal, L. N., Swartz, W. H., Bhartia, P. K., Boersma, K. F., Veefkind, J. P., Gleason, J. F., and Pickering, K. E.: A new stratospheric and tropospheric NO_2 retrieval algorithm for nadir-viewing satellite instruments: applications to OMI, Atmospheric Measurement Techniques, 6, 2607–2626, https://doi.org/10.5194/amt-6-2607-2013, 2013.

Burkholder, J., Sander, S., Abbatt, J., Barker, J., Cappa, C., Crounse, J., Dibble, T., Huie, R., Kolb, C., Kurylo, M., Orkin, V., Percival, C., Wilmouth, D., and Wine, P.: Chemical kinetics and photochemical data for use in atmospheric studies; evaluation number 19, Tech. rep., Pasadena, CA: Jet Propulsion Laboratory, National Aeronautics and Space Administration, URL `http://hdl.handle.net/2014/45510`, last access: 21 February 2022, 2020.

Burrows, J. P., Weber, M., Buchwitz, M., Rozanov, V., Ladstätter-Weißenmayer, A., Richter, A., DeBeek, R., Hoogen, R., Bramstedt, K., Eichmann, K.-U., Eisinger, M., and Perner, D.: The Global Ozone Monitoring Experiment (GOME): Mission Concept and First Scientific Results, Journal of the Atmospheric Sciences, 56, 151 – 175, URL `https://journals.ametsoc.org/view/journals/atsc/56/2/1520-0469_1999_056_0151_tgomeg_2.0.co_2.xml`, 1999.

Burrows, J. P., Borrell, P., and Platt, U.: The Remote Sensing of Tropospheric Composition from Space, Springer Berlin Heidelberg, https://doi.org/10.1007/978-3-642-14791-3, 2011.

Cede, A., Tiefengraber, M., Gebetsberger, M., and Spinei Lind, E.: Pandonia Global NetworkData Products Readme Document, Tech. rep., PGN-DataProducts-Readme, version 1.8-5, 31 December 2021, available at: `https://www.pandonia-global-network.org/home/documents/reports`, last access: 2 December 2022, 2021.

Chimot, J., Vlemmix, T., Veefkind, J. P., de Haan, J. F., and Levelt, P. F.: Impact of aerosols on the OMI tropospheric NO_2 retrievals over industrialized regions: how accurate is the aerosol correction of cloud-free scenes via a simple cloud model?, Atmospheric Measurement Techniques, 9, 359–382, https://doi.org/10.5194/amt-9-359-2016, 2016.

Compernolle, S., Verhoelst, T., Pinardi, G., Granville, J., Hubert, D., Keppens, A., Niemeijer, S., Rino, B., Bais, A., Beirle, S., Boersma, F., Burrows, J. P., De Smedt, I., Eskes, H., Goutail, F., Hendrick, F., Lorente, A., Pazmino, A., Piters, A., Peters, E., Pommereau, J.-P., Remmers, J., Richter, A., van Geffen, J., Van Roozendael, M., Wagner, T., and Lambert, J.-C.: Validation of Aura-OMI QA4ECV NO_2 climate data records with ground-based DOAS networks: the role of measurement and comparison uncertainties, Atmospheric Chemistry and Physics, 20, 8017–8045, https://doi.org/10.5194/acp-20-8017-2020, 2020.

Compernolle, S., Argyrouli, A., Lutz, R., Sneep, M., Lambert, J.-C., Fjæraa, A. M., Hubert, D., Keppens, A., Loyola, D., O'Connor, E., Romahn, F., Stammes, P., Verhoelst, T., and Wang, P.: Validation of the Sentinel-5 Precursor TROPOMI cloud data with Cloudnet, Aura OMI O_2–O_2, MODIS, and Suomi-NPP VIIRS, Atmospheric Measurement Techniques, 14, 2451–2476, https://doi.org/10.5194/amt-14-2451-2021, 2021.

Constantin, D.-E., Merlaud, A., Van Roozendael, M., Voiculescu, M., Fayt, C., Hendrick, F., Pinardi, G., and Georgescu, L.: Measurements of Tropospheric NO2 in Romania Using a Zenith-Sky Mobile DOAS System and Comparisons with Satellite Observations, Sensors, 13, 3922–3940, https://doi.org/10.3390/s130303922, 2013.

Crippa, M., Guizzardi, D., Muntean, M., Schaaf, E., Dentener, F., van Aardenne, J. A., Monni, S., Doering, U., Olivier, J. G., Pagliari, V., et al.: Gridded emissions of air pollutants for the period 1970–2012 within EDGAR v4. 3.2, Earth Syst. Sci. Data, 10, 1987–2013, https://doi.org/10.5194/essd-10-1987-2018, 2018.

Crippa, M., Oreggioni, G., Guizzardi, D., Muntean, M., Schaaf, E., Lo Vullo, E., Solazzo, E., Monforti-Ferrario, F., Olivier, J. G., and Vignati, E.: Fossil CO2 and GHG emissions of all world countries, Luxemburg: Publication Office of the European Union, https://doi.org/10.2760/655913, 2019.

Crippa, M., Solazzo, E., Huang, G., Guizzardi, D., Koffi, E., Muntean, M., Schieberle, C., Friedrich, R., and Janssens-Maenhout, G.: High resolution temporal profiles in the Emissions Database for Global Atmospheric Research, Scientific data, 7, 1–17, https://doi.org/10.1038/s41597-020-0462-2, 2020.

Danckaert, T., Fayt, C., Van Roozendael, M., De Smedt, I., Letocart, V., Merlaud, A., and Pinardi, G.: QDOAS Software user manual Version 3.2, URL `https://uv-vis.aeronomie.be/software/QDOAS/QDOAS_manual.pdf`, last access: 14 July 2022, 2017.

de Foy, B., Wilkins, J. L., Lu, Z., Streets, D. G., and Duncan, B. N.: Model evaluation of methods for estimating surface emissions and chemical lifetimes from satellite data, Atmospheric Environment, 98, 66–77, https://doi.org/10.1016/j.atmosenv.2014.08.051, 2014.

de Foy, B., Lu, Z., Streets, D. G., Lamsal, L. N., and Duncan, B. N.: Estimates of power plant NOx emissions and lifetimes from OMI NO2 satellite retrievals, Atmospheric Environment, 116, 1–11, https://doi.org/10.1016/j.atmosenv.2015.05.056, 2015.

de Graaf, M.: TROPOMI ATBD of theAerosol Optical Thickness, Tech. rep., S5P-KNMI-L2-0033-RP, Issue 3.0.0, available at `https://data-portal.s5p-pal.com/products/aot.html`, last access: 21 December 2022, 2022.

Dickerson, R. R., Stedman, D. H., and Delany, A. C.: Direct measurements of ozone and nitrogen dioxide photolysis rates in the troposphere, Journal of Geophysical Research: Oceans, 87, 4933–4946, https://doi.org/10.1029/JC087iC07p04933, 1982.

Dimitropoulou, E., Hendrick, F., Pinardi, G., Friedrich, M. M., Merlaud, A., Tack, F., De Longueville, H., Fayt, C., Hermans, C., Laffineur, Q., Fierens, F., and Van Roozendael, M.: Validation of TROPOMI tropospheric NO_2 columns using dual-scan multi-axis differential optical absorption spectroscopy (MAX-DOAS) measurements in Uccle, Brussels, Atmospheric Measurement Techniques, 13, 5165–5191, https://doi.org/10.5194/amt-13-5165-2020, 2020.

Dimitropoulou, E., Hendrick, F., Friedrich, M. M., Tack, F., Pinardi, G., Merlaud, A., Fayt, C., Hermans, C., Fierens, F., and Van Roozendael, M.: Horizontal distribution of tropospheric NO_2 and aerosols derived by dual-scan multi-wavelength multi-axis differential optical absorption spectroscopy (MAX-DOAS) measurements in Uccle, Belgium, Atmospheric Measurement Techniques, 15, 4503–4529, https://doi.org/10.5194/amt-15-4503-2022, 2022.

Dittman, M. G., Ramberg, E., Chrisp, M., Rodriguez, J. V., Sparks, A. L., Zaun, N. H., Hendershot, P., Dixon, T., Philbrick, R. H., and Wasinger, D.: Nadir ultraviolet imaging spectrometer for the NPOESS Ozone Mapping and Profiler Suite (OMPS), in: Earth Observing Systems VII, vol. 4814, pp. 111–119, International Society for Optics and Photonics, https://doi.org/10.1117/12.453748, 2002.

Donner, S.: Mobile MAX-DOAS measurements of the tropospheric formaldehyde column in the Rhein-Main region, Master's thesis, University of Mainz, http://hdl.handle.net/11858/00-001M-0000-002C-EB17-2, last access: 15 August 2022, 2016.

Douros, J., Eskes, H., van Geffen, J., Boersma, K. F., Compernolle, S., Pinardi, G., Blechschmidt, A.-M., Peuch, V.-H., Colette, A., and Veefkind, P.: Comparing Sentinel-5P TROPOMI NO_2 column observations with the CAMS regional air quality ensemble, Geoscientific Model Development, 16, 509–534, https://doi.org/10.5194/gmd-16-509-2023, 2023.

Drosoglou, T., Bais, A. F., Zyrichidou, I., Kouremeti, N., Poupkou, A., Liora, N., Giannaros, C., Koukouli, M. E., Balis, D., and Melas, D.: Comparisons of ground-based tropospheric NO_2 MAX-DOAS measurements to satellite observations with the aid of an air quality model over the Thessaloniki area, Greece, Atmospheric Chemistry and Physics, 17, 5829–5849, https://doi.org/10.5194/acp-17-5829-2017, 2017.

EDGAR Emissions Database for Global Atmospheric Research: Air and Toxic pollutants - World NOx emissions by sector [data set], URL `https://edgar.jrc.ec.europa.eu/air_pollutants`, last access: 2 April 2023.

Eskes, H. and Eichmann, K.: S5P MPC Product Readme Nitrogen Dioxide, Tech. rep., Report S5P-MPC-KNMI-PRF-NO2, issue 2.2, 20 July 2022, ESA, available at https://sentinel.esa.int/web/sentinel/technical-guides/sentinel-5p/products-algorithms, last access: 23 September 2022, 2022.

European Environment Agency: Industrial Reporting under the Industrial Emissions Directive 2010/75/EU and European Pollutant Release and Transfer Register Regulation (EC) No 166/2006, 2007-2021 ver. 8.0 [data set], URL `https://www.eea.europa.eu/data-and-maps/data/industrial-reporting-under-the-industrial-7`, last access: 3 May 2023.

Faustini, A., Rapp, R., and Forastiere, F.: Nitrogen dioxide and mortality: review and meta-analysis of long-term studies, European Respiratory Journal, 44, 744–753, https://doi.org/10.1183/09031936.00114713, 2014.

Finlayson-Pitts, B. J. and Pitts Jr, J. N.: Chemistry of the upper and lower atmosphere: theory, experiments, and applications, Elsevier, https://doi.org/10.1016/B978-0-12-257060-5.X5000-X, 2000.

Friedrich, M. M., Rivera, C., Stremme, W., Ojeda, Z., Arellano, J., Bezanilla, A., García-Reynoso, J. A., and Grutter, M.: NO_2 vertical profiles and column densities from MAX-DOAS measurements in Mexico City, Atmospheric Measurement Techniques, 12, 2545–2565, https://doi.org/10.5194/amt-12-2545-2019, 2019.

Georgoulias, A. K., van der A, R. J., Stammes, P., Boersma, K. F., and Eskes, H. J.: Trends and trend reversal detection in 2 decades of tropospheric NO_2 satellite observations, Atmospheric Chemistry and Physics, 19, 6269–6294, https://doi.org/10.5194/acp-19-6269-2019, 2019.

Goldberg, D. L., Lu, Z., Streets, D. G., de Foy, B., Griffin, D., McLinden, C. A., Lamsal, L. N., Krotkov, N. A., and Eskes, H.: Enhanced Capabilities of TROPOMI NO2: Estimating NO X from North American Cities and Power Plants, Environmental science & technology, 53, 12 594–12 601, 2019.

Goldberg, D. L., Anenberg, S. C., Griffin, D., McLinden, C. A., Lu, Z., and Streets, D. G.: Disentangling the impact of the COVID-19 lockdowns on urban NO2 from natural variability, Geophysical Research Letters, 47, e2020GL089 269, https://doi.org/10.1029/2020GL089269, 2020.

Goldberg, D. L., Anenberg, S. C., Kerr, G. H., Mohegh, A., Lu, Z., and Streets, D. G.: TROPOMI NO2 in the United States: A detailed look at the annual averages, weekly cycles, effects of temperature, and correlation with surface NO2 concentrations, Earth's future, 9, e2020EF001 665, https://doi.org/10.1029/2020EF001665, 2021.

Hains, J. C., Boersma, K. F., Kroon, M., Dirksen, R. J., Cohen, R. C., Perring, A. E., Bucsela, E., Volten, H., Swart, D. P. J., Richter, A., Wittrock, F., Schoenhardt, A., Wagner, T., Ibrahim, O. W., van Roozendael, M., Pinardi, G., Gleason, J. F., Veefkind, J. P., and Levelt, P.: Testing and improving OMI DOMINO tropospheric NO2 using observations from the DANDELIONS and INTEX-B validation campaigns, Journal of Geophysical Research: Atmospheres, 115, https://doi.org/10.1029/2009JD012399, 2010.

Hendrick, F., Pinardi, G., Van Roozendael, M., Apituley, A., Piters, A., Richter, A., Wagner, T., Kreher, K., Friess, U., and Lampel, J.: Fiducial Reference Measurements for Ground-Based DOAS Air-Quality Observations, Deliverable D13 ESA Contract No.4000118181/16/I-EF, URL `https://frm4doas.aeronomie.be/ProjectDir/Deliverables/FRM4DOAS_D13_Campaign_Planning_Document_20161021_final.pdf`, last access 14 July 2022, 2016.

Hersbach, H., Bell, B., Berrisford, P., Biavati, G., Horányi, A., Muñoz Sabater, J., Nicolas, J., Peubey, C., Radu, R., Rozum, I., Schepers, D., Simmons, A., Soci, C., Dee, D., and Thépaut, J.-N.: ERA5 hourly data on single levels from 1979 to present, Copernicus Climate Change Service (C3S) Climate Data Store (CDS), 10, https://doi.org/10.24381/cds.adbb2d47, last access: 31 August 2022, 2018.

Heue, K.-P., Richter, A., Bruns, M., Burrows, J. P., v. Friedeburg, C., Platt, U., Pundt, I., Wang, P., and Wagner, T.: Validation of SCIAMACHY tropospheric NO_2-columns with AMAXDOAS measurements, Atmospheric Chemistry and Physics, 5, 1039–1051, https://doi.org/10.5194/acp-5-1039-2005, 2005.

Hilboll, A., Richter, A., and Burrows, J. P.: Long-term changes of tropospheric NO_2 over megacities derived from multiple satellite instruments, Atmospheric Chemistry and Physics, 13, 4145–4169, https://doi.org/10.5194/acp-13-4145-2013, 2013b.

Holland, F., Hofzumahaus, A., Schäfer, J., Kraus, A., and Pätz, H.-W.: Measurements of OH and HO2 radical concentrations and photolysis frequencies during BERLIOZ, Journal of Geophysical Research: Atmospheres, 108, PHO 2–1–PHO 2–23, https://doi.org/10.1029/2001JD001393, 2003.

Hönninger, G., von Friedeburg, C., and Platt, U.: Multi axis differential optical absorption spectroscopy (MAX-DOAS), Atmospheric Chemistry and Physics, 4, 231–254, https://doi.org/10.5194/acp-4-231-2004, 2004.

Huijnen, V., Eskes, H. J., Poupkou, A., Elbern, H., Boersma, K. F., Foret, G., Sofiev, M., Valdebenito, A., Flemming, J., Stein, O., Gross, A., Robertson, L., D'Isidoro, M., Kioutsioukis, I., Friese, E., Amstrup, B., Bergstrom, R., Strunk, A., Vira, J., Zyryanov, D., Maurizi, A., Melas, D., Peuch, V.-H., and Zerefos, C.: Comparison of OMI NO_2 tropospheric columns with an ensemble of global and European regional air quality models, Atmospheric Chemistry and Physics, 10, 3273–3296, https://doi.org/10.5194/acp-10-3273-2010, 2010.

Ialongo, I., Hakkarainen, J., Hyttinen, N., Jalkanen, J.-P., Johansson, L., Boersma, K., Krotkov, N., and Tamminen, J.: Characterization of OMI tropospheric NO2 over the Baltic Sea region, Atmospheric Chemistry and Physics, 14, 7795, 2014.

Ibrahim, O., Shaiganfar, R., Sinreich, R., Stein, T., Platt, U., and Wagner, T.: Car MAX-DOAS measurements around entire cities: quantification of NO_x emissions from the cities of Mannheim and Ludwigshafen (Germany), Atmospheric Measurement Techniques, 3, 709–721, https://doi.org/10.5194/amt-3-709-2010, 2010.

Irie, H., Takashima, H., Kanaya, Y., Boersma, K. F., Gast, L., Wittrock, F., Brunner, D., Zhou, Y., and Van Roozendael, M.: Eight-component retrievals from ground-based MAX-DOAS observations, Atmospheric Measurement Techniques, 4, 1027–1044, https://doi.org/10.5194/amt-4-1027-2011, 2011.

Jacob, D. J.: Introduction to atmospheric chemistry, Princeton University Press, 1999.

John M. Wallace, P. V. H.: Atmospheric Science, Elsevier Science Publishing Co Inc, URL `https://www.ebook.de/de/product/4444872/john_m_university_of_washington_seattle_u_s_a_wallace_peter_v_university_of_washington_seattle_u_s_a_hobbs_atmospheric_science.html`, 2006.

Judd, L. M., Al-Saadi, J. A., Szykman, J. J., Valin, L. C., Janz, S. J., Kowalewski, M. G., Eskes, H. J., Veefkind, J. P., Cede, A., Mueller, M., Gebetsberger, M., Swap, R., Pierce, R. B., Nowlan, C. R., Abad, G. G., Nehrir, A., and Williams, D.: Evaluating Sentinel-5P TROPOMI tropospheric NO_2 column densities with airborne and Pandora spectrometers near New York City and Long Island Sound, Atmospheric Measurement Techniques, 13, 6113–6140, https://doi.org/10.5194/amt-13-6113-2020, 2020.

Kim, J., Jeong, U., Ahn, M.-H., Kim, J. H., Park, R. J., Lee, H., Song, C. H., Choi, Y.-S., Lee, K.-H., Yoo, J.-M., Jeong, M.-J., Park, S. K., Lee, K.-M., Song, C.-K., Kim, S.-W., Kim, Y. J., Kim, S.-W., Kim, M., Go, S., Liu, X., Chance, K., Miller, C. C., Al-Saadi, J., Veihelmann, B., Bhartia, P. K., Torres, O., Abad, G. G., Haffner, D. P., Ko, D. H., Lee, S. H., Woo, J.-H., Chong, H., Park, S. S., Nicks, D., Choi, W. J., Moon, K.-J., Cho, A., Yoon, J., kyun Kim, S., Hong, H., Lee, K., Lee, H., Lee, S., Choi, M., Veefkind, P., Levelt, P. F., Edwards, D. P., Kang, M., Eo, M., Bak, J., Baek, K., Kwon, H.-A., Yang, J., Park, J., Han, K. M., Kim, B.-R., Shin, H.-W., Choi, H., Lee, E., Chong, J., Cha, Y., Koo, J.-H., Irie, H., Hayashida, S., Kasai, Y., Kanaya, Y., Liu, C., Lin, J., Crawford, J. H., Carmichael, G. R., Newchurch, M. J., Lefer, B. L., Herman, J. R., Swap, R. J., Lau, A. K. H., Kurosu, T. P., Jaross, G., Ahlers, B., Dobber, M., McElroy, C. T., and Choi, Y.: New Era of Air Quality Monitoring from Space: Geostationary Environment Monitoring Spectrometer (GEMS), Bulletin of the American Meteorological Society, 101, E1 – E22, https://doi.org/10.1175/BAMS-D-18-0013.1, 2020.

Kreher, K., Van Roozendael, M., Hendrick, F., Apituley, A., Dimitropoulou, E., Frieß, U., Richter, A., Wagner, T., Lampel, J., Abuhassan, N., Ang, L., Anguas, M., Bais, A., Benavent, N., Bösch, T., Bognar, K., Borovski, A., Bruchkouski, I., Cede, A., Chan, K. L., Donner, S., Drosoglou, T., Fayt, C., Finkenzeller, H., Garcia-Nieto, D., Gielen, C., Gómez-Martín, L., Hao, N., Henzing, B., Herman, J. R., Hermans, C., Hoque, S., Irie, H., Jin, J., Johnston, P., Khayyam Butt, J., Khokhar, F., Koenig, T. K., Kuhn, J., Kumar, V., Liu, C., Ma, J., Merlaud, A., Mishra, A. K., Müller, M., Navarro-Comas, M., Ostendorf, M., Pazmino, A., Peters, E., Pinardi, G., Pinharanda, M., Piters, A., Platt, U., Postylyakov, O., Prados-Roman, C., Puentedura, O., Querel, R., Saiz-Lopez, A., Schönhardt, A., Schreier, S. F., Seyler, A., Sinha, V., Spinei, E., Strong, K., Tack, F., Tian, X., Tiefengraber, M., Tirpitz, J.-L., van Gent, J., Volkamer, R., Vrekoussis, M., Wang, S., Wang, Z., Wenig, M., Wittrock, F., Xie, P. H., Xu, J., Yela, M., Zhang, C., and Zhao, X.: Intercomparison of NO_2, O_4, O_3 and HCHO slant column measurements by MAX-DOAS and zenith-sky UV–visible spectrometers during CINDI-2, Atmospheric Measurement Techniques, 13, 2169–2208, https://doi.org/10.5194/amt-13-2169-2020, 2020.

Kunhikrishnan, T., Lawrence, M. G., von Kuhlmann, R., Richter, A., Ladstätter-Weißenmayer, A., and Burrows, J. P.: Analysis of tropospheric NOx over Asia using the model of atmospheric transport and chemistry (MATCH-MPIC) and GOME-satellite observations, Atmospheric Environment, 38, 581–596, 2004.

Lampel, J., Pöhler, D., Tschritter, J., Frieß, U., and Platt, U.: On the relative absorption strengths of water vapour in the blue wavelength range, Atmospheric Measurement Techniques, 8, 4329–4346, https://doi.org/10.5194/amt-8-4329-2015, 2015.

Lange, K., Richter, A., and Burrows, J. P.: Variability of nitrogen oxide emission fluxes and lifetimes estimated from Sentinel-5P TROPOMI observations, Atmospheric Chemistry and Physics, 22, 2745–2767, https://doi.org/10.5194/acp-22-2745-2022, 2022.

Lange, K., Richter, A., Schönhardt, A., Meier, A. C., Bösch, T., Seyler, A., Krause, K., Behrens, L. K., Wittrock, F., Merlaud, A., Tack, F., Fayt, C., Friedrich, M. M., Dimitropoulou, E., Van Roozendael, M., Kumar, V., Donner, S., Dörner, S., Lauster, B., Razi, M., Borger, C., Uhlmannsiek, K., Wagner, T., Ruhtz, T., Eskes, H., Bohn, B., Santana Diaz, D., Abuhassan, N., Schüttemeyer, D., and Burrows, J. P.: Validation of Sentinel-5P TROPOMI tropospheric NO_2 products by comparison with NO_2 measurements from airborne imaging DOAS, ground-based stationary DOAS, and mobile car DOAS measurements during the S5P-VAL-DE-Ruhr campaign, Atmospheric Measurement Techniques, 16, 1357–1389, https://doi.org/10.5194/amt-16-1357-2023, 2023.

Laughner, J. L. and Cohen, R. C.: Direct observation of changing NOx lifetime in North American cities, Science, 366, 723–727, https://doi.org/10.1126/science.aax6832, 2019.

Leitão, J., Richter, A., Vrekoussis, M., Kokhanovsky, A., Zhang, Q. J., Beekmann, M., and Burrows, J. P.: On the improvement of NO_2 satellite retrievals – aerosol impact on the airmass factors, Atmospheric Measurement Techniques, 3, 475–493, https://doi.org/10.5194/amt-3-475-2010, 2010.

Leue, C., Wenig, M., Wagner, T., Klimm, O., Platt, U., and Jähne, B.: Quantitative analysis of NO x emissions from Global Ozone Monitoring Experiment satellite image sequences, Journal of Geophysical Research: Atmospheres, 106, 5493–5505, https://doi.org/10.1029/2000JD900572, 2001.

Levelt, P. F., van den Oord, G. H., Dobber, M. R., Malkki, A., Visser, H., de Vries, J., Stammes, P., Lundell, J. O., and Saari, H.: The ozone monitoring instrument, IEEE Transactions on geoscience and remote sensing, 44, 1093–1101, https://doi.org/10.1109/TGRS.2006.872333, 2006.

Levelt, P. F., Stein Zweers, D. C., Aben, I., Bauwens, M., Borsdorff, T., De Smedt, I., Eskes, H. J., Lerot, C., Loyola, D. G., Romahn, F., Stavrakou, T., Theys, N., Van Roozendael, M., Veefkind, J. P., and Verhoelst, T.: Air quality impacts of COVID-19 lockdown measures detected from space using high spatial resolution observations of multiple trace gases from Sentinel-5P/TROPOMI, Atmospheric Chemistry and Physics Discussions, 2021, 1–53, https://doi.org/10.5194/acp-2021-534, 2021.

Liu, F., Beirle, S., Zhang, Q., Dörner, S., He, K., and Wagner, T.: NOx lifetimes and emissions of cities and power plants in polluted background estimated by satellite observations, Atmospheric Chemistry and Physics, 16, 5283, https://doi.org/10.5194/acp-16-5283-2016, 2016.

Liu, F., Page, A., Strode, S. A., Yoshida, Y., Choi, S., Zheng, B., Lamsal, L. N., Li, C., Krotkov, N. A., Eskes, H., van der A, R., Veefkind, P., Levelt, P. F., Hauser, O., and

Joiner, J.: Abrupt decline in tropospheric nitrogen dioxide over China after the outbreak of COVID-19, Science Advances, 6, eabc2992, https://doi.org/10.1126/sciadv.abc2992, 2020a.

Liu, M., Lin, J., Kong, H., Boersma, K. F., Eskes, H., Kanaya, Y., He, Q., Tian, X., Qin, K., Xie, P., Spurr, R., Ni, R., Yan, Y., Weng, H., and Wang, J.: A new TROPOMI product for tropospheric NO_2 columns over East Asia with explicit aerosol corrections, Atmospheric Measurement Techniques, 13, 4247–4259, https://doi.org/10.5194/amt-13-4247-2020, 2020b.

Lorente, A., Folkert Boersma, K., Yu, H., Dörner, S., Hilboll, A., Richter, A., Liu, M., Lamsal, L. N., Barkley, M., De Smedt, I., Van Roozendael, M., Wang, Y., Wagner, T., Beirle, S., Lin, J.-T., Krotkov, N., Stammes, P., Wang, P., Eskes, H. J., and Krol, M.: Structural uncertainty in air mass factor calculation for NO_2 and HCHO satellite retrievals, Atmospheric Measurement Techniques, 10, 759–782, https://doi.org/10.5194/amt-10-759-2017, 2017.

Lorente, A., Boersma, K. F., Stammes, P., Tilstra, L. G., Richter, A., Yu, H., Kharbouche, S., and Muller, J.-P.: The importance of surface reflectance anisotropy for cloud and NO_2 retrievals from GOME-2 and OMI, Atmospheric Measurement Techniques, 11, 4509–4529, https://doi.org/10.5194/amt-11-4509-2018, 2018.

Lorente, A., Boersma, K., Eskes, H., Veefkind, J., Van Geffen, J., de Zeeuw, M., van der Gon, H. D., Beirle, S., and Krol, M.: Quantification of nitrogen oxides emissions from build-up of pollution over Paris with TROPOMI, Scientific reports, 9, 1–10, https://doi.org/10.1038/s41598-019-56428-5, 2019.

Loyola, D., Lutz, R., Argyrouli, A., and Spurr, R.: S5P/TROPOMI ATBD Cloud Products, Tech. rep., S5P-DLR-L2-ATBD-400I, Issue 2.3, available at `https://sentinel.esa.int/documents/247904/2476257/Sentinel-5P-TROPOMI-ATBD-Clouds`, last access: 10 May 2023, 2021.

Lu, K. D., Hofzumahaus, A., Holland, F., Bohn, B., Brauers, T., Fuchs, H., Hu, M., Häseler, R., Kita, K., Kondo, Y., Li, X., Lou, S. R., Oebel, A., Shao, M., Zeng, L. M., Wahner, A., Zhu, T., Zhang, Y. H., and Rohrer, F.: Missing OH source in a suburban environment near Beijing: observed and modelled OH and HO_2 concentrations in summer 2006, Atmospheric Chemistry and Physics, 13, 1057–1080, https://doi.org/10.5194/acp-13-1057-2013, 2013.

Lu, Z., Streets, D., De Foy, B., Lamsal, L., Duncan, B., and Xing, J.: Emissions of nitrogen oxides from US urban areas: estimation from Ozone Monitoring Instrument retrievals for 2005-2014, Atmospheric Chemistry and Physics Discussions (Online), 15, https://doi.org/10.5194/acp-15-10367-2015, 2015.

Ma, J. Z., Beirle, S., Jin, J. L., Shaiganfar, R., Yan, P., and Wagner, T.: Tropospheric NO_2 vertical column densities over Beijing: results of the first three years of ground-based MAX-DOAS measurements (2008–2011) and satellite validation, Atmospheric Chemistry and Physics, 13, 1547–1567, https://doi.org/10.5194/acp-13-1547-2013, 2013.

Martin, R. V., Jacob, D. J., Chance, K., Kurosu, T. P., Palmer, P. I., and Evans, M. J.: Global inventory of nitrogen oxide emissions constrained by space-based observations of NO2 columns, Journal of Geophysical Research: Atmospheres, 108, https://doi.org/10.1029/2003JD003453, 2003.

Meier, A. C., Schönhardt, A., Bösch, T., Richter, A., Seyler, A., Ruhtz, T., Constantin, D.-E., Shaiganfar, R., Wagner, T., Merlaud, A., Van Roozendael, M., Belegante, L., Nicolae, D., Georgescu, L., and Burrows, J. P.: High-resolution airborne imaging DOAS measurements of NO_2 above Bucharest during AROMAT, Atmospheric Measurement Techniques, 10, 1831–1857, https://doi.org/10.5194/amt-10-1831-2017, 2017.

Merlaud, A.: Development and use of compact instruments for tropospheric investigations based on optical spectroscopy from mobile platforms, Presses univ. de Louvain, 2013.

Merlaud, A., Tack, F., Constantin, D., Georgescu, L., Maes, J., Fayt, C., Mingireanu, F., Schuettemeyer, D., Meier, A. C., Schönardt, A., Ruhtz, T., Bellegante, L., Nicolae, D., Den Hoed, M., Allaart, M., and Van Roozendael, M.: The Small Whiskbroom Imager for atmospheric compositioN monitorinG (SWING) and its operations from an unmanned aerial vehicle (UAV) during the AROMAT campaign, Atmospheric Measurement Techniques, 11, 551–567, https://doi.org/10.5194/amt-11-551-2018, 2018.

Munro, R., Eisinger, M., Anderson, C., Callies, J., Corpaccioli, E., Lang, R., Lefebvre, A., Livschitz, Y., and Albinana, A. P.: GOME-2 on MetOp, in: Proc. of The 2006 EUMETSAT Meteorological Satellite Conference, Helsinki, Finland, vol. 1216, p. 48, 2006.

Noxon, J. F.: Nitrogen Dioxide in the Stratosphere and Troposphere Measured by Ground-Based Absorption Spectroscopy, Science, 189, 547–549, https://doi.org/10.1126/science.189.4202.547, 1975.

Peters, E., Wittrock, F., Großmann, K., Frieß, U., Richter, A., and Burrows, J. P.: Formaldehyde and nitrogen dioxide over the remote western Pacific Ocean: SCIAMACHY and GOME-2 validation using ship-based MAX-DOAS observations, Atmospheric Chemistry and Physics, 12, 11 179–11 197, https://doi.org/10.5194/acp-12-11179-2012, 2012.

Petty, G. W.: A first course in atmospheric radiation, Sundog Pub, 2006.

Petty, G. W.: A first course in atmospheric thermodynamics, Sundog Publishing, 2008.

Pinardi, G., Van Roozendael, M., Hendrick, F., Theys, N., Abuhassan, N., Bais, A., Boersma, F., Cede, A., Chong, J., Donner, S., Drosoglou, T., Dzhola, A., Eskes, H., Frieß, U., Granville, J., Herman, J. R., Holla, R., Hovila, J., Irie, H., Kanaya, Y., Karagkiozidis, D., Kouremeti, N., Lambert, J.-C., Ma, J., Peters, E., Piters, A., Postylyakov, O., Richter, A., Remmers, J., Takashima, H., Tiefengraber, M., Valks, P., Vlemmix, T., Wagner, T., and Wittrock, F.: Validation of tropospheric NO_2 column measurements of GOME-2A and OMI using MAX-DOAS and direct sun network observations, Atmospheric Measurement Techniques, 13, 6141–6174, https://doi.org/10.5194/amt-13-6141-2020, 2020.

Platt, U. and Perner, D.: Direct measurements of atmospheric CH2O, HNO2, O3, NO2, and SO2 by differential optical absorption in the near UV, Journal of Geophysical Research: Oceans, 85, 7453–7458, https://doi.org/10.1029/JC085iC12p07453, 1980.

Pommier, M., McLinden, C. A., and Deeter, M.: Relative changes in CO emissions over megacities based on observations from space, Geophysical research letters, 40, 3766–3771, 2013.

Popp, C., Brunner, D., Damm, A., Van Roozendael, M., Fayt, C., and Buchmann, B.: High-resolution NO_2 remote sensing from the Airborne Prism EXperiment (APEX) imaging spectrometer, Atmospheric Measurement Techniques, 5, 2211–2225, https://doi.org/10.5194/amt-5-2211-2012, 2012.

Prunet, P., Bacour, C., Price, I., Muller, J., Lewis, P., Vountas, M., von Hoyningen-Huene, W., Burrows, J., Schlundt, C., Bréon, F., Gonzales, L., North, P., and Fischer, J abd Domenech, C.: A Surface Reflectance DAtabase for ESA's Earth Observation Missions (ADAM), Tech. rep., ESA Final Report NOV-3895-NT-12403, Noveltis, URL `https://nebula.esa.int/sites/default/files/neb_study/1089/C4000102979ExS.pdf`, 2013.

Richter, A.: Absorptionsspektroskopische Messungen stratosphärischer Spurengase über Bremen, 53° N, Ph.D. thesis, Universität Bremen, 1997.

Richter, A. and Burrows, J.: Tropospheric NO2 from GOME measurements, Advances in Space Research, 29, 1673–1683, https://doi.org/https://doi.org/10.1016/S0273-1177(02)00100-X, 2002.

Rozanov, V., Rozanov, A., Kokhanovsky, A., and Burrows, J.: Radiative transfer through terrestrial atmosphere and ocean: Software package SCIATRAN, Journal of Quantitative Spectroscopy and Radiative Transfer, 133, 13–71, https://doi.org/10.1016/j.jqsrt.2013.07.004, 2014.

Schönhardt, A., Altube, P., Gerilowski, K., Krautwurst, S., Hartmann, J., Meier, A. C., Richter, A., and Burrows, J. P.: A wide field-of-view imaging DOAS instrument for two-dimensional trace gas mapping from aircraft, Atmospheric Measurement Techniques, 8, 5113–5131, https://doi.org/10.5194/amt-8-5113-2015, 2015.

Schreier, S. F., Richter, A., and Burrows, J. P.: Near-surface and path-averaged mixing ratios of NO_2 derived from car DOAS zenith-sky and tower DOAS off-axis measurements in Vienna: a case study, Atmospheric Chemistry and Physics, 19, 5853–5879, https://doi.org/10.5194/acp-19-5853-2019, 2019.

Schreier, S. F., Richter, A., Peters, E., Ostendorf, M., Schmalwieser, A. W., Weihs, P., and Burrows, J. P.: Dual ground-based MAX-DOAS observations in Vienna, Austria: Evaluation of horizontal and temporal NO2, HCHO, and CHOCHO distributions and comparison with independent data sets, Atmospheric Environment: X, 5, 100 059, https://doi.org/10.1016/j.aeaoa.2019.100059, 2020.

Seinfeld, J. H. and Pandis, S. N.: Atmospheric Chemistry and Physics, John Wiley & Sons Inc., Hoboken, New Jersey, 2006.

Serdyuchenko, A., Gorshelev, V., Weber, M., Chehade, W., and Burrows, J. P.: High spectral resolution ozone absorption cross-sections - Part 2: Temperature dependence, Atmospheric Measurement Techniques, 7, 625–636, https://doi.org/10.5194/amt-7-625-2014, 2014.

Seyler, A., Wittrock, F., Kattner, L., Mathieu-Üffing, B., Peters, E., Richter, A., Schmolke, S., and Burrows, J. P.: Monitoring shipping emissions in the German Bight using MAX-DOAS measurements, Atmospheric Chemistry and Physics, 17, 10 997–11 023, https://doi.org/10.5194/acp-17-10997-2017, 2017.

Shah, V., Jacob, D. J., Li, K., Silvern, R. F., Zhai, S., Liu, M., Lin, J., and Zhang, Q.: Effect of changing NO_x lifetime on the seasonality and long-term trends of satellite-observed tropospheric NO_2 columns over China, Atmospheric Chemistry and Physics, 20, 1483–1495, https://doi.org/10.5194/acp-20-1483-2020, 2020.

Shaiganfar, R., Beirle, S., Sharma, M., Chauhan, A., Singh, R. P., and Wagner, T.: Estimation of NO_x emissions from Delhi using Car MAX-DOAS observations and comparison with OMI satellite data, Atmospheric Chemistry and Physics, 11, 10 871–10 887, https://doi.org/10.5194/acp-11-10871-2011, 2011.

Smith, S. C., Lee, J. D., Bloss, W. J., Johnson, G. P., Ingham, T., and Heard, D. E.: Concentrations of OH and HO_2 radicals during NAMBLEX: measurements and steady state analysis, Atmospheric Chemistry and Physics, 6, 1435–1453, https://doi.org/10.5194/acp-6-1435-2006, 2006.

Solomon, S., Schmeltekopf, A. L., and Sanders, R. W.: On the interpretation of zenith sky absorption measurements, Journal of Geophysical Research: Atmospheres, 92, 8311–8319, https://doi.org/10.1029/JD092iD07p08311, 1987.

Spinei, E., Cede, A., Swartz, W. H., Herman, J., and Mount, G. H.: The use of NO_2 absorption cross section temperature sensitivity to derive NO_2 profile temperature and stratospheric–tropospheric column partitioning from visible direct-sun DOAS measurements, Atmospheric Measurement Techniques, 7, 4299–4316, https://doi.org/10.5194/amt-7-4299-2014, 2014.

Stavrakou, T., Müller, J.-F., Boersma, K. F., De Smedt, I., and Van Der A, R.: Assessing the distribution and growth rates of NOx emission sources by inverting a 10-year record of NO2 satellite columns, Geophysical Research Letters, 35, 2–6, https://doi.org/10.1029/2008GL033521, 2008.

Stavrakou, T., Müller, J.-F., Bauwens, M., Boersma, K., and van Geffen, J.: Satellite evidence for changes in the NO2 weekly cycle over large cities, Scientific reports, 10, 1–9, https://doi.org/10.1038/s41598-020-66891-0, 2020.

Tack, F., Merlaud, A., Iordache, M.-D., Danckaert, T., Yu, H., Fayt, C., Meuleman, K., Deutsch, F., Fierens, F., and Van Roozendael, M.: High-resolution mapping of the NO_2 spatial distribution over Belgian urban areas based on airborne APEX remote sensing, Atmospheric Measurement Techniques, 10, 1665–1688, https://doi.org/10.5194/amt-10-1665-2017, 2017.

Tack, F., Merlaud, A., Meier, A. C., Vlemmix, T., Ruhtz, T., Iordache, M.-D., Ge, X., van der Wal, L., Schuettemeyer, D., Ardelean, M., Calcan, A., Constantin, D., Schönhardt, A., Meuleman, K., Richter, A., and Van Roozendael, M.: Intercomparison of four airborne imaging DOAS systems for tropospheric NO_2 mapping – the AROMAPEX campaign, Atmospheric Measurement Techniques, 12, 211–236, https://doi.org/10.5194/amt-12-211-2019, 2019.

Tack, F., Merlaud, A., Iordache, M.-D., Pinardi, G., Dimitropoulou, E., Eskes, H., Bomans, B., Veefkind, P., and Van Roozendael, M.: Assessment of the TROPOMI tropospheric NO_2 product based on airborne APEX observations, Atmospheric Measurement Techniques, 14, 615–646, https://doi.org/10.5194/amt-14-615-2021, 2021.

Thalman, R. and Volkamer, R.: Temperature dependent absorption cross-sections of O2–O2 collision pairs between 340 and 630 nm and at atmospherically relevant pressure, Phys. Chem. Chem. Phys., 15, 15 371–15 381, https://doi.org/10.1039/C3CP50968K, 2013.

Tilstra, L.: TROPOMI ATBD of the directionally dependent surface Lambertian-equivalent reflectivity, Tech. rep., KNMI Report S5P-KNMI-L3-0301-RP, Issue 1.2.0, available at `https://www.temis.nl/surface/albedo/tropomi_ler.php`, last access: 13 September 2022, 2022.

Tilstra, L. G., Tuinder, O. N. E., Wang, P., and Stammes, P.: Directionally dependent Lambertian-equivalent reflectivity (DLER) of the Earth's surface measured by the GOME-2 satellite instruments, Atmospheric Measurement Techniques, 14, 4219–4238, https://doi.org/10.5194/amt-14-4219-2021, 2021.

Ulrich Platt, J. S.: Differential Optical Absorption Spectroscopy, Springer-Verlag GmbH, https://doi.org/https://doi.org/10.1007/978-3-540-75776-4, 2008.

Valin, L., Russell, A., and Cohen, R.: Variations of OH radical in an urban plume inferred from NO2 column measurements, Geophysical Research Letters, 40, 1856–1860, https://doi.org/10.1002/grl.50267, 2013.

Valin, L. C., Russell, A. R., and Cohen, R. C.: Chemical feedback effects on the spatial patterns of the NO_x weekend effect: a sensitivity analysis, Atmospheric Chemistry and Physics, 14, 1–9, https://doi.org/10.5194/acp-14-1-2014, 2014.

van der A, R. J., Eskes, H. J., Boersma, K. F., van Noije, T. P. C., Van Roozendael, M., De Smedt, I., Peters, D. H. M. U., and Meijer, E. W.: Trends, seasonal variability and dominant NOx source derived from a ten year record of NO2 measured from space, Journal of Geophysical Research: Atmospheres, 113, D04 302, https://doi.org/10.1029/2007JD009021, 2008.

van Geffen, J., Boersma, K. F., Eskes, H., Sneep, M., ter Linden, M., Zara, M., and Veefkind, J. P.: S5P TROPOMI NO_2 slant column retrieval: method, stability, uncertainties and comparisons with OMI, Atmospheric Measurement Techniques, 13, 1315–1335, https://doi.org/10.5194/amt-13-1315-2020, 2020.

van Geffen, J., Eskes, H., Boersma, K., and Veefkind, J.: TROPOMI ATBD of thetotal and tropospheric NO_2 data products, Tech. rep., 5P-KNMI-L2-0005-RP, Issue 2.4.0, available at `https://sentinel.esa.int/documents/247904/2476257/sentinel-5p-tropomi-atbd-no2-data-products`, last access: 18 December 2022, 2022a.

van Geffen, J., Eskes, H., Compernolle, S., Pinardi, G., Verhoelst, T., Lambert, J.-C., Sneep, M., ter Linden, M., Ludewig, A., Boersma, K. F., and Veefkind, J. P.: Sentinel-5P TROPOMI NO_2 retrieval: impact of version v2.2 improvements and comparisons with OMI and ground-based data, Atmospheric Measurement Techniques, 15, 2037–2060, https://doi.org/10.5194/amt-15-2037-2022, 2022b.

Vandaele, A., Hermans, C., Simon, P., Carleer, M., Colin, R., Fally, S., Mérienne, M., Jenouvrier, A., and Coquart, B.: Measurements of the NO_2 absorption cross-section from 42 000 cm^{-1} to 10 000 cm^{-1} (238–1000 nm) at 220 K and 294 K, Journal of Quantitative Spectroscopy and Radiative Transfer, 59, 171–184, https://doi.org/10.1016/S0022-4073(97)00168-4, 1998.

Veefkind, J., Aben, I., McMullan, K., Förster, H., de Vries, J., Otter, G., Claas, J., Eskes, H., de Haan, J., Kleipool, Q., van Weele, M., Hasekamp, O., Hoogeveen, R., Landgraf, J., Snel, R., Tol, P., Ingmann, P., Voors, R., Kruizinga, B., Vink, R., Visser, H., and Levelt, P.: TROPOMI on the ESA Sentinel-5 Precursor: A GMES mission for global observations of the atmospheric composition for climate, air quality and ozone layer applications, Remote Sensing of Environment, 120, 70–83, https://doi.org/10.1016/j.rse.2011.09.027, the Sentinel Missions - New Opportunities for Science, 2012.

Verhoelst, T., Compernolle, S., Pinardi, G., Lambert, J.-C., Eskes, H. J., Eichmann, K.-U., Fjæraa, A. M., Granville, J., Niemeijer, S., Cede, A., Tiefengraber, M., Hendrick, F., Pazmiño, A., Bais, A., Bazureau, A., Boersma, K. F., Bognar, K., Dehn, A., Donner, S., Elokhov, A., Gebetsberger, M., Goutail, F., Grutter de la Mora, M., Gruzdev, A., Gratsea, M., Hansen, G. H., Irie, H., Jepsen, N., Kanaya, Y., Karagkiozidis, D., Kivi, R., Kreher, K., Levelt, P. F., Liu, C., Müller, M., Navarro Comas, M., Piters, A. J. M., Pommereau, J.-P., Portafaix, T., Prados-Roman, C., Puentedura, O., Querel, R., Remmers, J., Richter, A., Rimmer, J., Rivera Cárdenas, C., Saavedra de Miguel, L., Sinyakov, V. P., Stremme, W., Strong, K., Van Roozendael, M., Veefkind, J. P., Wagner, T., Wittrock, F., Yela González, M., and Zehner, C.: Ground-based validation of the Copernicus Sentinel-5P TROPOMI NO_2 measurements with the NDACC ZSL-DOAS, MAX-DOAS and Pandonia global networks, Atmospheric Measurement Techniques, 14, 481–510, https://doi.org/10.5194/amt-14-481-2021, 2021.

Wagner, T., Ibrahim, O., Shaiganfar, R., and Platt, U.: Mobile MAX-DOAS observations of tropospheric trace gases, Atmospheric Measurement Techniques, 3, 129–140, https://doi.org/10.5194/amt-3-129-2010, 2010.

Wallace, J. M. and Hobbs, P. V.: Atmospheric science: an introductory survey, vol. 92, Elsevier, URL `https://www.ebook.de/de/product/4444872/john_m_university_` `of_washington_seattle_u_s_a_wallace_peter_v_university_of_washington_seattle_u_s_a_hobbs_atmospheric_science.html`, 2006.

Wang, P., Richter, A., Bruns, M., Rozanov, V. V., Burrows, J. P., Heue, K.-P., Wagner, T., Pundt, I., and Platt, U.: Measurements of tropospheric NO_2 with an airborne multi-axis DOAS instrument, Atmospheric Chemistry and Physics, 5, 337–343, https://doi.org/10.5194/acp-5-337-2005, 2005.

Williams, J. E., Boersma, K. F., Le Sager, P., and Verstraeten, W. W.: The high-resolution version of TM5-MP for optimized satellite retrievals: description and validation, Geoscientific Model Development, 10, 721–750, https://doi.org/10.5194/gmd-10-721-2017, 2017.

Wittrock, F., Oetjen, H., Richter, A., Fietkau, S., Medeke, T., Rozanov, A., and Burrows, J. P.: MAX-DOAS measurements of atmospheric trace gases in Ny-Ålesund - Radiative transfer studies and their application, Atmospheric Chemistry and Physics, 4, 955–966, https://doi.org/10.5194/acp-4-955-2004, 2004.

World Health Organization: WHO / Air Pollution, URL `https://www.who.int/health-topics/air-pollution`, last access: 10 March 2023, 2023.

Wu, F. C., Xie, P. H., Li, A., Chan, K. L., Hartl, A., Wang, Y., Si, F. Q., Zeng, Y., Qin, M., Xu, J., Liu, J. G., Liu, W. Q., and Wenig, M.: Observations of SO_2 and NO_2 by mobile DOAS in the Guangzhou eastern area during the Asian Games 2010, Atmospheric Measurement Techniques, 6, 2277–2292, https://doi.org/10.5194/amt-6-2277-2013, 2013.

Xue, X., Hu, J., Xiang, D., Li, H., Jiang, Y., Fang, W., Yan, H., Chen, J., Wang, W., Su, X., Yu, B., Wang, Y., Xu, Y., Wang, L., Li, C., Chen, Y., Zhao, D., Kan, H., Ge, J., Huo, Y., and Chen, R.: Hourly air pollution exposure and the onset of symptomatic arrhythmia: an individual-level case–crossover study in 322 Chinese cities, CMAJ, 195, E601–E611, https://doi.org/10.1503/cmaj.220929, 2023.

Zheng, B., Tong, D., Li, M., Liu, F., Hong, C., Geng, G., Li, H., Li, X., Peng, L., Qi, J., Yan, L., Zhang, Y., Zhao, H., Zheng, Y., He, K., and Zhang, Q.: Trends in China's anthropogenic emissions since 2010 as the consequence of clean air actions, Atmospheric Chemistry and Physics, 18, 14 095–14 111, https://doi.org/10.5194/acp-18-14095-2018, 2018.

List of Figures

List of Tables

List of Abbreviations

ADAM	A surface reflectance DAtabase for ESA's earth observation Missions
AERONET	Aerosol Robotic NETwork
AirMAP	Airborne imaging DOAS instrument for Measurements of Atmospheric Pollution
AMF	Air mass factor
AOT	Aerosol optical thickness
B3dCTM	Bremen 3D chemistry transport model
BAMF	Box air mass factor
BIRA	Royal Belgian Institute for Space Aeronomy
BRDF	Bidirectional reflection distribution function
BSAG	Bremer Straßenbahn AG
CAMS	Copernicus Atmosphere Monitoring Service
CEMS	Continuous Emission Monitoring System
COVID-19	Coronavirus disease 2019
DLER	Directionally dependent Lambertian equivalent reflectivity
DOAS	Differential optical absorption spectroscopy
dSCD	Differential slant column density
ECMWF	European Centre for Medium-Range Weather Forecast
EDGAR	Emissions Database for Global Atmospheric Research
EMG	Exponentially modified Gaussian

EPA	Environmental Protection Agency
E-PRTR	European Pollutant Release and Transfer Register
ERA5	European Reanalysis fifth generation
ESA	European Space Agency
FOV	Field of view
FRESCO-S	Fast Retrieval Scheme for Clouds from Oxygen absorption bands – Sentinel
FRESCO-W	Fast Retrieval Scheme for Clouds from Oxygen absorption bands – Wide
FWHM	Full width at half maximum
GEMS	Geostationary Environment Monitoring Spectrometer
GEOS-Chem	Goddard Earth Observing System Chemistry Model
GOME	Global Ozone Monitoring Experiment
IPA	Independent pixel approximation
IR	Infrared
IUP	Institute of Environmental Physics Bremen
LER	Lambertian equivalent reflectivity
LUT	Look-up table
MAX-DOAS	Multi-axis DOAS
MMF	Mexican MAX-DOAS Fit
MPIC	Max Planck Institute for Chemistry
NIR	Near infrared
OFFL	Offline
OMI	Ozone Monitoring Instrument
PAL	Product Algorithm Laboratory
PGN	Pandonia Global Network
REG	Regional

RMS	Root mean square
RPRO	Reprocessed
RTM	Radiative transfer model
S5P	Sentinel-5 Precursor
SCD	Slant column density
SCIAMACHY	Scanning Imaging Absorption Spectrometer for Atmospheric Chartography
SZA	Solar zenith angle
TEMPO	Tropospheric Emissions Monitoring of Pollution
TM5	Transport Model 5
TOA	Top of the atmosphere
TROPOMI	TROPOspheric Monitoring Instrument
UV	Ultraviolet
VCD	Vertical column density
VIIRS	Visible Infrared Imaging Radiometer Suite
VZA	Viewing zenith angle
WRF-Chem	Weather Research and Forecasting model coupled with Chemistry

Acknowledgment

I am very thankful for the opportunity to do my PhD in the DOAS group at the Institute of Environmental Physics of University of Bremen.

First, I would like to thank Prof. John P. Burrows for the opportunity of this PhD and being part of his research group. Thank you for the many opportunities I got during my PhD and for your always good advice and support on my work.

I want to thank Prof. Thomas Wagner for reviewing this dissertation as a second examiner, being part of my PhD committee meetings, and for the helpful comments and discussions on the different occasions.

Special thanks to Andreas Richter for being such a good PhD supervisor. Thanks for your scientific advice, your explanations, and feedback on my work during our weekly meetings, but also always in between, your always open door and quick and supportive email replies. You introduced me to the DOAS world, and I am very thankful for all the opportunities and exchange you made possible. It was always nice being on conferences or campaigns together with you. Your support, ideas, time, and effort made my PhD time special and this thesis possible.

I thank the whole DOAS group, past and present members, for the always nice atmosphere in the last years. There was always someone for any kind of question, valuable discussions, and support in all parts of my work, from learning DOAS, resolving Python issues, and support in lab work and campaigns. Besides that, I also enjoyed the several group activities outside of IUP a lot. Special thanks to Andreas M. and Anja for introducing me to the world of AirMAP, helpful discussions, and late-night email exchanges. Thanks to Andreas M. and Leonardo for always helpful and patient Python support. Thanks to André, Tim, and Lisa for the great time we spent together in the lab and the exchange during the last years. No SCIATRAN AMF runs without Tim, thank you for the always good and quick help. Thank you, Bianca and Sora for being so nice office mates.

I was lucky that I could participate in several measurement campaigns and instrumental work during my PhD time, starting in Vienna, the QA4EO-DE-Ruhr campaign, the GMAP and SIJAQ campaign in Korea, and the tram DOAS project. I am very thankful for these opportunities and would like to thank all the people who participated in these campaigns, who made them possible and of course very special. Besides the DOAS group,

many thanks to the colleagues from Mainz, BIRA, FU-Berlin, and Korea. Many people from the different groups were involved in providing instruments, setting them up, spending hours driving for the car DOAS measurements, providing the data, and having good discussions about the measurement results. These measurements are an important part of this thesis and would not have been possible without every single contribution.
I want to thank the Bremer Straßenbahn AG, who made the tram DOAS installation on one of their trams possible.
Many thanks to the colleagues and friends who (more or less) volunteered to proofread this thesis, you improved it a lot. Thank you, Andreas, Simon, Miri, Sarah, and Morten, for your time and effort.
All in all, my PhD years have been very exciting, with many new experiences, getting to know the DOAS community, and meeting many nice people.
Finally, I would like to thank my friends, family, and especially Morten for the nice time together outside of university but also for listening to and discussing my PhD experiences and issues and always supporting me, especially during these last years.

Eigenständigkeitserklärung

Hiermit erkläre ich, dass ich die vorliegende Arbeit ohne unerlaubte fremde Hilfe angefertigt habe, dass ich weiterhin keine anderen als die angegebenen Quellen und Hilfsmittel benutzt und die den benutzten Werken wörtlich oder inhaltlich entnommenen Stellen als solche kenntlich gemacht habe.

Bremen, Mai 2023

Kezia Lange